GEOPHYSICAL SURVEYS AIMED TO SAVE HUMAN LIVES BY FACILITATING

SAFETY ASSESSMENT

by

Vladislav F. Kaminskiy

B.Sc. Moscow State University, 1999

M.Sc. Moscow State University, 2000

Submitted to the Graduate Faculty of

Geology and Planetary Science in partial fulfillment

of the requirements for the degree of

Doctor of Philosophy

University of Pittsburgh

2008

GEOPHYSICAL SURVEYS AIMED TO SAVE HUMAN LIVES BY FACILITATING

SAFETY ASSESSMENT

Vladislav F. Kaminskiy, M.Sc.

Moscow State University, 2000

UNIVERSITY OF PITTSBURGH

Faculty of Geology and Planetary Science

This dissertation was presented

by

Vladislav F. Kaminskiy

It was defended on

February 21, 2008

and approved by

Thomas Anderson, Professor, Department of Geology and Planetary Science

Ian Skilling, Assistant Professor, Department of Geology and Planetary Science

Michael Rosenmeier, Assistant Professor, Department of Geology and Planetary Science

Rafael Quimpo, Professor, Department of Civil and Environmental Engineering

William P. Harbert, Associate Professor, Department of Geology and Planetary Science

GEOPHYSICAL SURVEYS AIMED TO SAVE HUMAN LIVES BY FACILITATING

SAFETY ASSESSMENT

Vladislav F. Kaminskiy, PhD

University of Pittsburgh, 2008

Two research projects by the Water and Energy Team of the National Energy Technology Laboratory were carried out in collaboration between the US Department of Energy and the University of Pittsburgh. Both projects are related to investigating current and potential impacts of abandoned coal mines on the adjacent populated regions.

The first project was carried out in West Virginia over 14 active and abandoned coal slurry impoundments (Appendix A) in order to remotely investigate their current condition and potential hazards related to the mine-waste pools. Three main scenarios of impoundment failure are overtopping of the impoundment, internal erosion (piping) and entry of unconsolidated material into adjacent mine voids due to subsidence. To characterize these potential hazards, helicopter-mounted electromagnetic (HEM) surveys were completed to identify fluid saturated zones within coal waste and to delineate the paths of filtrate fluid flow. Attempts were also made to identify flooded mine workings underlying the impoundment areas. A total of 431 flight lines were processed, each from 2 to over 4 km in length, in total more than 1300 line-kilometers of HEM survey. Follow-up, ground-based resistivity surveys verified the results of the HEM investigations. The HEM and ground-based geophysical surveys proved to be effective in delineating the phreatic surface, determining seep locations, imaging areas of unconsolidated slurry, locating areas where process water has invaded adjacent aquifers, potentially depicting the possible location of flooded underground mine workings and locating infiltration zones.

The second project took place in southwestern Pennsylvania. In order to image beneath the surface and identify zones of possible gas accumulation and migration routes, reflection seismic surveys were completed in this area. Seismic imaging was successful in identifying regions of subsurface gas accumulation. Because of the urban nature of the survey, it was very challenging to collect and process seismic reflection data.

TABLE OF CONTENTS

LIST OF TABLES

LIST OF FIGURES

PREFACE

Both geophysical approaches described in this dissertation were targeted to study processes known to cause loss of human lives in the past. In the first project the survey flown with Fugro Resolve™ multi-frequency electromagnetic system was interpreted in terms of potential hazards, caused by construction and development of coal refuse impoundments. Their potential to fail was examined from a new prospective, leading to multiple opportunities for further development in this direction such as performing remote impoundment safety assessment based only on geophysical data.

In the second project, 3D reflection seismic survey was carried out in urban setting. The complexity of the study problem was related to many uncertainties involved including unknown source of methane, unknown release mechanism and unknown subsurface distribution within reservoirs of unknown depth and geometry. Therefore studies, in addition to 3D seismic reflection survey, emphasized in this dissertation, were carried out including: marine seismic profiling, geochemical surveys (Thomas et al, 2007), magnetic surveys (Hammack and Veloski, 2006), trace CH_4 gas analysis, geologic reconnaissance, rock tests and groundwater modeling.

1. FIRST PROJECT (COAL WASTE IMPOUNDMENTS STUDY)

1.0. INTRODUCTION

1.0.0. Preface

On February 26, 1972, a coal waste impoundment on Buffalo Creek in West Virginia collapsed, releasing approximately 500 million liters (132 million gallons) of water (Davies et al, 1972). The resulting flood killed 125 people, injured 1,100, and left more than 4,000 homeless. Factors contributing to the impoundment failure included heavy rainfall and deficiencies in the foundation of the dam that led to slumping and sliding of the waterlogged refuse bank. This disaster resulted in regulations that govern the design of embankment structures for new impoundments (National Research Council, 2002). Since the implementation of regulations, no new embankments have failed. However, other types of impoundment failure have released water and coal slurry into streams. Some of these involved the breakthrough of water and coal slurry from impoundments into underground mines. The most notable incident occurred on October 11, 2000 near Inez, Kentucky where 946 million liters (250 million gallons) of water and 117 million liters (31 million gallons) of coal slurry from an impoundment broke into an underground mine and flowed via mine workings into local streams (National Research Council, 2002). Aquatic life was destroyed along kilometers of stream and temporary shut downs were imposed on a large electric generating plant and numerous municipal water treatment facilities. This incident caused Congress to request the National Research Council to examine ways to reduce the potential for similar accidents in the future. In Appendix B all known impoundment spills are summarized. The report is called "Coal Waste Impoundments, Risks, Responses, and Alternatives" (National Research Council, 2002) documents the findings and recommendations of the National Research Council.

Figure 1. (A): Regional map showing the counties of West Virginia. (B): Higher resolution map showing the location of the HEM surveys. The three sites discussed in detail in this manuscript are outlined.
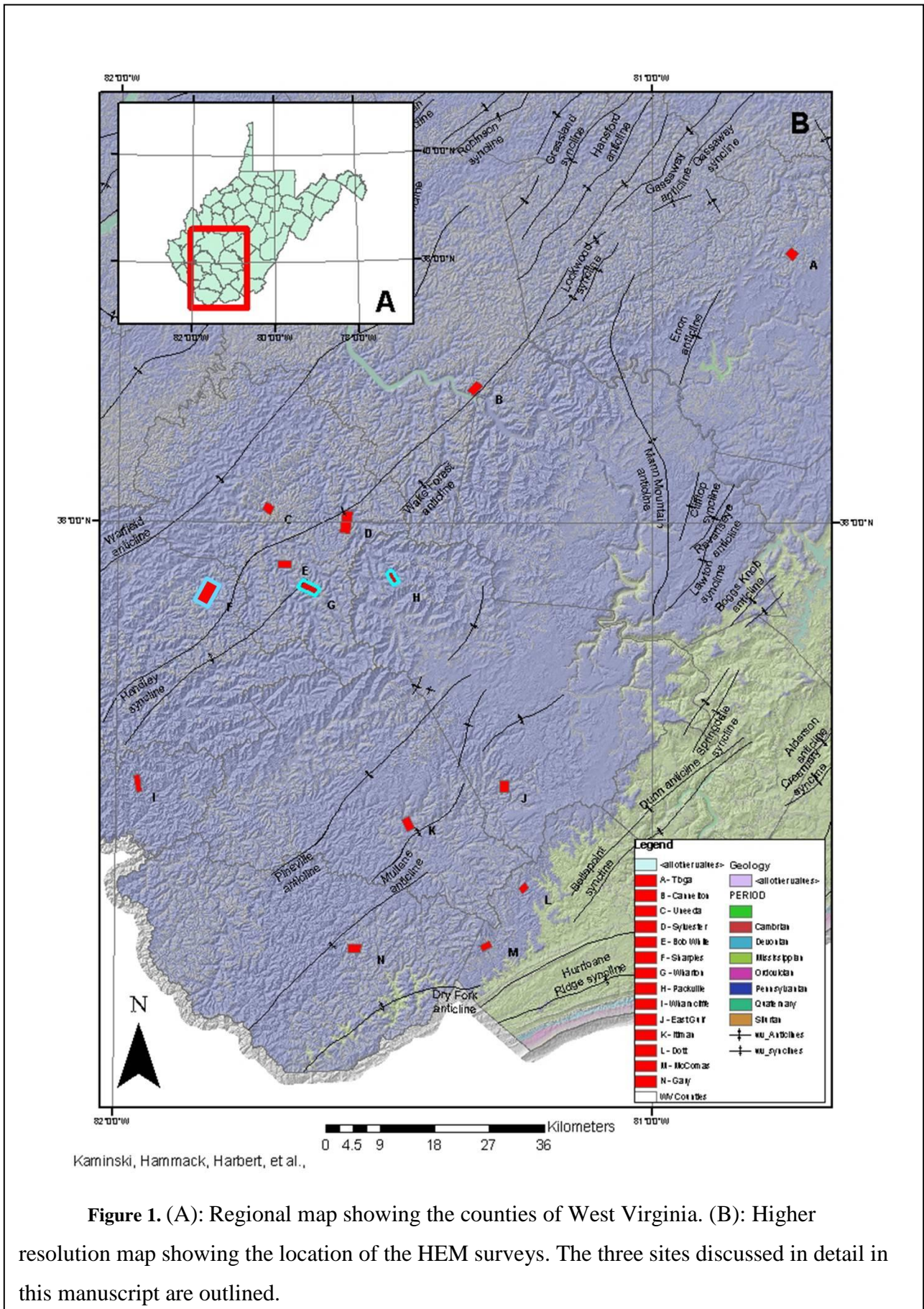
In response to the recommendations of the National Research Council, the National Technology Transfer Center (NTTC) at Wheeling, West Virginia contracted Fugro Airborne Surveys to conduct helicopter electromagnetic (HEM) surveys of 14 coal waste impoundments in southern West Virginia (Figure 1). The Water and Energy Team of the United States Department of Energy (DOE), National Energy Technology Laboratory (NETL) was asked to process, interpret, and validate survey data. These surveys were part of a federally funded pilot project to help reduce the dangers of coal slurry impoundments by identifying saturated zones within the coal waste, delineating the paths of filtrate flow beneath the impoundment, through the embankment, and into adjacent strata or receiving streams and identifying flooded mine workings underlying or adjacent to a waste impoundment. Such information could be useful for predicting impoundment failures or detecting possible impoundment-related contamination of local streams and aquifers.

1.0.1. Construction of a coal waste impoundment

A coal refuse impoundment is a structure designed to accommodate waste material accumulated from a coal-producing mine. It consists of two major elements: the basin and the embankment (Figure 2). The basin is bounded on the upstream side by valley walls and on the downstream side by the embankment. Basin is underlain by fine-grained coal waste, which is delivered to the upstream side of the embankment via a slurry pipeline and released at a spigot point. The spigot point is moved periodically across the embankment face, thereby creating a series of coalescing, delta-like depositional structures where coarser material accumulates in the vicinity of spigot point and finer material is carried further away. The flooded portion of the basin is sometimes called a ''decant pond'' because clarified water is returned to the coal cleaning plant for reuse when sedimentation is complete.

The embankment is a dam-like structure that consists of coarse-grained coal waste sometimes mixed with clay or gravel to adjust its hydraulic permeability (k) in order to route groundwater drainage to a scheme designed by geotechnical construction of the dam.

4

Figure 2. An aerial photograph of an upstream raised coal waste impoundment; two main components are outlined here: basin and embankment.
(http://www.appvoices.org/images/MarshForkAerial_full.jpg)

While the impoundment is active, the embankment is constantly being raised to provide more space for coal waste disposal. There are three types of coal refuse impoundment embankment rising and these are:

   A) Upstream, the most common type for coal waste impoundments.
   B) Downstream, which is the most stable structure and is used at sites with high ratios of coarse to fine coal waste.
   C) Centerline, which is a compromise between upstream and downstream (Figure 3).

An upstream embankment is raised by placing lifts of coarse material on the top of the embankment and on the fine refuse in the basin near the embankment. The area of the basin where coarse coal waste is mechanically placed over unconsolidated fine coal waste is termed a "push-out". A key factor in embankment stability is the control of internal erosion, or piping, and erosion of the downstream face of the embankment.

Figure 3. Impoundment types showing (A): Upstream type, (B): Downstream type, (C): Centerline type.
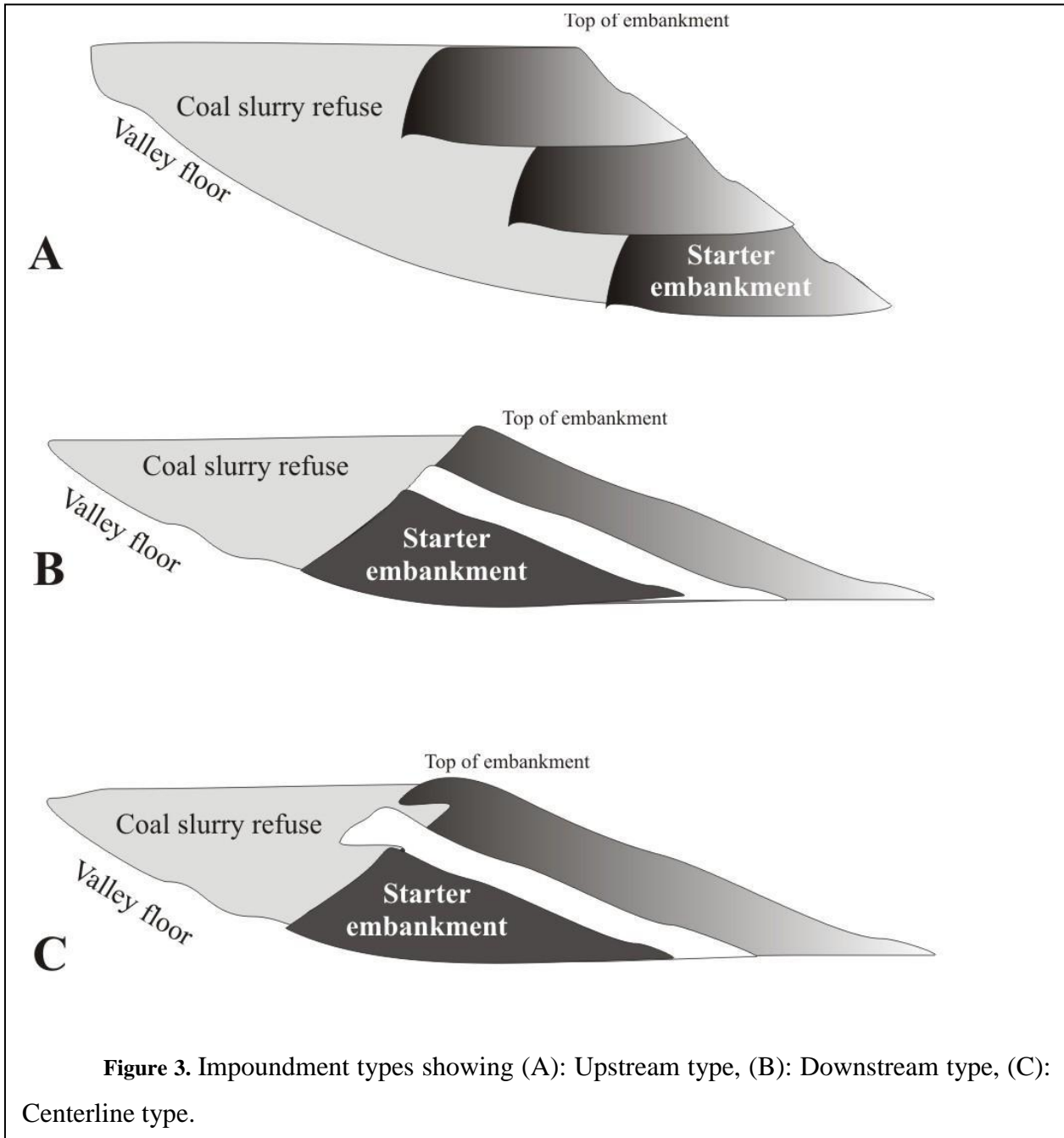
In some cases subsurface drains are installed to intercept seepage and safely convey it away from the embankment face. The embankment is designed to prevent migration of fines and to minimize water pressure and potential for piping on the downstream side of the embankment (National Research Counsel, 2002).

Piping is an underground erosion and natural drainage process, which can occur when there are openings large enough for soil particles to be washed into them and transported with the seeping water. Minimizing piping can be accomplished by the installation of filter and drain zones within the embankment that collect and route water to a downstream part of the embankment called toe (National Research Counsel, 2002). In addition to the "toe drain", there are several other drain types, including "chimney drains", "finger drains", and "blanket drains". Monitoring filtrate propagation through the coarse coal refuse and engineered drains is an important aspect in evaluating safety of an impoundment.

1.0.2. Failure models

Failure models of a coal slurry impoundment include embankment failure and basin failure. An embankment or basin can each fail in a number of ways. Most widely spread scenarios of embankment failure are due to internal erosion, earthquake effects and slope instability, while most likely scenarios of basin failures are leakage due to subsidence and overtopping. A primary factor differentiating causes of failure is the type of embankment construction. Failure causes differ between upstream and downstream types of construction. Slope instability and earthquake effects dominate among failures of upstream embankments, while foundation failure is more likely to occur in downstream-type embankments (Saxena, 1994; National Research Counsel, 2002).

Overtopping is another cause of impoundment failure, and results when the inflow exceeds the storage capacity of the impoundment. Overflow can occur when the basin is not constructed with sufficient capacity to contain large storm inflow or when engineered spillways are inadequate (ICOLD, 2001). Basin failure is most likely to occur in areas where current or past mining is in close proximity to the impoundment (Figure 4). Unfortunately, the location of underground mines is often poorly known due to lack of information. Factors that must be considered for prevention of basin failure are: subsidence, excessive seepage, and internal erosion. Subsidence disturbs the strata above and adjoining the mining area. It results in the opening of tensile cracks on the surface,

displacement along faults and joints, and some distortion of the strata around the working. The immediate roof tends to cave into the mine and the floor may heave (National Research Counsel, 2002).

Figure 4. Failure model of coal waste impoundment due to subsidence (Kaminski et al, 2006).
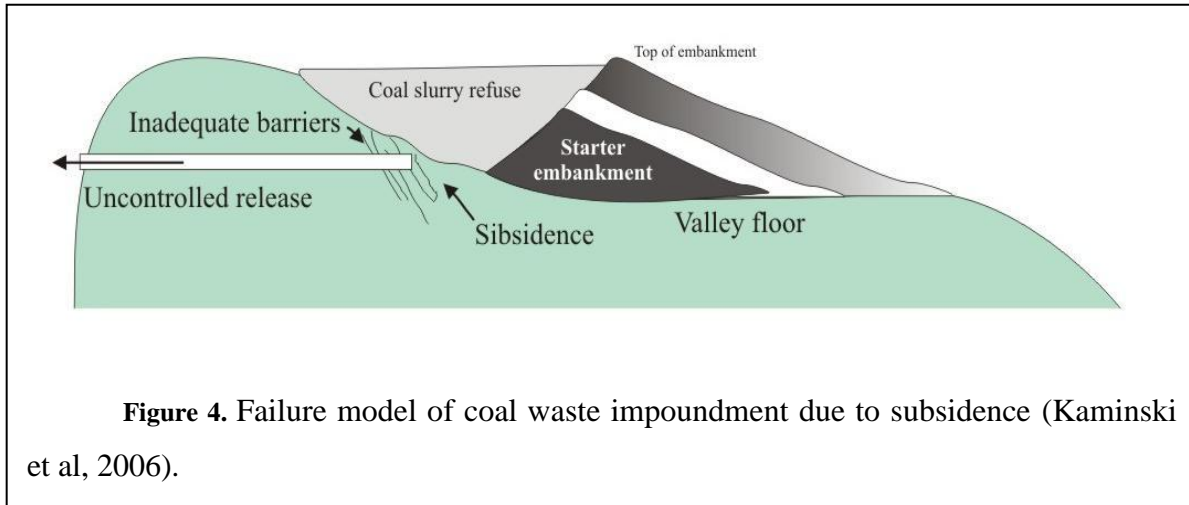
In summary, important factors responsible for impoundment failure include those related to leakage, naturally occurring joints and fractures, overflow, foundation failure, subsidence-induced tension or shear cracks and fractures at the bottom of the decant pond, sinkhole or pit subsidence, piping, or failure related to a catastrophic seismic or storm event (Saxena, 1994; National Research Counsel, 2002). Most of these factors and other possible modes of failure can be identified by electromagnetic geophysical surveys and mitigated. Hence accurate collection and processing of geophysical data can eliminate the need of invasive investigation methods in future.

1.1.   GEOLOGIC SETTING AND HISTORY

1.1.0.   Preface

Our study area is located in Southern West Virginia, which is a key-zones for coal production in the United States. The controlling factors of wide distribution of economical coals in the eastern United States are the paleoclimate and paleogeography of this region. It is of great importance to understand the origin and the evolution of the controlling structures and stratigraphic sequences of the region in order not only to adequately interpret geophysical data, but also to be able to predict the extent and magnitude of potential failure of coal refuse impounding structures based on geotechnical characteristics of the surrounding rocks and on their relative emplacement. This chapter provides a brief overview of the tectonic history and the stratigraphy of the study area.

1.1.1.   Tectonic history of Appalachians

The Paleozoic history of the Appalachians includes many geologic events following the breakup of Rhodinia (about 800 - 600 m.y.) such as transgressions, regressions and orogenies. Most of the present North American plate was located on what was then a piece of the supercontinent Laurentia. Laurentia took part in 3 major orogenic events that created the Appalachian orogenic belt. These events were Acadian orogeny (Ordovician), Taconic orogeny (Devonian) and the Allegheny orogeny (Permian) (Hatcher, 1989; Valentino et al, 1994).

During the Cambrian, Laurentia was surrounded by slowly subsiding passive rift margins and experienced extensive transgression characterized by the deposition of carbonates. This transgression continued into the Ordovician, followed by a major regression, which exposed the lower Ordovician and Cambrian sediments to rapid erosion, as there were no plants on the landmass. While the carbonates weathered, erosion reworked a substantial amount of exposed quartz sandstones. Later in Ordovician another transgression occurred, during which sea level changed by an estimated factor of some 100 meters. This alternation of transgressions and regressions left a notable. (Prothero and Dott, 2002)

During the middle to late Ordovician the Taconic orogeny occurred between 470 - 440 m.y. (Prothero and Dott, 2002). The Taconic plate, which approached Laurentia, was a volcanic arc. At that time eastern Laurentia was transitioning from a passive to active margin state and terrestrial red bed deposition took place, depositing red beds. Evidence of Taconic orogeny include volcanic ashes, ophiolites, flysh sequences (marine shales and sandstones, coarsening upward) and molasse indicating transition to a non-marine phase of sedimentation (Hatcher, 1989; Jones, 2005).

High sea level was maintained throughout the Silurian, when carbonates were widely deposited, but was followed by major regression in the Devonian eroding these carbonates (Jones, 2005). The Acadian orogeny took place 400 to 360 m.y. Limestones found in West Virginia suggest continuing transgression, while conglomerates in the East Appalachians indicate a forming forearc basin, which formed in front of a mountain belt. Uplift created a widespread regional unconformity. The Acadian orogeny also created multiple granite massifs. It is suggested that a thin strip of crust (Avallonia) drifted away from Africa to collide with Laurentia thus causing this orogenic event (Prothero and Dott, 2002).

During the Mississippian period no major tectonic events took place in the Appalachian region. Sea level experienced variations, but major continental flooding became rare and black carbonaceous shales accumulated throughout the Appalachians. In the early Pennsylvanian period regression exposed more land. The Pennsylvanian period is also famous for its cyclic sedimentation pattern responsible for creation of sequences called

cyclotherms. The following is a typical cyclotherm sequence from bottom to top: (Valentino et al, 1994; Jones, 2005).

1. Erosional surface at base
2. Sandstone with or without conglomerate
3. Shales, thin sands, coal seams.
4. Shale in a transition from non-marine to marine facies.
5. Marine limestone followed by shale in transition from marine to non-marine facies
6. Erosional surface

Units 1 to 4 in this sequence usually reveal logs, stems, leaves, bits of carbon and other evidence of non-marine sediment deposition.

Another orogenic event occurred in the Permian (250 - 260 m.y.). While much of North America was above sea level, Africa collided with it during the assembly of Pangea (Prothero and Dott, 2002). Evidence of this orogenic event includes folds in Permian aged rocks and an unconformity between the Pennsylvanian and the Permian strata throughout the southern Appalachians. Another distinctive feature of the Allegheny orogeny in Appalachians is Southwest-Northeast trending regional thrust faulting, indicating a maximum principle stress oriented in a Northwest - Southeast direction (Jones, 2005).

1.1.2. Stratigraphy and depositional environments

The surface geologic coverage of southern West Virginia, in general, is represented by Ordovician, Silurian Devonian, Mississippian and Pennsylvanian systems. The region of this study is limited to the extent of Boone, Kanawha, Logan, McDowell, Mercer, Mingo, Raleigh and Wyoming counties in West Virginia. Strata exposed in these counties are the lower Pennsylvanian series, except for Mercer County, where the contact is exposed between the lower Pennsylvanian and the upper Mississippian series. The Mississippian – Pennsylvanian boundary has been defined lithically and biostratigraphically at the

conformable contact between the Bluestone and the Pocahontas formations (Figure 5) (Cooper, 1944). Figure 5 shows a stratigraphic column including the boundary between the Mississippian and the Pennsylvanian systems.

Pocahontas formation

The Pocahontas formation (Figure 6) has a maximum thickness of up to 400 ft (122 m). It is truncated by a large unconformity at the base of the overlying New River formation. The base of the Pocahontas formation is characterized by medium-dark gray calcareous siltstones and shales, which coarsen up and grade into very fine grained ripple-marked sandstones (Englund et al, 1986). These beds are prodeltaic and grade upward to coarser distal-bar sediments of a propagating delta (Englund et al, 1979, 1986). Fossils found in this member include abundant and diverse marine invertebrates, such as trilobites, echinoid spines, several species of gastropods and coiled mantiloids (Gordon and Henry, 1981). Some coal beds including the Squire Jim coal, Simmons coal and Langraff coal (Milici et al, 2004) are present at the bottom of the formation but not widespread.

The overlying sandstone members consist of slumped, delta-front siltstone and sandstone succeeded by massive, channel fill sandstones of a distributary lobe (Englund et al, 1979). These sandstones contain five commercially valuable coal beds known as the Pocahontas 1 to 5 (Figure 6). Further upward these sandstones coarsen to massive quarts arenite interbedded with coal seams (Pocahontas 6, 7 and Goodwill) (Milici et al, 2004). The upper member of Pocahontas formation contains several shale beds as well as Pocahontas 8 and 9 coal beds with abundant, well-preserved compression and impression floras (lepidodendron, etc) (Englund et al, 1986).

Era	Group	Formation	Individual units
LOWER PENNSYLVANIAN	Pottsville	New River FM (maximum thickness: 900 ft)	Nutell sandstone
			Sewell coal
			Welch sandstone
			Welch coal
			Upper Raleigh sandstone
			Little Raleigh coal
			Lower Raleigh sandstone
			Beckley coal
			Quinnimount sandstone
			Fire Creek coal
			Pinevillesandstone
		Pocahontas FM (maximum thickness: 400 ft)	Pocahontas # 9 coal
			Pocahontas # 8 coal
			Flattop mount sandstone
			Goodwill coal
			Pocahontas # 7 coal
			Quartz arenite bed
			Pocahontas # 6 coal
			Quartz arenite bed
			Pocahontas # 6 coal
			Pocahontas # 5 coal
			Pocahontas # 4 coal
			Pocahontas # 3 coal
			Pocahontas # 2 coal
			Pocahontas # 1 coal
			Langdraff coal
			Simmons coal
			Squire Jim coal
			Lower sandstone member of Pocahontas

Figure 5. Stratigraphic column for lower Pennsylvanian rocks in West Virginia based on cross-sections of Mercer and Wyoming counties (Englund et al, 1986; Milici et al, 2004).

Pocahontas Formation outcrops

Figure 6. Outcrops of Pocahontas formation (light blue) in Southern West Virginia (WVGES, 1968).

New River Formation outcrops
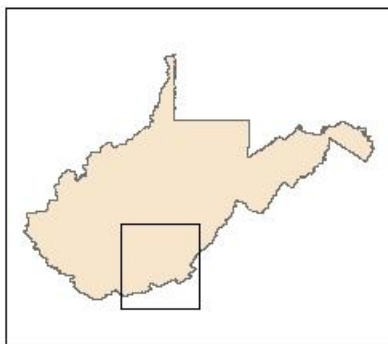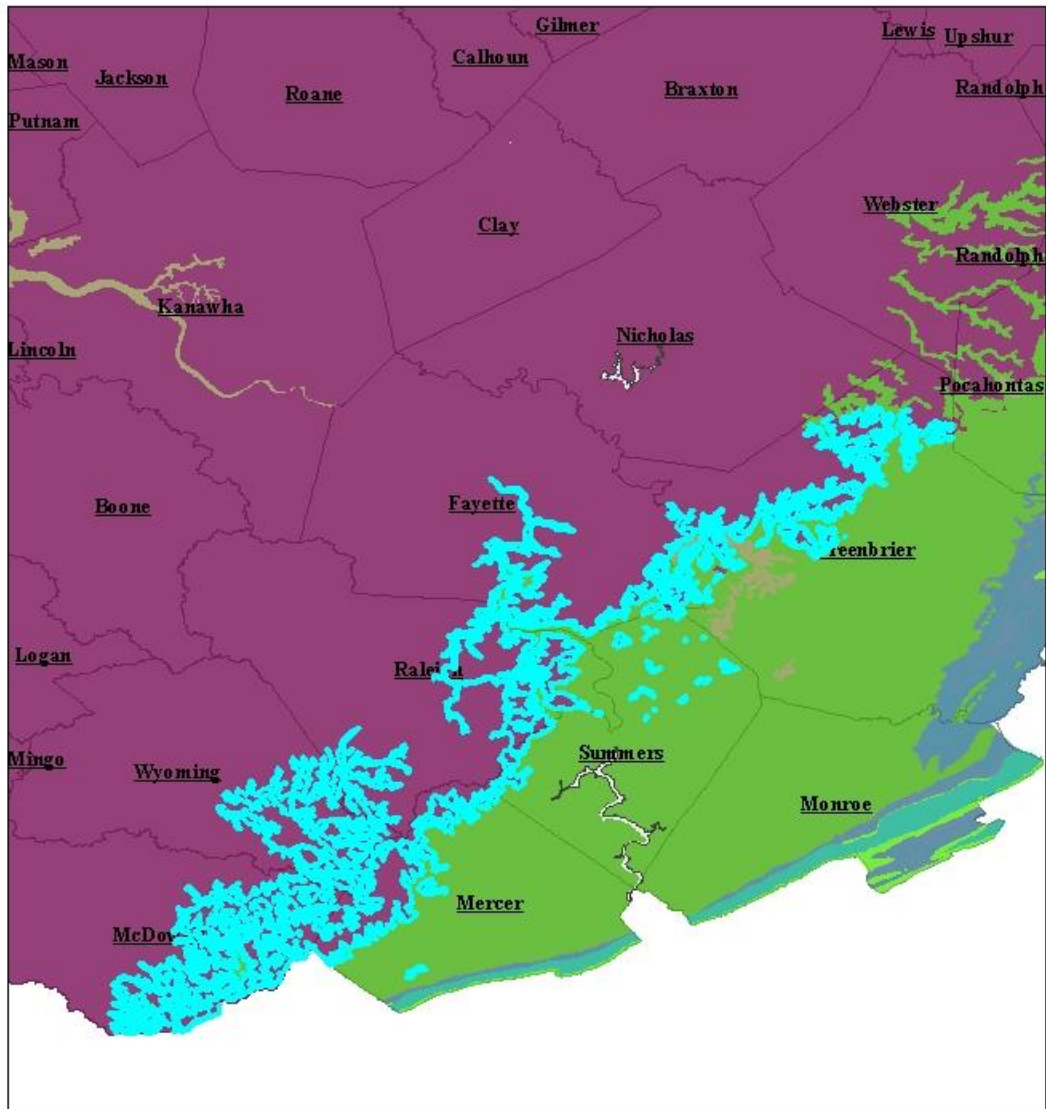
GEOLOGICAL PERIOD

- Cambrian
- Devonian
- Mississippian
- Ordovician
- Pennsylvanian
- Quaternary
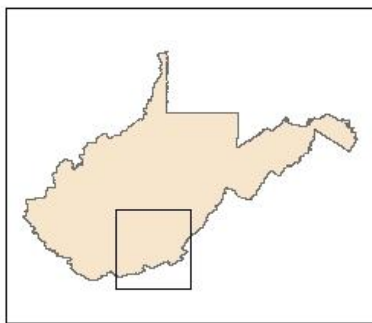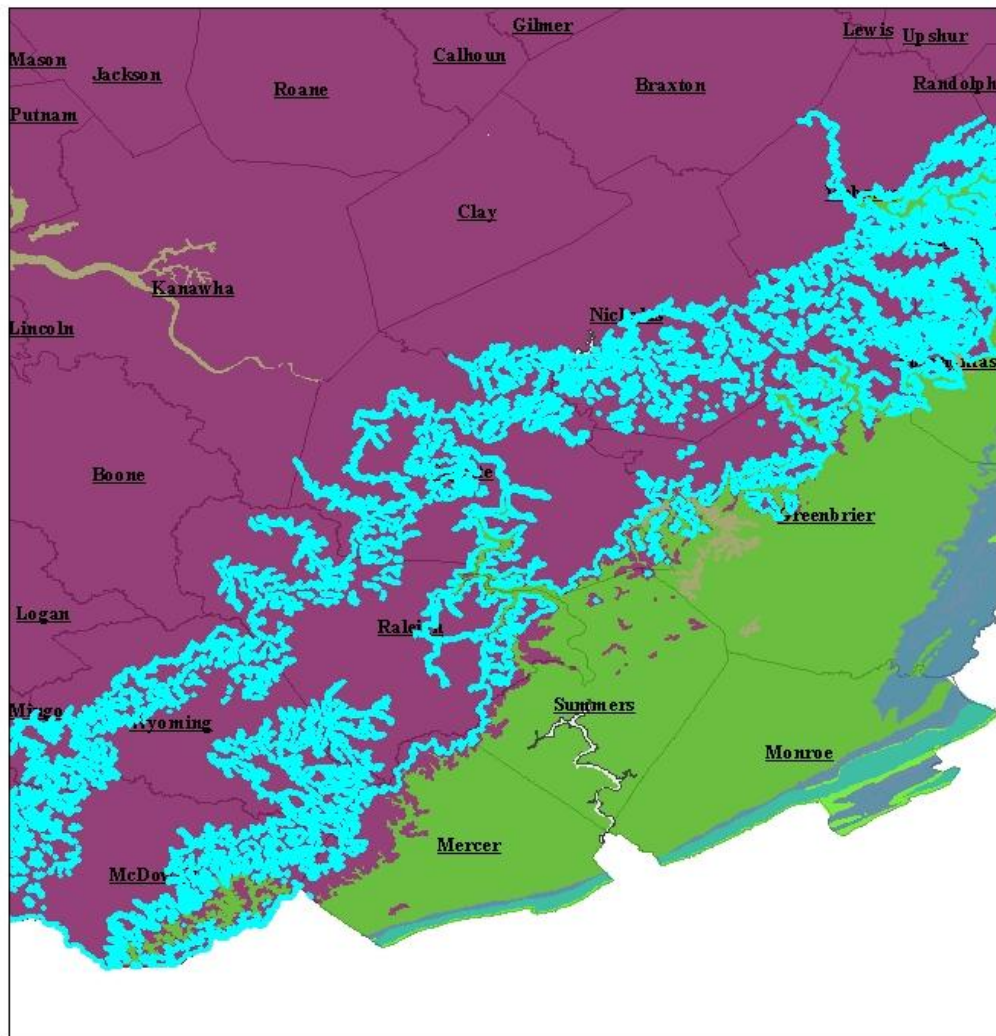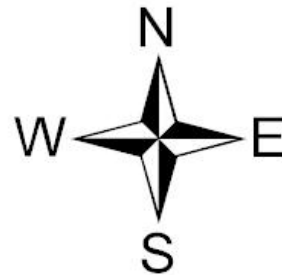
Figure 7. Outcrops of New River formation (light blue) in Southern West Virginia (WVGES, 1968).

New River formation

The entire New River formation is stratified from the top of the Pocahontas to the base of the Kanawha formation and reaches 900 ft (274.5 m) in thickness (Figure 7). The New River formation unconformably overlays the Pocahontas formation, with the Pineville sandstone member located at the base (Figure 5). The New River formation includes several beds of quartzose and conglomeratic sandstone. Intermediate beds consist of shale, siltstone, sandstone, coal and clay of back-barrier facies, including bay-fill sediments, which are flaser-bedded. Coal beds in this sequence are widespread, thin and include Fire creek coal, Beckley coal, Raleigh coals, and Sewell coal. The Nutell sandstone member (uppermost member of the New River formation) consists of quartzose sandstone of a barrier-bar complex. Fossil plants and fresh-water invertebrates including alethopteris, neuropteris, shpenopteris and stigmaria occur in several beds of the formation (Englund et al, 1986).

Kanawha formation

The contact between the New River and the overlying Kanawha formation is exposed in some areas of McDowell, Boone, Logan, Kanawha, Clay, Braxton, Wyoming and other counties in West Virginia (Figure 8). This contact also forms a boundary between the lower and the middle Pennsylvanian series (Fedorko and Blake, 1998) and is marked by a lithologic change from a sequence dominated by the quartzose, conglomeratic sandstone of the New River formation to a largely bay-fill, black-river sequence of shale, siltstone, sandstone (Englund et al, 1986). The total thickness of Kanawha formation reaches 620 m (2000 ft) (Figure 9) containing coals and impure limestones that accumulated in a subsiding foreland basin.

The lower part of Kanawha formation is mainly composed of medium-dark-gray shales, including the Douglas and Gilbert shales (Fedorko and Blake, 1998), thin crevasse-splay sandstone (McClure sandstone) and numerous coal beds, including the Lower Douglas, Douglas, Aily and Gilbert coals (Fedorko and Blake, 1998) typical for a lower-delta plain environment. The overlaying Eagle member is composed of calcareous sandy siltstone with

abundant marine fossils. On top of this member are cross-bedded silty shale, siltstone and fine-grained sandstone of the Crummies member contacting with No 2 gas coal bed, above which thick distributary channel sandstones predominate (Figure 9). The next member is dark-gray calcareous shale including the Dingess member and an unnamed marine zone with brachiopods and other marine invertebrates (Henry and Gordon, 1979; Fedorko and Blake, 1998). The overlaying Winifrede limestone member consists of calcareous shale with diverse marine faunae including brachiopods, gastropods and pelcypods (Henry and Gordon, 1979), while the shale underlying Coalburg coal seam has abundant plant impressions of lipidodendron and shpenopteris.

Paleoclimate

In terms of the paleoclimate and depositional environment interpretation, a chain of transgressive/regressive cycles can be recognized (Donaldson and Eble, 1991). Minor cycles show average duration of 2.5 - 3.0 m.y. and are represented by stratigraphic record over 100 m in thickness. These cycles are viewed as probably the result of changes in glaciations, which frequently occurred in Pennsylvanian time, inducing transgressions and regressions. Major cycles average 15 m.y. in duration and 550 m in thickness. They correspond to the boundaries between the Lower Pennsylvanian (Pocahontas formation and New River formation) and the Middle Pennsylvanian (Kanawha formation). Loading of the convergent continental margin caused by stacking of thrust sheets is thought to have initiated each major cycle (Donaldson and Eble, 1991).

The fossil record indicates that West Virginia, before the Allegheny orogeny (Permian), formed a tropical coastline, and underwent significant tidal processes, as well as extensive flooding events, due to its near-sea-level elevation (Martino, 1996). These processes are responsible for the formation of peat swamps, where coal seams ultimately formed.

Kanawha Formation outcrops
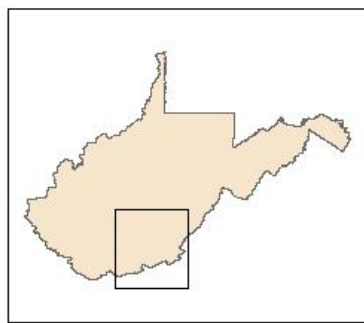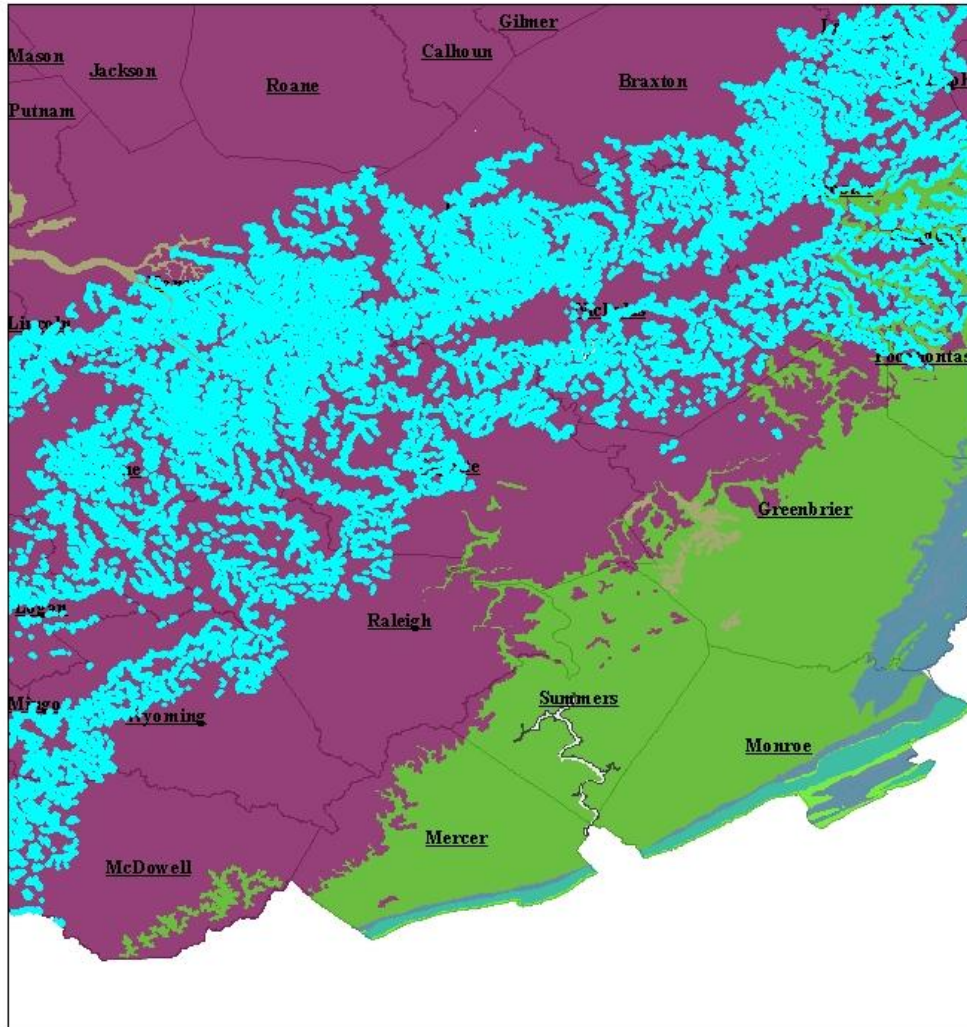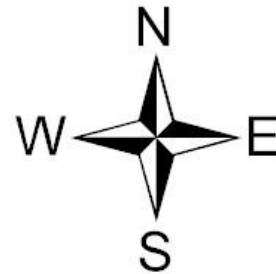
Figure 8. Outcrops of Kanawha formation (light blue) in Southern West Virginia (WVGES, 1968).

18

Era	Group	Formation	Individual units
MIDDLE PENNSYLVANIAN	Pottsville	Kanawha FM (maximum thickness: 2000 ft)	Kanawha Black Flint
			Stockton coal
			Coalburg coal
			Little Coalburg coal
			Winifrede Coal
			Winifrede shale
			Chilton coal
			Unnamed marine zone
			Fire clay coal
			Cedar grove coal
			Dingess shale
			Williamson coal
			Campbell creek limestone and shale
			Peerless coal
			Number 2 gas coal bed
			Powellton coal
			Crummies member
			Eagle coal
			Eagle limestone
			Betsie shale
			Matewan coal
			Middle war eagle coal
			Unnamed coal
			Oceania limestone
			Gilbert shale
			Gilbert coal
			Unnamed marine zone
			Duglas coal
			Douglas shale
			McClure sandstone
			Aily coal
			Lower Douglas coal

Figure 9. Stratigraphic column of Kanawha formation featuring detailed description of individual beds present throughout the extent of this formation (Martino, 1996; Fedorko and Blake, 1998).

1.2. BASICS OF ELECTROMAGNETIC SURVEYING

1.2.0. Preface

Each geophysical method is based on measuring some physical properties of geologic strata. The nomenclature associated with classification of geophysical methods contains emphasis on a particular physical property that the method aims to recover. For instance electromagnetic (EM) methods are capable of recovering magnetic and electric properties of the Earth: susceptibility and conductivity, from which, the conductivity studies will be mainly emphasized further. The task of this chapter is to provide adequate understanding of the physical meaning of this property, factors controlling electric conductivity in the rocks and how knowledge of spatial distribution of the conductivity in the subsurface can be translated to information describing geotechnical and hydrologic conditions of particular structures.

1.2.1. Electrical conductivity

Specific electrical resistivity of a substançe is quantitatively described as the resistance of a substance to the flow of electric current (Halliday, 1960). Physically, resistivity is proportional to the cross-sectional area of the cube and is in reverse proportion to the length of current path. Resistivity is measured in Ohm-meters (Ohm*m) and will be further referred to as ρ. The inverse value, σ, $= 1/\rho$ is called electrical conductivity and is measured in Siemens per meter (S/m). However Siemens is a large value, therefore a more widely used value is mille-Siemens per meter (mS/m), equal to 10^{-3} S/m.

Two main types of electrical conductance exist: ionic conductance and electronic-hole conductance (Yakubovsky and Lyahov, 1988). Ionic conductance can be described as ability of the medium to conduct directed motion of free ions (usually electrons), excited by an electric field. Electronic-hole conductance is a specific case of electrical conductance in

semiconductors, where atomic bonds are strong enough to restrict electrons from free travel. Under stronger field electrons can leave their original positions and join the outer electronic orbit of the neighboring atom thus filling a "hole" (the lack of electron in an outer orbit) and at the same time creating a "hole" available to be filled by another excited electron (Getman, 1943). Materials with the latter conductance type are called semiconductors, from which the most widely known is silicon (Yakubovsky and Lyahov, 1988).

Silicon is one of the main components of the Earth crust. The resistivity of geologic material, including silicate minerals ranges from 10^6 to 10^{15} Ohm*m, while the electrical resistivity of fluids ranges very widely. Pure water is a well known dielectri*c* material with a dielectric constant of 81 (dimensionless value also referred to as relative static permittivity), therefore the resistivity of pure water is extremely high and can reach 10^6 Ohm*m. Generally, the pore-filling fluid is a water-based solution of mineral salts. Mineral salts such as NaCl, are excellent sources of free electrons, which can be transported even by a weak electric current, therefore dissolved solids amount in solution directly affects the resistivity of fluid and ranges between 10^{-2} and 10^2 Ohm*m (10 to 10000 mS/m) (Yakubovsky and Lyahov, 1988; Mavko et al, 1998). This phenomenon became basic for multiple applications of electrical geophysical methods designed for mapping of water saturated geologic units based on their total dissolved solid (TDS) content (Fitterman and Deszcz-Pan, 1998; Hammack and Mabie, 2002; Paine, 2003).

Electric current flow paths are guided by the lowest electric conductivity available through the material (Yakubovsky and Lyahov, 1988). Therefore in water saturated rocks current mainly flows through the pore-filled fluid. Generally, the electric resistivity of a rock is a function of its water-saturation and conductivity of pore-filling fluid. In cases where the pore space is not interconnected electrical current has to travel through the rock matrix, and the decrease of porous space thereby leads to increase in electric resistivity of a rock.

Pore size plays a significant role in the electrical processes occurring on the boundary between matrix and fluid, where ions (usually negatively charged) are adsorbed and strongly bound to the rock matrix in the form of Electrical Double Layer (EDL, Figure 10) (Mavko et al, 1998). In general, the EDL is electrically neutral, unless an external electric current is introduced (Yakubovsky and Lyahov, 1988). However in the vicinity of the EDL the concentration of free ions available to carry electric charge is much higher, therefore the electrical conductivity of a rock is greater in rocks with a maximum EDL coverage (i.e. smaller pore size) (Yakubovsky and Lyahov, 1988; Shevnin et al, 2006). There is also a dependence between rock temperature and material electrical properties (Pabitra and Goode, 1992).

Summarizing the above, any rock type, as an electric conductor, can be described as a combination of the electric conductivity of the rock's solid component and the conductivities of fluids filling the pore space. As a consequence, the total electrical conductivity of a rock is sensitive to:

Figure 10. Electric Double Layer in micropores.
http://micromachine.stanford.edu/~dlaser/research_pages/silicon_eo_pumps.html.
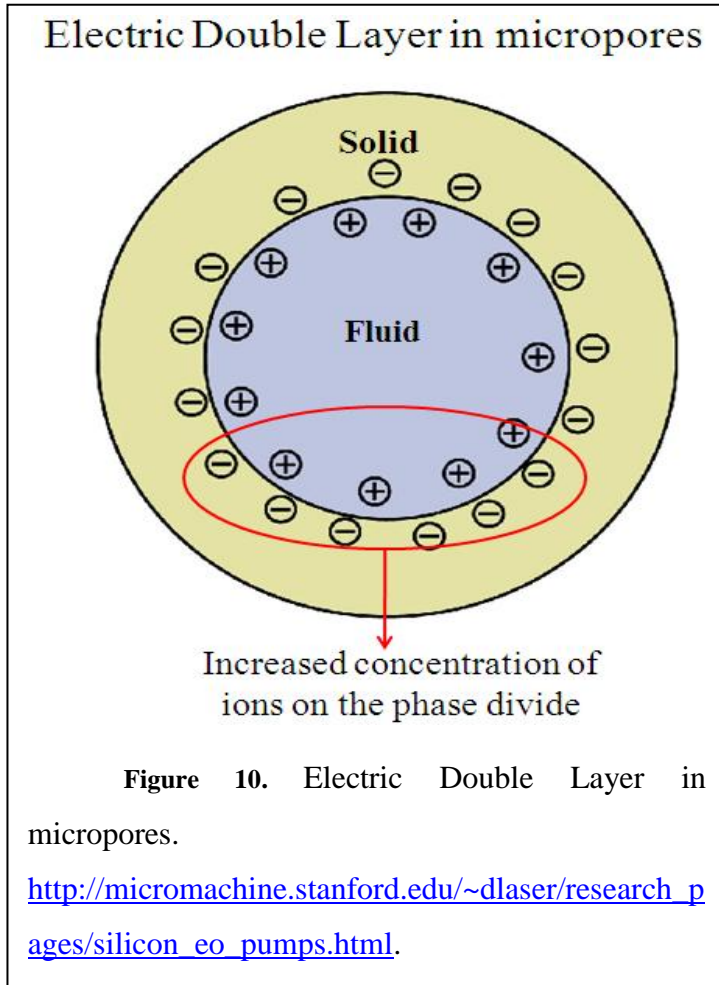
a. Water saturation of the rock,

b. Porosity of the rock,

c. Structure of the rock (pore size, shape, isotropy/anisotropy),

d. Interconnectivity of the pore space,

e. Temperature (Yakubovsky and Lyahov, 1988; Pabitra and Goode, 1992; Mavko et al, 1998; Shevnin et al, 2006).

1.2.2. Theory of electromagnetic soundings

Electromagnetic (EM) methods are based on the phenomenon of Electromagnetic induction. These methods study the behavior of electromagnetic fields, created by alternating currents, derived from technogenic or natural sources. EM studies can be done in both frequency and time domain.

In a standard application of the frequency domain EM method (FEM), an alternating harmonic electric current (AC) is passed through a transmitter coil (Tx). If the shape of the transmitter coil is circular, the coil can be described as a magnetic dipole (Griffith, 1999), inducing a primary magnetic field (H_p). The primary magnetic field is translated into the subsurface where it induces eddy currents (I_e) in conductive bodies (Figure 11). Eddy currents then create secondary magnetic fields (H_s), which are out of phase with respect to the primary field. Both, the primary and secondary fields penetrate through the receiver coil (Rx) and their component normal to the coil orientation induces electric currents in the receiver coil. Each field component differs in intensity, phase and orientation with respect to the primary magnetic field, therefore can be interpreted to constrain presence, shape, orientation and conductivity of objects in the subsurface (Sharma, 1986; Fraser, 1976, 1979). A graphical representation of the EM induction applied to mineral exploration is presented in Figure 11 (Reynolds, 1997).

FEM methods are based on Maxwell's electrodynamics equations (Maxwell, 1861). In our case we consider wave equations derived from Faraday's law and Ampere's law in differential form (equations 1.1 and 1.2), which in the case of planar wave travel, yield to solutions: $H(t) = H_o e^{i\omega t}$ and $E(t) = E_o e^{i\omega t}$, or applying Euler's formula: $H(t) = H_o \cos(\omega t) + iH_o \sin(\omega t)$; $E(t) = E_o \cos(\omega t) + iE_o \sin(\omega t)$ (Griffith, 1999)

$$\nabla^2 E - \frac{1}{c^2}\frac{\partial^2 E}{\partial t^2} = 0 \quad (1.1)$$

$$\nabla^2 H - \frac{1}{c^2}\frac{\partial^2 H}{\partial t^2} = 0 \quad (1.2)$$

Here, the coefficient "c" represents the speed of propagation of the EM wave. In free-space it equals to 2.998 * 10^8 m/s. In other media the velocity of EM wave propagation equals $\frac{1}{\sqrt{\mu\hat{\varepsilon}}}$, where the complex electric permittivity of the medium is $\hat{\varepsilon}$ and μ is the magnetic permeability (Griffith, 1999).

Figure 11. Generalized scheme of the electromagnetic induction method (modified from Reynolds 1997).
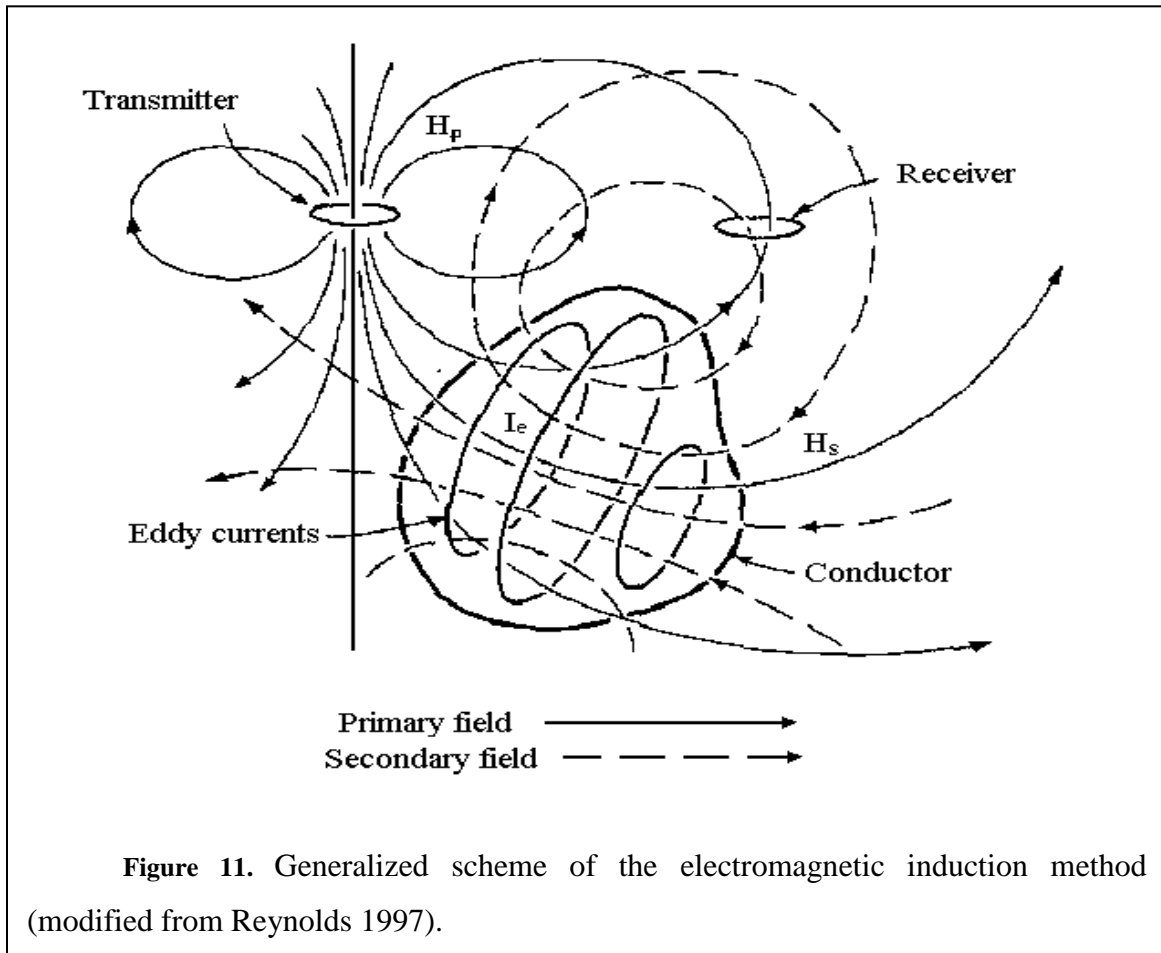
As it can be noted from Euler's form of EM field propagation, the field can be presented as a combination of real (inphase) and imaginary (quadrature) components, which in free-space are shifted in phase by 90° (Fraser, 1976; Fraser, 1978; Fraser, 1979; Yakubovsky and Lyahov, 1988; Sharma, 1996). Applying the second order time differential operator to

the right sides of equations 1.1 and 1.2 we can further derive equations 1.3 and 1.4 (Griffith, 1999).

$$\nabla^2 H = -\mu\hat{\varepsilon}\omega^2 H_0 e^{i\omega t} \quad \textbf{(1.3)}$$

$$\nabla^2 E = -\mu\hat{\varepsilon}\omega^2 E_0 e^{i\omega t} \quad \textbf{(1.4)}$$

In the case of wave propagation through medium we are dealing with the complex value of permittivity $\hat{\varepsilon} = \varepsilon + i(\sigma/\omega)$, which includes both dielectric constant and electrical conductance of medium (Griffith, 1999). This indicates that in the case of a large dielectric constant material (such as air) the dominant component of this value shifts towards absorption currents (j_a) and in the case of a good conductor (weak dielectric) the dominant component shifts towards conductivity currents (j_c). Complex permittivity value is determined by the combination of j_a and j_c, therefore equations 1.3 and 1.4 can be rewritten as 1.5 and 1.6 (Sharma, 1986).

$$\nabla^2 H = i\mu\sigma\omega H - \varepsilon\mu\omega^2 H \quad \textbf{(1.5)}$$

$$\nabla^2 E = i\mu\sigma\omega E - \varepsilon\mu\omega^2 E \quad \textbf{(1.6)}$$

Equations 1.5 and 1.6 are the basic equations describing the propagation of magnetic (H) and electric (E) field in an isotropic, homogeneous medium with physical properties, ε (dielectric constant), μ (magnetic susceptibility) and σ (electric conductance). The term $\sigma/\omega\varepsilon$ is important because it represents the ratio of conductivity currents over absorption currents (j_c/j_a). In regions of moderate to high conductivity, such as saline water, massive sulfides or graphite, $\sigma \approx 1 - 100$ mS/m, $\varepsilon \approx 10\varepsilon_0$ (permittivity of free-space) and $\mu \approx \mu_0$ (susceptibility of free-space); therefore, with such assumptions and when the source frequency is low enough, the absorption currents are much smaller than the conductivity currents (so that the second terms of 1.5 and 1.6 can be neglected). Hence, in regions of appreciable conductivity (sedimentary strata) equations 1.5 and 1.6 can be reduced to the following forms (Sharma, 1986):

$$\nabla^2 H = i\omega\mu\sigma H \quad \textbf{(1.7)}$$

25

$$\nabla^2 E = i\omega\mu\sigma E \quad \textbf{(1.8)}$$

The generalized wave propagation equation has a form of $\nabla^2 X + k^2 X = 0$, where the wavenumber (k) is a spatial analog of frequency and in case of equations 1.7 and 1.8 equals $\sqrt{i\mu\sigma\omega}$ (Yakubovsky and Lyahov, 1988).

Phase shift is a phenomenon caused by polarization of the EM wave transmission by the medium. There are three types of polarization: linear (no phase shift, only amplitude variation), circular (no amplitude variation, phase shift equal to 90°) and elliptic (both amplitude and phase shift are present). Phase shift is a function of the medium conductance. By analogy with an electric circuit, a subsurface conductor can be assigned resistance r and inductance L. The phase lag at the receiver will then be defined as ($\pi/2$ + arctan(ωL/r)), (Telford et al, 1990). This relationship shows that in case of high resistance ωL/r essentially zero and therefore the phase lag is $\pi/2$, while in cases of high conductance ωL/r increases infinitely, which results in the phase of the secondary field practically becoming 180° (π) (Telford et al, 1990).

Another phenomenon critical for understanding FEM methods is that in a homogeneous conductor of infinite thickness - current density j_c and therefore the electric field, decreases with depth. The depth at which attenuation reaches the order of 1/e (37%) is called the skin depth and equals $\delta = \dfrac{1}{\sqrt{\mu\pi f\sigma}}$ (Telford et al, 1990). The physical meaning of this parameter is the inverse of wavenumber from the wave propagation equation (Yakubovsky and Lyahov, 1988). Skin-depth is a function of the operating frequency as well as of the half-space conductivity. This phenomenon is referred to as the skin-effect. The maximum operational depth for a particular frequency is the depth at which the signal amplitude attenuates to the same order as the system noise level.

Depth of penetration increases with decrease in operating frequency (Figure 12) (Telford et al, 1999). The skin-effect is a key concept in designing modern airborne geophysical equipment capable of retrieving electrical properties simultaneously from different depths (geophysical sounding).

Figure 12. Variation of skin depth with frequency (f) of a plane electromagnetic wave (http://www.fugroairborne.com).
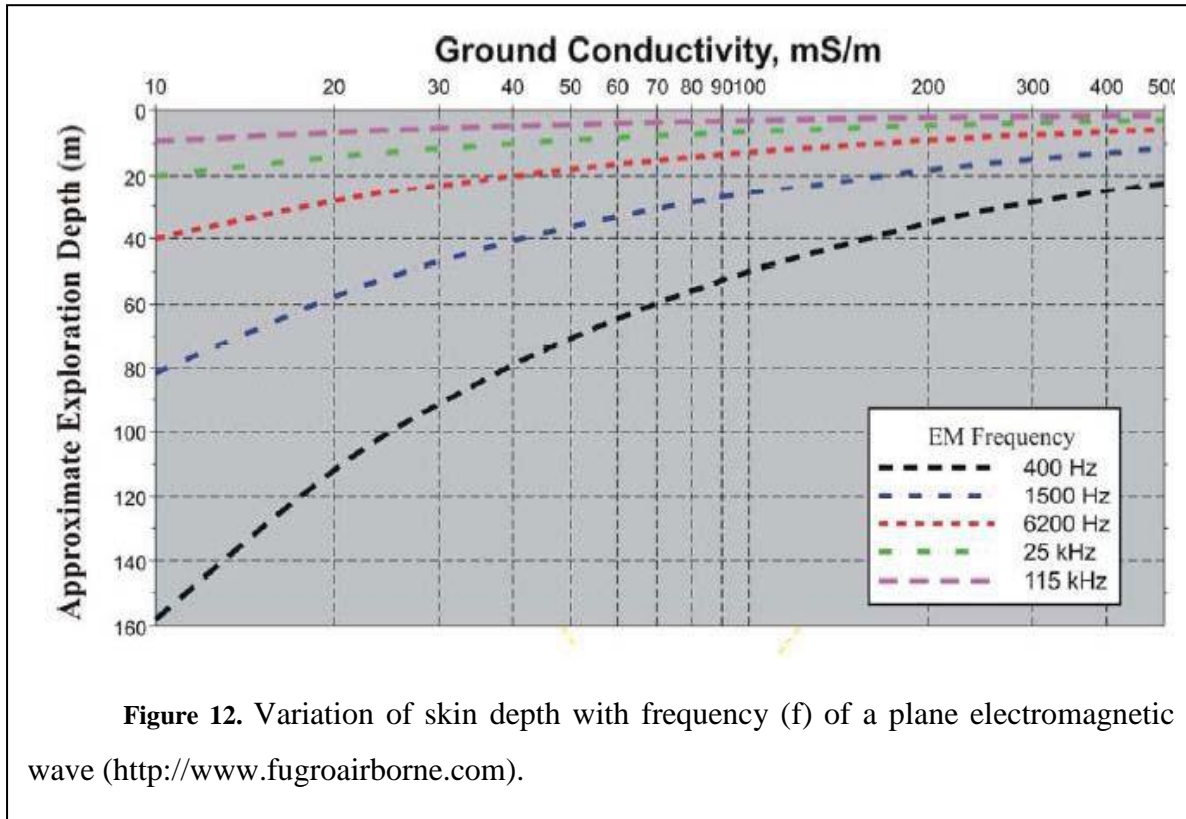
The modified Maxwell's equations 1.7 and 1.8 can be solved for electrical conductivity, resulting in complex function of conductivity and frequency, however under certain approximations they can be simplified (Telford et al, 1990). It can be useful to operate with a value known as the induction number (B = s/δ). When B is much smaller than 1, then solutions to the differential equations 1.7 and 1.8 can be approximated in a linear form of equation 1.9, that shows correlation between apparent conductivity and H_s/H_p (amplitude ratio) in units of percent (McNeill, 1980).

$$\sigma_a = \frac{4}{\omega \mu_0 s^2} \left(\frac{H_s}{H_p} \right) \quad (1.9)$$

Where:

σ_a is the apparent conductivity (S/m)

H_s is the secondary magnetic field arriving to the Rx

H_p is the primary magnetic field induced by Tx

$\omega = 2\pi f$ - angular frequency where f is the frequency measured in Hz

μ_0 is the permeability of free space

s – is the distance between the transmitter and receiver (McNeill, 1980)

In summary, in spite of tremendous complexity of electromagnetic fields' behavior in presence of anisotropic inhomogeneous medium, as for instance groundwater saturated layered Earth, under certain approximations it is possible to derive desired parameters (electrical conductivity) with sufficient level of accuracy to allow further interpretation of these data. Furthermore, such simplifying approximations are applicable for a very wide variety of real life situations.

1.2.3. Helicopterborne modification of FEM survey

In many types of airborne FEM survey the transmitter consists of multiple coils operated at different frequencies. In the geometry used for our survey each transmitter coil was circular and computationally represented by a magnetic dipole when alternating electric current was used (Fraser 1976, 1978, 1979). In general, the orientation of the coil may vary depending on the type of desired targets, but most often the orientation is coplanar with respect to Earth's surface. This position orients the coil's dipole moment along a vertical coordinate axis and is referred to in literature as a "vertical coplanar" orientation. Receiver is emplaced in the same unit as the transmitter in such a manner that their relative orientation would remain unchanged (Fraser 1976, 1978, 1979). For each transmitter coil there is a corresponding receiver coil which registers signals of the same frequency. Figure 13 shows transmitter - receiver geometry for the Resolve™ system as described by Fugro Airborne Surveys (2005). This particular system was used by Fugro Airborne Surveys for the West Virginia impoundment project.

Figure 13. "Resolve" 6 frequency electromagnetic System as described by Fugro Airborne Surveys, Inc (from Fugro Airborne Surveys) (http://www.fugroairborne.com/service/images/Edited_ResolveGraphic2.gif).

The operation of extraction of depth and conductivity information from measurements is a part of the "inverse problem" in geophysics (Christensen, 2002; Zhdanov, 2002; Avdeev, 2005; Cox and Zhdanov, 2007). Mathematically, this problem is non-linear and yields an infinite number of solutions in conductivity/depth domain (Tikhonov, 1963; Tikhonov and Arsenin, 1977). However Sengpiel (1988) introduced an algorithm which, under certain approximations, allowed solving the problem of extracting conductivity and depth information for both uniform half-space and layered earth models (Sengpiel, 1988; Sengpiel and Simeon, 2000). In order to utilize this algorithm inphase and quadrature components of the magnetic field must be measured separately.

The horizontal resolution of AEM system (region of its spatial sensitivity, or its footprint) is defined as the square area centered under the transmitter that contains the induced currents responsible for 90% of the observed secondary magnetic field at the receiver. The system properties responsible for the size of footprint are ground conductivity, survey altitude and transmitter - receiver geometry (Liu and Becker, 1990). Flight lines are usually

spaced according to the desired survey scale. The survey scale is chosen dependent on the target size, depth and orientation. In general, line spacing should not exceed estimated footprint plus half of the estimated target size (Reid et al, 2006). In the case of the West Virginia impoundment survey, line spacing was equal to 50 meters (Fugro Airborne Surveys, 2003).

To calculate the components of H_s - an electromotive force (EMF) ε is being measured in the receiver coil (Rx). ε obeys a relationship: $\varepsilon = \mu\omega H_{s0}\sin(\omega t + \phi_0)$, where ϕ_0 is the phase shift of the electromagnetic signal received at Rx with respect to the source signal Transmitter (Tx) (Telford et al, 1990). However to separately measure the inphase, quadrature and phase shift of the signal requires that internally induced voltage of a form $A_0\sin(\omega t)$ be present in the Rx coil in addition to the measured signal and furthermore it must be inphase with the transmitter induced field of the same frequency. The two signals will then be digitally integrated and their product $H_{s1}\sin(\omega t + \phi_0)*A_0\sin(\omega t)$, where H_{s1} equals $\mu\omega H_{s0}$ can be rewritten as equation 1.10 (Yakubovsky and Lyahov, 1988). Trigonometric conversions are used to reduce $H_{s1}\sin(\omega t + \phi_0)*A_0\sin(\omega t)$ to:

$H_{s1}A_0\sin^2(\omega t)\cos(\phi_0) + \cos(\omega t)\sin(\phi_0)\sin(\omega t)$, which equals

$H_{s1}A_0[1/2\cos(\phi_0) - 1/2\cos(\phi_0) + \sin^2(\omega t)\cos(\phi_0) + 1/2\sin(2\omega t)\sin(\phi_0)] =$

$H_{s1}A_0/2\{\cos(\phi_0)[1 - 2\sin^2(\omega t)] + \sin(2\omega t)\sin(\phi_0)\}$, which using identities:

$\cos(\alpha - \beta) = \cos(\alpha)\cos(\beta) + \sin(\alpha)\sin(\beta)$ and $\cos(2\alpha) = 1 - 2\sin^2(\alpha)$ equals 1:10:

$$\frac{H_{s1}*A_0}{2}\cos\varphi_0 - \frac{H_{s1}*A_0}{2}\cos(2\omega t + \varphi_0) \quad (1.10)$$

In this equation the first member (relevant to $\cos\phi_0$) has a constant value linearly dependant on the phase shift, and the second member (relevant to $\cos(2\omega t + \phi_0)$ oscillates with double the frequency of Transmitter impulse. Therefore the second component can be filtered using a low-pass filter (integrator), while the first component can be measured with DC voltmeter (Yakubovsky and Lyahov, 88).

Before the actual survey starts the airborne EM system must be calibrated. The calibration takes place at minimum altitude of 500 meters so that inphase and quadrature H_s components would be normalized over the freespace response and hence set equal to zero and the phase shift would be equal to exactly 90°. Such calibration takes place before each flight, and may occur during the survey.

1.2.4. Direct and inverse geophysical problems: creation of conductivity depth imagery (CDI)

Conductivity depth image (CDI) can be called a final product of FEM data processing. The problem of reconstructing the distribution of physical parameters in subsurface is fundamental and called an *Inverse Problem* of geophysics (Christensen, 2002; Zhdanov, 2002; Avdeev, 2005; Cox and Zhdanov, 2007). In our particular case it narrows to reconstruction of two-dimensional distribution of apparent electrical conductivity throughout a vertical cross-section adjacent to a flight line. Mathematically, the described above problem is non-linear (also "ill-posed" in literature), as the parameters that determine the structure of the medium are coefficients of partial differential equations (1.5 and 1.6) while the solutions to these equations are known only in a discrete number of points throughout the 3D space (Tikhonov, 1963; Tikhonov and Arsenin, 1977).

Usually a starting model is assigned in conductivity-depth domain in order to create the first approximation (Cox and Zhdanov, 2007). The final solution however would be calculated at last step of an iterational process assigned to solve the *Direct Problem* of geophysics (calculate form and intensity of EM fields at every point of given space from known electromagnetic properties of the cross-section) (Tikhonov and Arsenin, 1977). To make the solution unique and depend stably on the data it is necessary to include a stabilizing functional (Tikhonov and Arsenin, 1977). This functional is a part of the penalty functional that trades off between the data misfit and a priori information given in the model or/and data. This functional in many ways determines model smoothness, boundary

sharpness and data shift (Haber, 2005). Choice of such a stabilizer is of extreme importance since it heavily impacts on the obtained solution (Farquharson and Oldenburg, 1998).

In the standard nomenclature a solution is sought as a stationary point of a penalty functional (Tikhonov and Arsenin, 1977).

$$\varphi(\mathbf{m},\lambda) = \varphi_d(\mathbf{m}) + \lambda * R(\mathbf{m},\mathbf{m}^{\text{ref}}) \underset{\mathbf{m}}{\rightarrow} \min \quad (1.11)$$

Where $\varphi(m,\lambda) = \frac{1}{2}\left\|d^{obs} - F(m)\right\|^2$ (data misfit); $d^{\text{obs}} = (d_1^{obs} \ldots \ldots d_N^{obs})$ is the complex valued vector of measured parameters (H_s components, flight altitude and phase lag); m^{ref} is the reference model, $R(m,m^{\text{ref}})$ is the stabilizing functional (model of smoothness), a typical selection of $R(m,m^{\text{ref}})$ is $\frac{1}{2}\left\|W(m - m^{ref})\right\|^2$ (model norm); $m = \log(\sigma)$, σ is the apparent conductivity; F(m) is the forward model mapping algorithm and $\lambda{>}0$ is the regularization Lagrange multiplier. λ may be chosen with three different criteria: fixed tradeoff (FTO), L-curve convergence and generalized cross-validation (GCV). FTO allows user to assign λ, and the latter is further adjusted according to the discrepancy principle (Farquharson and Oldenburg, 2004). L-curve convergence criterion is sought by calculating a point of maximum curvature using logarithmically scaled relationship of data misfit versus model norm. This point is thought to correspond to equal emphasis of data misfit and model structure of the inversion (Farquharson and Oldenburg, 2004). The GCV-criterion is an automated algorithm, which calculates the data misfit after leaving out each data point and assigning λ as the value which produced the minimum misfit (Farquharson and Oldenburg, 2004).
.

The necessary conditions to minimize functional in form (1.11) are delivered by the stationary point condition: $g = \frac{d\varphi}{dm} = 0$. Traditionally, to find a solution to this optimization problem geophysicists apply nonlinear Newton-type iterations, such as the classical full Newton, Gauss–Newton, quasi–Newton iterations, or some modification thereof (Avdeev,

2005). This in turn entails, at each step of Newton-type iteration, the computation of the sensitivity matrix (Avdeev, 2005).

The calculations at every iterational step are based on forward modeling algorithms (or forward mapping algorithms) described further, however the initial conductivity-depth distribution assignment is very important. It can be pre-assigned, chosen randomly or else acquired using a different inversion-type algorithm, which does not require forward mapping or choice of the stabilization functional. Such method has been described by Sengpiel (1988). The Sengpiel algorithm derives a complex transfer function "c" (or generalized skin-depth) from data for secondary magnetic field.

In the case of uniform field the real part of the transfer function c_0 is equal to the depth z_0 of a "centroid" of the inphase current system and the imaginary part can be used to determine the ambient resistivity $\rho_a = 2\mu_0\omega(\mathrm{Im}(c_0))$. If the primary field originates from an oscillating magnetic dipole, the resulted field components can be presented by a continuous spectrum of wavelengths. Mundry (1984) gave a simplified expression for the normalized secondary magnetic field Z at height h above layered Earth model. This expression can be determined as (1.12) in cases, when h > 3.3s, where s is the distance from transmitter to receiver.

$$Z \cong \left(\frac{s}{h}\right)^3 G_j \int_0^\infty k^2\, R_1\, e^{-2k} dk \quad (1.12)$$

In 1.12 G_j is a factor dependant on the coil configuration, $k = 2\pi(L/h)$ is the normalized wavenumber where the wavelength (L) is measured in units of flight altitude (h) and R_1 is a complex reflection factor, dependant on the layered ground (Sengpiel, 1988; Sengpiel and Simeon, 2000). As R_1 is the only complex component of 1.12 it can be shown that by applying the generalized mean value theorem of integral calculus separately to real and imaginary parts under the integral sign 1.12 can be rewritten as two separate integrals (real and imaginary) in a form of Z = Re(Z) + i*Im(Z) (Sengpiel, 1988). Further, for horizontally stratified ground, which can be interpreted in terms of equivalent half-space, the centroid depth is calculated as $d_a + D_a*\mathrm{Re}(Z)$, where $d_a = D_a - h$ and D_a is the apparent

distance from the transmitter - receiver system to the surface of equivalent half-space (Sengpiel, 1988).

Another modification of initial conductivity-depth distribution based on emplacement of mirror images of transmitter to the subsurface and comparison of measured EM total field and its derivative with pre-assigned field values derived from depths of these mirror images have been described by Macnae (Macnae et al, 1991). This algorithm was implemented in commercially distributed software EM Flow by Encom.

The algorithm was designed for calculations in time domain, featuring non-linear transformation of the amplitude of measured response at each recording time to an apparent image-mirror depth. This mirror image at a certain depth would produce the same field response, as measured, which if plotted on log-log scale relative to the image's depth would result in almost a linear relationship (Macnae et al, 1991).

Further, using the mirror image depth as a function of delay (or frequency in frequency domain) a differential formula 1.13 was obtained:

$$\boldsymbol{\sigma(h_i)} = \frac{1}{\mu_0} \frac{\partial^2 t_i}{\partial^2 h_i^2} \quad \textbf{(1.13)}$$

Where h_i are half-way between mirror image depth and the surface (Macnae et al, 1991). To solve this type equation Polzer (1985) derived a single integral equation (1.14) in order to reduce the relationship between the unknown conductivity and the known penetration depth and measurement times (frequencies in frequency domain) to a linear form 1.14:

$$\frac{t_i}{\mu_0} = \int_0^{h_i} (h_i - z)\sigma(z)dz \quad \textbf{(1.14)}$$

Where z is the vertical coordinate (Polzer, 1985)

However, when accurate forward modeling is needed for the iterational process described above, an integral equation approach is widely used. Maxwell's equations in differential form can be reduced to a second-order Fredholm's integral equation using Green's function (Dmitriev, 1969; Raiche, 1974; Hohmann, 1975; Weidelt, 1975, Tabarovsky, 1975; Zhdanov, 2006)

$$\mathbf{E(r)} = \mathbf{E_0(r)} + \int_{V^s} G_{=0}(\mathbf{r,r'})(\tilde{\sigma}\ \sigma_0)^*\mathbf{E(r')dr'} \quad (1.15)$$

In equation 1.15 $E_0(r)$ is known, G is the dyadic homogeneous Green's function in a form of 1.16 and r,r' is an arbitrary coordinate system, defined in curvilinear space. G_0 is a unique Green's function specified by the boundary conditions, I is the source of the field and V^s is the scattering volume, with $(\sigma - \sigma_0) \neq 0$.

$$\mathbf{G(r,r')} = \frac{1}{4\pi}\left[I + \frac{\nabla\nabla}{k^2}\right]G_0(r,r') \quad (1.16)$$

Equation 1.15 is also known as Electric Field Integral Equation (EFIE) which is used to solve field scattering problem in an unbound region. The main merit of integral equation modeling approach is that the scattering volume is the only subject to discretization, which allows to dramatically simplify the calculations (Zhdanov, 2006).

1.2.5. Direct current soundings and profiling

The difference between EM methods and Direct Current (DC) methods is that in case of latter, the apparent resistivity is being directly measured, rather than calculated from other measured parameters. Ohm's law governs the flow of current in the ground (Halliday, 1960; Sharma, 1986). It is the fundamental physical law used in DC resistivity surveys. The equation for Ohm's law is given by 1.17:

$$\mathbf{U = IR} \quad (1.17)$$

Where U is the voltage (Volts), I - is the electric field intensity (Amperes), and R is the electrical resistance of the material (Ohms) (Halliday, 1960).

In the case of DC resistivity surveys direct current is being injected into the ground through two current electrodes (Figure 14, C_1 and C_2) and measurement of the resulting difference in voltage at the two potential electrodes (P_1 and P_2) is being recorded. The recorded measurements are dependant on the C_1C_2 distance, P_1P_2 distance, the current travel path and on the electrical properties of the Earth (Sharma, 1986; Telford et al, 1990).

Figure 14. Schematic description of Dipole-Dipole array for DC resistivity profiling (Telford et al, 1990).
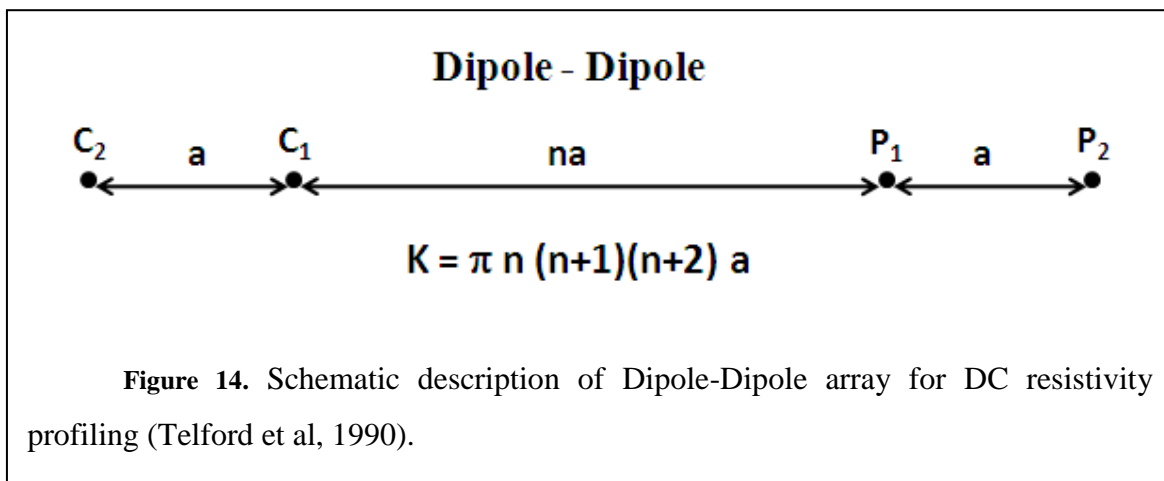
The measured voltage has to be normalized over the electric field intensity in order for the total resistance to be derived from the measurements (Telford et al, 1990). Furthermore, the total resistance is proportional to the cross-sectional area (orthogonal to current propagation) and is in reverse proportion with the linear distance between the potential electrodes (Yakubovsky and Lyahov, 1988). In the general case the equation for DC resistivity profiling array takes the form of 1.18 (Sharma, 1986; Yakubovsky and Lyahov, 1988):

$$\rho_a = K*V*(P_1P_2)/I \quad (1.18)$$

In this equation K is the coefficient, which depends on the arrangement of all electrodes used in the survey, and ρ_a is the apparent resistivity, which is the actual resistivity in a

single case when the medium penetrated by the electrical current in a homogeneous half-space. K from equation 1.18 in the general case is calculated according to 1.19 (Telford et al, 1990):

$$K = \frac{2\pi}{\frac{1}{r(C_1 P_1)} - \frac{1}{r(C_2 P_1)} - \frac{1}{r(C_1 P_2)} - \frac{1}{r(C_2 P_2)}} \quad \textbf{(1.19)}$$

In this equation **r** refers to distance between two electrodes. K has dimensionality of meters. By increasing the spacing between potential electrodes, an increase in volume of rocks affecting the measurements is achieved, therefore, according to equation 1.18 the spacing is controlling the depth of survey (Telford et al, 1990).

Types of electrode arrays also vary in regards to number of electrodes and their geometry. There are two, three and four electrode array configurations. In our particular case a four electrode array of dipole-dipole type was used. The dipole-dipole array is characterized by potential electrodes and current electrodes being paired and separated one pair from another at a distance significantly greater than the separation in each pair. The distance between pairs must be a multiple of distance between the potential electrodes (Figure 14) (Telford et al, 1990; Ward, 1990).

1.3. PROCESSING AND INTERPRETATION OF WEST VIRGINIA IMPOUNDMENT DATA.

1.3.1. Survey description and data processing

National Technology Transfer Center (NTTC) selected 14 impoundments (Figure 1) for airborne FEM surveys from a list of impoundments in southern West Virginia that were given a moderate or high hazard potential rating, based on the height of the embankment, the volume of material impounded, and the downstream effects of an impoundment failure (MSHA, 1974). Impoundments with moderate hazard potential are in predominately rural areas where failure may damage isolated homes or minor railroads, disrupting services or important facilities. Impoundments with a high hazard potential are those where failure could reasonably be expected to cause loss of human life, serious damage to houses, industrial and commercial buildings, important utilities, highways, and railroads.

The list of selected impoundments was transferred to the National Energy Technology Laboratory where flight areas were determined by constructing a bounding rectangle that enclosed the impoundment and ancillary structures, and included approximately a 1-km wide buffer around the impoundment.

All measurements were done using Fugro Airborne Surveys Resolve™ system. The system consists of five coplanar transmitter/receiver coil pairs operating at frequencies of 385, 1700, 6536, 28120 and 116300 Hz and one coaxial (orthogonal) transmitter/receiver coil pair operated at a frequency of 1.41 kHz. Separation for the five coplanar coil pairs was 7.9 m; separation for the coaxial coils was 9 m. During the survey transmitter coils were

constantly generating electric current; while measurements were being recorded from the receiver coil every tenth of a second (sampling rate of 10 Hz).

The surveys were flown using a Ecureuil AS350-B2 helicopter with the Resolve sensor (Figure 13) suspended about 30 m beneath the helicopter as a sling load. Survey data were acquired by flying parallel lines approximately 50 m apart while attempting to maintain the sensor at an altitude of 35 m. However, the average sensor height during these surveys was 45 m, as the rugged terrain, trees, and numerous power lines necessitated higher flight in certain areas for safety. At a nominal flight speed of 90 km/h, the 10 Hz data acquisition rate resulted in one reading every 2.5 meters along the flight line.

For coal refuse impoundments, conductive areas were expected to coincide with unconsolidated fine-grained coal waste material and along its flow path. This material is saturated with impoundment fluids known for their high conductivity.

Figure 15 shows an example of recorded H_s components over a subsurface conductive body tied to a surface conductivity map derived from 25 KHz. According to Figure 12, the effective depth for this survey at lowest frequency can be estimated as 100 meters, assuming the average apparent conductivity of sedimentary strata of 25 mS/m (40 Ohm*m).

Table 1 provides a list of all channels, which were recorded during the survey and provides a brief description of data collected. EM data were recorded as a set of inphase and quadrature readings synchronized via "fiducial" channel with the rest of the data. Raw EM data were filtered using 1D median and 1D mean filters in order to eliminate internal system noise. Mean filtering is designed to replace each value with the mean (average) value of neighboring points, including it. It works in a sliding window mode and represents a simple type of low-pass filter. Median filter has similar purpose; the difference is that it selects an odd number of points in the window sorted in ascending numerical order. The median value is located in the centre of such window and it is further selected to replace the first point of the window. Application of these filters is a standard practice to improve on the smoothness of signal and eliminate occasional

39

spikes, caused by reasons other than variations of physical parameters of measured Earth features.

Filtered EM channels were further corrected for temperature drift, leveled and used for apparent conductivity calculations for each recorded frequency. A set of Conductivity-depth images was delivered for each flight line over each impoundment.
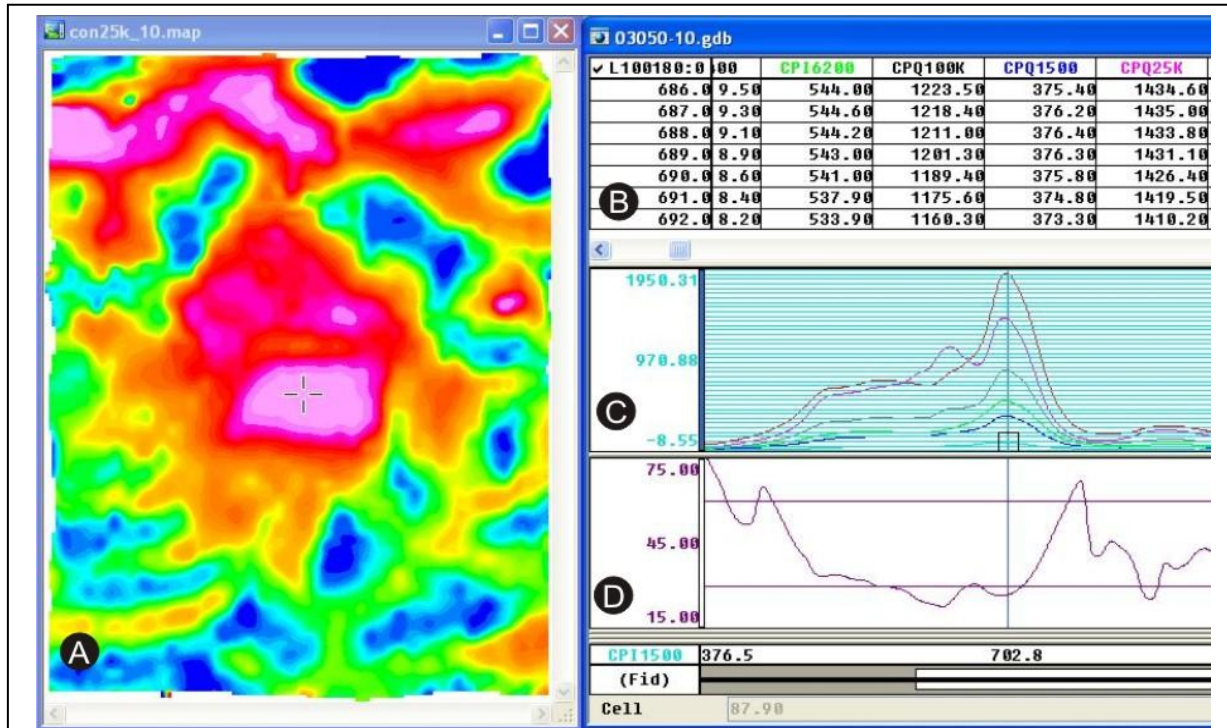
Figure 15. East Gulf impoundment as an example.(A): Map of apparent surface conductivity gridded for the 25 KHz channel (red – conductive, blue – resistive). The H_s measurements are normalized to the primary field H_p and are recorded in the units of parts per million (ppm). (B): Window containing processed inphase (CPI) and quadrature (CPQ) channels. L 100180 refers to flight line. (C): 6 channels (1700 Hz, 6536 Hz and 28120 Hz, both: inphase and quadrature are plotted as a function of fiducial. (D): The flight altitude is plotted in meters above surface, as measured by laser altimeter (Figure 13). Note that conductivity map (A) is linked to sections (C) and (D).

Chanel	Recorded data
X	Easting, Coordinate type UTM; Projection: Nad83; Zone 17N, Units: meters
Y	Northing, Coordinate type UTM; Projection: Nad83; Zone 17N, Units: meters
FID	Fiducial (this channel has dimensionality of seconds and is used to synchronize all the data)
LINE	Flight line number
UTC	Universal Time Count (time as in Greenwich, UK)
Z	Height of aircraft above WGS84 Spheroid in meters
ALTBIRDM	Radar altimeter elevation of EM bird above terrain (meters)
LASER	Laser altimeter elevation of EM bird above terrain (meters)
BARO	Barometrically calculated height of aircraft (meters)
DEMZ	Digital Elevation Model, calculated using Z and Laser channels
MAGR	Raw Total Magnetic field Intensity (TMI) measured in nano-Teslas (nT)
DIURNAL	Diurnal magnetic variation measured at a reference magnetic station on the ground (nT)
MAG	Final total magnetic intensity calculated from MAGR and DIURNAL channels (nT)
L400I	Raw 385 Hz coplanar inphase data, measured in parts per million of the primary field (ppm)
L400Q	Raw 385 Hz coplanar quadrature data, measured in parts per million of the primary field (ppm)
L1K7I	Raw 1413 Hz coaxial inphase data, measured in parts per million of the primary field (ppm)
L1K7Q	Raw 1413 Hz coaxial quadrature data, measured in parts per million of the primary field (ppm)
L1K5I	Raw 1700 Hz coplanar inphase data, measured in parts per million of the primary field (ppm)
LIK5Q	Raw 1700 Hz coplanar quadrature data, measured in parts per million of the primary field (ppm)
L6K2I	Raw 6536 Hz coplanar inphase data, measured in parts per million of the primary field (ppm)
L6K2Q	Raw 6536 Hz coplanar quadrature data, measured in parts per million of the primary field (ppm)
L25KI	Raw 28120 Hz coplanar inphase data, measured in parts per million of the primary field (ppm)
L25KQ	Raw 28120 Hz coplanar quadrature data, measured in parts per million of the primary field (ppm)
L100I	Raw 116300 Hz coplanar inphase data, measured in parts per million of the primary field (ppm)
L100Q	Raw 116300 Hz coplanar quadrature data, measured in parts per million of the primary field (ppm)
CPI400	Leveled 385 Hz coplanar inphase data, measured in parts per million of the primary field (ppm)
CPQ400	Leveled 385 Hz coplanar quadrature data, measured in parts per million of the primary field (ppm)
CXI1400	Leveled 1413 Hz coaxial inphase data, measured in parts per million of the primary field (ppm)
CXQ1400	Leveled 1413 Hz coaxial quadrature data, measured in parts per million of the primary field (ppm)
CPI1500	Leveled 1700 Hz coplanar inphase data, measured in parts per million of the primary field (ppm)
CPQ1500	Leveled 1700 Hz coplanar quadrature data, measured in parts per million of the primary field (ppm)
CPI6200	Leveled 6536 Hz coplanar inphase data, measured in parts per million of the primary field (ppm)
CPQ6200	Leveled 6536 Hz coplanar quadrature data, measured in parts per million of the primary field (ppm)
CPI25K	Leveled 28120 Hz coplanar inphase data, measured in parts per million of the primary field (ppm)
CPQ25K	Leveled 28120 Hz coplanar quadrature data, measured in parts per million of the primary field (ppm)
CPI115K	Leveled 116300 Hz coplanar inphase data, measured in parts per million of the primary field (ppm)
CPQ115K	Leveled 116300 Hz coplanar quadrature data, measured in parts per million of the primary field (ppm)

CON400	Apparent conductivity calculated for 385 Hz frequency (mS/m)
CON1500	Apparent conductivity calculated for 1700 Hz frequency (mS/m)
CON6200	Apparent conductivity calculated for 6536 Hz frequency (mS/m)
CON25K	Apparent conductivity calculated for 28120 Hz frequency (mS/m)
CON115K	Apparent conductivity calculated for 116300 Hz frequency (mS/m)
DEP400	Apparent depth calculated for 385 Hz frequency
DEP1500	Apparent depth calculated for 1700 Hz frequency
DEP6200	Apparent depth calculated for 6536 Hz frequency
DEP25k	Apparent depth calculated for 28120 Hz frequency
DEP115k	Apparent depth calculated for 116300 Hz frequency
CPPL	Coplanar power line monitor (monitoring activity at 60 Hz frequency)

Table 1. Channels recorded by Resolve FEM system during a survey (left) with detailed explanation of recorded data (right) (Fugro Airborne Surveys, 2003).

Data for conductivity depth imagery (CDI) profiles can be calculated in many different ways (Sengpiel, 1988; Constable et al, 1987; Huang and Palacky, 1991; Macnae, 1991; Farquharson and Oldenburgh, 1998; Christensen, 2002; Sattel, 2005). For the West Virginia impoundment project, the CDIs were calculated using three different inversion algorithms: Sengpiel algorithm, implemented in Emigma software package (Sengpiel, 1988, Sengpiel and Simeon, 2000); inversion based on regularization solutions, implemented in EM Flow software (Macnae, 1991), EM1DFM software (Farquharson and Oldenburgh, 1998, UBC-GIF, 2000). EM Flow uses an approach to CDI calculation described in Macnae et al, 1991, 1998); EM1DFM is a layered earth inversion program, which fits a modeled response to the input data by minimizing an objection function (Constable et al, 1987; Farquharson et al, 2003).

Comparisons of these algorithms implemented to those flight lines, which played significant role in further data interpretation can be seen in Figure 16, Figure 17, Figure 18, Figure 19, Figure 20 and Figure 21. Locations of these flight lines relative to the impoundments will be shown further in interpretation section.

42
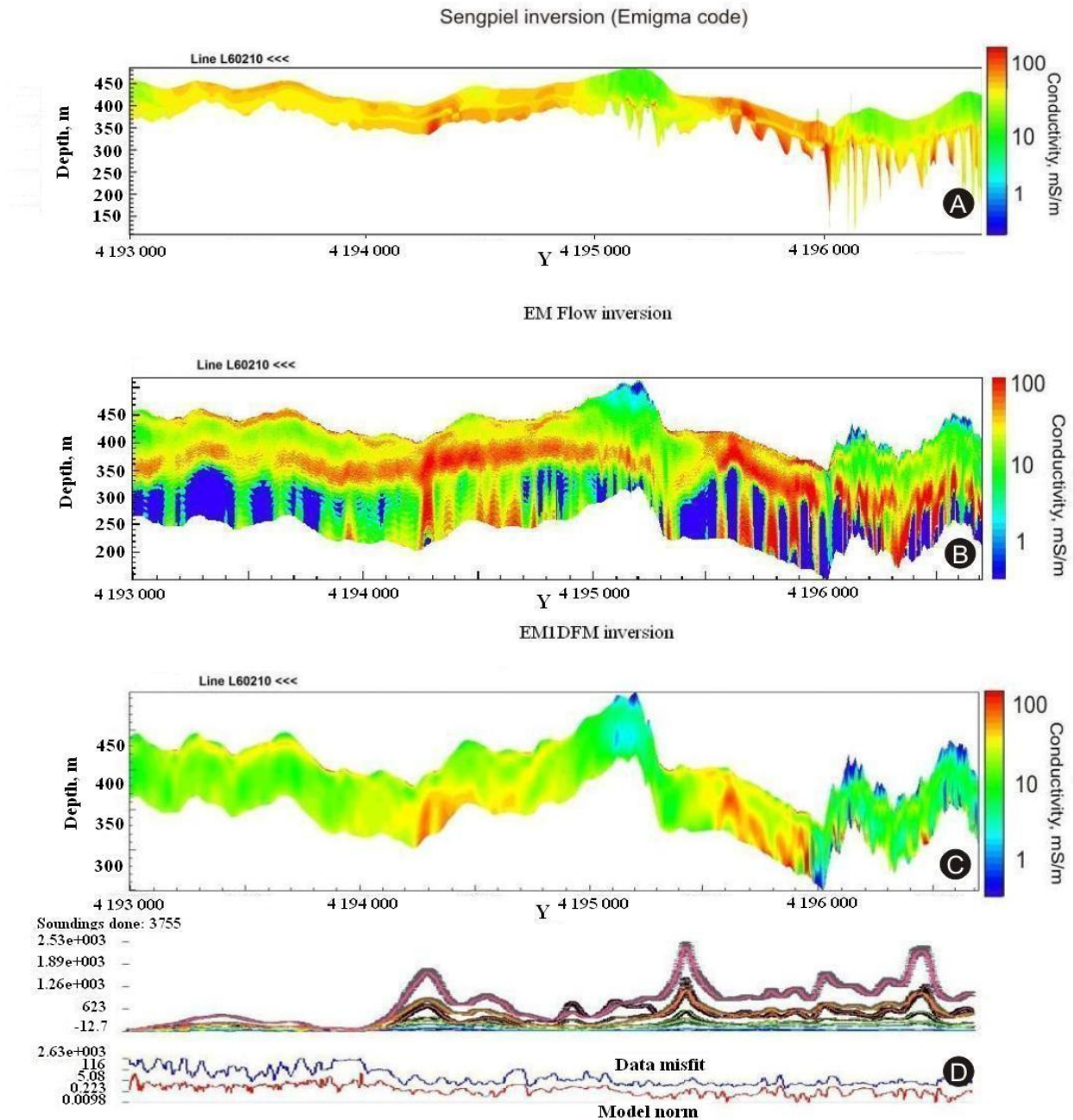
Figure 16. Conductivity depth images derived from three different inversion algorithms applied to flight line 60210. (A): Sengpiel technique. (B): EM Flow algorithm. (C): EM1DFM inversion with stabilization functional. (D): Data misfit and model norm for EM1DFM inversion are plotted for each observation point.

43
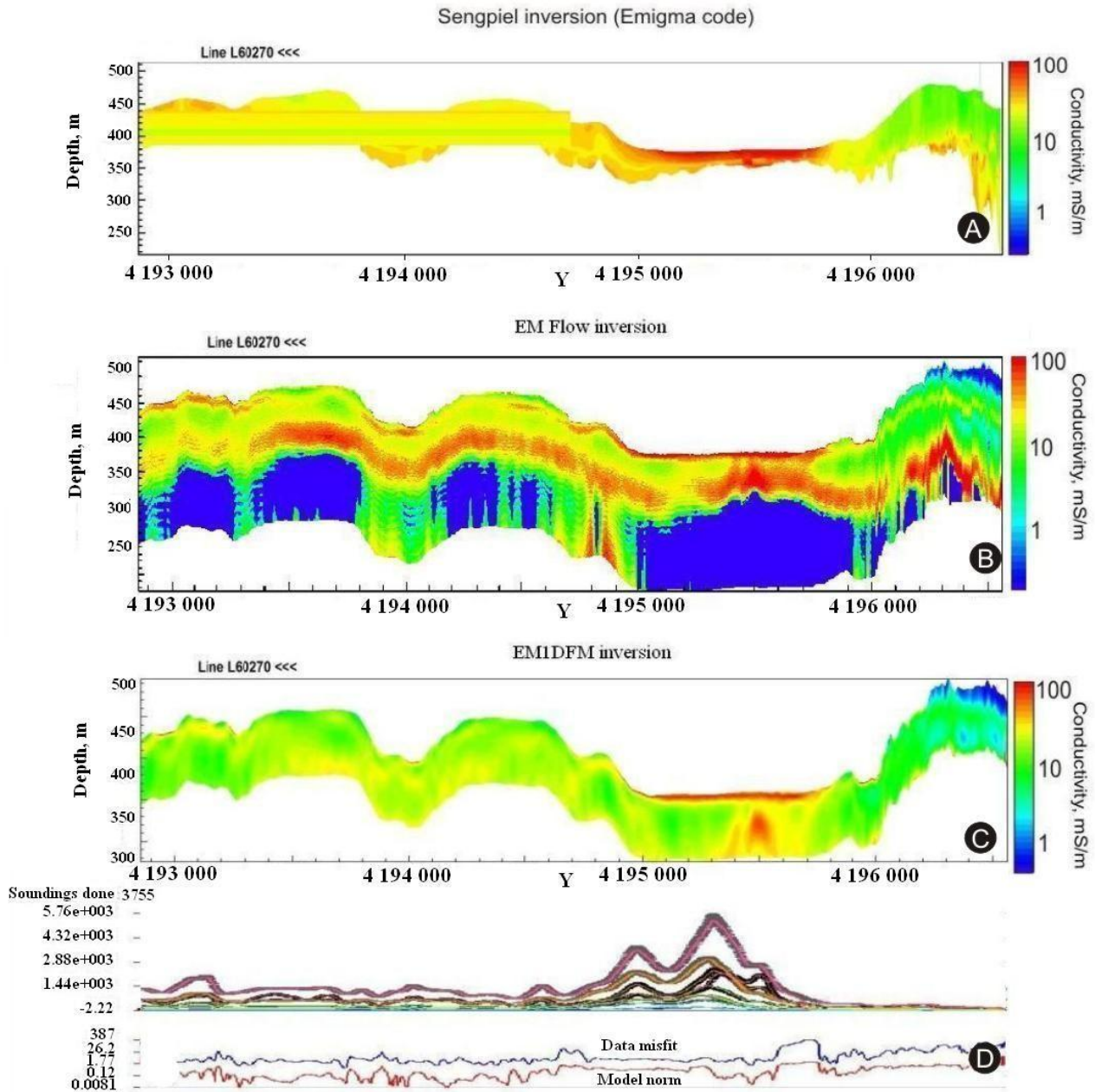
Figure 17. Conductivity depth images derived from three different inversion algorithms applied to flight line 60270. (A): Sengpiel technique. (B): EM Flow algorithm. (C): EM1DFM inversion with stabilization functional. (D): Data misfit and model norm for EM1DFM inversion are plotted for each observation point.
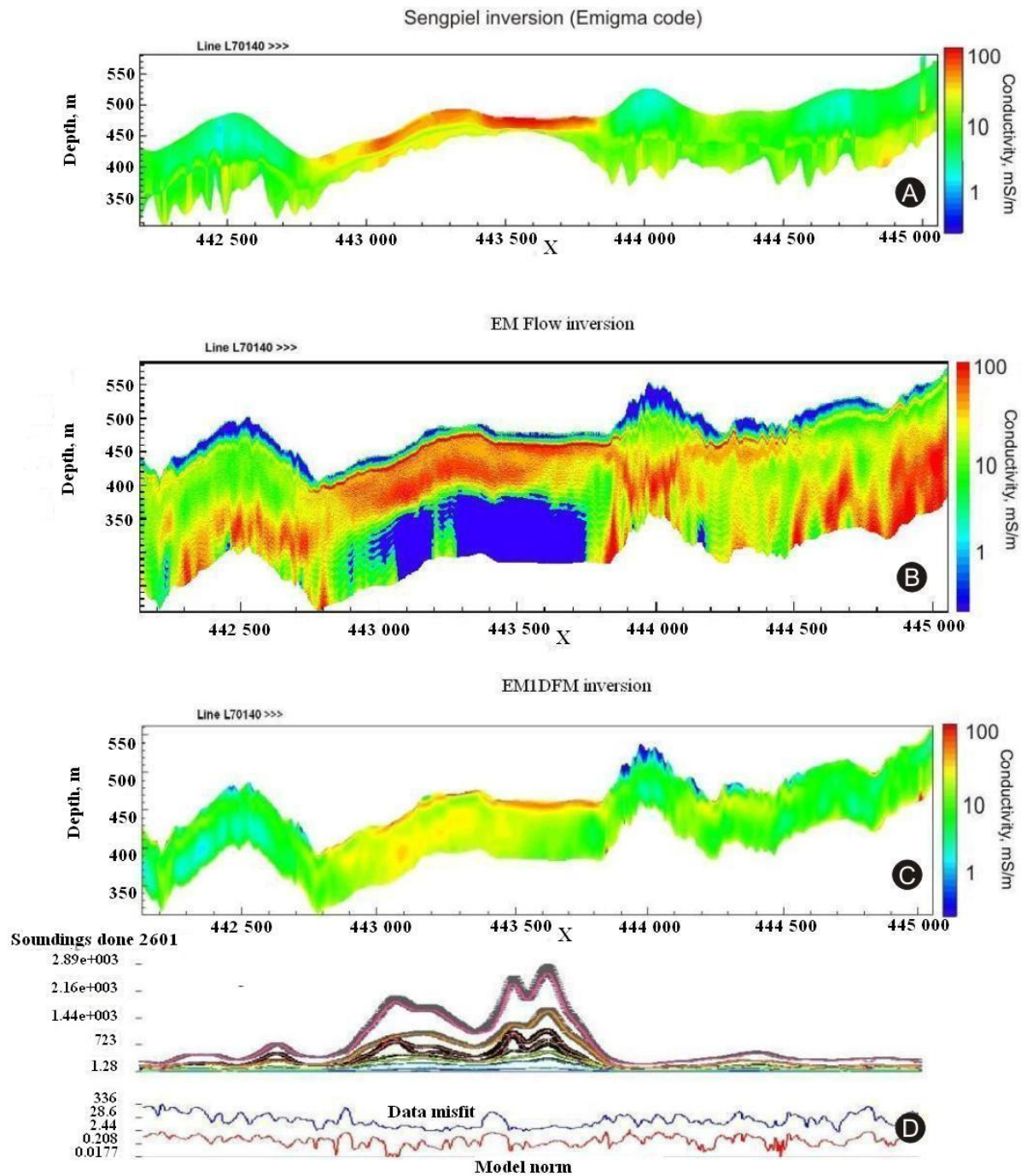
Figure 18. Conductivity depth images derived from three different inversion algorithms applied to flight line 70140. (A): Sengpiel technique. (B): EM Flow algorithm. (C): EM1DFM inversion with stabilization functional. (D): Data misfit and model norm for EM1DFM inversion are plotted for each observation point.
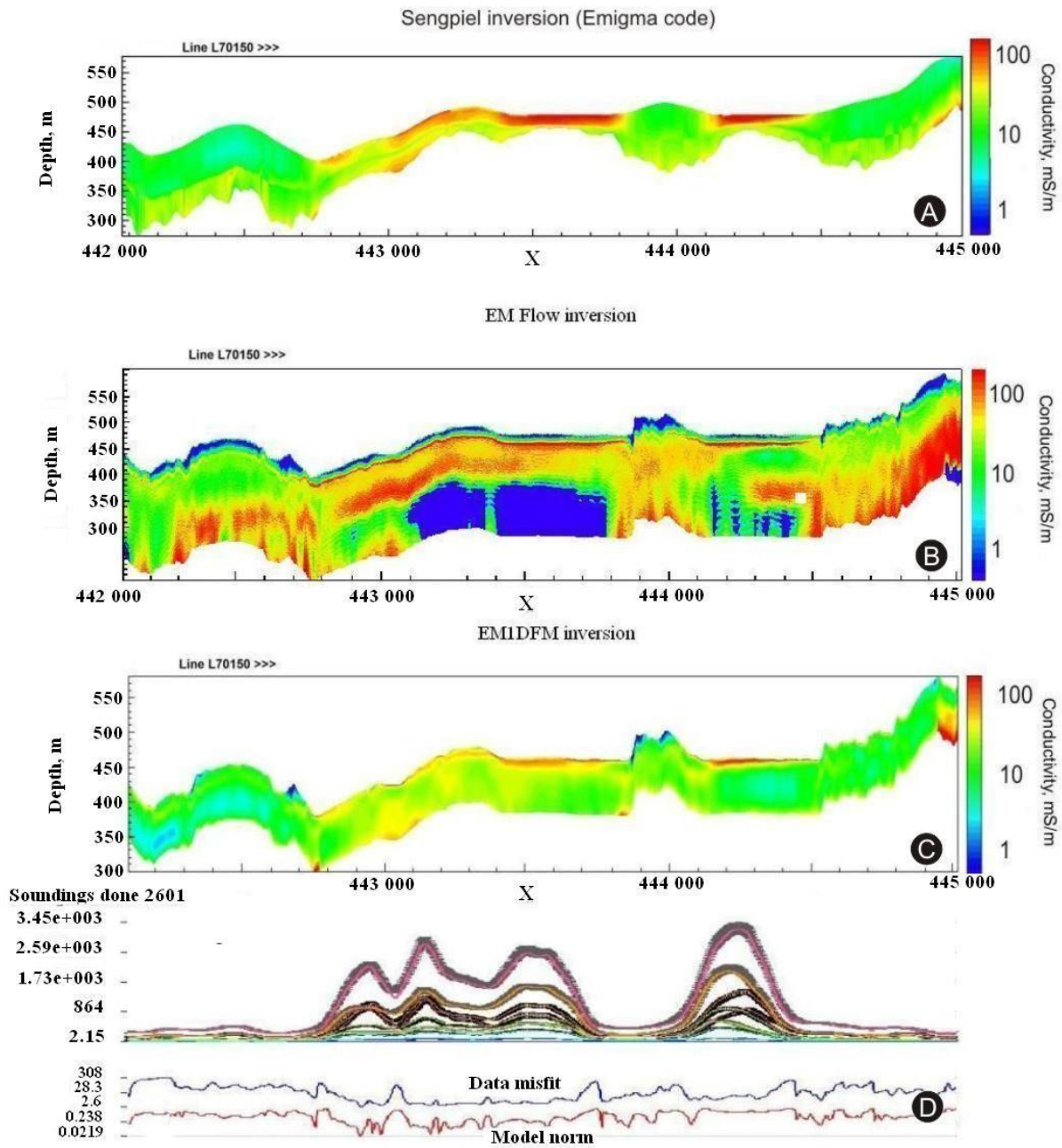
Figure 19. Conductivity depth images derived from three different inversion algorithms applied to flight line 70150. (A): Sengpiel technique. (B): EM Flow algorithm. (C): EM1DFM inversion with stabilization functional. (D): Data misfit and model norm for EM1DFM inversion are plotted for each observation point.
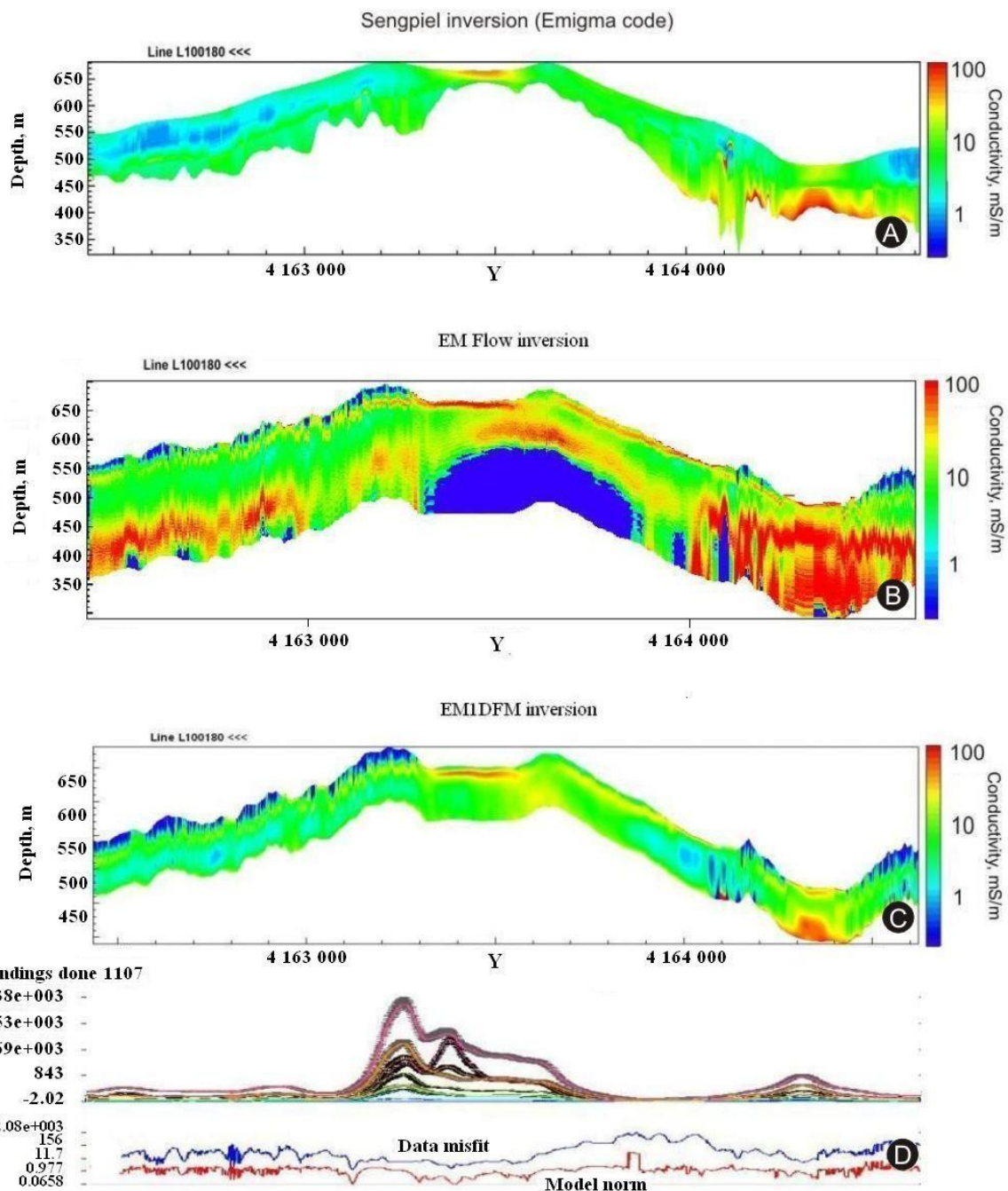
Figure 20. Conductivity depth images derived from three different inversion algorithms applied to flight line 100180. (A): Sengpiel technique. (B): EM Flow algorithm. (C): EM1DFM inversion with stabilization functional. (D): Data misfit and model norm for EM1DFM inversion are plotted for each observation point.
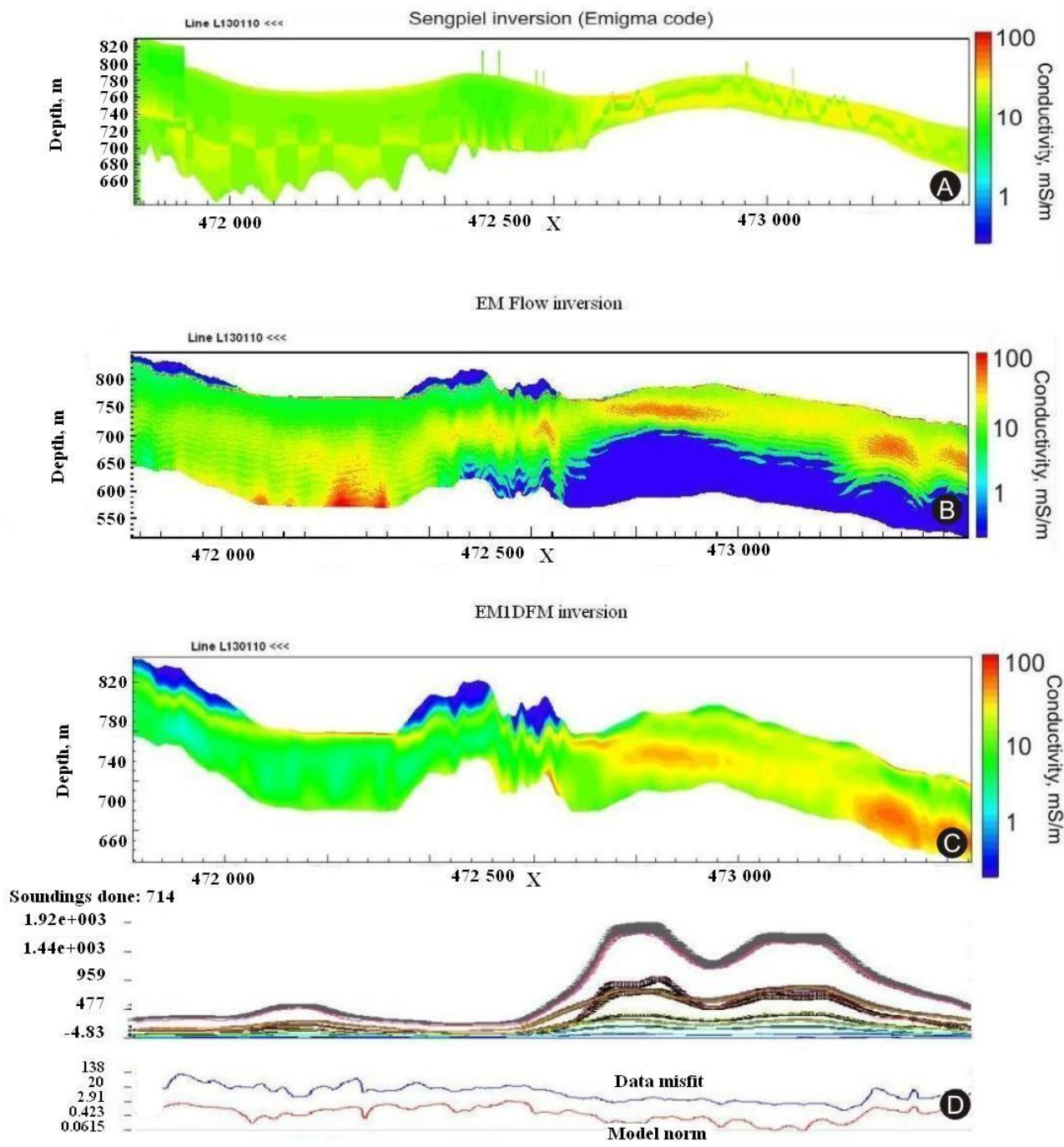
Figure 21. Conductivity depth images derived from three different inversion algorithms applied to flight line 130110. (A): Sengpiel technique. (B): EM Flow algorithm. (C): EM1DFM inversion with stabilization functional. (D): Data misfit and model norm for EM1DFM inversion are plotted for each observation point.

48

Ideally, CDIs showing the vertical distribution of apparent conductivity along flight lines can be used to determine hydrologic conditions beneath the decant pond and within the embankment. Further, the CDIs may show the location of underground mines if the mines are filled with electrically conductive fluid and are within 50 m of the surface (Hammack, Kaminski, et al, 2007). Limitations, such as signal penetration, internal system noise and alternating current (AC) power line interference with the lowest frequency (385 Hz) (Al-Fouzan et al, 2004) can significantly impact the quality of the geophysical signal required to determine the CDI sections.

1.3.2. Reproducibility of geophysical data and verification with ground-based resistivity system

In this helicopter-borne electromagnetic (HEM) survey there are locations where flight lines overlap (Figure 22) because of the deviations from original flight paths. Deviations were caused by winds blowing the helicopter temporarily off course or by the EM gondola (containing transmitter and receiver) swinging on the 30 m cable. In Figure 22, the dashed lines show locations where measurements on adjacent lines were within a few meters, which falls within the footprint of HEM (essentially a circular area with a 30 m radius centered on ground directly below the sensor). The CDIs for the two flight lines share general similarities while conductivity soundings derived from EM1DFM 1D inversion are nearly identical for the two lines at the coincident location. This provides assurance that the HEM system is reproducibly responding to conditions specific to that location and that the results derived from both flight lines are reasonably accurate. With some HEM systems, there is directional lag in the data collection so that the data are dependent on flight direction. In this study however the results were nearly identical at a coincident location even considering opposite flight directions.

Independent ground verification was necessary to assure that the correct conductivities and depths were restored from measured data. Verification may be derived from available knowledge of the site or from tests performed on the ground specifically to calibrate or corroborate airborne data. Ground verification activities at three of the fourteen impoundments were performed in the summer and fall of 2005, more than two years after the helicopter survey. The impoundments selected for ground investigations were the Brushy Fork impoundment, the Jarrell's Branch impoundment and the presently inactive Monclo impoundment. Brushy Fork impoundment and the Monclo impoundment are large upstream raised impoundments whereas Jarrell's Branch impoundment is a downstream raised impoundment. Dipole-dipole DC resistivity profiling was used in order to verify airborne soundings.
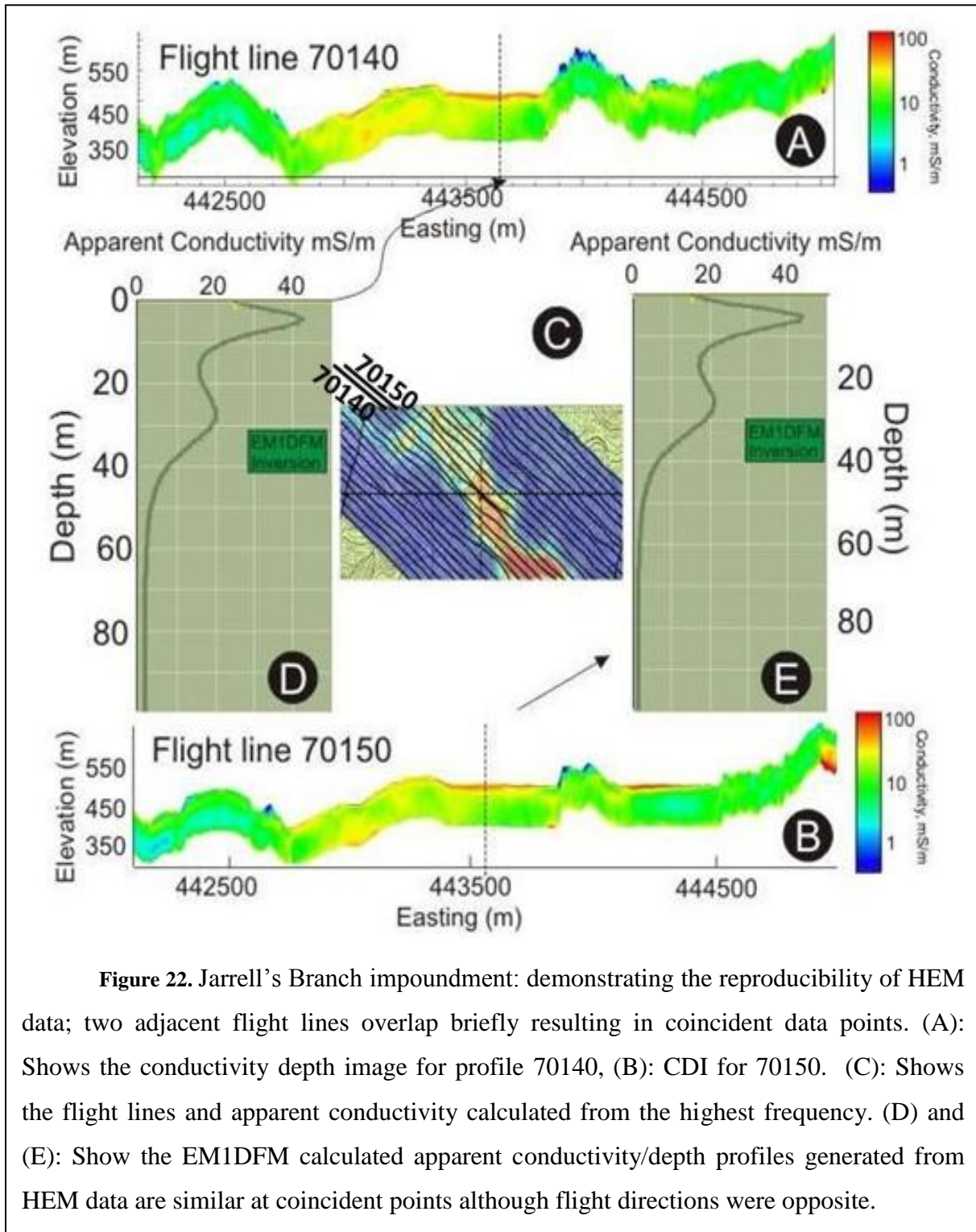
Figure 22. Jarrell's Branch impoundment: demonstrating the reproducibility of HEM data; two adjacent flight lines overlap briefly resulting in coincident data points. (A): Shows the conductivity depth image for profile 70140, (B): CDI for 70150. (C): Shows the flight lines and apparent conductivity calculated from the highest frequency. (D) and (E): Show the EM1DFM calculated apparent conductivity/depth profiles generated from HEM data are similar at coincident points although flight directions were opposite.

These surveys employed Advanced Geosciences' Supersting R8 IP and Supersting +28 R8 IP instruments with 56-electrode Swift cables and 28-electrode passive cables, respectively.

Electrode spacing was between 1 m and 6 m, depending on the area to be surveyed. Resistivity profiles were obtained along segments of flight lines or across push-outs using a single cable deployment; 28 electrode passive cables were used for flight line segments and 56-electrode Swift cables were used for push outs. Resulting data were processed using resistivity imaging software (AGI, 2007). Inverted resistivity data were converted to conductivity and displayed as conductivity/depth profiles.

Interviews with company engineers responsible for construction of the impoundment were performed as ground investigations. Tentative interpretations of the HEM data were presented to these engineers and they were asked to comment on the accuracy of the interpreted results based on their knowledge of impoundment construction and the routine monitoring that is performed at each site. In general, the engineers found the HEM interpretations to be accurate based on their knowledge of impoundment hydrology. The consensus of the engineers was that the HEM surveys were a useful tool for managing impoundments.

Validation of HEM data with ground measurements was difficult because during the two years between airborne and ground surveys impoundments were active and significantly changed their decant pond geometry as large amounts of coal waste were continually being disposed over the push-out. The push-out itself has been gradually migrating away from initial dam. For example, about 350,000 tons of coarse coal waste is placed on the embankment at the Brushy Fork impoundment each month. Our concern was that hydrologic conditions existing at the time of the 2003 helicopter survey may have been significantly altered by 2005 when ground surveys took place. For this reason, ground verification activities were primarily conducted at the Monclo impoundment, which was inactive between the time of the helicopter and ground surveys. Segments of two adjacent flight lines that crossed the decant pond (now dry) within the Monclo impoundment were chosen for resistivity profiles (AA' and BB', Figure 23). A third profile was acquired (CC', Figure 23) perpendicular to profiles AA' and BB'.
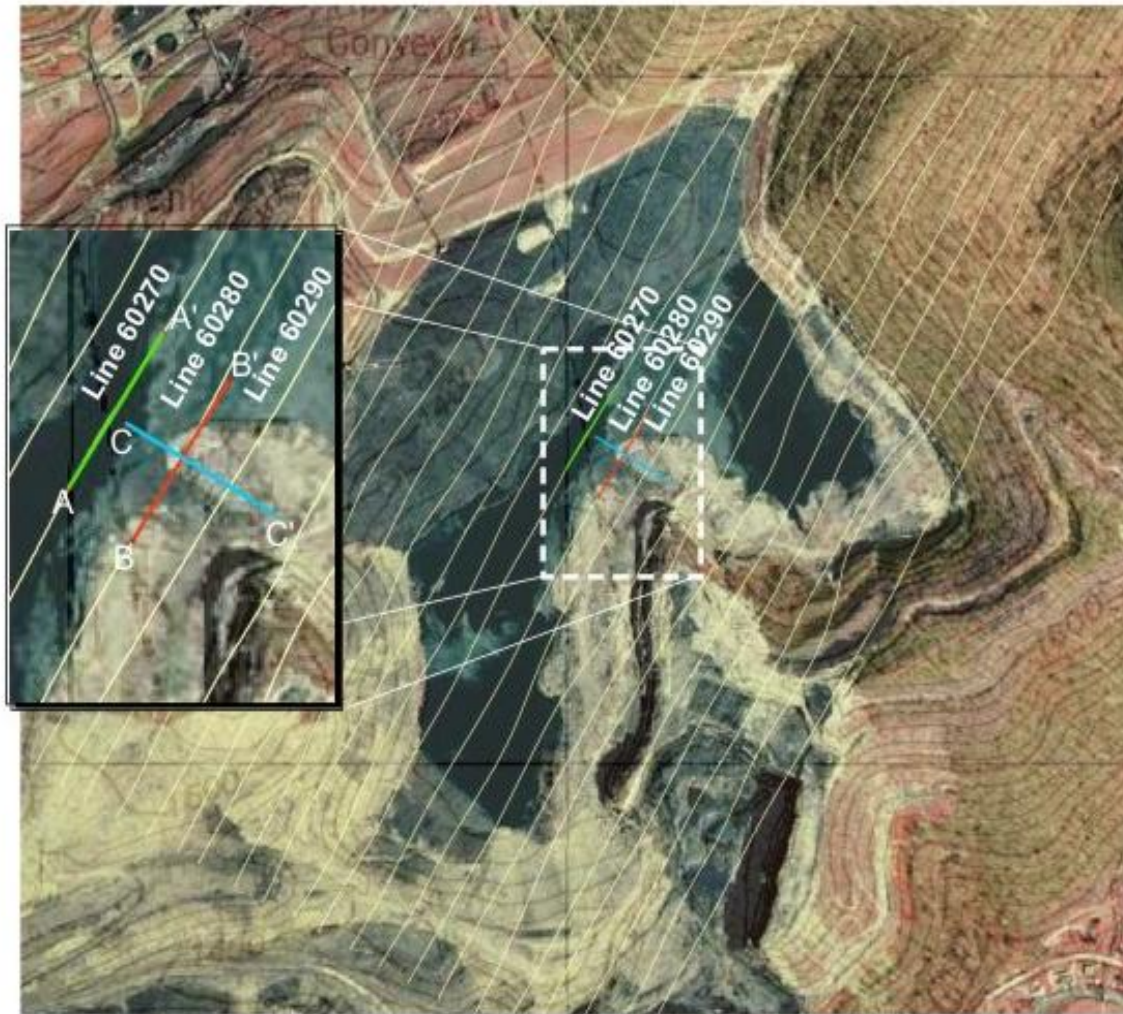
Figure 23. Digital orthophoto of the Monclo impoundment near Sharples, WV showing the locations of flight lines from the helicopter survey (light yellow). Inset map shows the location of three resistivity profiles (AA',BB' and CC') that were acquired using DC resistivity method to corroborate helicopter survey results.

Figure 24 shows an HEM conductivity/depth profile for a segment of flight line 60270 and a resistivity profile (plotted as conductivity) acquired on the ground at the same location. Both profiles show a 2-5 m thick low conductivity (5-20 mS/m) surface layer that is predominantly coarse coal waste. The surface material was dry and electrode locations had to be wetted in order to obtain interpretable resistivity data. Beneath the resistive surface layer is a conductive layer that is discontinuous in the resistivity data but continuous in the HEM data. This can be explained by the fact that the footprint of the HEM instrument is

larger and it cannot distinguish small features that may be present in DC resistivity results. Instead HEM renders the layer containing discontinuous conductive features as a uniform conductive layer, which has the correct depth and thickness. Beneath the conductive layer is a thick resistive layer that contains a conductive anomaly also visible in the HEM data.
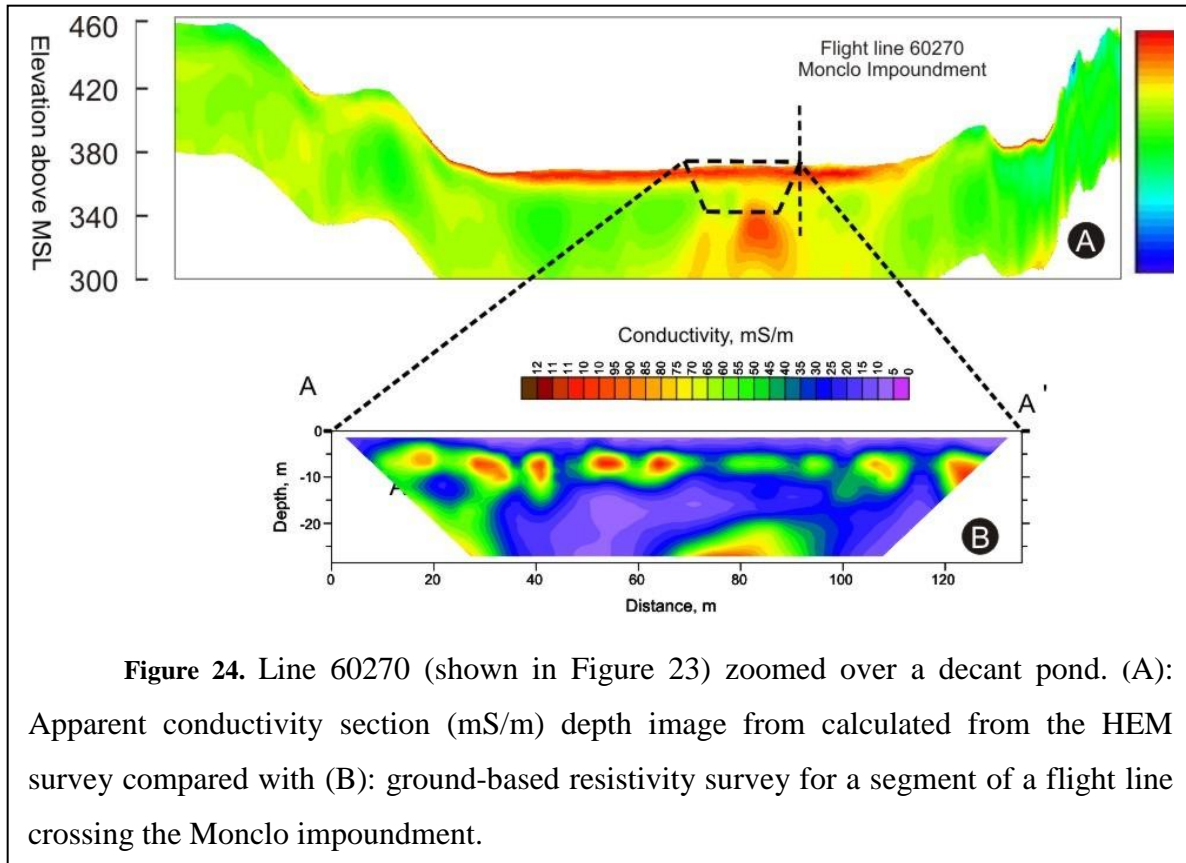
Figure 24. Line 60270 (shown in Figure 23) zoomed over a decant pond. (A): Apparent conductivity section (mS/m) depth image from calculated from the HEM survey compared with (B): ground-based resistivity survey for a segment of a flight line crossing the Monclo impoundment.

Only the uppermost part of the conductive anomaly is within the exploration limit of the resistivity survey, but the emplacement of this deep conductive anomaly is at the same location and depth, as indicated by the HEM data. Resistivity surveys from segments B and C also corroborated HEM results and provided confidence that the HEM surveys could be relied upon to provide useful information pertaining to the location of conductive and resistive layers within impoundments.

Resistivity profiles also were obtained from active push outs at the Brushy Fork impoundment and the Jarrell's Branch impoundment and compared to airborne data (Figure 25 and Figure 26). Because resistivity surveys were performed two years after the helicopter survey - HEM results from 2003 push outs had to be compared with resistivity

results from 2005 push outs, even though the 2005 push outs may have been in a different location. For this comparison to be truly meaningful there would have had to be no significant changes in the coal waste material or its handling between 2003 and 2005.

Figure 25. Combination of ground-based (Supersting resistivity) and airborne (Fugro-Resolve) geophysical techniques implemented to analyze the push-out and the dam at Brushy Fork impoundment. (A): An HEM derived apparent conductivity map gridded from 116300 Hz frequency channels conductivity and laid over a digital raster graphic. (B): Apparent resistivity cross-section over the dam. (C): The field survey profiles were laid across five HEM flight-lines in this higher resolution map of the 116300 Hz HEM derived apparent conductivity. (D): CDI cross-section of the apparent resistivity data collected at the push-out, with the profile laid across four HEM flight-lines (80090, 80100, 80110 and 80120). Field photographs were taken at the Brushy Fork impoundment.

Figure 26. Jarrell's Branch impoundment: combination of ground-based (Supersting resistivity) and airborne (Fugro-Resolve) geophysical techniques over the push-out. (A): An HEM apparent conductivity map derived from 116300 Hz frequency channels and laid over a digital raster graphic. (B): Apparent resistivity cross-section over the 2003 push-out location. Conductive layer (blue) is interpreted as unconsolidated slurry over resistive (red) bedrock. (C): Enlarged image of airborne-derived conductivity showing emplacement of the groundtruth profile. (D): Resistivity profile is chosen to cross two airborne trajectories. Please note the differences in color scales for airborne data (red: high conductivity, blue – low) and ground data (red – high resistivity, blue – low).

Nevertheless, resistivity profiles from the 2005 survey of Jarrell's Branch push-out did compare well with HEM data from same push out. In Figure 27, both helicopter electromagnetic data and resistivity profiles from a push out at Jarrell's Branch Impoundment show a resistive surface layer that we know to be coarse coal waste placed

56

on the surface of the push out. The resistive layer is thicker in the 2005 resistivity profile than in the 2003 HEM sounding because additional coarse coal refuse had been disposed there by 2005.
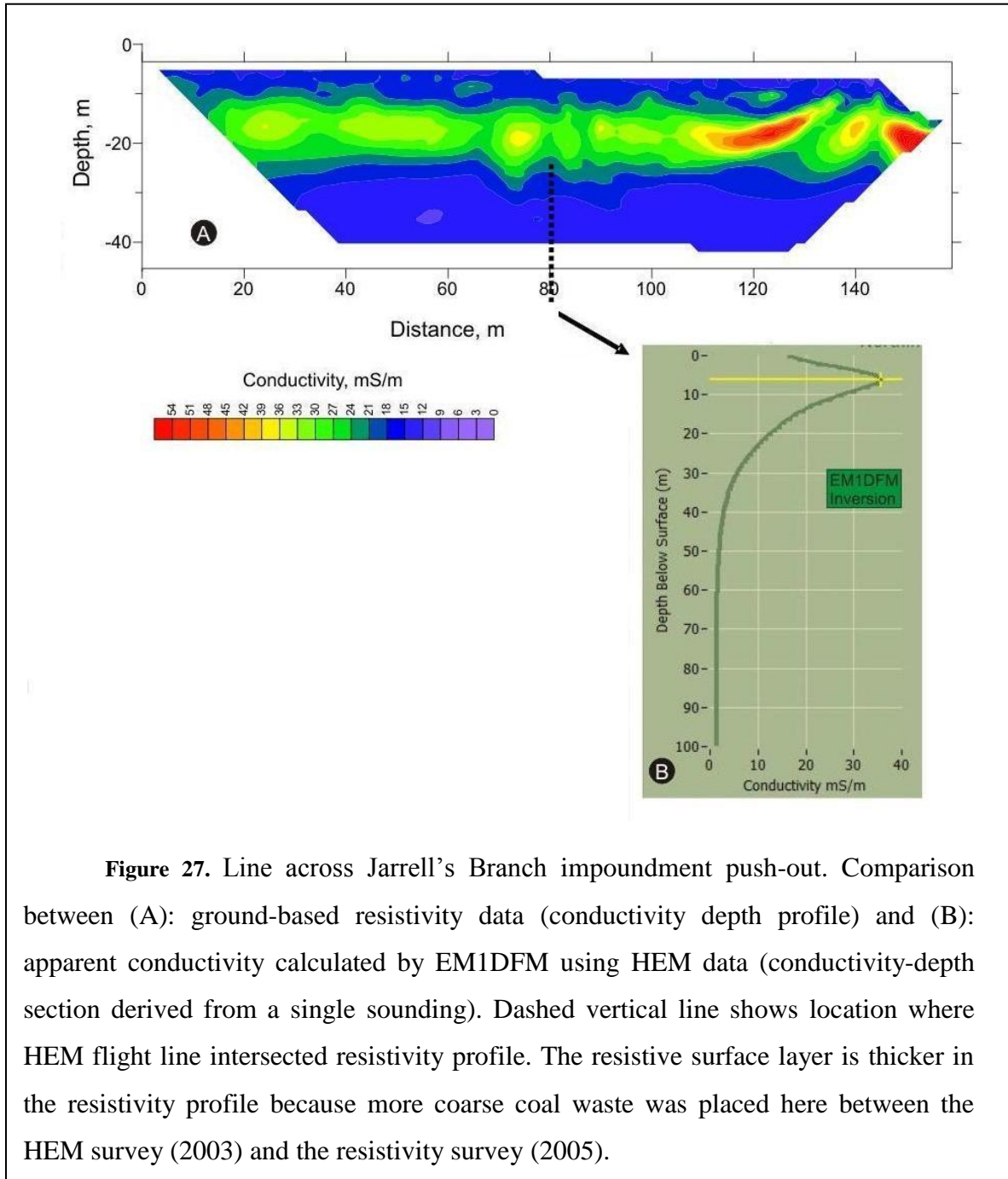
Figure 27. Line across Jarrell's Branch impoundment push-out. Comparison between (A): ground-based resistivity data (conductivity depth profile) and (B): apparent conductivity calculated by EM1DFM using HEM data (conductivity-depth section derived from a single sounding). Dashed vertical line shows location where HEM flight line intersected resistivity profile. The resistive surface layer is thicker in the resistivity profile because more coarse coal waste was placed here between the HEM survey (2003) and the resistivity survey (2005).

Although a resistive base (further interpreted as bedrock) was observed at the Jarrell's Branch impoundment (Figure 26 and Figure 27) there is no evidence of same signature at

57

the Brushy Fork impoundment even to a depth of about 50 m in the airborne or field survey (Figure 25).

Overall, groundtruth at an inactive Monclo and active Jarrell's Branch impoundments confirmed that the HEM depiction of conductivity is spatially accurate in both the horizontal and vertical planes. Based on these findings, we can be reasonably assured that conductive anomalies in the HEM data are real and can be found at the location and depth depicted.

1.3.3. Interpretation of geophysical data

The primary goal of this study was to evaluate HEM as a means to quickly screen coal waste impoundments and look for indicators of potential failure. HEM was expected to be a good tool for determining hydrologic conditions within the impoundments because of the contrast in electrical conductivity between:

1) Coal waste and bedrock
2) Vadose (unsaturated) and phreatic (saturated) zones within coarse coal waste
3) Consolidated and unconsolidated fine coal waste
4) Flooded underground mines and bedrock.

Basic hydrologic terminology includes vadose and phreatic zones in respect to description of groundwater saturation of the subsurface. Vadose zone includes strata from the surface to the groundwater table and can be described as permeable medium, allowing movement of groundwater to the phreatic zone. Water saturation of vadose zone is a function of the precipitation intensity, internal hydrologic conductivity and time. The phreatic zone is saturated with groundwater at all times, in consequence its extent and geometry are controlled by the groundwater table, internal hydrologic conductivity, amount of inflow/outflow and terrain (Gupta and Singhal, 1999).

58

Electric conductivity of impoundment water is much greater than the bulk conductivity of dry coal refuse or bedrock matrix. Differences in apparent conductivity for an individual impoundment are generally controlled by level of groundwater saturation. The following general observations can be made:

1) Bedrock provides less pore space to accommodate conductive fluids; therefore coal waste is in general more conductive than bedrock.
2) Saturated coarse coal waste of phreatic zone is more conductive than unsaturated material, composing the crest of the embankment and the vadose zone in general.
3) Consolidated coal waste is dry and therefore less conductive than unconsolidated material.
4) Flooded underground mines are more conductive than bedrock with any level of groundwater saturation.

Generalizing the above, saturated material with high porosity will be the most conductive. Saturated, well compacted material (lower porosity) will be somewhat less conductive. The least conductive material will be poorly compacted coarse coal waste, which is placed above the water table. HEM data can provide a clear demarcation between the vadose and phreatic zones within the embankment, because of significant conductivity differences between saturated and unsaturated material. When material is obviously below the water table, HEM provides an indication of porosity; more porous material will be more conductive, however, HEM does not provide an indication of permeability, although attempts to statistically correlate electrical conductivity and fluid permeability were made (Wendroth et al, 2006).

The decant basin is the most conductive part of a coal waste impoundment (Figure 28) because it often contains conductive, standing water several meters deep. In this case, the surface is less conductive than deeper areas of the decant basin, which may indicate that the conductive surface water has infiltrated or that lifts of coarse coal waste have been placed on the surface of the basin. The embankment crest is usually the least conductive area because it is composed of coarse coal waste placed high above the water table. The

59

downstream embankment commonly contains conductive layers that represent the paths taken by water filtering through the embankment. Seeps and springs are located where conductive layers are at or near the ground surface.
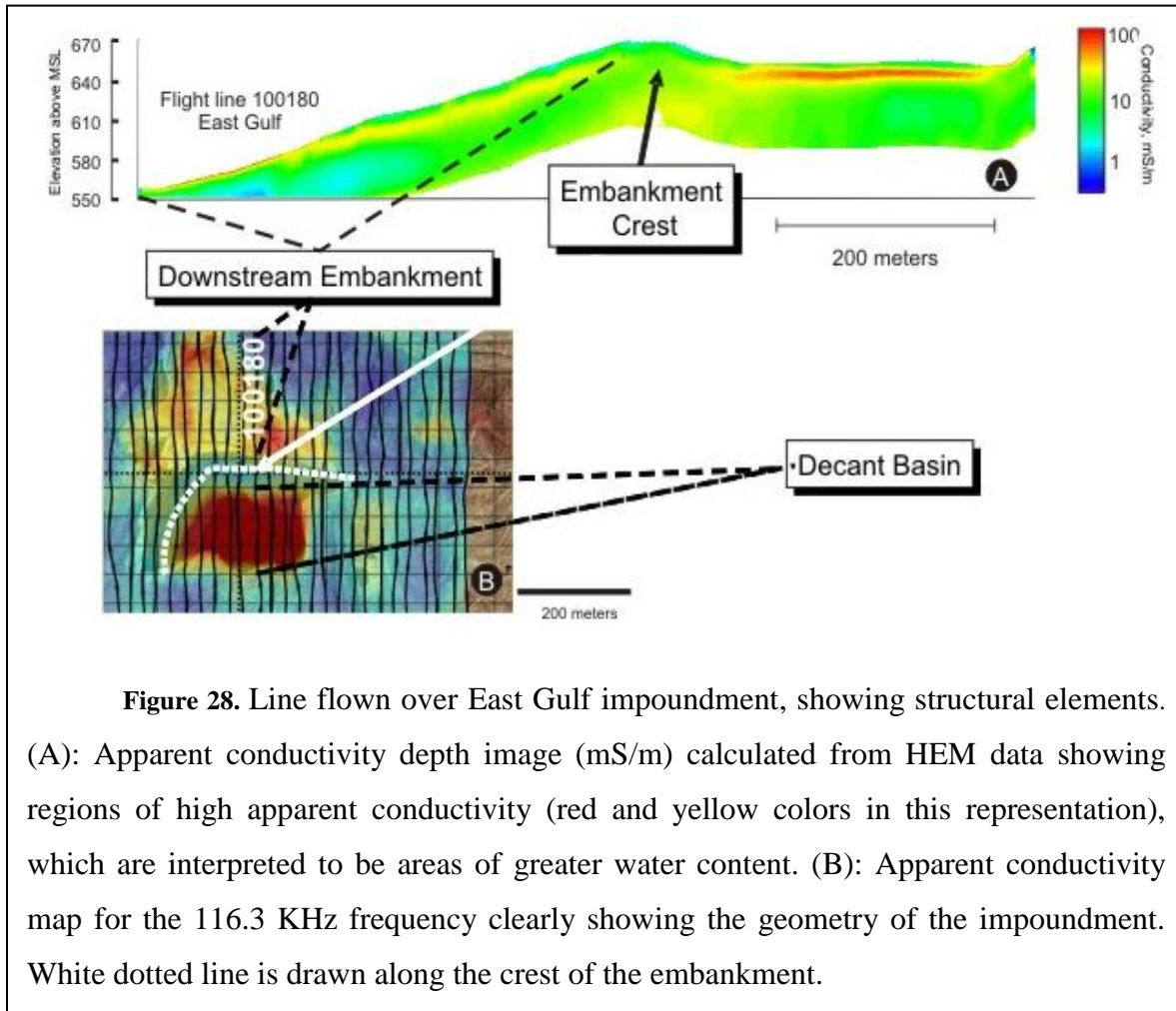
Figure 28. Line flown over East Gulf impoundment, showing structural elements. (A): Apparent conductivity depth image (mS/m) calculated from HEM data showing regions of high apparent conductivity (red and yellow colors in this representation), which are interpreted to be areas of greater water content. (B): Apparent conductivity map for the 116.3 KHz frequency clearly showing the geometry of the impoundment. White dotted line is drawn along the crest of the embankment.

Bedrock signature, unconsolidated slurry versus consolidated material

Beneath the resistive surface at Jarrell's Branch impoundment is a conductive layer that we interpret to be unconsolidated coal slurry (Figure 26 and Figure 27). Resistive bedrock can be seen beneath the coal slurry layer. The distribution of conductivity beneath this push out supports our assumption that conductivity is proportional to a material's water content; coal slurry has higher water content and is, therefore, more conductive than coarse coal waste. However, high clay mineral content may also increase conductivity.

At the Brushy Fork impoundment, coarse coal refuse placed on the surface of the push-out is more conductive than the surface layer at Jarrell's Branch impoundment (Figure 27). This difference can be attributed to the Brushy Fork impoundment material being moister and more clay-rich than that the coarse refuse at Jarrell's Branch pond.

So far no direct relationship allows determining exact groundwater level at a particular location. In order to accurately identify phreatic surface, HEM results must be corroborated with hydrologic data from piezometers or groundwater monitoring wells. It is important to establish such relationship for a specific rock type, as the conductivity of saturated zone may vary from one rock type to another, due to changes in porosity and other physical properties. After accurate mapping of phreatic surface based on experimentally established relationships, HEM data can be used to substitute for traditional measurements in making impoundment regulatory decisions.

Control of Phreatic Surface

The phreatic surface is defined as the top of the zone of saturation or water table, which is open to atmospheric pressure. Normally, phreatic surface is being engineered in order to prevent piping and surface erosion and to assure slope stability. Especially for the upstream impoundments it is important that groundwater would emerge at the base (toe) of the dam, therefore hydraulic conductivity (K) of the impoundment material has to increase dam-ward in order to assure gradual drawdown in this direction, as shown in Figure 29. Certain hydrologic conditions discussed further in the document are undesirable in impoundments and can be recognized in CDIs generated from HEM survey data.

Figure 28 shows a normally seeping impoundment. The CDI shows conductors (yellow-red) that represents unconsolidated fine-grained slurry in the basin and filtrate flow through the embankment, emerging near the base of the downstream slope. The resistive surface layer in the basin is a push out of coarse coal refuse. In general, most impoundments exhibited normal filtrate seepage through the embankment with the phreatic surface emerging near the bottom of the dam.
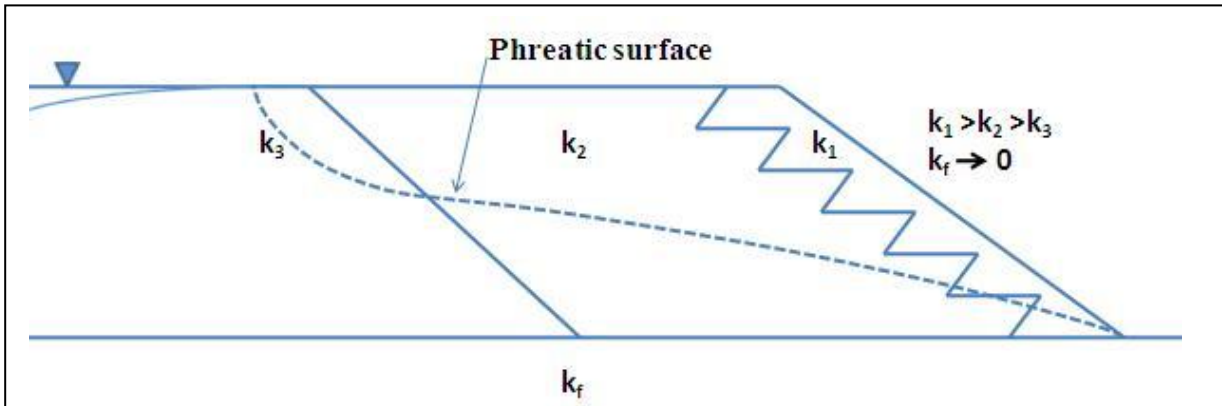
Figure 29. Engineered geometry of phreatic surface within the tailings impoundment. In this figure, the variable k is the hydraulic conductivity; specific hydraulic conductivity coefficients: k_1 – hydraulic conductivity of the embankment, comprised of coarse coal refuse material mixed with clay, k_2 – hydraulic conductivity of the intermediate zone, k_3 – hydraulic conductivity of consolidated coal slurry close to the spigot point and k_f - hydraulic conductivity of the bedrock (Modified from Saxena, 1994).
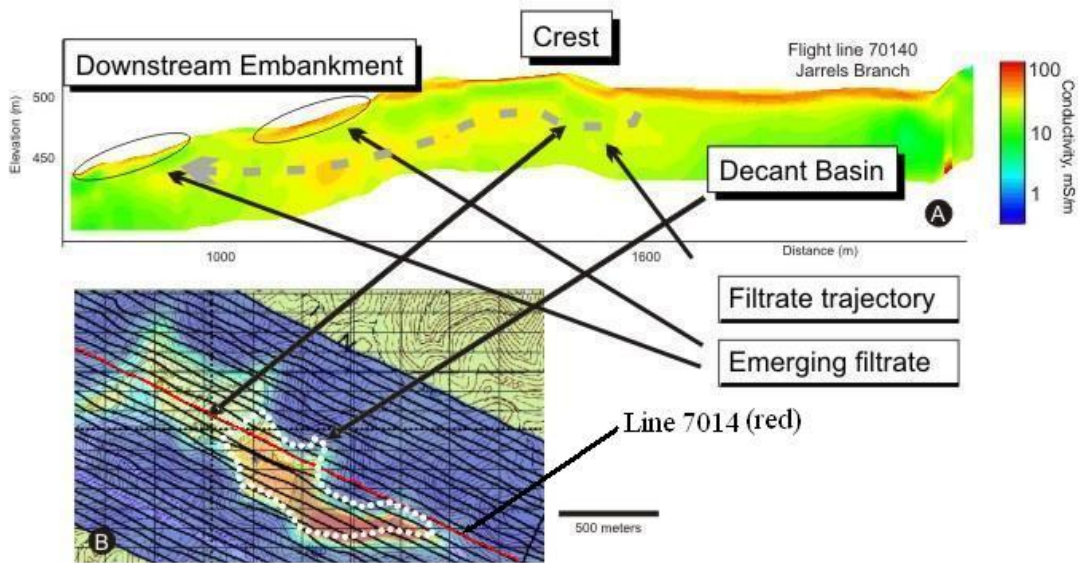
Figure 30. (A): Apparent conductivity depth image (mS/m) calculated from HEM data collected over Jarrell's Branch impoundment showing regions of high apparent conductivity (red and yellow colors in this representation). Filtrate flow trajectory is delineated on the image as well as areas of emerging filtrate. (B): Apparent conductivity map for the highest frequency collected clearly showing the geometry of the impoundment.

Brushy Fork and Jarrell's Branch impoundments are examples of an upstream and a downstream raised embankment, respectively. The hydrologic environments that have developed within the embankments of these two impoundments are very different. Figure 30 shows a CDI from a flight line at the Jarrell's Branch impoundment. This design facilitates the incorporation of drains into the downstream embankment, particularly blanket drains. In Figure 30, conductors can be seen within the downstream embankment, which are interpreted to be filtrate flow zone. Filtrate emerges at base of terraces where toe drains provide routing of filtrate to trenches along either abutment. Filtrate flowing in the lower flow path does not emerge until it reaches the base of the embankment.

Unconsolidated coal slurry underneath the embankment

Interpretation of HEM derived CDIs from different impoundments allowed us to observe various effects by distinguishing fine material from coarser according to its fluid saturation and therefore, electrical conductivity. Among others are the effect of a changing spigot point location, which was detected from the distribution of unconsolidated coal slurry in the basin; invasion of filtrate into adjacent aquifers. Unconsolidated coal slurry located underneath an embankment, because of its susceptibility to seismic events, is of especial concern (Figure 31). This particular line was flown over the McComas impoundment and shows the presence of unconsolidated material underneath the dam embankment. Figure 31 is of great importance as it shows indications of potential failure due to slope instability. In such situation it is recommended to perform quantitative assessment of safety factor (FS) (Huang, 1983).
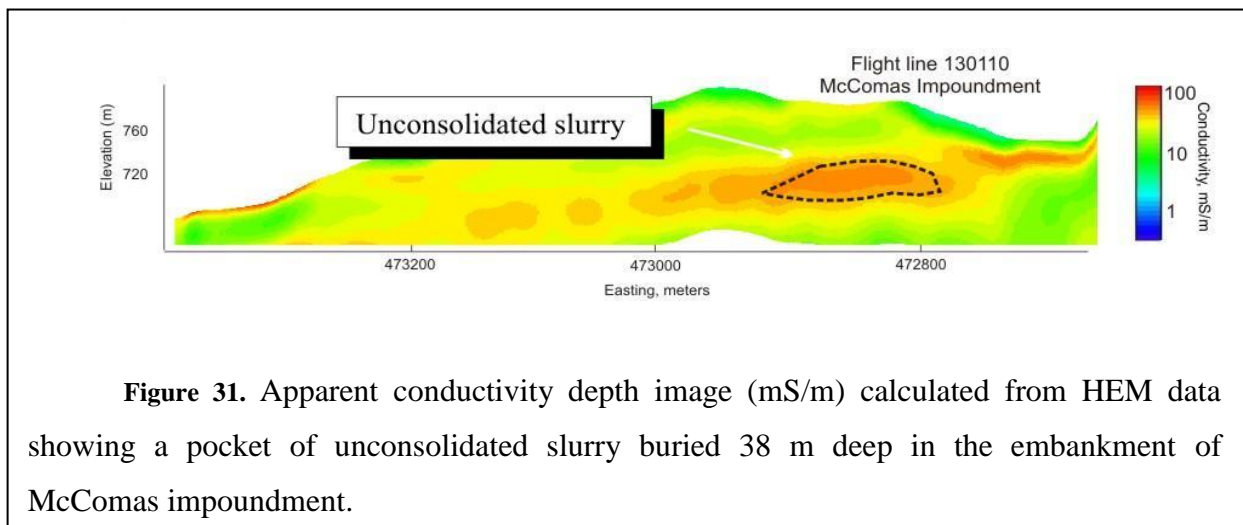
Figure 31. Apparent conductivity depth image (mS/m) calculated from HEM data showing a pocket of unconsolidated slurry buried 38 m deep in the embankment of McComas impoundment.

<u>Underground mine workings</u>

Figure 24 shows a discontinuous conductor about 30 m below the surface of the decant basin of the Monclo impoundment that may represent flooded underground mine workings. Resistivity surveys conducted as part of the ground verification activities confirmed the existence of this conductor. Although there are no records of an underground mine at this location and elevation, there are permits on record to auger mine the Winifrede coal of Kanawha formation at this particular depth. The Winifrede coal occurs at the same elevation as the conductive anomalies. We suspect that the Winifrede coal was auger mined from a strip bench now buried beneath the decant pond, and that the flooded auger bores are the source of the conductive anomalies. Although, HEM surveys of the 14 impoundments identified numerous flooded mine workings that are above drainage, this is the only CDI that may show flooded, underground mine workings beneath the impoundment.

1.3.4. Conclusions

Helicopter electromagnetic surveys provide a three-dimensional picture of the conductivity distribution within coal waste impoundments. NETL personnel have used ground resistivity surveys to confirm the accuracy of HEM results (i.e. to corroborate the location, depth, thickness, and conductivity of conductors). For the purposes of this study, water is assumed to be the most conductive component of coal waste impoundments, and conductive areas are assumed to be areas of greater water content. Hydrologic interpretations using HEM data from 14 coal refuse impoundments appear to justify this assumption. However, if hydrologic interpretations based on HEM data are to be used for making regulatory decisions, the interpretations must be substantiated with results from accepted sources of hydrologic data. Currently, we suggest that HEM results be used to target investigations that can directly measure physical or hydrological properties.

Results of this study suggest that conductivity-depth images generated from HEM data can be used to identify many hydrologic features of coal waste impoundments. For example, the pathways taken by filtrate through the embankment can be discerned readily by following conductors from the decant pond through the embankment until they emerge on the downstream face. One can predict areas prone to springs and seeps by noting where conductors are at or near the surface. Also, HEM should be able to detect flooded mine workings that are adjacent to coal waste impoundments. Detection of flooded mine workings beneath the impoundment is less certain, however, because the exploration depth of HEM is limited by the conductive materials that comprise the impoundment. HEM appears to be able to identify pockets of unconsolidated slurry in the decant pond or beneath the embankment.

Hydrologic features detectable by HEM have been linked to past impoundment failures. For example, HEM should be able to depict the location of the phreatic surface between the decant basin and its emergence on the downstream slope of the embankment. This knowledge will help identify sites of internal erosion (piping) or surface erosion. HEM can also locate large areas of unconsolidated slurry beneath the embankment that may be subject to fluid-like flow under certain conditions. Finally, any flow of water or slurry from the decant basin into flooded mine workings or aquifers will be detected by HEM if within the exploration depth of HEM.

Additional geotechnical properties of refuse impoundments such as slope stability factor (FS) may be evaluated by enhancing airborne surveying with additional radiometric data collection. Radiometric data in our view would be capable of providing clay content characteristics of the embankment and thus, hydraulic conductivity. In combination with porosity and groundwater table data derived from EM surveying and bulk density derived from core logs and independent analysis - these characteristics are sufficient to calculate FS.

2.   **SECOND PROJECT (METHANE SEEPAGE ASSESSMENT)**

2.0. INTRODUCTION

Three reflection seismic surveys where completed at a site in Southwestern Pennsylvania in support of a multidisciplinary effort to mitigate gas migration adjacent to abandoned wells of a gas field drilled through the Murrysville anticline (Figure 32). The goals of the reflection seismic surveys were to determine the location of natural gas accumulations and possible migration paths to the surface. The McKeesport gas field was short lived, but intensely explored.

Figure 32. Image showing the McKeesport Gas Field. This photo courtesy of Mr. Jim Sams, NETL/DOE.

Methane (CH_4) is a colorless, odorless gas that occurs as the principal component in natural gas reservoirs, and is often associated with coal (as coal bed methane or CBM). It can be formed by bacterial processes and the decomposition of vegetation in the absence of oxygen. It is less dense than air and can form explosive mixtures with air when present at concentrations of 5 to 15% (Lide, 1991).

A major underground storage gas leak caused explosion and fires in Hutchinson, Kansas, as described in Allison (2001), Nissen et al, (2003) and Xia, (2002). Geyser like fountains of natural gas and brine were observed during this event.

In this study three seismic methods were utilized along with geochemical, magnetic, stratigraphic, downhole and hydrogeological surveys. Geochemical survey revealed the gas composition was predominantly (>98%) CH_4 and therefore presumably associated with known coal beds. Magnetic geophysical surveying, carried out by R. Hammack and G. Veloski were helpful for mapping some previously unknown abandoned wells, which were possibly responsible for vertical gas migration. Furthermore, stratigraphic studies, strengthened by hydrologic modeling allowed creating the dynamic model of CH_4 escape and migration.

In the seismologic studies a sledge hammer source and 60 station reflection seismic lines were used to estimate depth to bedrock and rock velocities for shallow geologic units. These results confirmed potentially thick fill in the low velocity zone.

Marine reflection seismic profiles were also collected in order to locate gas seepage through the river bottom, responsible for visually detectable gas bubbles reported to appear on water. Most of the river bottom sediment appears to be quite thin where surveyed; however anomalous reflectors were seen along two marine lines, which could represent gas filled fractures. These observations led to a geologic investigation of the rocks immediately across the river from main study area in order to observe bedrock facies variations and to determine porosity and permeability for some surface samples. These samples showed

generally low porosity and permeability, demonstrating that in an unfractured state surface rocks could provide a "lid" or capping structure to vertical gas migration.

A three dimensional reflection seismic survey was further completed using an EnviroVib™ energy source. Although building land fill has to some extent obscured some portions of the lines, when processed using innovative crooked line processing techniques and determining seismic attributes reflections caused by actual subsurface geology were observed. These data were additionally processed to derive anomalous reflection zones from reflection amplitude variation with offset in the pre-stack dataset (AVO). These seismic data are interpreted to represent possible gas accumulation zones including shallow targets adjacent to Mahoning sandstone and Upper Freeport coal.

2.1. BASICS OF SEISMIC THEORY

2.1.0. Preface

Reflection seismology has been a central and standard method for oil and gas exploration since 1927 when the Geophysical Research Corporation working in the Maud oil field of Oklahoma commercially implemented the technique (Roden, 2005).

As part of the program to investigate the abandoned gas field region, reflection seismology was used to investigate the subsurface. In the following section, fundamental concepts related to reflection seismic surveys and our studies are summarized.

2.1.1. Reflection seismology components

Reflection seismology is a non-invasive geophysical system that consists of an energy source, an energy transfer medium and an energy receiving unit (Figure 33).

Energy source

In reflection seismic studies, the energy source can be anything producing an elastic disturbance in the earth medium, ranging from natural sources such as automobile traffic, trains or even earthquakes to controlled artificial energy sources of known force, waveform and amplitude, positioned at a precise location either on the surface or below it. These can include hammer-strikes, dynamite explosions, special weight-drop machinery, and for marine reflection surveys, marine transmitting transducers or air guns. The spatial location of energy sources in seismic exploration is called source point (SP) or energy point (EP) and the distance between

source points is called the source point interval. Energy released at the source point produces an elastic wave field which is both transmitted and reflected at impedance boundaries. Each reflection is delayed by the amount of time required to travel from the source to the reflected interface and back and decreases in amplitude with travel time due to spherical divergence of the elastic wave field and attenuation.

Figure 33. Reflection seismology basic theory visualization modified from:

http://www.isgs.uiuc.edu/app-geophy/images/seismic_reflection/reflection_surveying.gif.
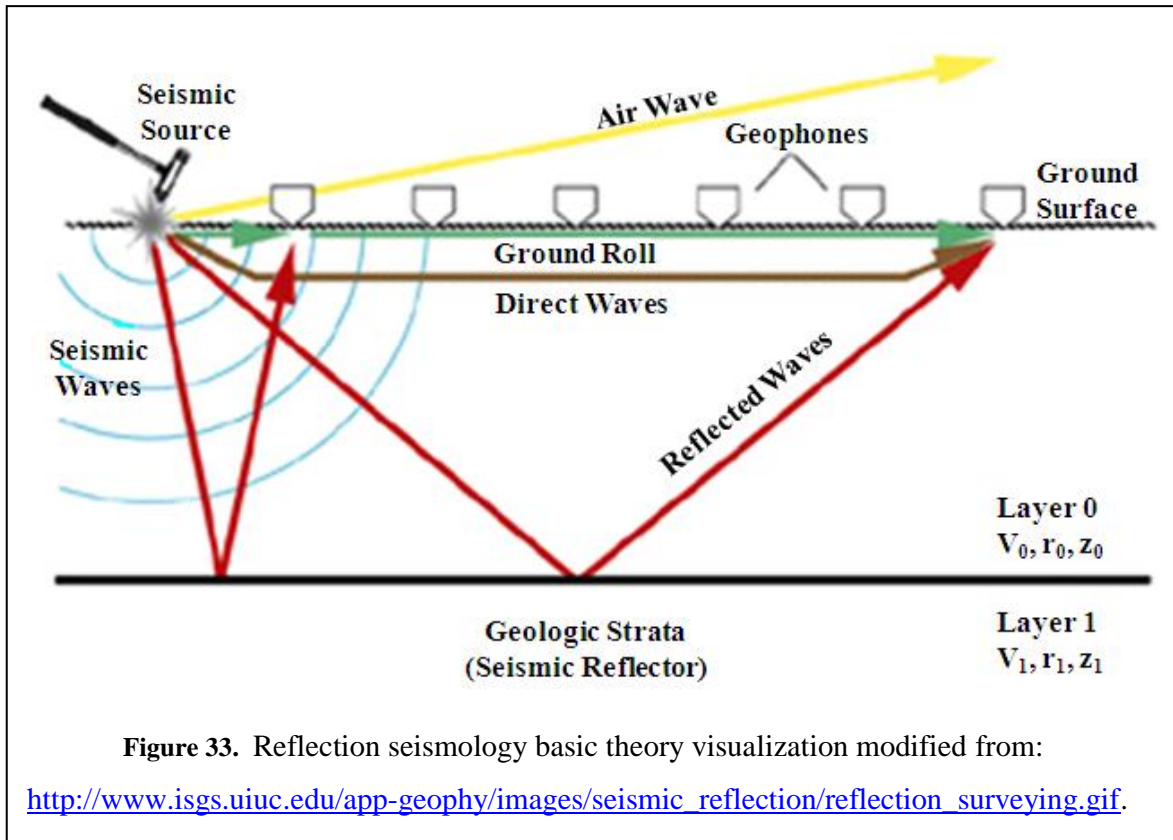
In 1953 Vibroseis™ technology was introduced to the geophysical community. Vibroseis™ uses a long source, frequency-variant signal of precisely known characteristics which are recorded. The signal is initiated usually by a heavy plate, attached to the bottom of a vehicle which comes in contact with the ground and vibrates for a continuous time window. During this time the frequency of vibration is gradually modulated to include an entire spectrum from lowest to highest frequencies (to perform one sweep). Benefits of shooting continuous frequency-varying signal include the ability to improve both depth of the survey and vertical resolution. Generated source signals are then correlated with the geophone records to yield a highly precise reflection record for each geophone. Vibroseis™ technology reduces the noise level of seismic acquisition.

Energy transfer medium

Elastic wave propagation can take place through solids, liquids, and gases. The transfer medium is the substance through which the elastic seismic waves propagate. In our study, this was earth material, or in the marine profiles, earth material and pore filling phases. In addition to surface waves (ground roll, Figure 33), which travel along the surfaces of material, elastic waves can travel through solids in two different styles of elastic deformation, each corresponding to a distinct elastic seismic wave. These are, elastic compression parallel to the direction of elastic wave field motion (this type of elastic wave is a P wave) or elastic deformation perpendicular to the direction of elastic wave propagation (this type of elastic wave is an S wave). Both are shown in Figure 34.
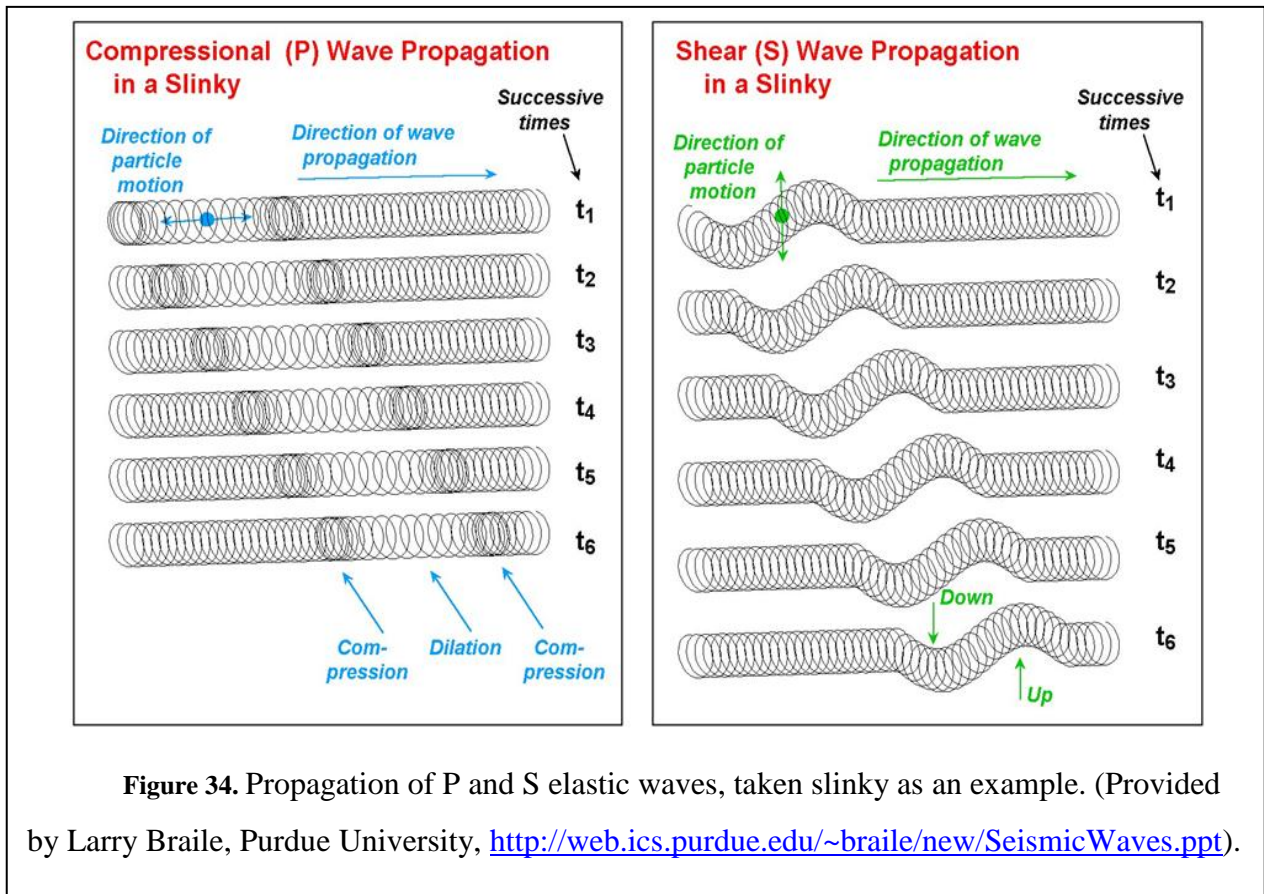
Figure 34. Propagation of P and S elastic waves, taken slinky as an example. (Provided by Larry Braile, Purdue University, http://web.ics.purdue.edu/~braile/new/SeismicWaves.ppt).

In fluids shear strength equals zero; therefore, they do not allow S-wave propagation. P-wave propagation is dependant on more physical properties than shear modulus and density, therefore P-wave does not vanish in fluid, although is is significantly attenuated. There are

two main physical laws involved in the process of seismic wave propagation through matter (Figure 35 and Figure 36):

- **F = ma** (Newton's second law of motion, where F is the force, applied to a body of mass m in order to produce motion with acceleration a)

- **E*(ΔL/L) = F/A** (Hooke's law of elastic deformation for a perfectly elastic rod of initial length L and cross-sectional area A, where force F, normalized over A represents stress, and deformation ΔL normalized over initial length L – represents strain. In this equation E – is the coefficient, called the Young's modulus which describes material's response to linear strain.

| Figure 36. Newton's second law of motion. | Figure 35. Illustration of Hooke's law. |
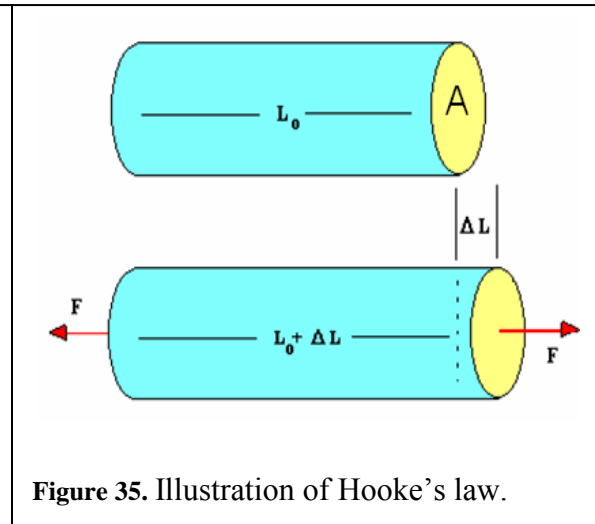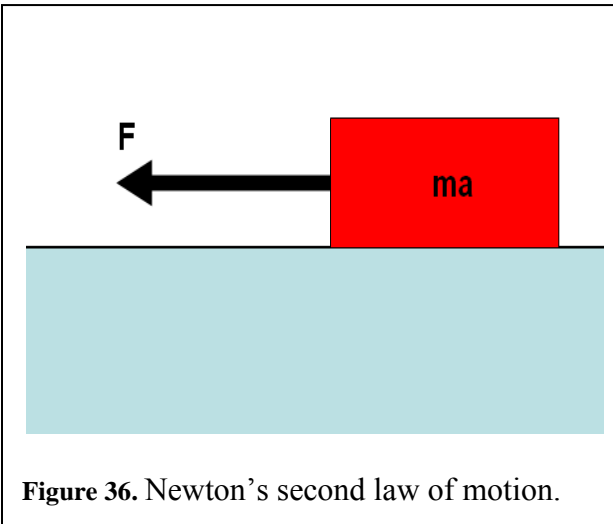
However when material is stretched in one direction, it tends to get thinner in the other two directions. The measure of this tendency is called Poisson's ratio and is defined by the equation 2.1(Talford, 1990):

$$\gamma_{yx} = -\frac{\varepsilon_x}{\varepsilon_y} \quad \text{(2.1)}$$

Where:

γ_{yx} is the resulting Poisson's ratio

ε_x is the transverse strain

ε_y is the axial strain

Poisson's ratio is a measure of transverse strain, normal to the applied load (Telford et al, 1990).

In the case of triaxial strain in a homogeneous medium the modulus of elasticity is referred to as the bulk modulus (K) and is equal to the volume stress ΔP normalized over volumetric strain ΔV. The bulk modulus describes the material's response to uniform stress.

For cases of S-wave propagation the shear modulus (μ) must be considered. By definition (Riley et al, 2007):

$$\mu \stackrel{\text{def}}{=} \frac{F/A}{\Delta x/h} = \frac{Fh}{\Delta xA} \quad \text{(2.2)}$$

Where F is the force, A is the area where the force is applied, F/ A is shear stress and Δx / h is shear strain, represented as ratio of linear size change (Δx) over thickness (h). As mentioned previously, the shear modulus of any fluid is zero.

γ, k, μ and ρ (density) are referred to as elastic moduli of a material. They are related in a series of equations, which allow calculating all of them, given any two. They define the velocities of elastic wave propagation through media. The P-wave velocity (V_p) is described by equation 2.3 (Sheriff and Geldart, 1995):

$$V_p = \sqrt{\frac{k+\frac{4}{3}\mu}{\rho}} \quad \text{(2.3)}$$

Where

k is the bulk modulus

μ is the shear modulus and

ρ the density of the material through which the wave is propagating

74

The S-wave velocity (V_s) is defined by the equation in the form of 2.4 (Sheriff and Geldart, 1995):

$$V_S = \sqrt{\frac{\mu}{\rho}} \quad \text{(2.4)}$$

As it was mentioned above, shear modulus of any fluid is zero; therefore, S waves experience attenuation related to rock porosity, void-filling phases, and fluid or gas filled fractures to a larger degree than P-waves.

<u>Energy receiving unit</u>

The energy receiving unit is sensitive to the physical displacement of the ground on the surface caused by elastic deformation. Geophones (Figure 33) are devices designed to register any such displacement. Usually only the vertical component of displacement is recorded, however some modifications of geophones allow acquiring separate readings for displacement in x, y and z directions. Geophones are placed in groups along profiles. The distance between profiles is referred to as the cross-line spacing, while the distance between groups of geophones is referred to as the receiver spacing. The distance between a source point and a geophone is called the offset.

2.1.2. Reflection and transmission coefficients

Acoustic impedance is a key concept in understanding reflection coefficients between rock layers. It is defined as $Z = V * \rho$, where V is the seismic velocity (of P-wave propagation) and ρ is the rock density. When an elastic wave propagates through the media and encounters a layer boundary, separating the mediums with different impedances – some of the energy will be reflected off the boundary, while some will continue propagation. Reflection and transmission coefficients are both dependent on medium impedance (Z). For a wave reflected from a boundary, the reflection and transmission coefficients are defined in equations 2.5 and 2.6 (Telford et al, 1990):

$$R = \frac{Z_1 - Z_0}{Z_1 + Z_0} \quad (2.5)$$

$$T = \frac{2Z_0}{Z_1 + Z_0} \quad (2.6)$$

Here Z_0 and Z_1 are impedances of the top and the bottom mediums respectively Figure 33.

2.1.3. Data acquisition

The most popular method of reflection seismic data acquisition is the Common Depth Point (CDP), which was invented by the geophysicist Harry W. Mayne in 1956 (Mayne, 1962), originally referred to by him as the CRP (common reflection point) processing. The method involves recording data from varied source and geophone locations and then combining the data during processing using a common depth point (CDP) or common midpoint (CMP) as a sorting and grouping key. The CDP or CMP position is shared between all sources receive pairs in this method. Summing these various pairs, after geometry-dependent corrections have been made, significantly increases the signal to noise ratio for each reflecting horizon.

In Figure 37, the offset axis $\Delta X = (g - s)$ where $\mathbf{g}$ is the geophone emplacement and $\mathbf{s} -$ is the shot-point. The mid-point axis X equals $(s + g)/2$ is a measurement of the averaged source and receiver distance along the seismic profile. Traces, located parallel to the mid-point axis at a fixed distance ΔX are called a common offset. These traces are always a fixed distance from the source and are sometimes used to determine the character of reflecting horizons during a reflection seismic survey. Finally, the collection paralleling the offset axis at a fixed mid-point X is called a common depth point (CDP) gather or a common mid-point gather (Schneider, 1984).
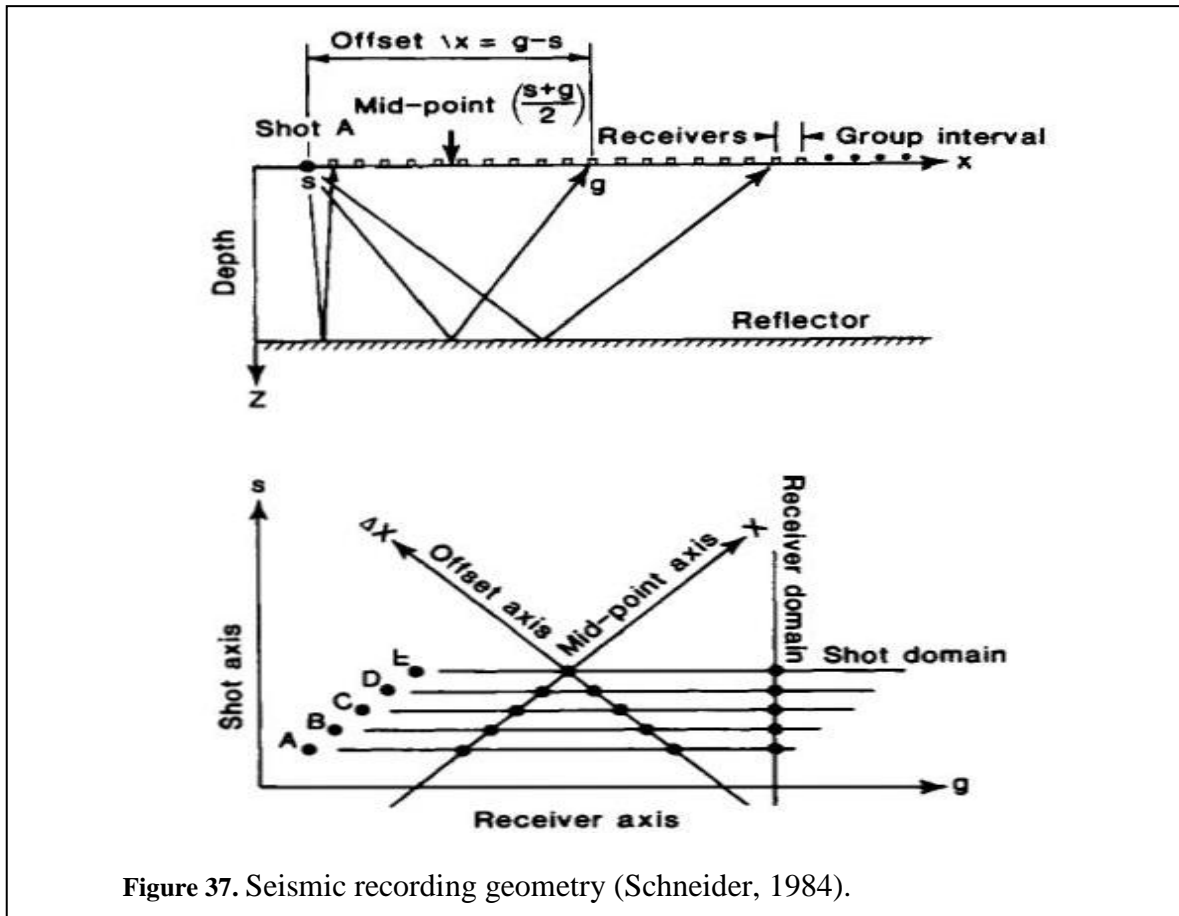
Figure 37. Seismic recording geometry (Schneider, 1984).

The CDP method requires shooting energy from multiple points, located along profiles. The shot point is advanced a small increment after each recording in order to obtain a high degree of overlapping coverage of subsurface. Significant redundancy of a survey serves for improving signal-to-noise ratio during signal processing. The lower portion of Figure 37 illustrates a useful technique for visualizing the interrelationships among overlapping recordings in a conventional 2D seismic survey. By plotting sourcepoint coordinate, s, against receiver coordinate g in a 2D orthogonal coordinate frame, the overlapping recording geometries can be visualized. The CDP method was a miracle breakthrough in the industry as it allowed to increase the signal to noise ratio by the amount of times equal to square root from the number of seismic traces participating to produce a single stack. CDP also allowed increased capabilities for seismic velocity analysis (Scneider, 1984; Telford et al, 1990)

2.2. SEISMIC DATA PROCESSING THEORY

2.2.1. Signal and noise

The fundamental tenet of seismic interpretation assumes that seismic reflections can be related to geologic boundaries in the subsurface. Since our observations are in the space-time domain, we must be able to invert the observed travel times to depth to obtain the desired subsurface geologic model (Schneider, 1984).

Prior to processing it is important to analyze the noise level in the data. Each seismic system has its own dynamic range. A dynamic range is an indicator of system quality and is measured in decibels (dB) It describes signal to noise ratio and the maximum possible value of this ratio is referred to as high dynamic range. In the signal spectrum (frequency domain) visible source noise usually is present as a high-frequency component, therefore by applying a low-pass filter to seismic data it is possible to significantly improve the signal to noise ratio (Telford et al, 1990). However, frequency-filtering operations is done in frequency domain, therefore prior to filtering the data set has to undergo a Fourier transform. The Fourier transform and inverse Fourier transform are the techniques of transferring data from time domain to frequency domain and from frequency domain to time domain. Mathematically it is expressed in the form of equations 2.7 and 2.8 (Telford et al, 1990)

$$F(\omega) = \sum f(t) e^{-i2\pi\omega t} \quad \text{(2.7)}$$

$$f(t) = \sum F(\omega) e^{-i2\pi\omega t} \quad \text{(2.8)}$$

In these equations f(t) represents a function in the time domain, F(ω) is the frequency domain function, w is the frequency and i equals $\sqrt{-1}$.

In seismic reflection processing the data is deconvolved, which is a procedure of extracting the reflectivity function from the seismic trace, thus improving the vertical resolution and recognition of events (Sheriff and Geldart, 1995).

In order to adjust the data considering differences in geophone elevations and the presence of a low-velocity zone in the subsurface due to either cultural or soil layer static corrections are being applied. Static correction transfers all the data collected on the surface to a horizontal datum, usually close to the Earth's surface (Telford et al, 1990). Static correction involves the small time-shifting of every seismic trace independently by an amount defined by difference in elevation and a known or estimated velocity model between the Earth's surface and the horizontal datum (Kant, 2004).

2.2.2. Normal moveout (NMO)

On common midpoint gather the reflections form a hyperbola with respect to offset plotted versus two-way travel time. The two-way travel time **t** of a horizontal reflector can be calculated according to equation 2.9 (Sheriff and Geldart, 1995):

$$t = \sqrt{\frac{x^2 + 4h^2}{V^2}} \quad \text{(2.9)}$$

Where **x** is the offset, h is the depth to the reflector and V is the average medium P-wave velocity.

The concept of normal move-out (NMO) is important because it allows the interpretator to understand reflection characteristics over a wide range of offsets (Sheriff and Geldart,

1995). The time difference caused by NMO can be calculated as 2.10 (Sheriff and Geldart, 1995):

$$t_{NMO} = x^2/2V^2t_0 = x^2/4Vh \quad (2.10)$$

Where t_0 is the travel time to the geophone at the sourcepoint, h is the depth to the reflector and x is the offset. If the normal moveout differs from the equation 2.10 by more than allowable experimental error – the event of reflection is not justified.

2.2.3. Velocity analysis

The average velocity to a reflector is a function of increase in reflection time, dependant on the offset distance. This analysis can be obtained from the CDP data. Following are suggested steps in order to perform accurate velocity analysis, as suggested by Waters, (Waters, 1978).

1. Selection of seismic traces, corrected for near-surface time differences, applied to a single subsurface point (common depth point).
2. Application of a geometrical correction factor to each trace based on an assumed velocity.
3. Assessment of correctness of this velocity, with an output of correction quality factor for each time window of the record, sometimes for each window centered on known reflections.
4. A change in a selected velocity over a pre-determined range.
5. A subjective picking technique, which selects the appropriate stacking velocity for each depth, record time or reflection time.

The accuracy and resolution of stacking velocities depends on acquisition factors such as offset, multiplicity, recorded bandwidth, the signal to noise ratio and lack of near or far offset traces or irregular spacing in the field (Sheriff and Geldart, 1995).

80

One further operation is common before traces are being stacked. It is called muting and consists of bringing each trace to zero in order to remove high-energy near-surface arrivals (Waters, 1978). The zeroing is done before a time given by the offset is divided by the muting velocity, although the processor may add a constant (Sheriff and Geldart, 1995).

2.2.4. Stacking

Stacking is a processing step designed to attenuate noise and to increase the signal to noise ratio. CDP stacking involves stacking of records from the common depth point and different source-receiver separations (offsets) (Kant, 2004). For j number of seismic traces contributing to a singe stack, it is convenient to measure overall energy of primary seismic trace (Sheriff and Geldart, 1995).

$$E_j = \sum_{i=1}^{M} A_{ij}^2 \quad \textbf{(2.11)}$$

In equation 2.11 - A_{ij} are the amplitudes of a trace at each sampling point and M is the number of values sampled on trace j. It is assumed that individual traces have different amplitudes because of different geophone placement and gain setting; therefore the traces in a single stack are usually scaled to a constant energy and further the sample values $S_k(i)$ at a constant time are averaged. For N traces to be added (Sheriff and Geldart, 1995):

$$S_k(i) = \frac{1}{N}\sum_{j=1}^{N}\frac{C}{E}A_{ij} \quad \textbf{(2.12)}$$

In equation 2.12 - C is a constant. The contributions of individual traces can be estimated via a correlation coefficient (CC), with a minimum value of CC of 1/N. Equation 2.12 is called a stacking relationship and is written as 2.13 (Sheriff and Geldart, 1995):

$$S(i) = \frac{1}{N}\sum\frac{C\prime}{C_1}A \quad (2.13)$$

Where C_1 is the correlation coefficient and $C\prime$ is a constant. Therefore, the output amplitude is divided by the number of traces entering the stack (Sheriff and Geldart, 1995); collection of such stacks is called a stacked record section.

2.2.5. Survey resolution

As with the EM soundings in seismic surveying resolution is a function of frequency of the signal. Furthermore in seismic surveying, especially when Vibroseis™ technology is implemented a range of frequencies is used with every sweep of the energy source (Sheriff, 1991). This range of frequencies is referred to as bandwidth. Bandwidth can be described either in Hz or in octaves (Liner, 2004). In hertz it is equal to difference between the highest and the lowest frequencies. In octaves it can be described as $\frac{\ln\left(\frac{f_2}{f_1}\right)}{\ln 2}$, where f_2 and f_1 are the highest and the lowest frequencies respectively. Dominant frequency of a survey is a mean value taken for f_1 and f_2 (Liner, 2004). Another definition of dominant frequency is the peak of the amplitude spectrum of a window in a seismic data.

Vertical resolution

The potential to image vertical detail in sub-surface features is limited by the wavelength of propagating wave. The maximum vertical resolution (ability to recognize the top and the bottom of an interval) is a function of bandwidth, the dominant frequency of the seismic signal and the noise level at the target depth. The occurrence of overlapping wavelength from closely spaced reflectors also limits vertical resolution. Vertical resolution is usually defined according to Rayleigh's criterion (Figure 38) stating that the bed thickness must be ¼ of the dominant wavelength (Sheriff, 1991). Therefore, for a seismic wave, propagating with seismic velocity V and oscillating with frequency f the dominant wavelength will be equal to V/f and therefore the vertical resolution will be V/4f.
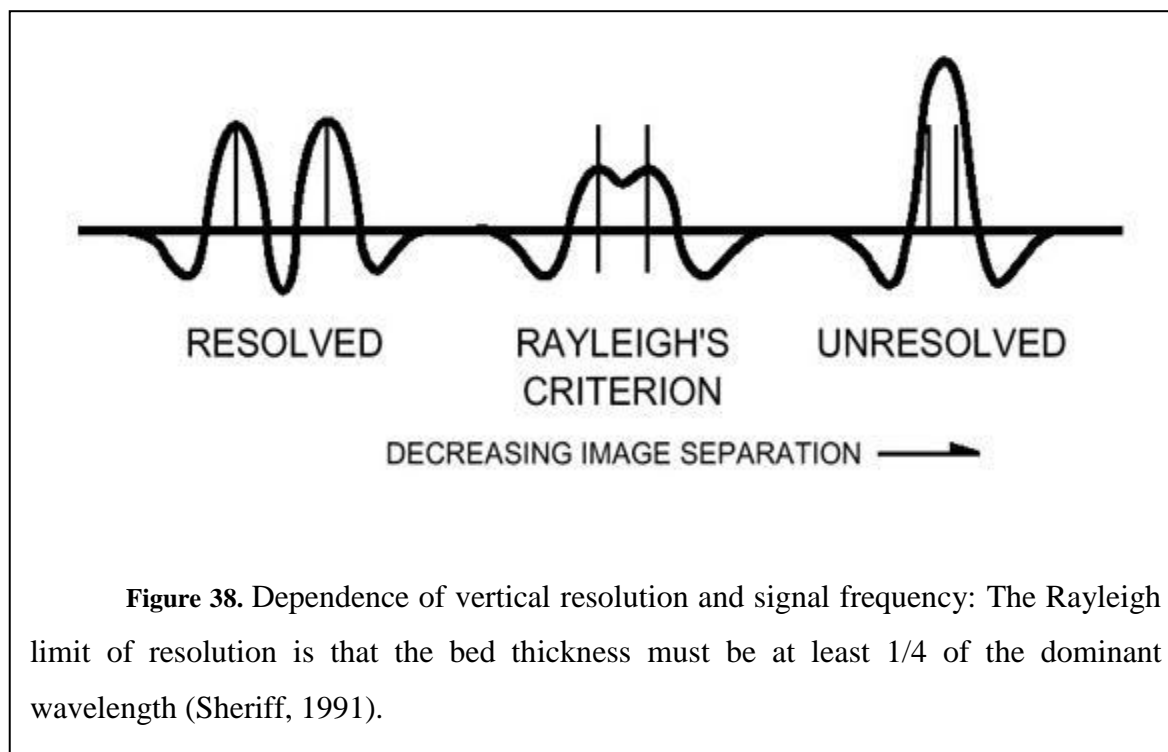
Figure 38. Dependence of vertical resolution and signal frequency: The Rayleigh limit of resolution is that the bed thickness must be at least 1/4 of the dominant wavelength (Sheriff, 1991).

Horizontal resolution

The horizontal resolution of a seismic survey is equal to the radius of the Fresnel zone (Sheriff, 2001). The Fresnel zone represents the part of a reflector imaged by the seismic wave front at a certain depth and spatial location. The reflected waves will interfere where their travel paths differ by less than a half wavelength. The segment of the reflecting surface involved in these reflections is called the Fresnel zone (Sheriff, 1991, 2001). A reflection that we think of as coming back to the surface from a point, is actually being reflected from an area with the diameter of the Fresnel zone.

Seismic resolution

In 3D seismic data an object is considered detectable if it is larger than either vertical or horizontal resolution limit. With increasing depth, the velocity and wavelength tend to increase; therefore frequency of the signal will decrease resulting in poorer resolution. Velocity increase with depth is due to compaction of sediment load under lithostatic pressure.

In order to increase the horizontal resolution of a survey stacked data is migrated. Migration is based on analytical transformation of wave equation (Claerbout and Dohrety, 1985). A concept is considered that wavefield at Earth's surface p(x, y, z = 0, t), where x and y are the horizontal coordinates of the system, z – vertical and t – is the time, represents boundary conditions of a more general wavefield p(x, y, z, t) reflected or diffracted in the subsurface (Buttkus, 2000). The objective is therefore to determine the true emplacement of target reflectors by applying downward continuation of surface wavefield in frequency domain. Figure 39 graphically describes how 3D migration allows improving on the data spatial resolution at depth.
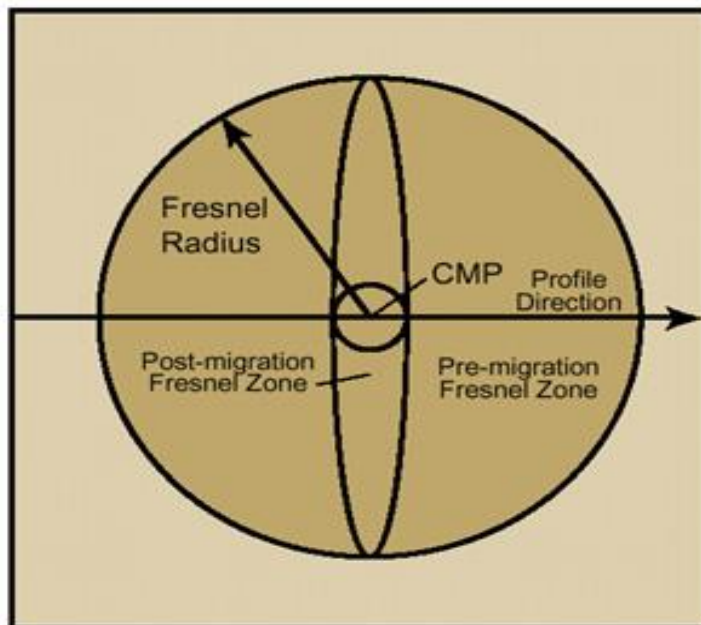
Figure 39. Decreasing radius of Fresnel zone (increasing horizontal resolution) by implementing 2D and 3D migration. 2D migration allows to decrease Fresnel zone in 1 direction (to an ellipse), while 3D migration allows to narrow the zone down to a smaller circle (Sheriff, 1991).

(http://www.searchanddiscovery.net/documents/geophysical/sheriff/images/fig04.htm)

2.2.6. AVO theory

Amplitude Variation with Offset (AVO) has been used successfully in hydrocarbon exploration to determine variation in pore-filling phases, such as gas content in gas sands (Rutherford and Williams, 1989). The theory is based on the fact that reflection coefficients may vary with increasing offset (Ostrander, 1984). Traditional AVO analysis involves calculations of AVO intercept and gradient from a linear fit of P-wave reflection amplitude to the sine squared of the incidence angle.

At a boundary between two ideally elastic, isotopic and homogeneous media – an incident wave will be partitioned into reflected P-wave, reflected S-wave, transmitted P-wave and transmitted S-wave, and the reflection coefficients will be a function on V_p, V_s, ρ_1, ρ_2 and α, where V_p – P-wave velocity; V_s – S-wave velocity; ρ_1 - density of the first medium; ρ_2 – density of the second medium and α – incidence angle.

The parameters V_p, V_s, ρ_1, and ρ_2 are dependent on such parameters as lithology, porosity, pore fluid, and confining pressure (Tatham, 1982). The P-wave reflection amplitude is a non-linear function of the angle of incidence derived from the Zoeppritz equations (2.14). Reflection at non-normal incidence leads to wave conversion and amplitude changes, especially near the critical angle (Sheriff et al, 1995).

$$R(\theta) = \frac{1}{2\cos^2(\theta)} Ip - 4\gamma 2\sin^2(\theta)Is + (2\gamma 2\sin^2(\theta) - 0.5\tan^2(\theta))D \quad \textbf{(2.14)}$$

Where: $I_p = (\Delta V_p/V_p + \Delta\rho/\rho)$ (Relative contrast in P-impedance)

$I_s = (\Delta V_s/V_s + \Delta\rho/\rho)$ (Relative contrast in S-impedance)

$D = \Delta\rho/\rho$ (Relative contrast in density)

γ - Estimate of background shear to compressional velocity ratio (V_p/V_s)

θ – angle of incidence

$\Delta V_p = V_{p2} - V_{p1}$,

$$V_p = (V_{p1} + V_{p2}) / 2,$$

$$\rho = (\rho_1 + \rho_2) / 2,$$

$$\Delta\rho = \rho_2 - \rho_1,$$

The Zoeppritz' equations have been simplified by Aki and Richards (Aki and Richards, 1980). The most commonly used approximation is presented in equation 2.15

$$\mathbf{R_{pp}(\theta) \approx R_0 + \{A_0\ R_0 + \Delta V_s / (1 - \sigma)2\}\ sin2\theta + \Delta V_p/2V_p(tan2\theta - sin2\theta)} \quad \mathbf{(2.15)}$$

Where $R_{pp}(\theta)$ – P-P reflection coefficient

R_0 – Normal incidence reflection

σ – Poisson's ratio

$A_0 = B_0 - 2(1 + B_0)[(1 - 2\sigma)/(1 - \sigma)]$

$B_0 = (\Delta V_p / V_p) / [\Delta Vp/Vp + \Delta\rho/\rho]$

Subscripts 1 and 2 refer to top and bottom layers respectively. The equation consists of three terms, with the first being representative of normal incidence, the second being most substantial for representation of intermediate angle reflections (0 to 30°), and the third being representative of greater angles ($>30^o$). Frequently, when the incidence angle is between 0° to 30°, it is convenient to use equation 2.16;

$$\mathbf{R_{pp} = R_0 + B\ sin2\theta} \quad \mathbf{(2.16)}$$

Where $B = A_0R_0 + \Delta\sigma/(1-\sigma)2$, or $R_{pp} = R_0 + B\theta^2$

In AVO analysis, R_0 is often called the intercept and the parameter B, the AVO gradient. As can be seen from these equations, the Poisson's ratio is extremely dependant on the V_p/V_s ratio. This relationship is graphically depicted in Figure 40, based on equation 2.17.

86

$$\sigma = \{Vp \, /Vs)^2 - 2\} \, / \, \{2Vp \, /Vs)^2 - 2\} \quad (2.17)$$

Figure 40. Dependence of Poisson's ratio with respect to V_p/V_s variation (Ostrander, 1984).
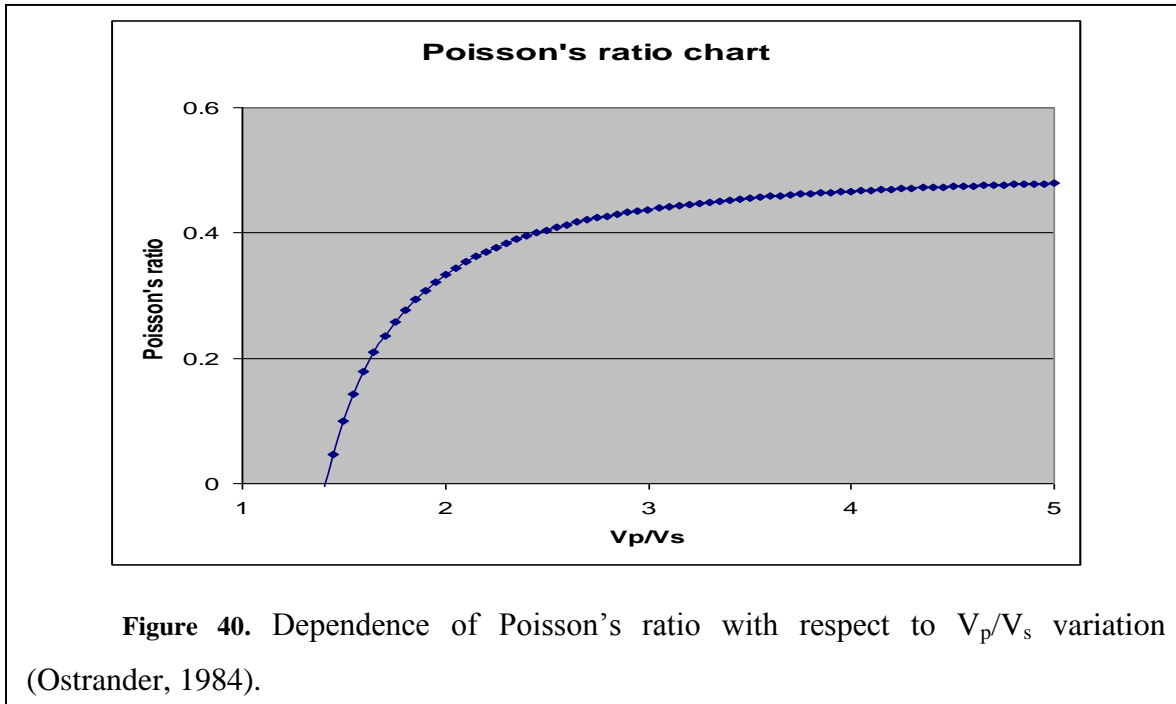
This becomes extremely important when V_p and V_s are being altered by introduction of natural gas to sandstone. A large drop in P-wave velocity and a small increase of S-wave velocity occurs when less than 5% of natural gas is introduced to a pore space of water-saturated sandstone (Gassmann, 1951).

Figure 42 demonstrates how gas saturation within a rock unit alters the V_p/V_s ratio. Reflection coefficients can be affected by changes in physical parameters of rocks. Ostrander (1984) showed theoretical behavior of P-P reflections as a function of increasing offsets. Ostrander did this analysis for multiple cases, however, when gas saturated sandstone is emplaced beneath a sealing shale unit of higher P-wave velocity, this would result in a lower Poisson's ratio and therefore, the absolute reflection coefficient would increase with the angle of incidence (Figure 41).
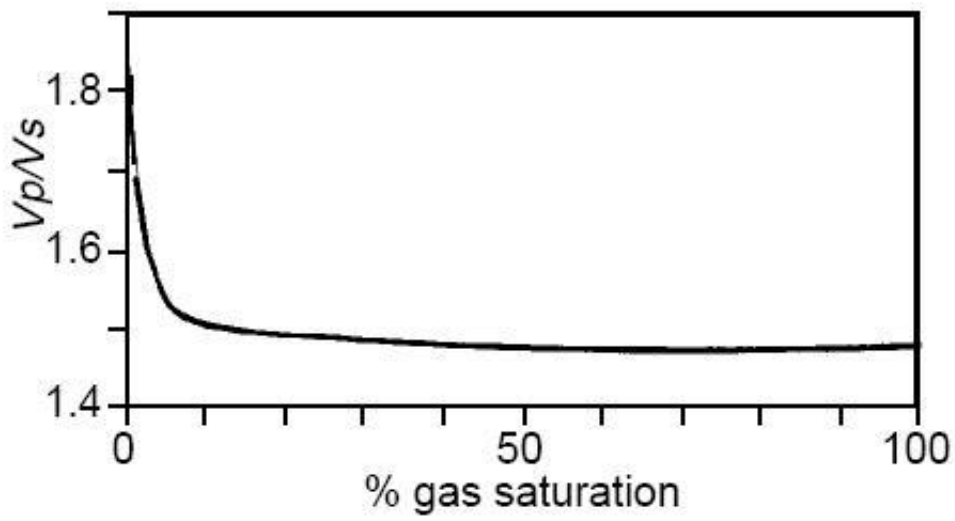
Figure 42. Dependence of Vp/Vs ratio with respect to the percentage of gas content in groundwater saturated sandstone (Ostrander, 1984).
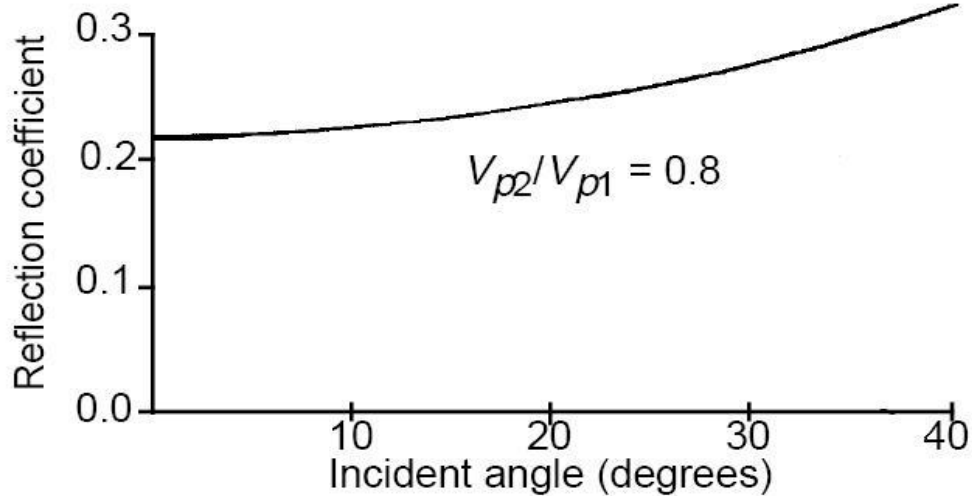
Figure 41. Dependence of the absolute value of the reflection coefficient from the angle of incidence. This relationship was shown by Ostrander (1984) for a specific case ($V_{p2}/V_{p1} = 0.8$), where V_{p2} is the velocity of P-wave in a sandstone and V_{p1} – is velocity of P-wave in a sealing shale unit.

Rutherford and Williams (1989) defined three classes of AVO anomalies for sandstone sealed by shale:

1. High impedance sands (characterized by positive intercept and high negative AVO gradient)
2. Near-zero impedance sands and (characterized by small positive or negative intercept and high negative AVO gradient)
3. Low impedance sands (characterized by high negative intercept and negative AVO gradient)

In our particular case, a potential seal-reservoir transition can be classified as class 3 (low impedance sands); therefore, the reflection coefficient should be negative. However, its absolute value of amplitude should be increasing with the angle of incidence.

For seismic data collected in field and interpreted further in this dissertation, the following equations were used (Aki and Richards, 1979):

$$\frac{A}{B} = \frac{4Vs^4 p^2 \dfrac{\cos i}{Vp} \dfrac{\cos j}{Vs} - (1 - 2Vs^2 p^2)^2}{4Vs^4 p^2 \dfrac{\cos i}{Vp} \dfrac{\cos i}{Vs} + (1 - 2Vs^2 p^2)^2} \qquad \textbf{(2.18)}$$

$$\frac{B}{C} = \frac{-4Vs^4 p \dfrac{\cos i}{Vp} + (1 - 2Vs^2 p^2)}{4Vs^4 p^2 \dfrac{\cos i}{Vp} \dfrac{\cos j}{Vs} + (1 - 2Vs^2 p^2)^2} \qquad \textbf{(2.19)}$$

In the equations A, B and C are amplitudes of incident wave, reflected wave and converted wave;

i – Angle of incidence

j – Angle equal to (90° - i)

p – Ray parameter (equal to $\sin(i)/V_p = \sin(j)/V_s$)

2.3. GEOLOGIC BACKGROUND

2.3.1. Stratigraphy

The area under study is located in Southwestern Pennsylvania. Geologic strata exposed on the surface are shown in Figure 43. All of the known rocks in Pittsburgh quadrangle are sedimentary. Strata exposed on the surface mainly belong to Conemaugh and Monongahela groups of Pennsylvanian system. These strata were lightly folded during Allegheny orogeny and feature a system of very shallow dipping synclines and anticlines with a general propagation direction of 45° to 50° (Johnson, 1929). The Murrysville anticline is directly adjacent to our area of interest and is known to have served as a controlling structure for gas production from the Speechley sandstone.

In the study region, sandstone and shale members are predominant although clays, limestones and coals are also abundant. Quaternary deposits are widespread across the area under interest, mainly localized in river and creek valleys; however some are found as terrace deposits on eroded flat surfaces, adjacent to slopes. Alluvium consists of layers of sand, clay and gravel on the flood-plains and in the beds of the rivers (Johnson, 1929). Figure 44 features composite cross-sections of the area. Cross-section AA' was chosen directed along the propagation of the hinge of Murrysville anticline, striking at 46°, while BB' is orthogonal to this direction striking at 314°.
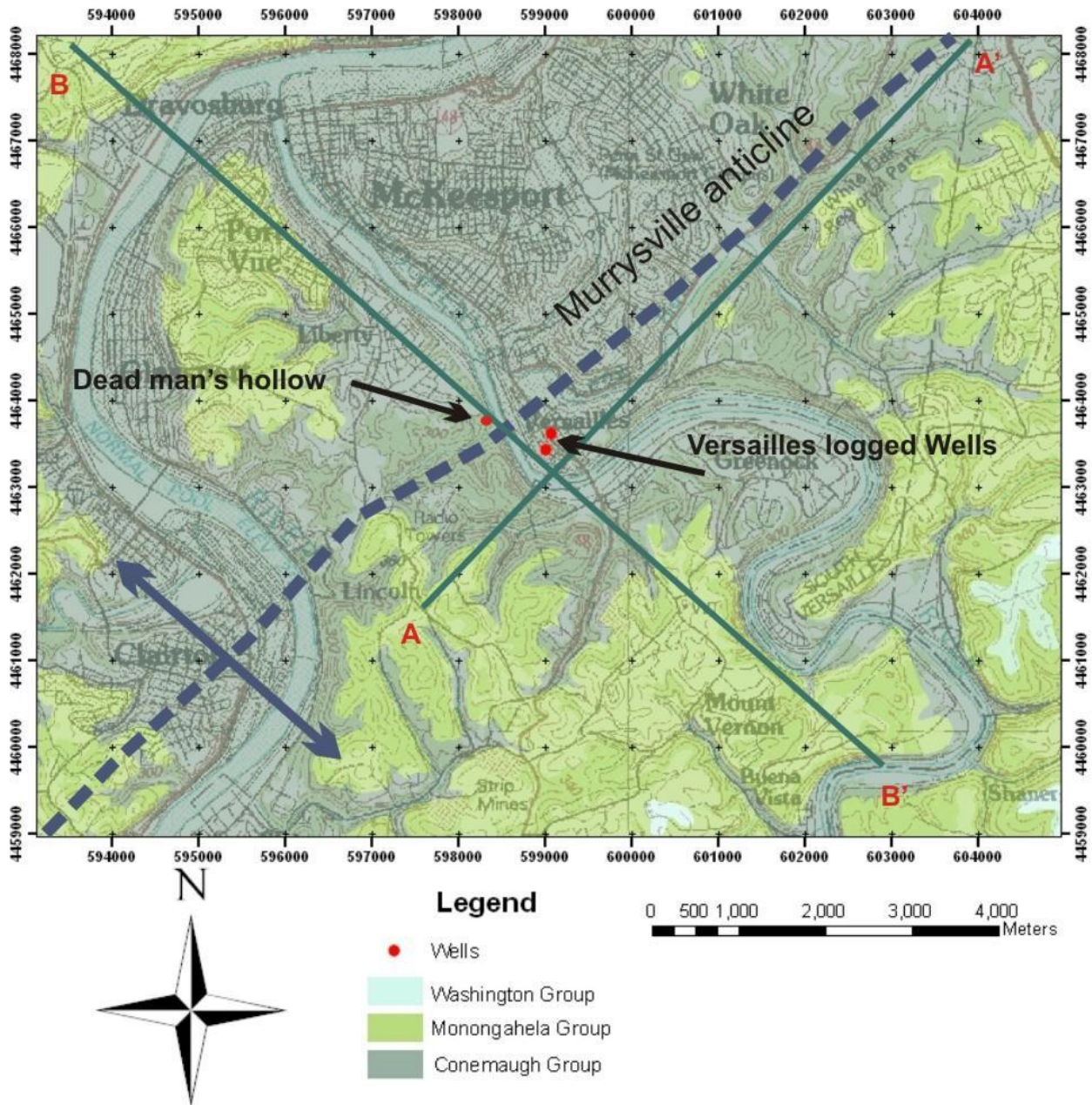
Figure 43. Geologic map of the area. Cross-sections AA' and BB' were reconstructed to the depth of 3000 feet in order to assist in 3D visualization of areal stratigraphy. Geologic data regarding Paleozoic formations for this map were acquired from Wagner, 1975. Quaternary geology data was acquired from Pennsylvania Bureau of Topographic and Geologic Survey, 2001 (Aerial geology map).

Figure 44. Cross-sections reconstructed from geologic map (Figure 43). (A): Cross-section AA' aligned along the direction of propagation of Murrysville anticline. (B): Cross-section BB' orthogonal to AA' azimuth. Abbreviations indicate marker beds for each stratigraphic group as following: UFC – Upper Freeport coal; KC – Kittanning coals; CC – Clarion coals; SC – Sharon coal; MCSS – Mauch Chunk sandstone; Big Lime – Loyahanna Formation; BSS – Burgoon sandstone; MSS – Murrysville sandstone; 100FSS – Hundred foot sandstone; SSS – Speechley sandstone. Abbreviations in the legend indicate age of geologic groups. From oldest to most recent: D – Devonian, M – Mississippian, P – Pennsylvanian, Q – Quaternary.

In addition to stratigraphy of the area being well described in the literature (Johnson 1929, Stout, 1943; Wagner, 1975; Harper et al, 1984; Milici, 2004; McDaniel, 2006), two wells were drilled as part of the original McKeesport gas field exploration and production activities: Borough garage well (well 1) and Walnut street well (well 2). They were surveyed by Century geophysics using caliper, density, sonic velocity and resistivity tools. Well locations are shown in Figure 45.
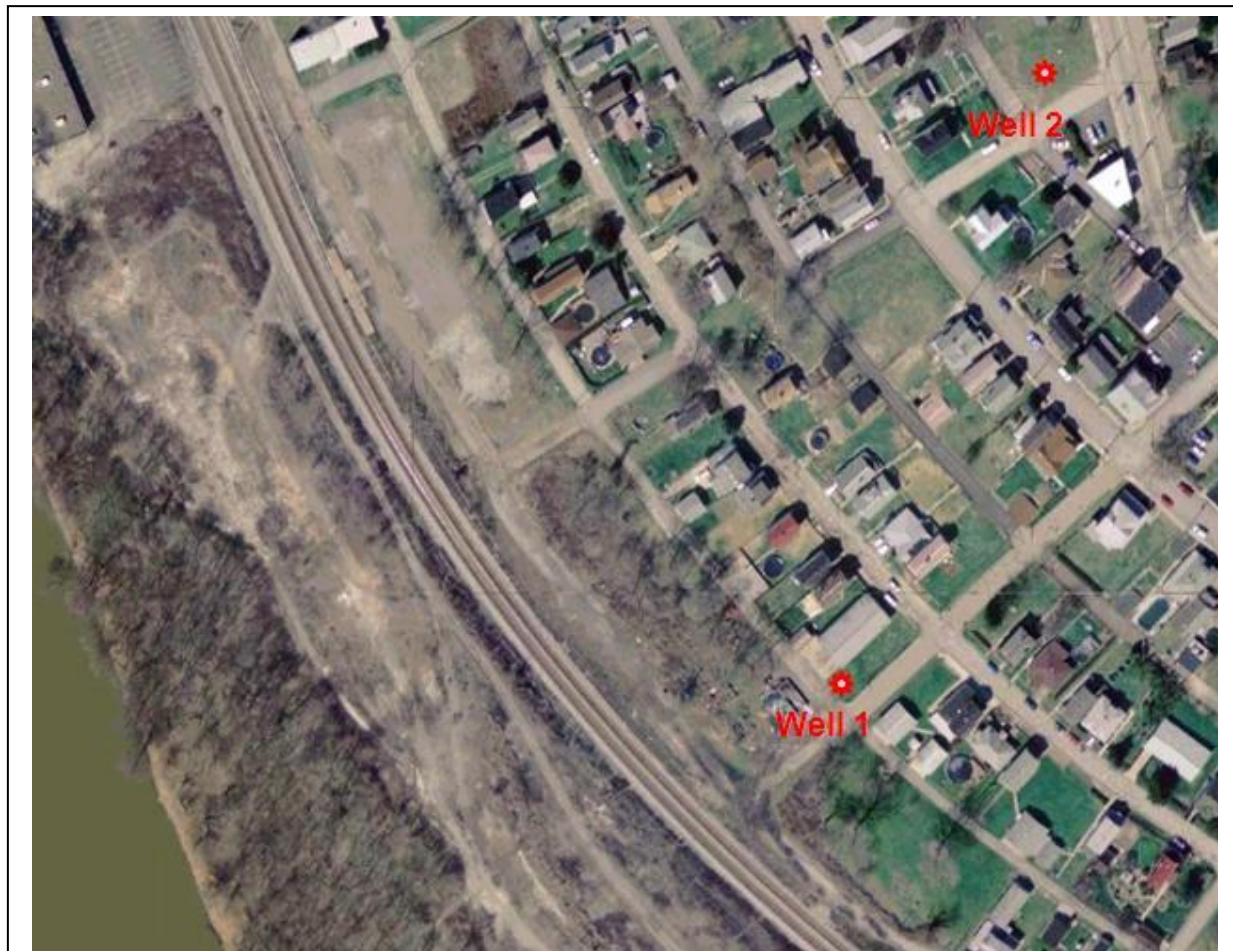
Figure 45. Aerial photograph of residential neighborhoods in Versailles, PA. Distance from well 1 to well 2 is 284 m. Well 1 was drilled to the depth 575 ft (175 m) and was logged to the depth of 479 ft (146 m). Well 2 had a total recorded depth of 581.50 ft (177 m).

<u>Conemaugh group</u>

Conemaugh group is upper Pennsylvanian in age and is dominated by siliciclastic strata, including claystone, shale, siltstone, and sandstone. It contains several named sandstone formations (or members), which include the Mahoning sandstone (Milici, 2004). Conemaugh group is stratigraphically marked by beds from Upper Freeport coal to Buffalo sandstone. Underlying Allegheny group comprises beds from Middle Kittanning coal to upper Freeport coal (Johnson, 1929; Stout, 1943; Edmunds, 1999). They have been well-studied in the past. They include sandstone, shale and marine limestone and coal beds, as shown in Figure 46.
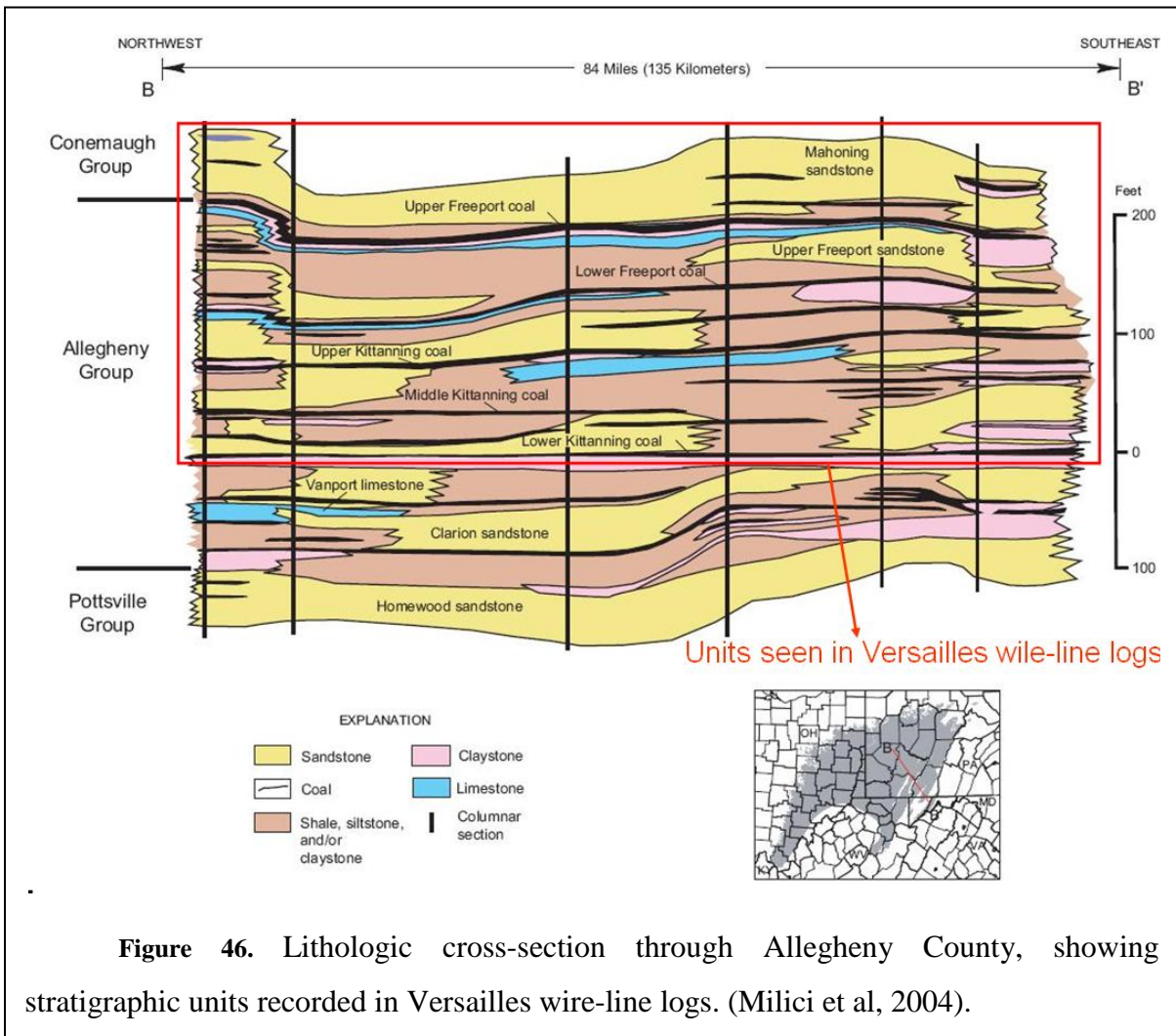
Figure 46. Lithologic cross-section through Allegheny County, showing stratigraphic units recorded in Versailles wire-line logs. (Milici et al, 2004).

The Buffalo sandstone is generally less than (100 ft) 30 m in thickness (Figure 47). Where well developed the sandstone is massive in character, coarse to pebbly in texture and gray

94
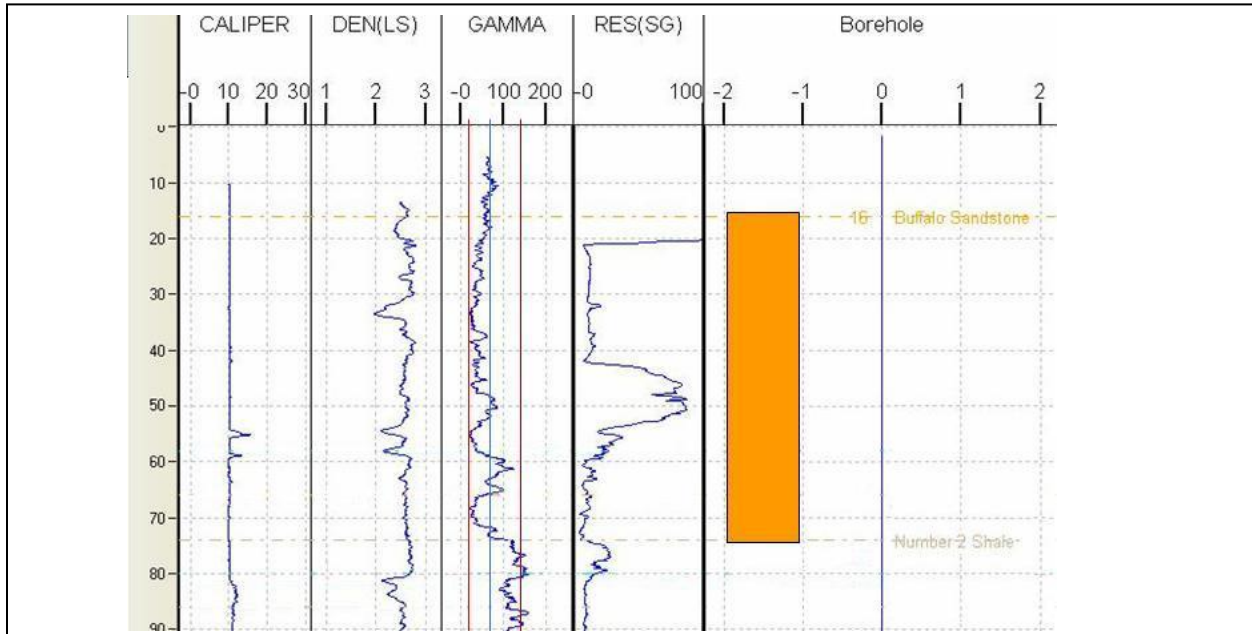
(A) Well 1
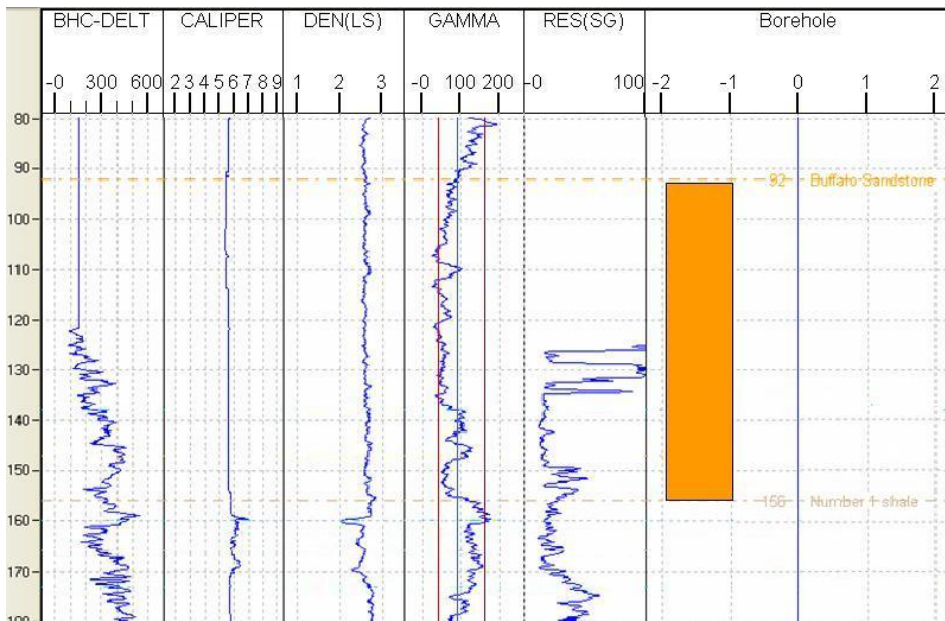
(B) Well 2

Figure 47. Combined density and gamma-ray well logs of Buffalo sandstone and Brush Creek coal. Units of depth are feet zeroed at surface. Stratum between 16 to 66 ft (4.9 to 20.1 m) on the first wire line can be correlated to stratum between 92 and 156 ft (28 to 47.5 m) on the second. Gamma readings exceeding the anticipated SS threshold most likely belong to the same member deposited in different facies.

to buff in color. It is recorded to be well consolidated, erosion-resistant and subject to darkening through exposure. The Buffalo sandstone has been an important resource utilized for construction purposes (churches, schools and heavy masonry). Under deep covering it becomes the Buell Run sand of the driller and yields petroleum, natural gas and brine (Stout, 1943). Some exposures of Buffalo member are recorded in the area under study and will be discussed further in this document.

The Brush Creek coal in the area under study only reaches a few feet in thickness; however it is a known source of coal bed methane and has been commercially developed in the past (Milici, 2004).

The Mahoning sandstone varies from a fine-grained to coarse-grained or conglomeratic sandstone. The pebbles, which are milky quartz and commonly not more than one-fourth inch in diameter, are for the most part confined to the basal portion of the deposits. The Mahoning sandstone is commonly cross-bedded. In places, this physical feature is prominently developed. Within the Mahoning sandstone, significant variation is observed in the hardness and in the weather resistance of the material. In general, it is poorly cemented and crumbles readily on exposure to the elements (Stout, 1943). Figure 48 shows combined density gamma ray logs for the Mahoning sandstone and underlying Upper Freeport coal.

Allegheny group

The Allegheny group was deposited in middle Pennsylvanian time. It contains several marine or brackish-water units in its base, such as the Vanport limestone, while the upper part of the Allegheny group is entirely non-marine. There are four major coal zones known within the Allegheny group, which makes it an important target for coal bed methane development (Milici, 2004). From oldest to youngest - these include the Lower Kittanning coal, the Upper Kittanning coal, the Lower Freeport coal, and the Upper Freeport coal (Ruppert et al, 2001). The bottom of this group is underlain by Clarion coal. Available data indicate that the average gas content for the Freeport coals is about 192 cf/ton, and about 252 cf/ton for the Kittanning coal beds (Bruner et al, 1995, 1998).
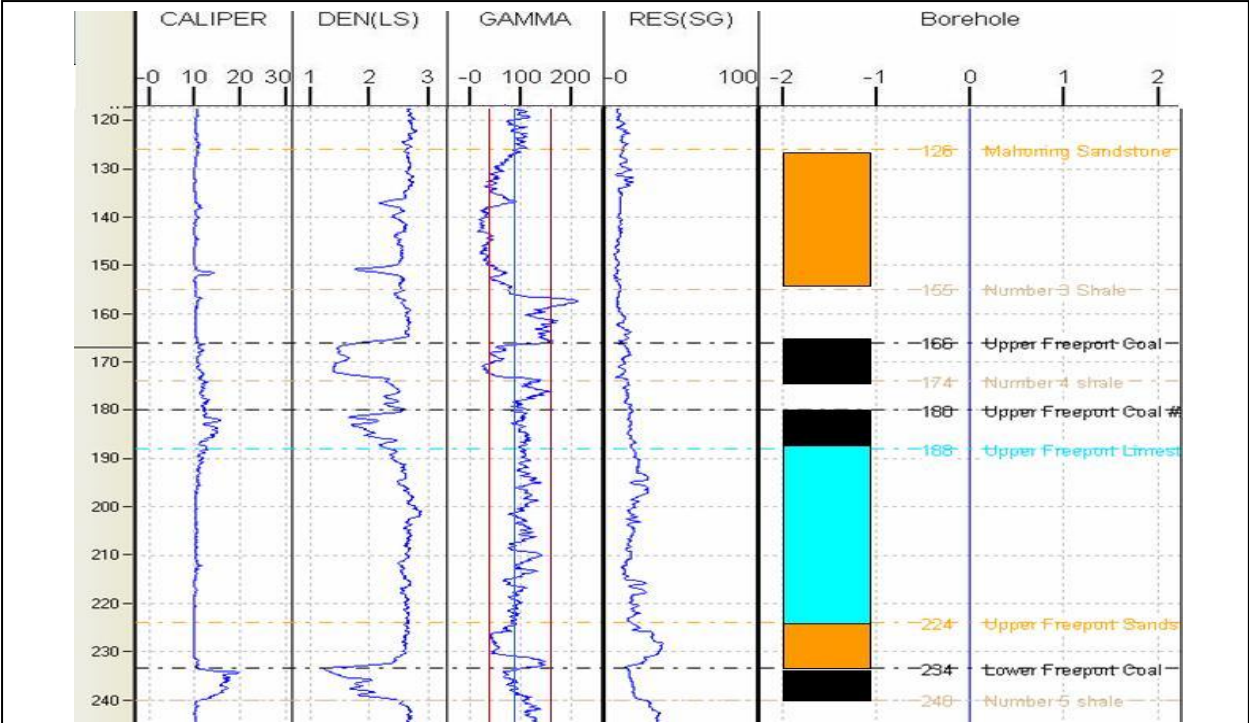
(A)   Well 1
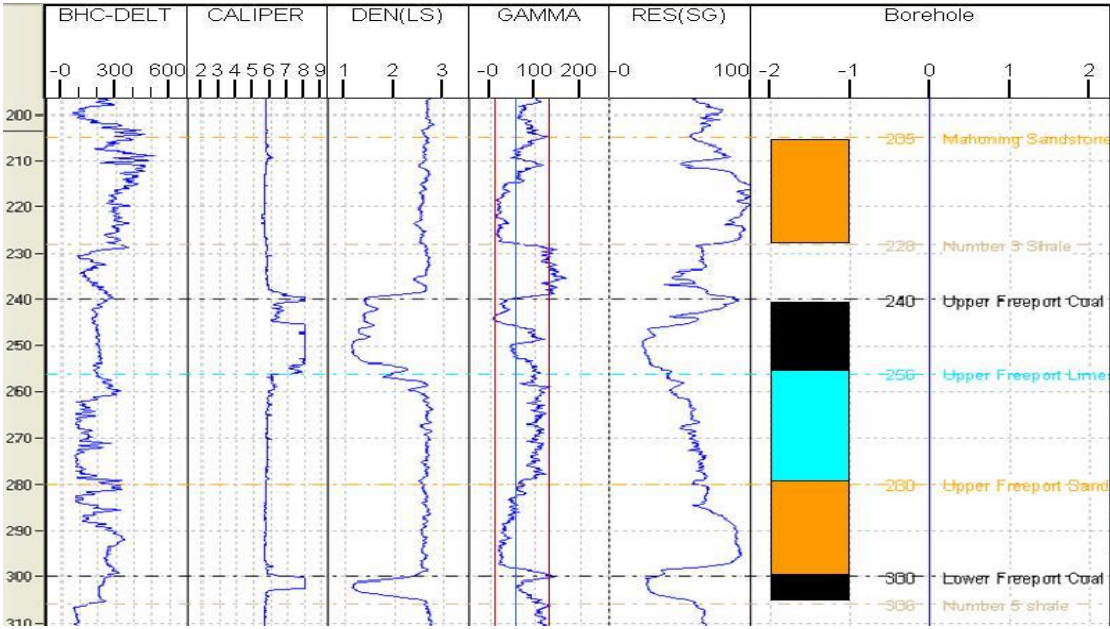
(B) Well 2

Figure 48. Downhole section showing combined density and gamma ray logs for Mahoning sandstone and Upper Freeport coal. Units of depth are feet below surface.

The Upper Freeport sandstone stratigraphically is located within the interval between the Lower Freeport coal and the Bolivar clay. It may be absent from the section, may fill only a part of the interval, may occupy this entire stratigraphic interval, or may expand so that it replaces overlying or underlying beds. It is generally loosely bonded, medium-grained sandstone, decidedly micaceous, and somewhat ferruginous in character. Clay matter also forms part of the bond. It is always cross-bedded, the planes being best marked on weathered surfaces. The color of the rock varies from light gray to brownish buff, the intensity of the shade depending on the quantity of the iron components present and on the degree of weathering. The Upper Freeport sandstone varies in thickness from 1 to 60 ft (0.3 to 18 m) (Stout, 1943).

The Lower Freeport sandstone is stratigraphically located in the interval between the Middle Kittanning coal and the Lower Freeport limestone. The deposits vary from 5 to 75 ft (23 m) or more in thickness. The Lower Freeport sandstone is generally massive in character, more or less marked by cross-bedding planes, somewhat micaceous in mineral content and medium to coarse in texture. The freshly quarried stone varies in color from very light gray, through yellowish and drab to reddish brown, the shades depending largely on the state of oxidation of the iron components. The chief bonding material is iron oxide in the limonite form. In Ohio, the Lower Freeport sandstone was employed for building purposes. At various places along the line of outcrop across the state it has served many purposes such as construction of houses, blast furnaces, mills and mill dams, carding mills, retaining walls, culverts, bridges, abutments and foundations (Stout 1943).

The Upper Freeport, Lower Freeport, Upper Kittanning, and Middle Kittanning coals are considered thermally mature with respect to methane generation; the. Much of the coal bed methane gas is probably of thermogenic origin. In southwestern Pennsylvania, microbial gas in Pennsylvanian coal beds has been reported mixed with thermogenic gases (Laughrey and Baldassare, 1998). Microbial methane associated with coal beds has been generated from the formation of the first Pennsylvanian peat deposits to the present day, where surface waters interact with shallow coal beds (Laughrey and Baldassare, 1998). It is interesting to note that the lower Kittanning coal bed yielded a gas content of 352 cubic

feet per ton (cf/ton) under ambient conditions, one of the highest then ever measured from a coal bed in the bituminous coal fields of Pennsylvania (Puglio and Innacchione, 1979).

In general, the stratigraphic sequence deposited during the Pennsylvanian period represents a classic thermocline sequence with alteration of transgressive and regressive cycles. In the upper part of the stratigraphic section (above the Upper Kittanning coal), most of the units can be correlated to each other, showing that changes in depositional environments are of regional scale. Geologic units below the Upper Kittanning coal have been interpreted to have been deposited in meandering river system present in the area in middle Pennsylvanian time, which could be responsible for the greater complexity of sediment load throughout the same area.

Pottsville group

Pottsville group varies in thickness. It includes all strata from Clarion coals to Mercer coal bed. While predominant rocks are sandstones, their continuity is disrupted by facies variations, as well as known coal beds are generally discontinuous. Because of this discontinuity, mining is not common in the Pottsville group, except for Mercer coal zone. The basal contact of Pottsville group is apparently everywhere disconformable and from south to north overlies increasingly older Mississippian and possibly uppermost Devonian rocks (Edmunds et al, 1999).

Older strata

Pennsylvanian strata disconformably overlie Mississippian deposits (Edmunds et al, 1999). Mississippian sequence is comprised of three main groups (Mauch Chunk, Grienbrier (Loyahanna) and Burgoon (Pocono) (Figure 49). Mauch chunk is terrestrial, predominantly composed of red beds (Mauch Chunk sandstone) conformably deposited over massive limestone units of Grienbrier group (Loyahanna limestone or "Big Lime"). Another disconformity marks the base of Loyahanna limestone yielding to terrestrial deposits of Burgoon group (Burgoon sandstone). The overall Mississippian sequence reveals alternating transgression and regression cycles which can be followed further into Devonian age (Johnson, 1929; Harper, 1989).
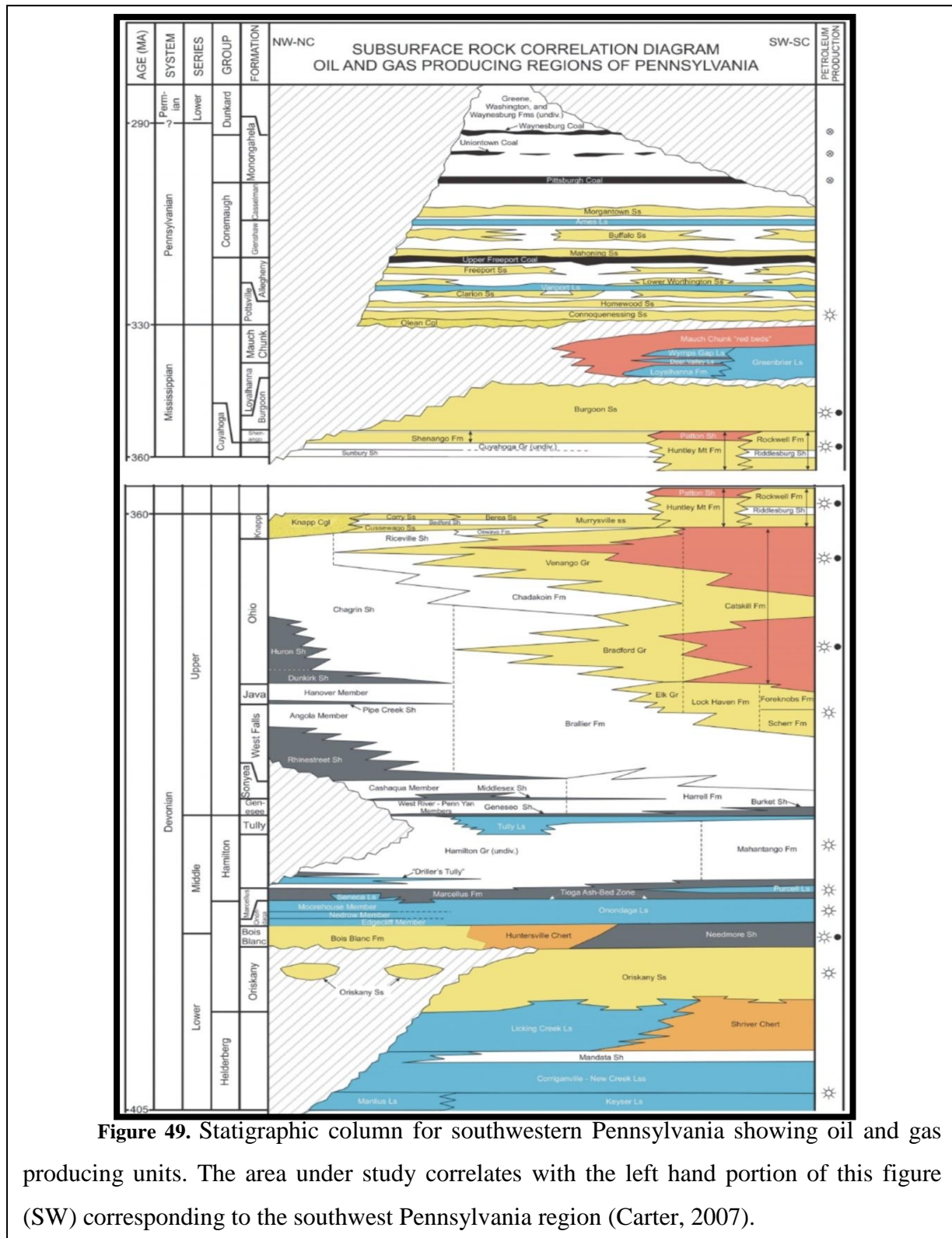
Figure 49. Statigraphic column for southwestern Pennsylvania showing oil and gas producing units. The area under study correlates with the left hand portion of this figure (SW) corresponding to the southwest Pennsylvania region (Carter, 2007).

100

There is a disconformity between the Devonian rocks and the overlying Mississippian strata. The Devonian rocks shows two distinctive marker beds throughout the southern Allegheny County: the Murrysville sandstone and the Hundred Foot sandstone formations, which used to be sources for gas production in the area in early 1900's. These sandstones are interbedded with shale markers. The overall sequence from youngest to oldest is shown in Figure 50.
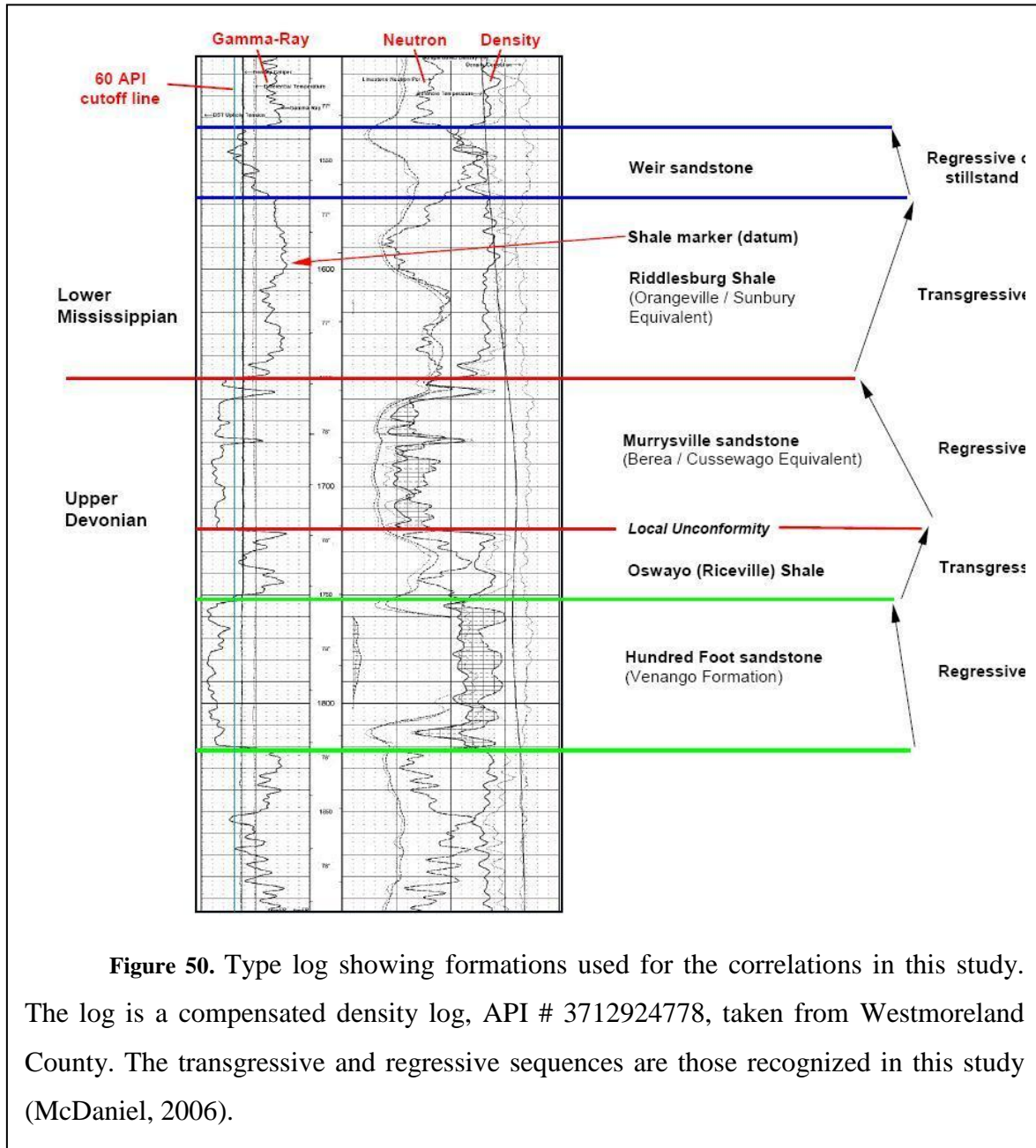
Figure 50. Type log showing formations used for the correlations in this study. The log is a compensated density log, API # 3712924778, taken from Westmoreland County. The transgressive and regressive sequences are those recognized in this study (McDaniel, 2006).

The Murrysville sandstone was deposited in environments varying from fluvial to deltaic. In general, the Murrysville is dull greenish-yellow to gray and may contain conglomeratic lenses with pebble-size grains, greater than 5 mm in diameter. Siltstone and shale are also present in this unit. The Murrysville is thought to represent a fluvial environment that transported sediments westward into a shallow restricted sea that covered much of Ohio, western Pennsylvania, and West Virginia during the late Devonian (Harper et al, 1989; Harper and Laughrey, 1987).

Underlying Murrysville sandstone is the Riceville shale, both members of Venango group. Riceville shale consists mostly of white, light-gray and tan, fossiliferous siltstone and gray silty-shale with mudstone. It is deposited conformably over the Hundred Foot sand (Johnson, 1929). The Riceville represents deeper-marine sediments deposited just prior to the westward progradation of the Murrysville delta system (Lyahov and Ettensohn, 1995).

The Hundred Foot sandstone is the lowermost unit in this study. It is fine to coarse in texture with some conglomerate at the basal part, grains are angular to subangular in shape, consist mostly of quartzite and are white to gray in color. Interbedded siltstone and shale are common throughout much of the Hundred Foot within the study area. The Hundred Foot sandstone is thought to be migrating barrier-bar sandstone.

2.3.2. Interpretation of well logs

Some initial core descriptions were found originally composed for "McKeesport coal and coke company". They were recorded to the bottom of Upper Freeport coal and mostly reflect the following sequence: surface zone at the top, 0 to 30 ft (0 to 8 m); member of thin-bedded shales, varying in color and composition from dark to gray and from terrestrial to shallow marine and tidal with significant lime content; Buffalo sandstone (35 to 75 ft or 11 to 23 m thick); shale unit (0 to 50 and more ft thick); Mahoning sandstone (11 to 50 ft or 3 to 15 m thick) and underlying Upper Freeport coal.

Existing wells were logged by the Century Geophysical Corporation in December 2006. The data was then transferred to the University of Pittsburgh in LAS format (Log ASCII Standard). The wire-line tools used for surveying were natural gamma ray, sonic velocity, density (LS, SS and CDL) and caliper measurements. The well logs have been interpreted with respect to an expected stratigraphic sequence of sandstone, shale, limestone, and coal units and after reviewing the interpretation of Mr. Mark Thomas of EG&G, who kindly provided his interpretation and basic viewing software to us. We completed our analysis of the wire line logs using Seismic Micro Technologies Kingdom Suite. Composite stratification of well logs can be found in Table 2. Some marker beds from this stratification were subjected to more detailed analysis. Physical properties were averaged based on the stratigraphic correlation and recorded in Table 3.

In the preliminary analysis, coal beds were primarily identified as units of lower density (as recorded by LS density) and lower radioactivity (Bond et al, 1969). Thickness of coal under some general assumptions can be derived from density records within about 2 inches of core measurements, with each boundary picked in the mid point of deflection (Bond et al, 1969). Sandstone, limestone, and shale beds were identified using gamma logs annotated with reference lines.

Basic interpretation of downhole response in these wells required two clearly defined marker reference lines, for sandstone and shale, to be determined. The sand reference line was determined using the gamma log and the response of the Mahoning sandstone with a 15 API response value observed between 218 ft (66.5 m) to 228 ft (69.5 m) depth in well number 1. The shale line was determined from shale unit number 3 (Table 4) with a gamma log response value of 135 API observed between 228 ft (69.5 m) and 240 ft (73.2 m) depth in well 1. Limestones and shales are similar in composition and depositional environments and vary in total gamma count values from 80 to 140 API units, therefore as shales in general tend to contain more clay particles detectable in total gamma count - in order to distinguish between shales and limestones a threshold was selected equal to 120 API units for the averaged total gamma count (Table 4)

System	Group	Well 2		Well 1	
		Depth to top (ft)	Formation top name	Depth to top (ft)	Formation top name
Upper Pennsylvanian	Conemaugh	92	Buffalo sandstone	16	Buffalo sandstone
		138	Buffalo limestone or shale	58	Buffalo limestone or shale
		147	Buffalo sandstone 2	66	Buffalo sandstone 2
		156	Number 1 shale	74	Number 1 shale
		160	Number 1 limestone or shale	80	Number 1 limestone or shale
		166	Number 2 shale	86	Number 2 shale
		173	Number 2 limestone or shale	95	Number 2 limestone or shale
		205	Mahoning sandstone	126	Mahoning sandstone
		228	Number 3 shale	155	Number 3 shale
		240	Upper Freeport coal	166	Upper Freeport coal
Middle Pennsylvanian	Allegheny	256	Upper Freeport limestone or shale	174	Number 4 shale
				180	Upper Freeport coal
		280	Upper Freeport sandstone	188	Upper Freeport limestone or shale
				224	Upper Freeport sandstone
		300	Lower Freeport coal	233.5	Lower Freeport coal
		306	Number 5 shale	240	Number 5 shale
		324	Number 1 sandstone	251	Number 1 sandstone
		331	Number 6 shale	258	Number 6 shale
		342	Number 3 limestone or shale	269	Number 3 limestone or shale
		367.5	Number 2 sandstone	290	Number 2 sandstone
		374	Number 4 limestone or shale	294	Number 1 coal
		388	Number 7 shale	297.5	Intermediate shale #
		394	Number 5 Limestone or shale	302	Number 2 coal
		406	Upper Kittanning coal	304	Number 4 Limestone or shale
		423	Number 6 Limestone or shale	315	Number 7 shale
		476	Number 4 sandstone	321	Number 5 limestone or shale
		493	Number 8 shale	338	Upper Kittanning coal
		500	Number 5 sandstone	350	Number 6 Limestone or shale
		512	Number 9 shale	373	Number 3 sandstone
		548	Number 6 sandstone	418	Middle Kittanning coal
		557	Number 10 shale	424	Number 9 shale
		566	Lower Kittanning coal	434	Number 6 sandstone
		571	Number 11 shale	446	Number 10 shale

Table 2. Detailed interpretation of stratigraphy based on two borehole well logs.

Formation	Thk, well 1	Thk, well 2	Sonic, Km/s	Gamma 1, API units	Gamma 2, API units	Gamma mean	Rho 1, Ohm*m	Rho 2, Ohm*m	Rho mean	Den 1, g/cm³	Den 2, g/cm³	Density average
Buffalo sandstone	64.00	58.00	N/A	65.60	49.61	57.61	N/A	N/A	N/A	2.61	2.56	2.59
Mahoning sandstone	23.00	29.00	N/A	48.14	48.24	48.19	85.07	N/A	N/A	2.59	2.54	2.56
Number 3 shale	12.00	11.00	N/A	129.01	143.60	136.30	63.11	N/A	N/A	2.54	2.58	2.56
Upper Freeport coal	16.00	16.00	1.55	60.45	73.12	66.78	42.91	N/A	N/A	1.45	1.79	1.62
Upper Freeport limestone or shale	24.00	36.00	2.41	101.36	98.96	100.16	57.37	N/A	N/A	2.60	2.62	2.61
Upper Freeport sandstone	20.00	9.50	1.54	47.26	79.03	63.15	76.36	N/A	N/A	2.62	2.51	2.56
Lower Freeport coal	6.00	6.50	1.43	87.72	92.41	90.06	35.75	N/A	N/A	1.77	1.77	1.77
Number 5 shale	18.00	11.00	3.91	120.90	124.19	122.54	67.50	N/A	N/A	2.71	2.68	2.70
Number 2 sandstone	6.50	4.00	2.19	63.72	91.05	77.38	71.49	N/A	N/A	2.58	2.41	2.49
Number 4 limestone or shale	14.00	11.00	4.12	116.41	105.10	110.76	56.37	39.81	48.09	2.61	2.64	2.63
Upper Kittanning coal	17.00	12.00	1.43	97.49	77.32	87.41	40.80	N/A	N/A	1.93	1.57	1.75
Number 6 limestone or shale	53.00	23.00	3.00	110.67	86.57	98.62	57.40	53.32	55.36	2.59	2.64	2.62
Number 9 shale	36.00	10.00	4.00	133.70	106.46	120.08	57.37	61.43	59.40	2.72	2.67	2.69
Number 6 sandstone	9.00	12.00	4.77	82.65	63.80	73.22	81.83	60.34	71.09	2.71	2.56	2.64
Middle Kittanning coal	N/A	6.00	N/A	N/A	58.69	N/A	N/A	29.66	N/A	N/A	1.30	N/A
Lower Kittanning coal	6.00	N/A	1.27	111.20	N/A	N/A	54.33	N/A	N/A	2.18	N/A	N/A

Table 3. Calculated geophysical parameters acquired from borehole logging: Thk – Thickness of a layer; Sonic – Sonic velocity derived from Borehole corrected channel (BHC) and converted into kilometers per second; Gamma – total natural gamma ray count in units of American Petroleum Institute; Rho – Apparent electrical resistivity in Ohm-meters; Den – Density of rock in grams per cubic centimeter. Please note that some of the parameters are marked as N/A because of either poor data quality or total absence of data.
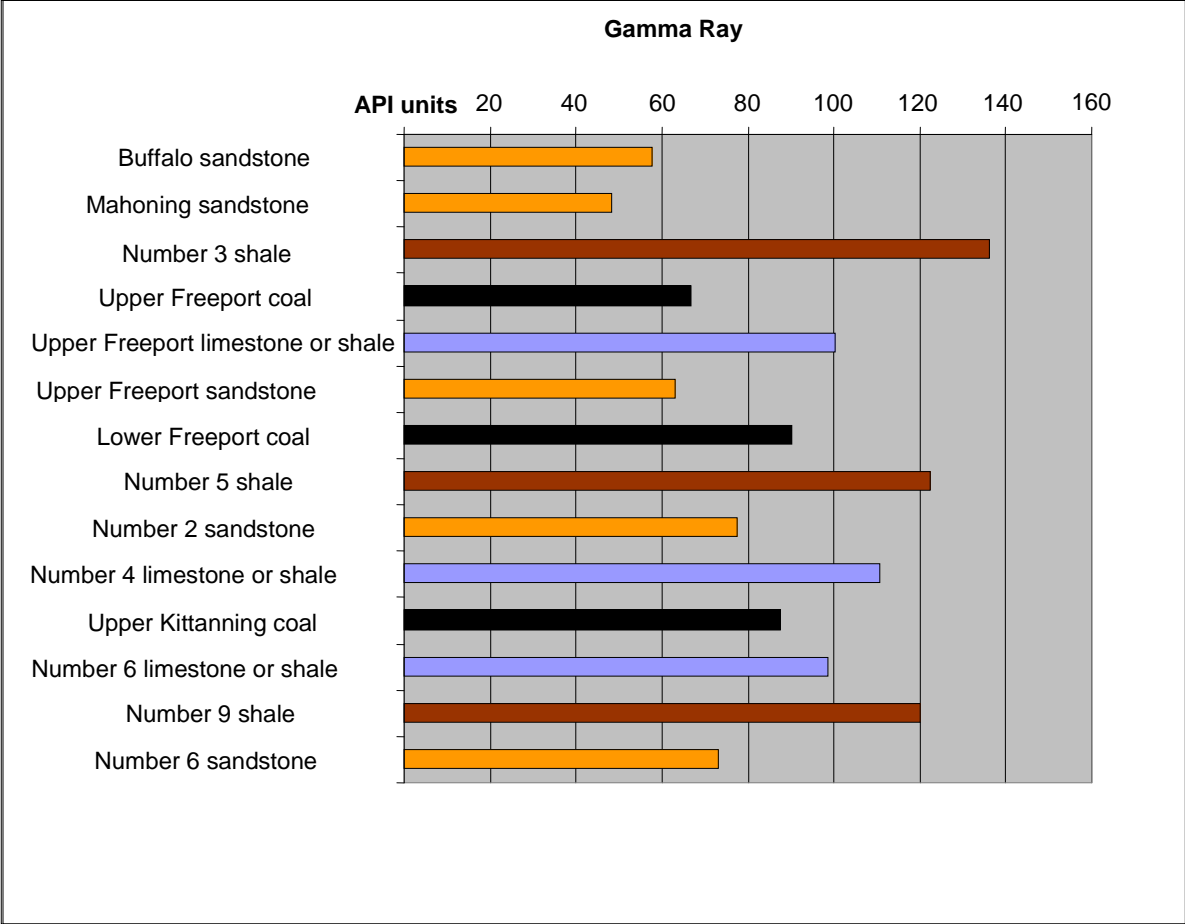
Table 4. Gamma ray characteristics of selected units. Black bars - coal, orange bars - sandstone, blue bars - limestone units, brown bars - shale units.

Other data, such as caliper variation, and resistivity (Table 5) were used as supplementary information for the survey. Density and sonic velocity (Table 6) were further used in seismic data interpretation for velocity analysis and for establishing time-depth relationship. The composite stratigraphic column derived from well log interpretation is presented in Figure 51 and Figure 52.
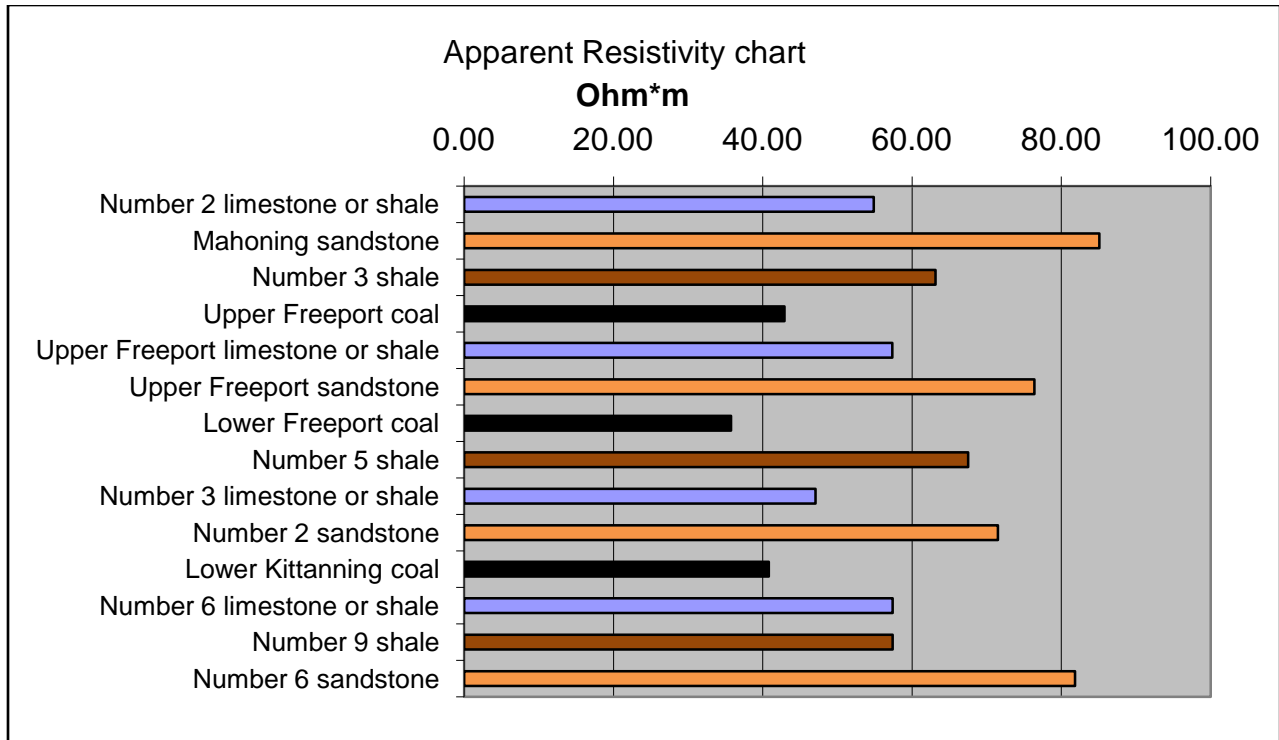
Table 5. Averaged electric properties of selected units.
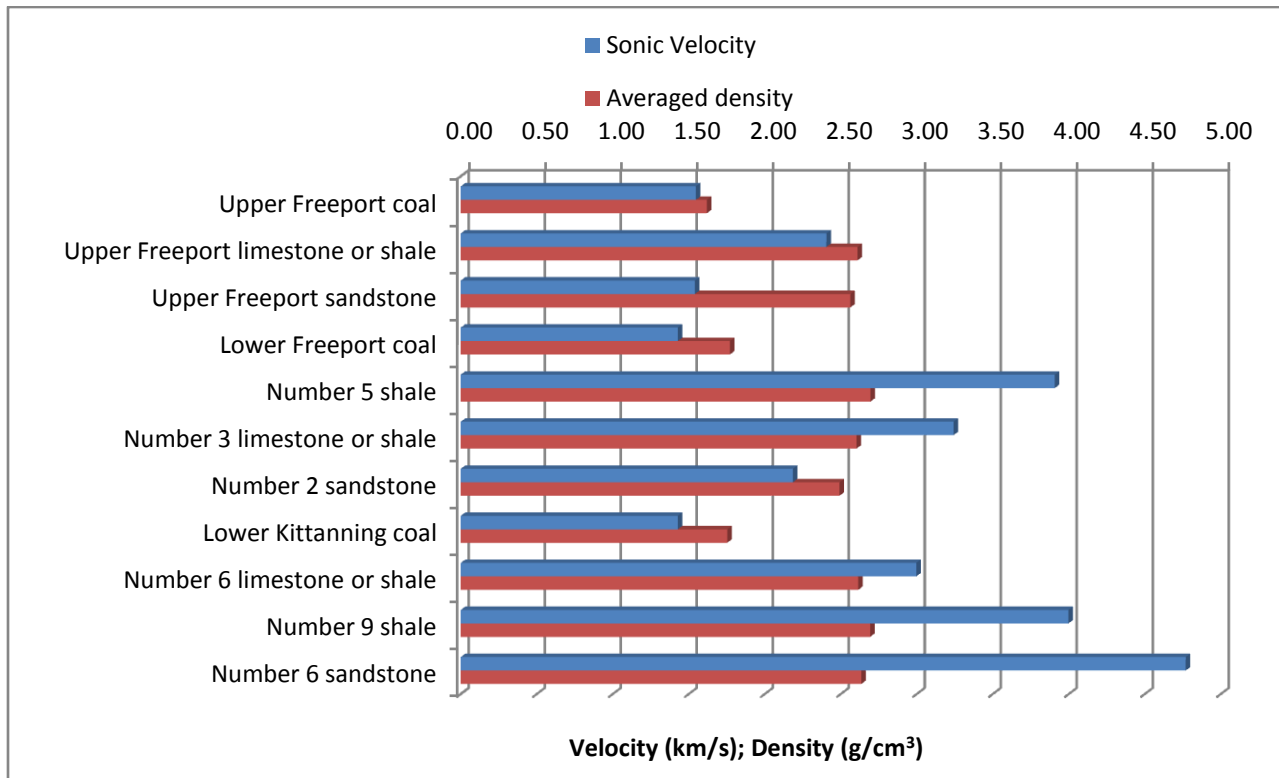
Table 6. Sonic velocities and averaged densities of the most distinctive marker beds.
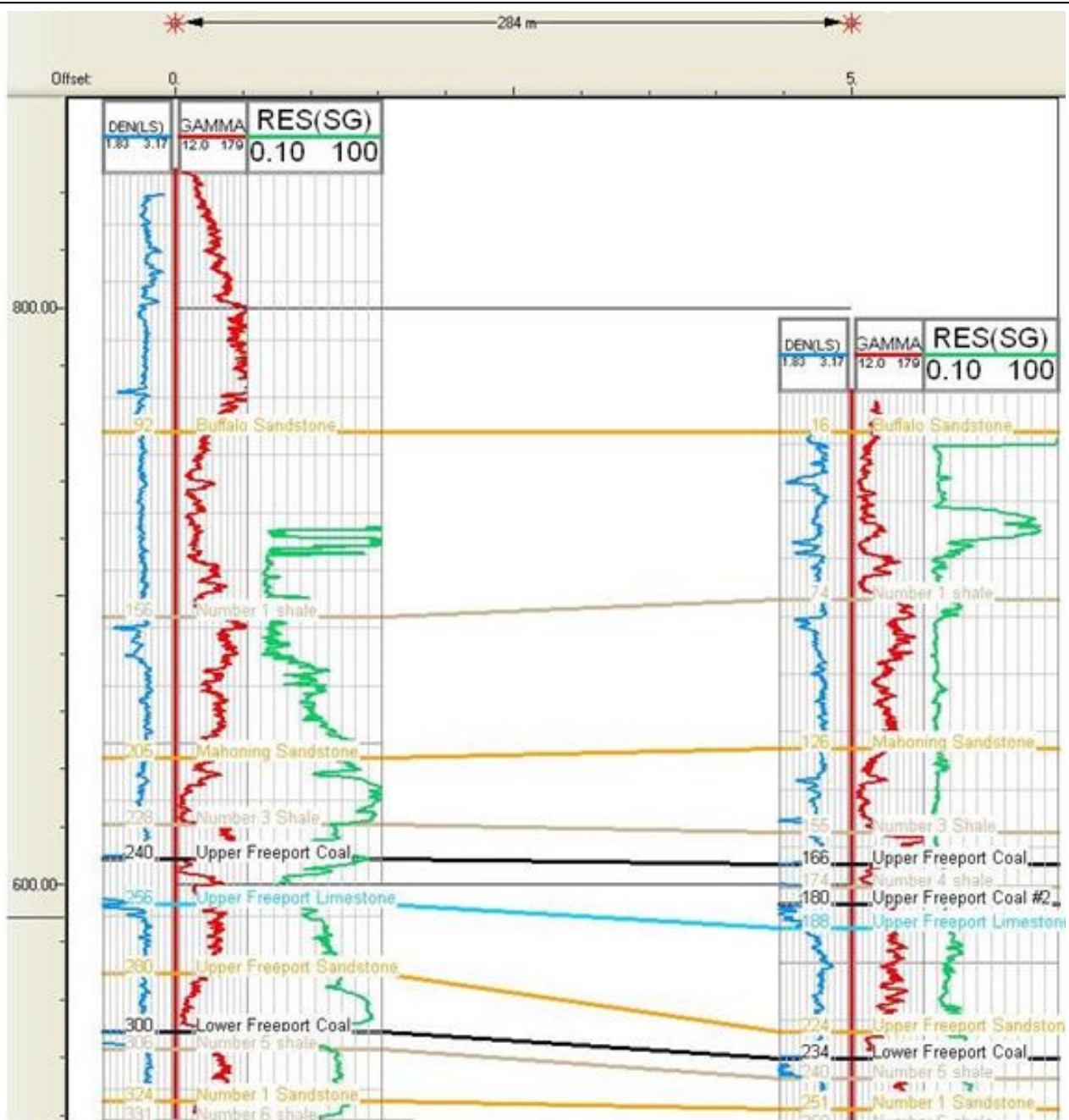
Figure 51. Correlation of well 1 (right) with well 2 (left) interpreted section is between 520 and 850 ft (160 and 260 m) above mean sea level (MSL). Refer to Table 2 for the lithologies.

108
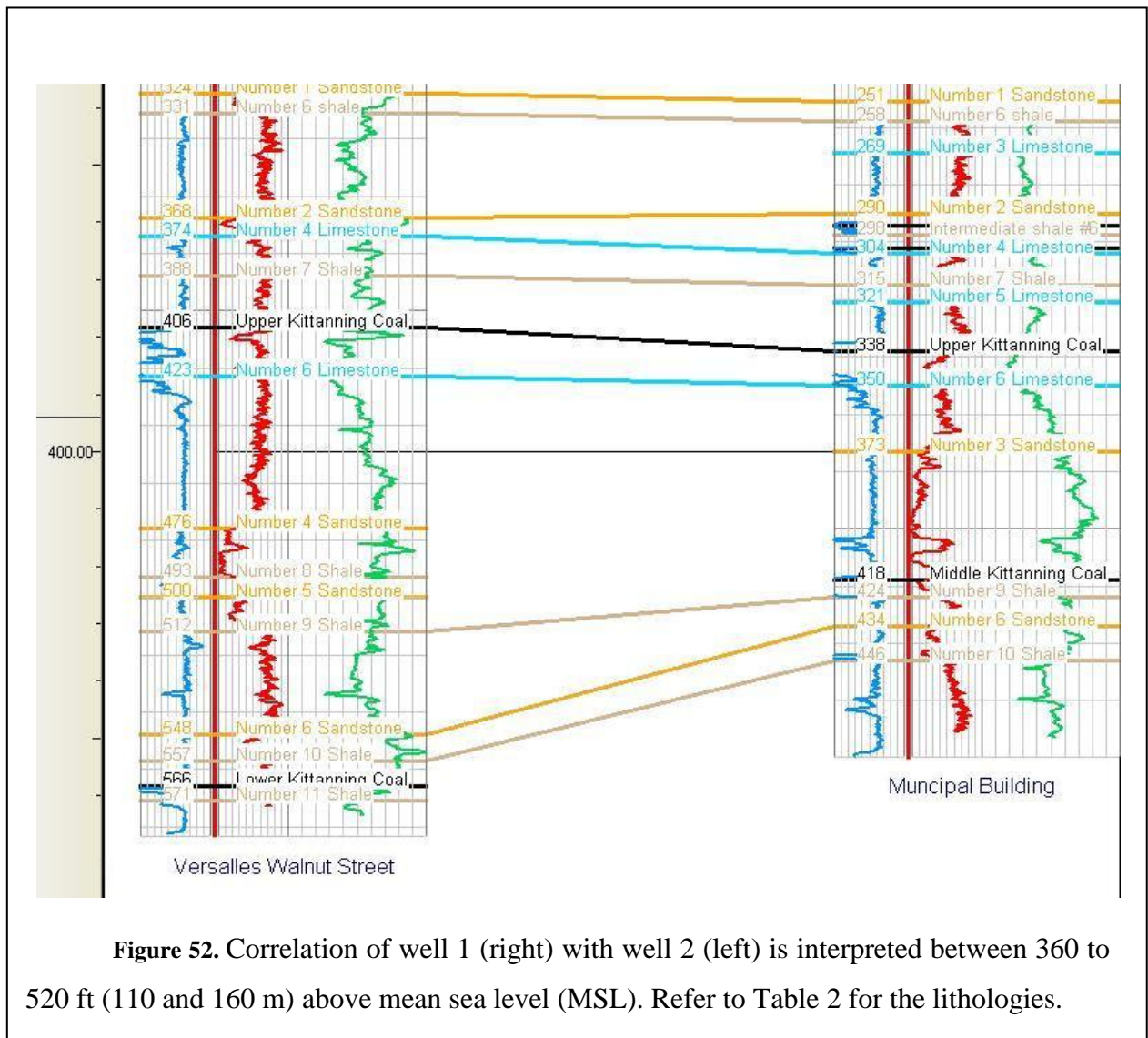
Figure 52. Correlation of well 1 (right) with well 2 (left) is interpreted between 360 to 520 ft (110 and 160 m) above mean sea level (MSL). Refer to Table 2 for the lithologies.

2.3.3. Coal as a reservoir for methane

Coal bed methane (CBM) can be produced chemically and biologically (by bacteria) from organic matter which can comprise up to 100% of coal seam. It is stored in the methane by a process called adsorption (Squarek and Dawson, 2006). While biologic precipitation of CH_4 can start immediately after the deposition – chemical precipitation is a process, which requires thermal maturity of the coal seam (Laughrey and Baldassare 1998). Thermal maturity criterion can be met when coal seam gradually submerges under accumulating sediment load. With   sufficient depth of burial, compaction and coalification – coal beds of Pottsville, Conemaugh and Allegheny groups were heated enough to generate thermogenic gas in the eastern part of Appalachian basin. Currently commercial production of CBM is

109

known within our interval of interest from Upper Freeport and Lower Kittanning coals, with the total CBM concentration of Lower Kittanning coal reaching 352 cf/ton (Burner et al, 1998; Milici, 2004).

Coal seams are generally weaker compared to the enclosing strata. Subjected to structural deformation (faulting and folding) fracture systems are formed within the coal beds, creating enough accommodation space for CBM migrate. Therefore effective methane accumulation depends on the presence of such fracture system in addition to natural fractures (face and butt cleats).

Natural fracture systems usually appear in a shape of closely spaced orthogonal cleat systems (face cleats and butt cleats) during early coalification process (Burner et al, 1998). In Appalachian basin it is common for secondary fracture system to occur as a result of tectonic activity and to be superimposed upon previously existing cleats. These secondary fracture systems significantly increase the fracture porosity. However according to Lyahov and Hinkle (1997). In general, porosity of a coal bed does not exceed 10%.

Furthermore, Milici (2004) has described the occurrence of bedding parallel faults and associated structures within coal beds in Tennessee and Virginia that may significantly increase fracture porosity, both within the coal beds and in the enclosing strata.

Methane is usually present in the coal seams in near-liquid state. Permeability of coal seams is mainly due to cleat systems. Long distance migration of CBM along coal beds is unlikely, especially if the coal beds are wet, because formation waters would inhibit desorption of methane into a fracture network. In contrast, relatively porous sandstone beds adjacent to coal source rocks may provide a network of fractures and pore spaces sufficient to support long-distance migration of desorbed gases (Milici 2004). Seals, preventing CBM migration from the coal bed can be either impermeable rocks overlaying the coal beds (shales, limy shales) or groundwater contained in the pore space of coal seams, which would increase the pressure trapping CBM within the coal bed.

2.3.4. Geologic reconnaissance

A geologic reconnaissance of the region directly across area under study was conducted in order to encounter and visually identify members of the stratigraphic column in the vicinity of the township. As there were no outcrops found close to the known logged wells, geological data were collected from the opposite side of Youghiogheny River (Figure 53). A biking trail, following the river from the Boston Bridge park was examined in order to get access to the best exposed outcrops in the area. A total of three stops were made on the
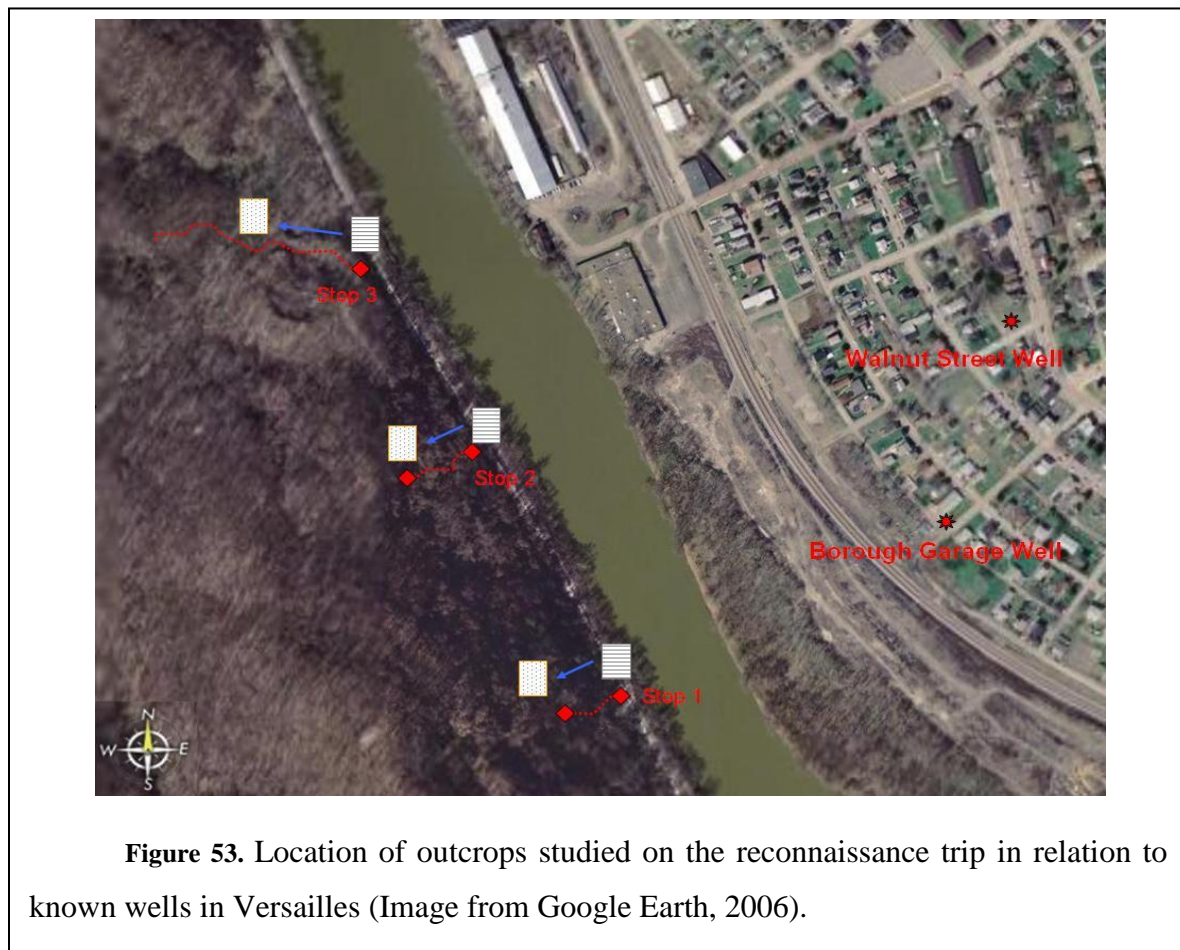
Figure 53. Location of outcrops studied on the reconnaissance trip in relation to known wells in Versailles (Image from Google Earth, 2006).

way and a total of five outcrops were documented and sampled (Table 7). On Figure 53 locations of observation stops are marked relative to the locations of logged wells, along with schematic summary of observations.

Number	Color	Mineral Composition	Grain size	Roundness	Name	Fossils, Comments
1	Gray-Brown	Quartz, feldspar, mica	Very fine-grained	Well-rounded	Shale	Thin-bedded in the outcrop
2	Gray	Quartz, feldspar, mica	Fine grained	Well-Rounded	Siltstone	Dirty siltstone, some cross-bedding in the outcrop
3	Gray-Brown	Quartz, feldspar, mica	Very fine grained	Well-rounded	Shale	No fossils
4	Gray	Quartz, feldspar, mica	Fine grained	Well-rounded	Sandstone	Plant fossils
5	Gray	Quartz, feldspar, mica	Fine grained	Well-rounded	Sandstone	Slightly higher mica content, slightly coarser-grained than sample 4

Table 7. Rock samples collected in area under study

The first stop (40 °18'45"N; 79 °50'13"W) was approximately 500 meters (1640 feet) NW from the beginning of the trail. The outcrop is located on the left from the road, exposing about 5 vertical meters (16 feet) of thin-bedded grey-brownish shales (Figure 54, sample 1). The exposure is located approximately 10 meters (32 feet) above the base water level. The shales are micro-grained; bed thickness does not exceed 7-10 millimeters (0.28 inches to 0.39 inches). No reaction with HCl was noted. The attitude of these beds is sub-horizontal, no folding or unconformity was noticed. About 20 vertical meters (66 feet) above the outcrop (up the slope), another exposure was encountered. A thicker-bedded (also sub-horizontal) micaceous siltstone (sample 2) is micro-grained. When studied as a Whole, these two outcrops represent a stratigraphic column coarsening and thickening upward and presumably deposited in a fluvial environment.

Following the trail further in the NW direction, the same grey-brown shales can be observed on the left side (Figure 54). Stop 2 (40 ^{o}18'57.22"N; 79 ^{o}50'21"W) is located about 500 to 700 meters (1640 feet to 2297 feet) away from stop 1. At the lowest point of this stop, the shales fully repeat those exposed at the first outcrop; therefore, no sample was taken. Approximately 20 vertical meters (66 feet) higher, another outcrop was found (sample 3). The exposed rocks are shaly, but with thicker bedding and coarser-grained matrix compared to the rocks at the base. This is presumably a transitional zone from shales to siltstones, which were encountered further up the slope (sample 4), approximately 70 vertical meters (230 feet) above the water level. Sample 4 is very similar to sample 2.

Figure 54. 3D view of the region under study with local photographs: Stop 1: 1a – shale; stop 2: 2a – shale, 2b – sandstone; stop 3: 3a – shale, 3b – siltstone, 3c – cross-bedding in sandstone. (Image from Google Earth, 2007).
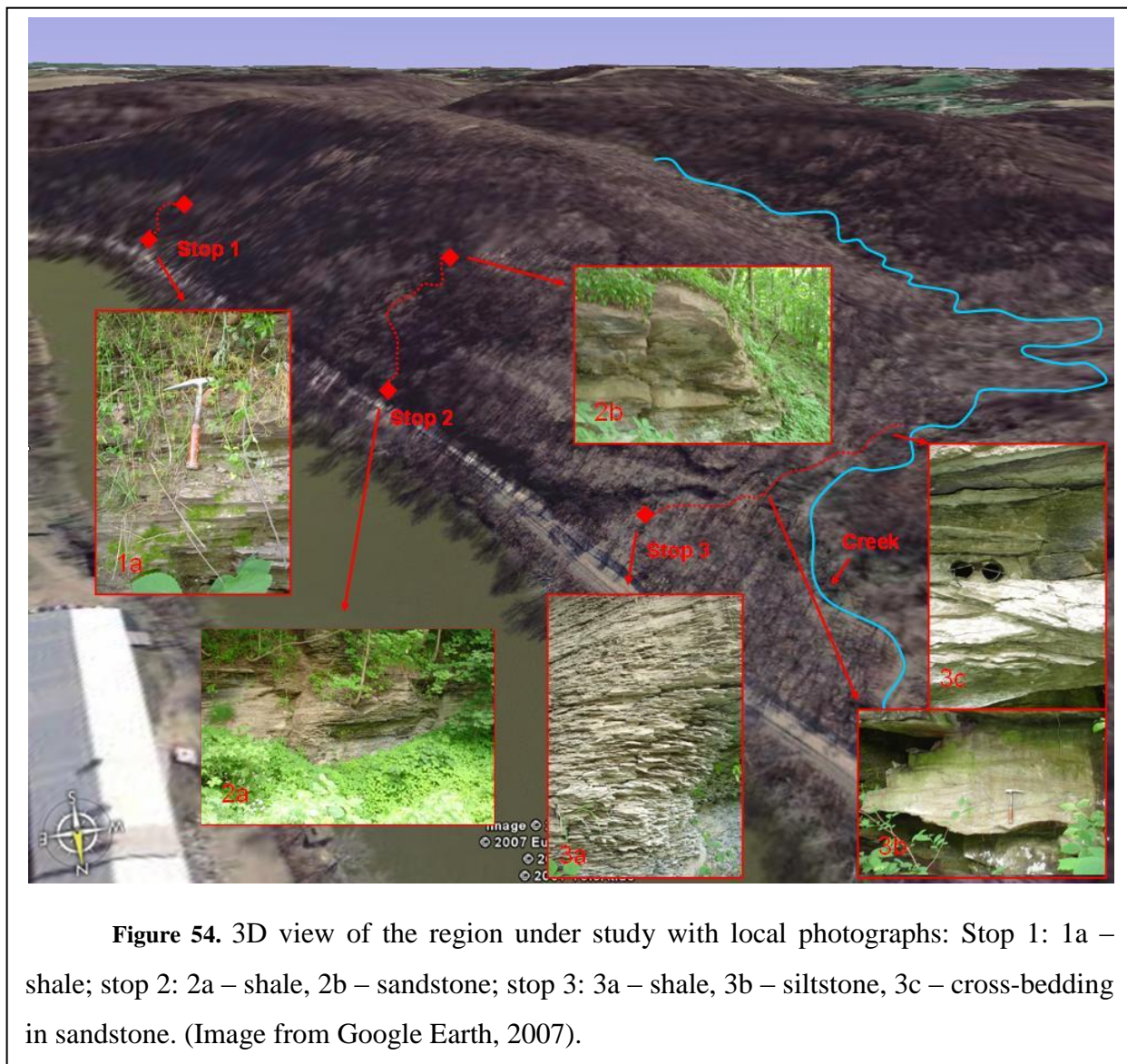
Following the trail further in the NW direction a sign "Dead Man's Hollow" can be observed on the left side, approximately 500 meters (1640 ft) away from Stop 2. A pathway separates to the left from the original trail and Stop 3 (40°19'04"N; 79 ^{o}50'26.5"W) is located about 10-15 meters (33 - 49 ft) along that pathway. The pathway goes into the valley of a small creek (Figure 54) and exposes an elongated outcrop on the left measured vertically 5-7 meters (16 - 23 ft) roughly at and extending laterally another 100-150 meters (328 - 492 ft) westbound along the southern boundary of the valley. At the base, the rocks are grey shales (Figure 54), which are extremely thin-bedded (1-3 mm thickness; 0.04 inch to 0.12 inch) and otherwise similar to those observed at stops 1 and 2. Moving further west, the shale grades into micaceous siltstones and sandstones (sample 5), revealing facies change within the same formation. In Figure 55 cross-bedding is depicted.

Based on the Geologic map (Wagner, 1975), altitude variation from 760 to 960 ft (232 to 293 m) above the mean sea level (MSL), the sub-horizontal attitude of the bedding and the elevations of the known wells (771 ft (235 m), well 1 and 847 ft (258 m), well 2). These rocks belong to the Conemaugh group. In Figure 56, a correlation model with the existing two wells is shown. According to this figure, the encountered rocks should be a part of the Buffalo member of the Conemaugh group.

Figure 55. Various types of cross-bedding encountered at stop 3. 3a – trough cross-bedding, 3b – hummocky cross-bedding, 3c – planar cross-bedding.
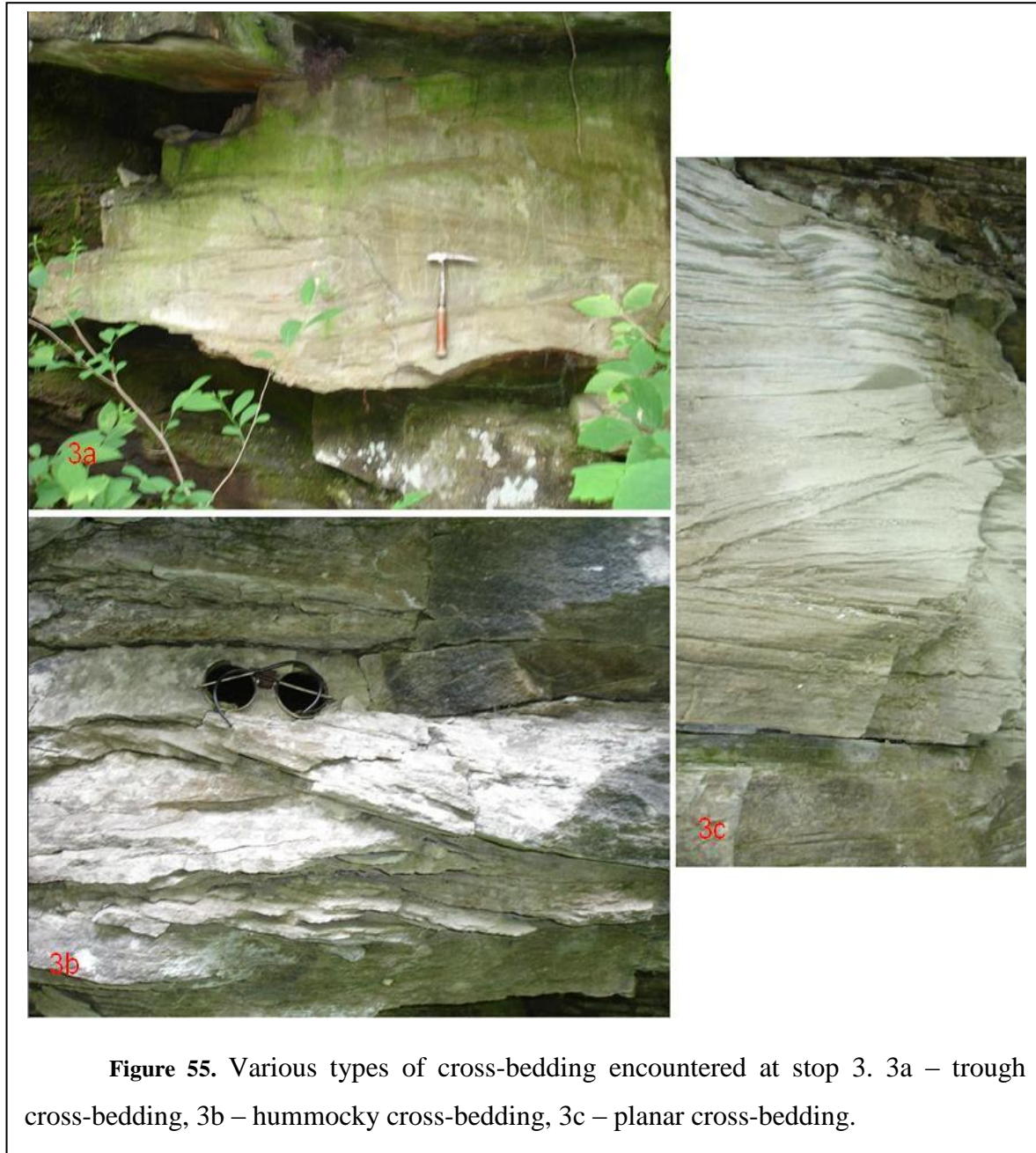
In our interpretation, the observed rocks were formed in a fluvial non-marine environment, as most of the material composing the terrigeneous shale and siltstones is of terrigenic origin. No lime material was present in any of the samples (no reaction with HCl). In Figure 57, a simplified model of facies change within a single formation is depicted, which

Figure 56. Correlation of observed outcrops and logged wells.

Figure 57. Schematic description of proposed facies variation within Buffalo member of Conemaugh group in surveyed area.
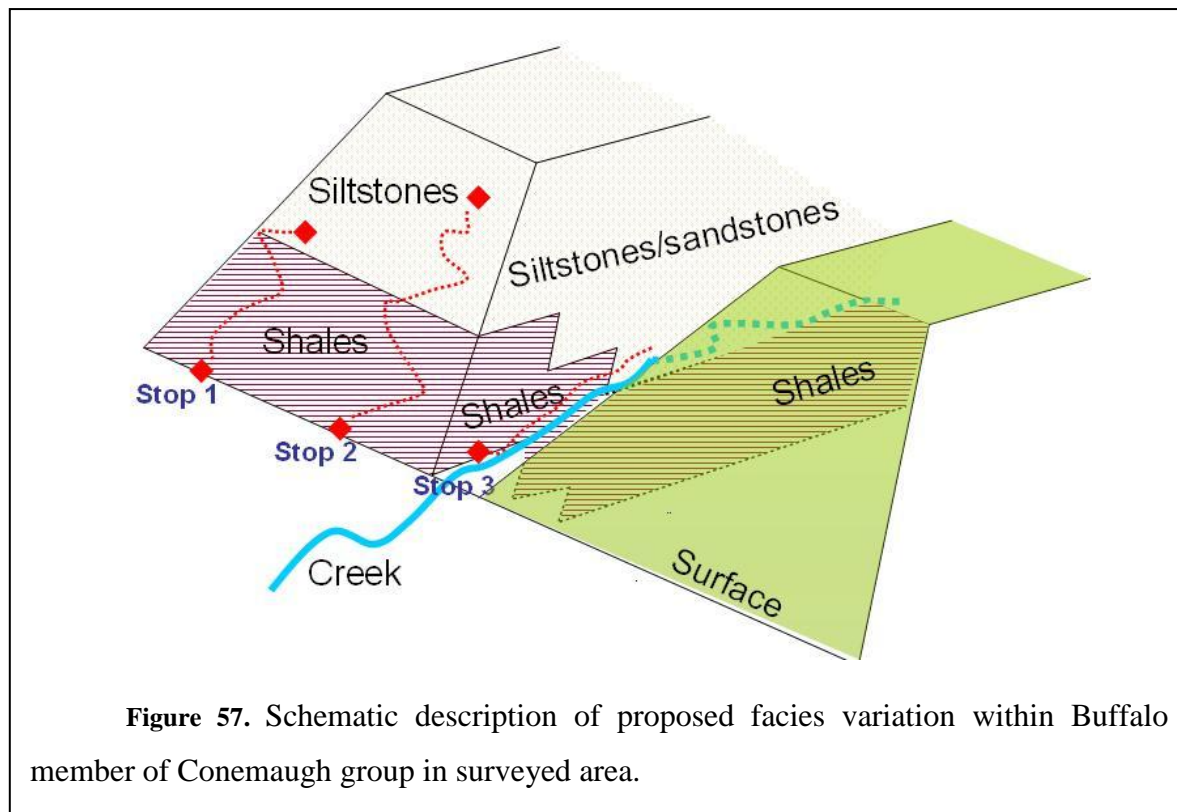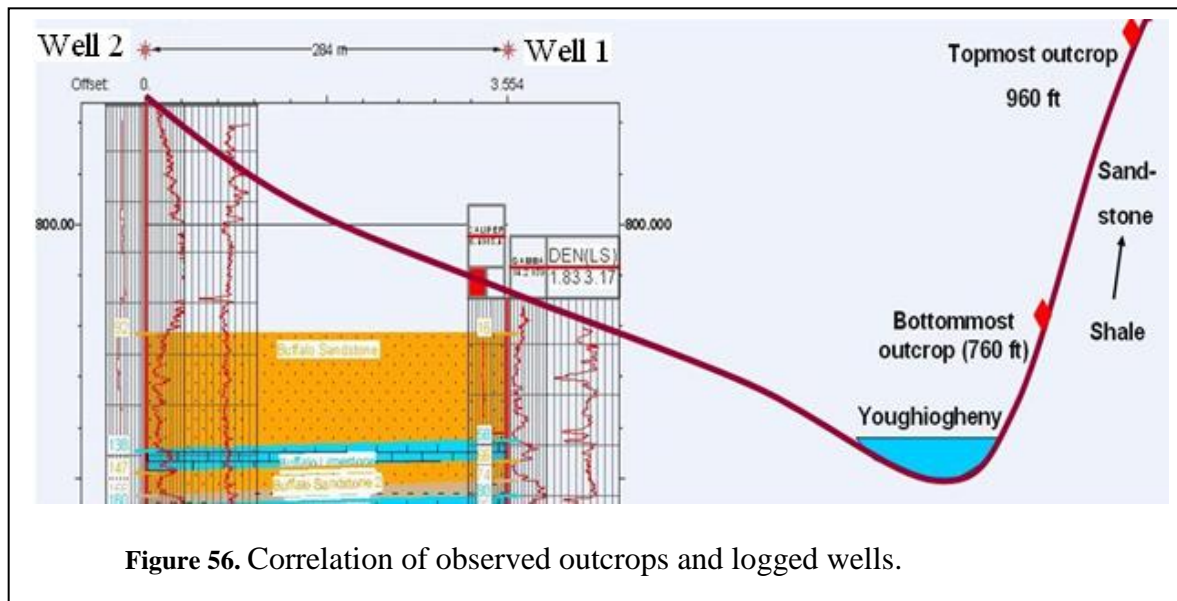
would explain field observations. It is speculative to interpret depositional environments of the material in more detail; however, transitions from shale to siltstones and to sandstones with notable facies changes could characterize a braided or meandering river system, and samples 4 and 5 could be described as typical channel sandstone. Deposition in a fluvial

116

environment would also explain the presence of mica (muscovite) in some of the samples, as it presumably had to travel from distances of hundreds of miles or kilometers (no volcanic activity is known in the vicinity of the encountered outcrops).

In terms of potential for hydrocarbon accumulation further analysis is needed. However, rough field techniques (the rule of tongue) were used to identify the siltstones and sandstones as rocks with micro-porous fabric (potential reservoirs) and the shale as impermeable rocks with extremely low effective porosity (potential seal). If siltstones and sandstones of the group are proven to allow natural gas migration, it would be fair to assume that in an environment of facial changes, there could be stratigraphic traps present in the region under study.

2.3.5. Experimental calculations of effective porosity and hydraulic conductivity

The samples were tested for effective porosity as well as for hydraulic conductivity. In order to prepare the samples for tests, they were cut into cubes, measured, accurately weighed (some of them repeatedly) in a dry state and their densities were calculated.

A porosity test was conducted using a 1 liter a glass tube, sealed from one end and scaled at 10 ml intervals. The tube had an opening wide enough to accommodate samples in raw or partially cut state and to allow 800 milliliters of tap water in addition to each sample. All the equipment necessary for these tests was available at the soils laboratory at the Department of Civil Engineering, University of Pittsburgh, with the help of Dr. J.S. Lin and Dr. R. Quimpo.

For each sample the tube was filled with 800 ml of H_2O and then the dry sample was dropped into the tube, raising the water level in the tube by its volumetric content. Further, its specific gravity was calculated, as its total mass normalized by its volume. For each sample 5 to 10 hours were allowed in order for the water to saturate the rock; then samples were removed from water, wiped externally and weighed again. The specific gravity at 21°

117

C was determined to be 0.961 kg/m^3. Based on the change in sample masses, porosity was calculated according to equation 2.20

$$p = (\Delta m/0.961)/V*100\% \qquad (2.20)$$

Where p is the effective porosity and Δm is the mass of the water contained in sample, in grams (representative of the volume of interconnected pore space in milliliters). In Table 8, the measurements are provided along with the calculated density and effective porosity values.

Samples	V(H$_2$O)	V sample, ml	m_{dry}	$m_{dry(2)}$	m_{sat}	Δm	ρ, (dry rock)	Effective porosity, (%)
1	800	50	124.5		125.7	1.2	2.49	2.50
2	800	56	145.1		146.9	1.8	2.59	3.34
3	800	25	59.3	59.4	60.1	0.8	2.37	3.33
4	800	68	170.7		176.1	5.4	2.51	8.26
5	800	69	173	173	177.6	4.6	2.51	6.94

Table 8. Effective Porosity V H$_2$O – volume of water used for the experiment in milliliters. V sample – measured volume of sample in pre-cut or partially-cut state. m_{dry} – electronically measured mass of dry sample. $m_{dry(2)}$ - mass of dry sample electronically measured. m_{sat} – electronically measured mass of a water-saturated sample. Δm is the difference between the dry mass and the saturated mass. ρ (dry rock) - calculated density (specific gravity) of dry sample. Effective porosity (%) – percentage of interconnected pore-space filled with water upon the completion of the experiment.

     * Two out of 5 samples (1 and 4) had to be pre-cut in order to be fit into the experimental tube. All of the samples were further cut into accurate geometrical shapes for the second.

Hydraulic conductivity was determined using a slightly modified version of the falling head test in soil mechanics. According to Darcy's law, during gradual discharge, the equation for the coefficient of permeability (Cernica, 1995) is:

$$-a*dh/dt = k*(h/L)*A \qquad (2.21)$$

Where a is the area of a standpipe

dh/dt is the time derivative of hydraulic drawdown

k - hydraulic conductivity (meters per second)

h water level in the standpipe and

A is the cross-sectional area of the sample

Solving this differential equation using the method of separating variables and then integrating, we can derive Equation 2.22 for k (Cernica, 1995):

$$k = \frac{aL}{At_f} \ln \frac{h_0}{h_f} \quad \textbf{(2.22)}$$

In order to complete the experiment, rock samples were cut into cubic shapes (Table 9) at the Rock laboratory of the Department of Geology and Planetary Science (University of Pittsburgh).

In Table 9 linear dimensions (x,y,z) of the samples are shown in millimeters and meters; in addition, the cross-sectional area A is calculated as well as the total volume of each sample cube (both in cubic meters and in milliliters)

Samples	x (mm)	y (mm)	z (mm) (L)	X (m)	Y (m)	Z (m) (L)	A (m^2)	Vol (ml)	Vol (m^3)
1	90.00	32.00	13.00	0.090	0.032	0.013	0.002880	37.440	0.000037
2	40.00	37.00	21.00	0.040	0.037	0.021	0.001480	31.080	0.000031
3	39.00	30.00	12.00	0.039	0.030	0.012	0.001170	14.040	0.000014
4	60.00	42.00	13.00	0.060	0.042	0.013	0.002520	32.760	0.000033
5	59.00	26.00	23.00	0.059	0.026	0.023	0.001534	35.282	0.000035

Table 9. Linear dimensions (x,y,z) of the samples after they were cut in the laboratory, shown in millimeters and meters; in addition, the cross-sectional area A is calculated as well as the total volume of each sample cube (both in cubic meters and in milliliters).

No equipment was available for this test at the University of Pittsburgh so an apparatus was designed and constructed in order to complete the experiment. A standpipe with a radius of 0.5 cm was used. The standpipe was equipped with a 10 milliliter scale bar (total of ten scale markings at 1 ml per scale). The beginning elevation of water table above the relative surface (floor) was 1.07 meters.

For each sample, flow was allowed until the drawdown in the standpipe reached 100 millimeters. Then the time was measured for such drawdown to occur and the desired coefficient was calculated according to equation 2.22. Finally, the values were calculated for the experimental hydraulic coefficients and recorded in Table 10.

Sample	A (m^2)	L (m)	a (m^3)	h_0 (m)	hf (m)	t, sec	k (m/sec)
1	0.002880	0.013	7.854E-05	1.07	0.97	7020	4.95495E-09
2	0.001480	0.021	7.854E-05	1.07	0.97	2800	3.90503E-08
3	0.001170	0.012	7.854E-05	1.07	0.97	10020	7.88774E-09
4	0.002520	0.013	7.854E-05	1.07	0.97	900	4.41698E-08
5	0.001534	0.023	7.854E-05	1.07	0.97	180	6.41882E-07

Table 10. Results of hydraulic conductivity experiment.

These results are significant because they show low porosities (common for Appalachian region) of the sampled units and variation in hydraulic conductivity. These results suggest that gas pockets may be sealed by stratigraphic traps, and stratigraphic traps may be result of rapid facies variation in the area. Therefore leakage to the surface probably occurs along fractures or abandoned well bores rather than through solid bedrock.

2.4. SEISMIC SURVEYS

2.4.1. Marine seismic survey

As part of this geophysical project, marine reflection surveys were completed at the site. These single channel reflection seismic surveys used the EdgeTech (http://www.EdgeTech.com) full spectrum sub-bottom profiler (FS-SB) as an energy source. The FS-SB uses chirp technology to generate and transmit a wideband FM pulse that is linearly swept over a full spectrum range. The full spectrum pulse waveform is amplified by a 2 kW power amplifier, which drives the transmitting transducer. The reflected waveform is recorded by two hydrophones located in a tow vehicle. The

Figure 58. Marine line 02 showing possible gas filled fracture. The high reflectivity of this region may be associated with gas filled voids in fractures.
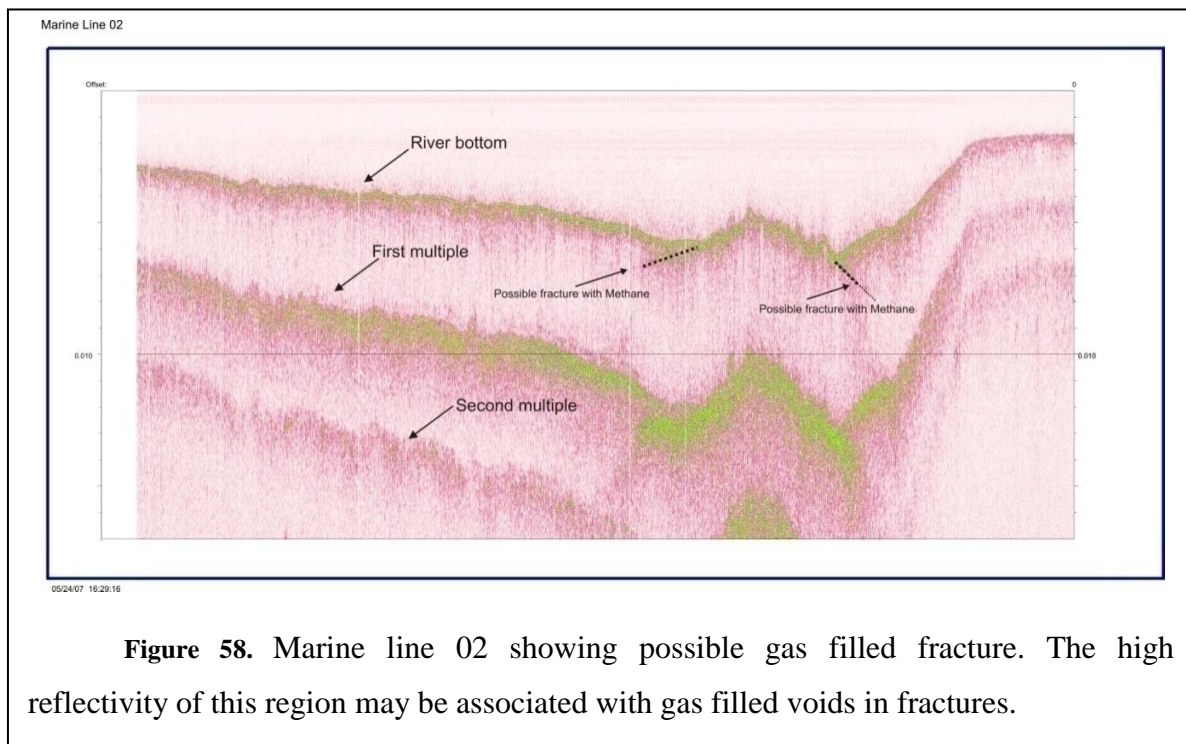
frequency range of the 20 ms pulse is 2-16 kHz. Interpreted profiles are shown below, and all data is shown in an attachment to this report (Kaminski, Harbert et al, 2007).

Figure 59. Marine line 05 showing a possible high reflectivity feature possibly related to a gas-filled fracture.
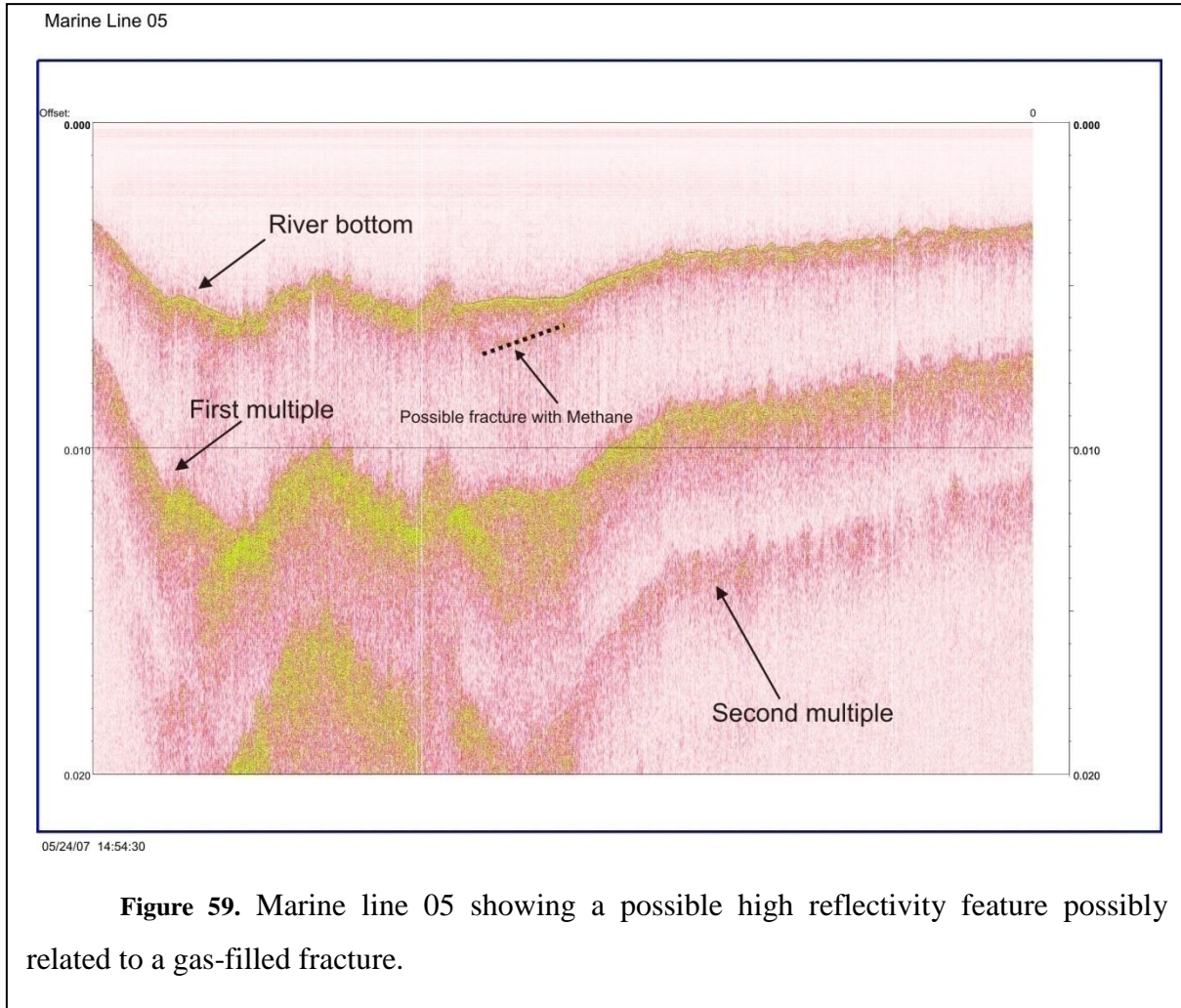
On reflection seismic profiles, sub-bottom bathymetry was clearly imaged and some sub-bottom features observed. Two of the profiles showed regions of enhanced reflectivity (Figure 58 and Figure 59). One of the profiles showed an erosional feature in-filled with sediment (Figure 60).

Because this was a single channel system no processing was completed on the marine lines other than frequency filtering, reflection amplitude adjustment, or gain manipulation.
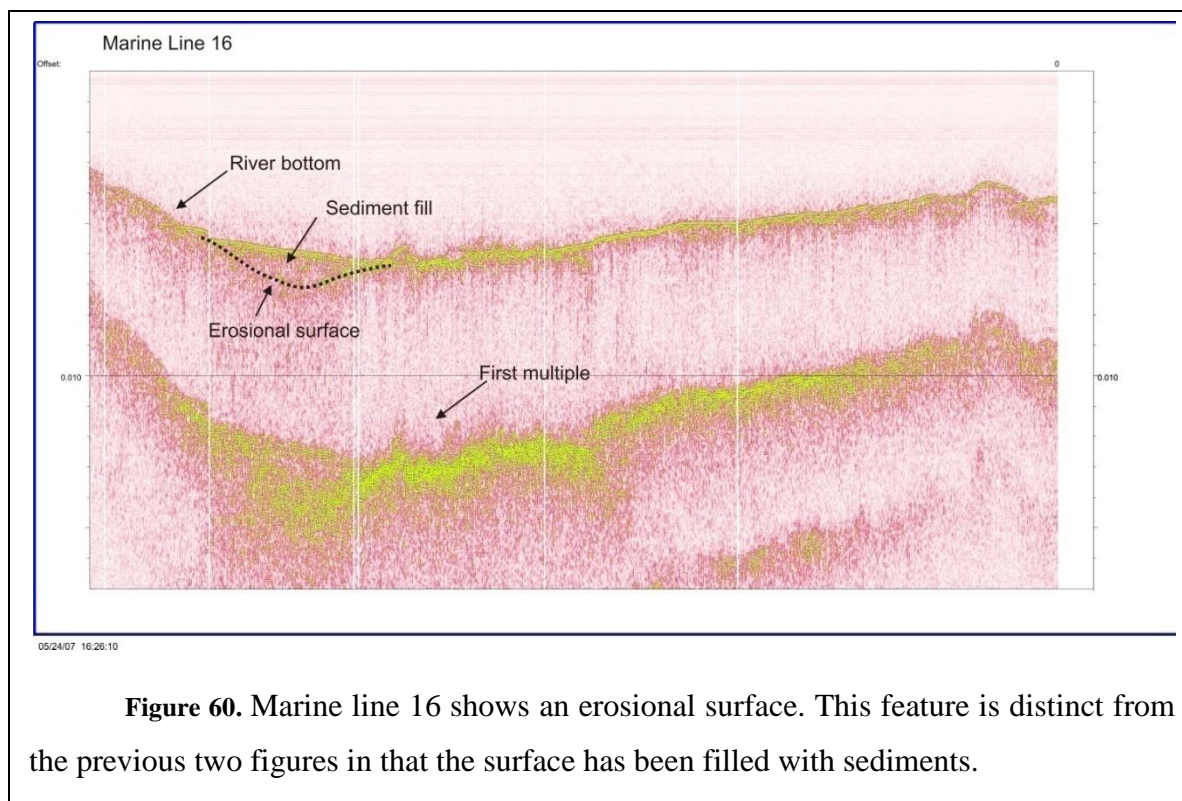
Figure 60. Marine line 16 shows an erosional surface. This feature is distinct from the previous two figures in that the surface has been filled with sediments.

2.4.2. 3D land reflection seismic survey configuration

The most informative survey completed at the site was a three dimension (3D) reflection seismic survey using an I/O reflection seismic system II. The system employed I/O RSX and I/O ALX electronic boxes and an IVI EnviroVib™ vibrator truck. RSX boxes provided necessary amplification for the recorded signal, digitized the analog input signal to 24-bit digital packets and communicated with other portions of the receiver array. The RSX boxes also monitored the functionality of recording lines, geophones and electronic components. The reflection seismic geophone lines were connected with ALX boxes, which were then connected to the seismic recording truck. The entire receiver array or chain of detectors was controlled from a data recording vehicle and synchronized with the energy-source in order to accurately acquire data. The amplification of the I/O System II from the vertical component geophone to the initial recording of the signal was approximately a factor of $4*10^6$.

The EnviroVib™ used a SIB-100 seismic vibrator controller system to control the energy source. Communication between the I/O System II electronics and the SIB-100 was accomplished via a RST-100 seismic source radio trigger system. This system was interfaced with the recording truck electronics by Mr. Wayne Mathis of HL Technologies, who was responsible for quality control of the recording electronics and recording of the seismic data. The EnviroVib™ system was swept four times at each energy point and these signals were stacked to increase the signal to noise ratio of the final trace recorded at each geophone location. The correlated geophone records were then written to tape in standard SEG-D format. Pre-stacked reflection seismic data were recorded at a sampling rate of 1 ms and written as a signed 24 bit value with a record length of 5 seconds.

Elastic P-waves arrivals were recorded in this survey using OYO GS20DX vertical component geophones. These geophones recorded the superimposed reflections from each of the subsurface reflecting horizons. Geophones were emplaced every 40 ft (12.2 m) one from another along each profile. There were a total of three geophone lines and four SP lines laid out. Distance between these profiles was variable and depended greatly on the geometry of densely populated residential neighborhood. This distance was no less than 40 m, but no greater than 100 m.

2.4.3. Seismic data processing

The processing of 3D seismic data included receiver and static determination and correction, Butterworth filtering, 3D crooked line processing and predictive deconvolution, as well as techniques related to data processing of reflection amplitude variation with offset (AVO) before stacking to invert the data for Poisson's ratio and shear wave reflectivity.

Immediately after being recorded the seismic traces were cross-correlated with the EnviroVib™ source sweep (Dobrin, 1976). The entire length of the sweep was used in the cross-correlation process. The cross-correlated record accurately shows the locations of the reflecting horizons. All reflection seismic lines and seismic attributes for these lines are listed in Appendix C. Three geophone lines and four SP lines further yielded 12 common

midpoint (CMP) lines. A CMP map pointing the locations of all CMP's in the 3D seismic survey is shown in Figure 61.
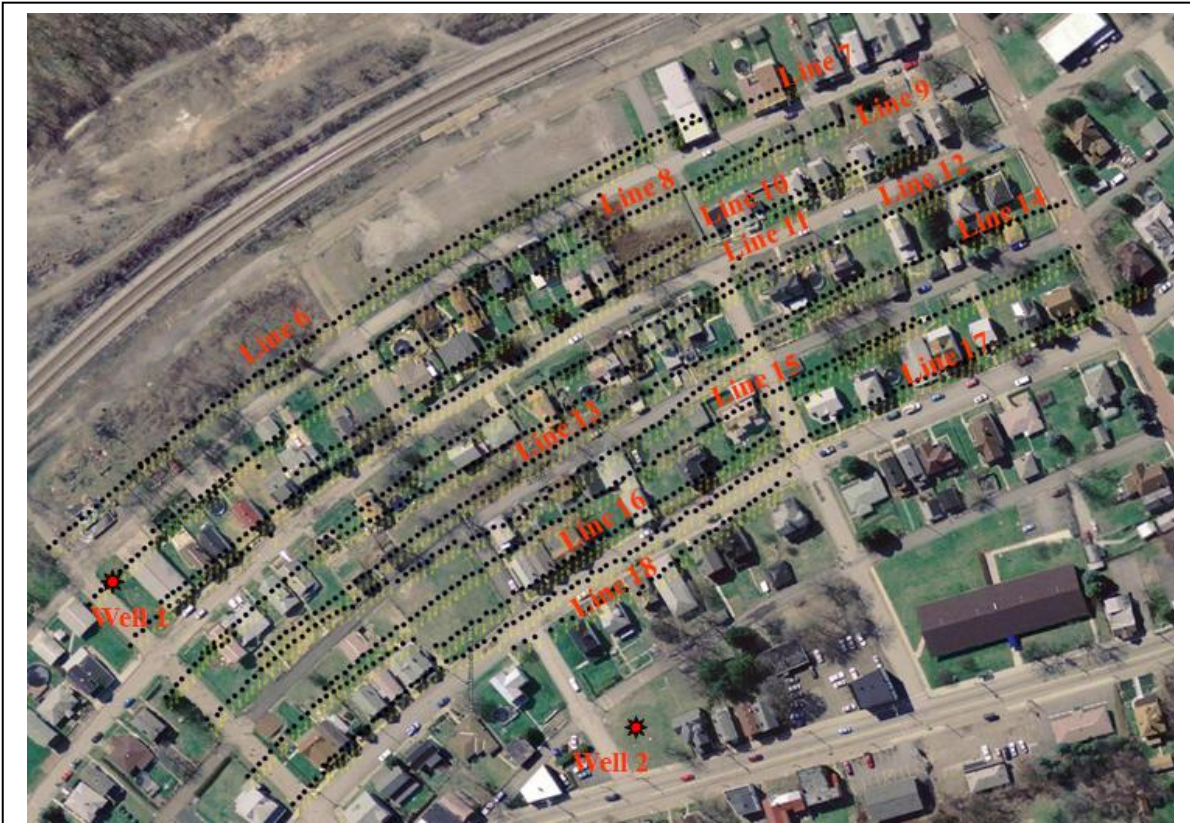
Figure 61. Common midpoint locations. Four energy lines and three geophone lines resulted in a total of 12 CMP lines, approximately 25 m apart from one another.

Specific processing parameters included the bin size (in-line) of 10.0 ft (3.05 m) and the bin size cross line (x-line) of 37.5 ft (11.4 m). In the frequency spectrum signal recorded by our geophone array, there was a high-frequency component. By applying a band-pass frequency filter to seismic traces, it was possible to significantly improve the signal to noise ratio. Butterworth band-pass filtering was applied using a low cut-off frequency of 10 Hz with a low roll-off rate of 18.0 dB/oct and a high cut frequency of 70 Hz with a high roll-off rate of 18 dB/oct. A zero phase selection was used for the Butterworth filter operation. Floating datum statics were calculated and stored in separate receiver and source datum databases.

An additional step related to seismic reflection processing was that the reflection data was deconvolved. Predictive deconvolution parameters included a length of 55 ms, pre-whitening of 3.5%, inverse filter with length of 50 ms and a design length window of 100 ms.

The data were then statically corrected to a reference datum. All of these steps were completed at the trace level in 3D processing operations using software from Parallel Geoscience Corporation (Figure 62). Some acquisition related geometry artifacts are present because of the variation in geometry of the energy points and geophones. This type of 3D geometry of energy points and geophones is called a swath acquisition (Cordsen et al, 2000) and can produce a variation in fold between lines.

Figure 62. Processing sequence for 3D reflection seismic survey. (Software: PGC V 2.2.6.)
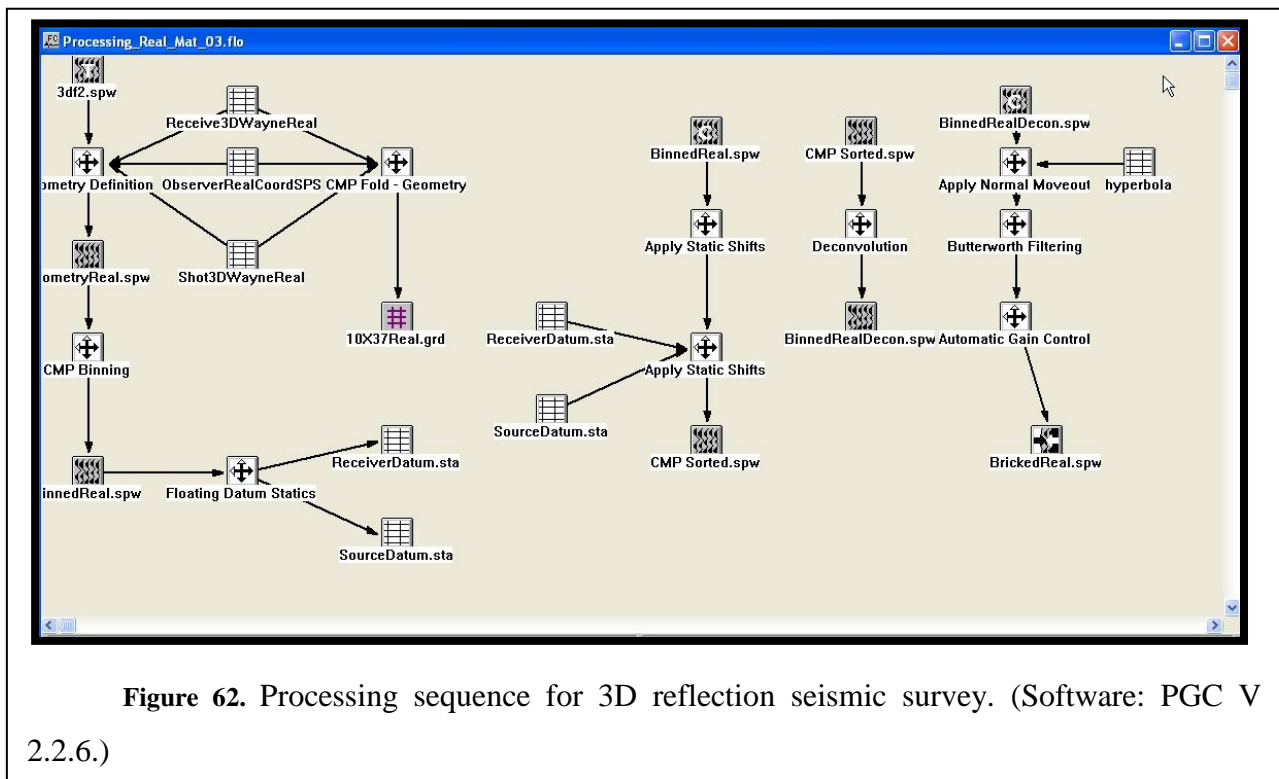
Several zones of seismic attribute variation were identified. Clear reflectors were observed in the seismic lines collected within the area under study including amplitude variation along reflecting horizons. Unfortunately, in some regions, probably because of the presence of relatively unconsolidated overburden or fill, transmission of elastic waves was

126

significantly attenuated. These regions are referred to as "wipe out" zones. Because of this and the variation in fold related to our swath acquisition with curved geophone and energy lines, it was decided to focus on the highest quality lines and reflectors and apply a more advanced processing technique available in the Parallel Geosciences package, amplitude variation with angle (referred to as AVA or AVO processing), to extract seismic attributes at specific CMP locations.

2.4.4. Velocity analysis

Velocity analysis was performed based on the sonic velocity data acquired by century geophysics in 2006 as a result of downhole survey of two wells located in area under study. There were a total of four velocity zones identified for well 1 and five – for well 2, (Figure 63 and Figure 64).

Sonic velocity readings were only provided for the well 2 and only for a limited and shallow portion of the stratigraphic column. Therefore in many cases either the averaged or interpolated values were used or in case of well 2 – the values were extrapolated from well 1, based on the stratigraphic and lithologic correlation discussed earlier.

Figure 63. Velocity analysis of well 1. Zone four provided most detailed description of velocity-depth relationship based on direct downhole sonic velocity measurements provided for this zone.
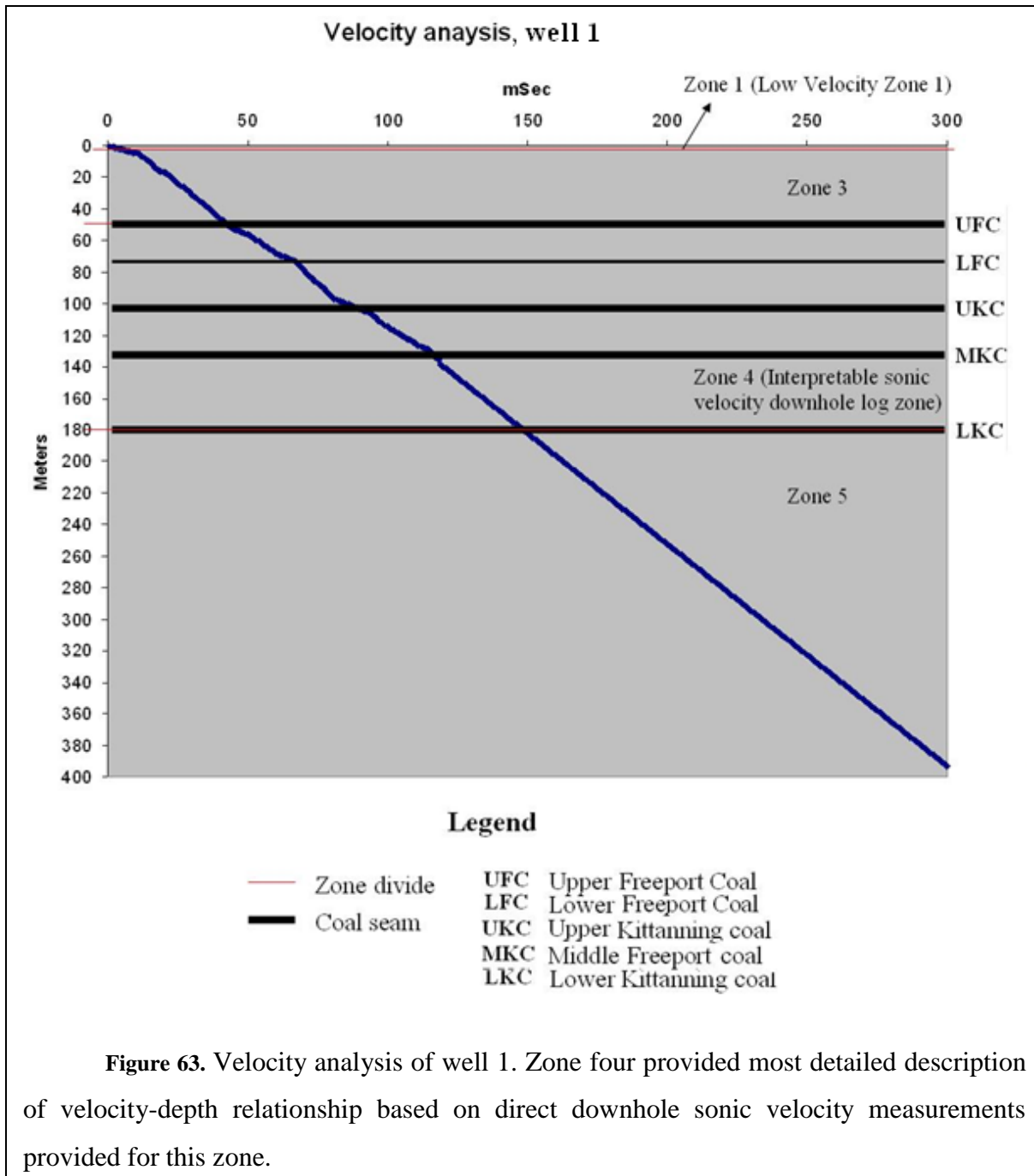
Zone 1 is a near-surface low velocity zone (further LVZ). It is present in both well logs (Figure 65) with thickness varying from 3.2 meters at well 2 to 5 meters in case of well 1. The velocity through LVZ was estimated at 0.91 km/sec based on 1D modeling performed using SurfSeis 1.80 software.

Figure 64. Velocity analysis (well 2).
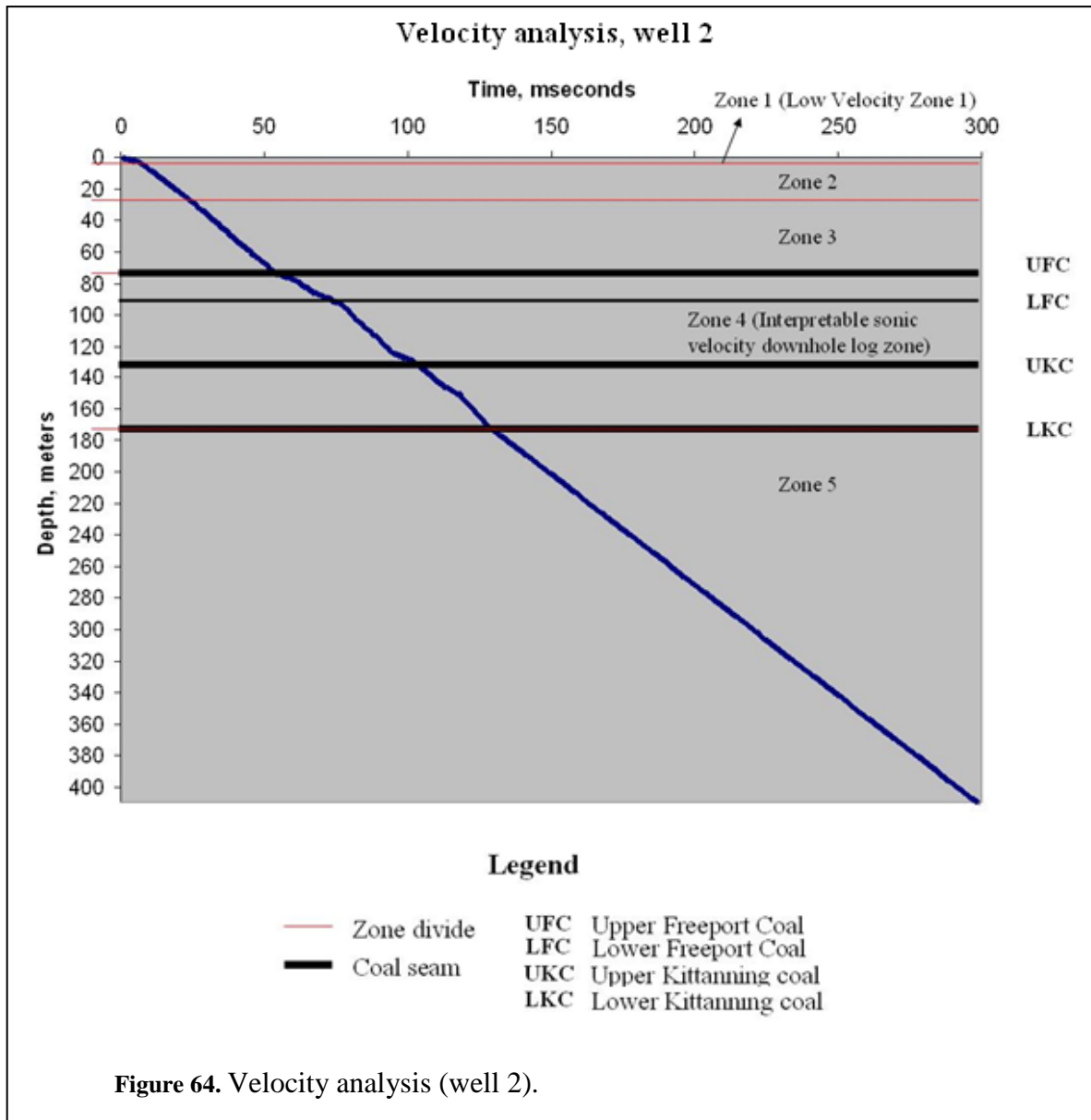
Zone two is only present in case of well 2 (Figure 64) and is represented by strata located at depths from 3.2 m to 28.5 m, stratigraphically higher than any strata in well 1, however with no record of valid sonic velocity readings. The weighted average value was assigned to this zone equal to 2.81 km/sec (the averaged sonic velocity for entire cross-section, wherever valid readings were available, Table 11). This value was calculated based on averaging of 3387 sonic velocity readings taken from well 2 wire log.
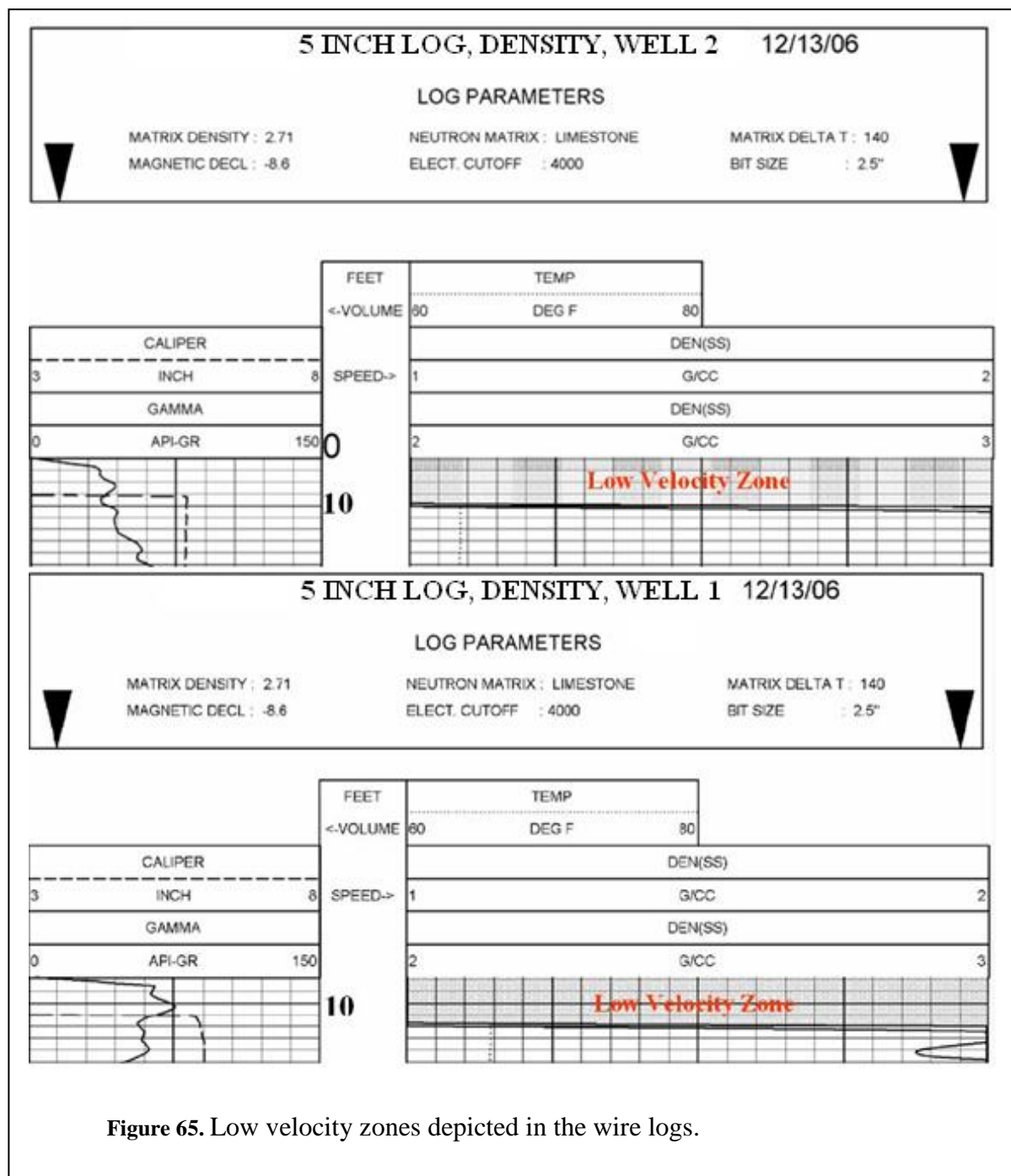
Figure 65. Low velocity zones depicted in the wire logs.

Zone three is the part of the cross-section bound by LVZ at the top to the Upper Freeport coal (bottom of Conemaugh group). Well 1 is again missing reliable sonic velocity readings. Therefore, known sonic velocity values from same type units stratified in well 1 and correlated with well 2 were used to calculate arithmetically averaged velocities for sandstone, shale, limestone and coal.

130

Sandstones		Limestones		Shales		Coals		
UFSS	1.54	UFL	2.4	#5	3.9	UFC	1.54	
#1	4.2	#4	4.12	#6	3.24	LFC	1.42	
#2	2.18	#6	3	#7	3.56	UKC	1.49	
#3	2.07			#8	3.6	LKC	1.616	
#5	3.67			#9	4			
#6	4.76			#10	4.18			
Average	**3.07**		**3.17**		**3.75**		**1.52**	**Total: 2.81**

Table 11. Averaged sonic log P-wave velocities of sedimentary beds stratified from wire line log in study area in units of km/sec. UFSS – Upper Freeport sandstone; UFL – Upper Freeport limestone; UFC – Upper Freeport coal; LFC – Lower Freeport coal; UKC – Upper Kittanning coal; LKC – Lower Kittanning coal.

The thickness of zone three in vicinity of well 1 is 45m (5 to 50 meters) and is 55 m in vicinity of well 2 (28.5 to 73.5 meters) This zone includes the Buffalo and Mahoning sandstones, as well as Brush Creek coal and is bound by Upper Freeport coal at the bottom, but doesn't include the latter (Figure 63 and Figure 64).

Zone 4 includes all the strata from Upper Freeport coal to lower Kittanning coal and is characterized by interpretable and accurate sonic velocity data available from well 2. This data was further extrapolated onto well 1 using stratigraphic correlation (Figure 51 and Figure 52) and assumption of sub-horizontal dip of the layers.

In the vicinity of well 1 – zone 4 includes all the strata in the depth range between 50 meters and 180 meters. Although the Lower Kittanning coal is located below the deepest horizon of well 1 – it will be further shown that 180 meters is a fairly accurate estimate for the depth to this horizon based on seismic reflection data. In vicinity of well 2 – zone 4 is comprised of all the strata between 73.5 meters and 174 meters.

Zone five was defined as all strata beneath the interpretable extent of well log sonic velocity data. Since no detailed data on sonic velocity measurements were available

beneath the 175 meter depth the zones were assigned an average generalized velocity of 2.81 km/sec (similar to zone 2)

2.4.5. Interpretation of reflection Seismic Data

Processed reflection seismic data were carefully examined and plotted tied to common midpoint (further CMP) locations. CMP locations were aligned to form 12 lines (Figure 61).

Further, stacked reflection seismic data amplitudes were plotted versus calculated Poisson ratio coefficients and shear wave reflectivity charts. According to the analysis of CBM reservoirs – there could be two types of natural gas deposits in the area under study: CBM trapped within a coal seam and CBM which escaped from a coal seam, trapped in a reservoir adjacent to the coal seam. Peng (2006) emphasized six main concepts applicable to interpretation of CBM deposits (Peng et al, 2006).

1. Gas always lowers Poisson's ratio in sandstone
2. Cleats and fractures in coal seam result in higher Poisson's ratio.
3. Top of gas sands can be recognized by negative AVO gradient
4. Top of the CBM reservoir has a positive AVO gradient
5. Coal seams have strikingly high reflection amplitude
6. Gas sands cause low impedance values

Energy reflected at various interfaces can be represented in terms of reflection coefficients as a function of acoustic impedances of two media (Sheriff and Geldart, 1995). In Table 12 the expected impedances are calculated for all media interfaces in zone 4, well 1.

Interface	Layers bounding interface *	Time (mSec)	Depth (m)**	Depth (ft)	First medium V1 (km/sec)	First medium ρ1 (g/cm3)	Second medium V2 (km/sec)	Second medium ρ2 (g/cm3)	Z1	Z2	R
Sandstone over shale	Buffalo sandstone ***	24	22.09	72.47	3.07	2.56	3.75	2.67	7.8592	10.0125	0.120487
Shale over coal	Number 1 shale ***	25	23.64	77.54	3.75	2.67	1.52	1.52	10.0125	2.3104	-0.62502
Coal over shale	Brush Creek coal ***	26	25.41	83.35	1.52	1.52	3.75	2.64	2.3104	9.9	0.621568
Shale over sandstone	Number 1 shale ***	34	36.56	119.92	3.75	2.64	3.07	2.54	9.9	7.7978	-0.11878
Sandstone over shale	Mahoning sandstone ***	40	45.712	149.94	3.07	2.54	3.75	2.58	7.7978	9.675	0.107436
shale over coal	Number 3 shale ***	42	49.03	160.82	3.75	2.58	1.54	1.79	9.675	2.7566	-0.55652
Coal over limestone	Upper Freeport coal	50	56.27	184.58	1.54	1.79	2.4	2.62	2.7566	6.288	0.390443
Limestone over sandstone	Upper Freeport limestone	60	67.84	222.52	2.4	2.62	1.54	2.51	6.288	3.8654	-0.2386
Sandstone over coal	Upper Freeport sandstone	64	70.92	232.63	1.54	2.51	1.42	1.77	3.8654	2.5134	-0.21195
Coal over shale	Lower Freeport coal	66	72.34	237.28	1.42	1.77	3.9	2.68	2.5134	10.452	0.612291
Shale over sandstone	Number 5 shale	68	75.00	246.01	3.9	2.68	4.2	2.64	10.452	11.088	0.029526
Sandstone over shale	Number 1 sandstone	69	76.95	252.40	4.2	2.64	3.24	2.6	11.088	8.424	-0.13653
Shale over limestone	Number 6 shale	71	80.67	264.62	3.24	2.6	3.17	2.59	8.424	8.2103	-0.01285
Limestone over sandstone	Number 3 limestone ***	75	87.18	285.94	3.17	2.59	2.18	2.41	8.2103	5.2538	-0.21958
Sandstone over shale	Number 2 sandstone	76	88.80	291.27	2.18	2.41	3.75	2.37	5.2538	8.8875	0.256957
Shale over limestone	Intermediate shale ***	77	89.89	294.85	3.75	2.37	4.12	2.64	8.8875	10.8768	0.100651
Limestone over shale	Number 4 limestone	80	95.71	313.94	4.12	2.64	3.56	2.67	10.8768	9.5052	-0.06729
Shale over coal	Number 7 shale	89	102.62	336.60	3.56	2.67	1.49	1.75	9.5052	2.6075	-0.56946
Coal over limestone	Upper Kittanning coal	94	106.30	348.67	1.49	1.75	3	2.64	2.6075	7.92	0.504631
Limestone over sandstone	Number 6 limestone	98	112.28	368.29	3	2.64	2.07	2.53	7.92	5.2371	-0.20391
Sandstone over shale	Number 3 sandstone	107	122.06	400.35	2.07	2.53	3.6	2.26	5.2371	8.136	0.216771
Shale over sandstone	Number 8 shale	109	124.13	407.14	3.6	2.26	3.67	2.46	8.136	9.0282	0.05198
Sandstone over coal	Number 5 sandstone	111	126.20	413.93	3.67	2.46	1.52	1.3	9.0282	1.976	-0.64086
Coal over shale	Middle Kittanning coal ***	114	128.73	422.24	1.52	1.3	4	2.67	1.976	10.68	0.687737
Shale over sandstone	Number 9 shale	116	131.48	431.25	4	2.67	4.76	2.56	10.68	12.1856	0.065846
Sandstone over shale	Number 6 sandstone	117	133.47	437.79	4.76	2.56	4.18	2.6	12.1856	10.868	-0.05715
	Number 10 shale				4.18	2.6			10.868		

All values calculated from wire line log

* - See Table 2 for details

** - Depth is calculated to the medium boundary for well #2

*** - For these layers no measured sonic velocity value is available, therefore averaged velocity from Table 3 was used.

Table 12. Calculated acoustic impedance for media interface (velocity zones 2 and 3) and P-wave reflection coefficients. Z_1 – acoustic impedance of the first medium Z_2 – Acoustic impedance of the second medium R – reflection coefficient at the interface.

The coal seams themselves, if they are thick enough can be easily detected using seismic reflection data, as they show low acoustic impedance and therefore – high values of reflection coefficients. Such reflectors are present in collected data, however the question of vertical resolution arises related to minimum thickness of a coal seam detectable by this survey. Taken 110Hz as dominant frequency, 1.52 km/s as average P-wave velocity in coals (Table 11) and Rayleigh's criterion as a guideline – a presumption can be justified that minimum thickness of a detectable coal seam would have to be at least 3.45 meters (11.33 ft). A sufficient thickness according to the well logs has been shown for Upper Freeport, Upper Kittanning, and Lower Kittanning coal seams. Middle Kittanning coal seam is under question, because its maximum interpreted thickness only reaches 6 - 7 ft (2 - 2.5 m), however considering the shallow emplacement of this unit and the assumption that well log interpretation may yield some uncertainties it still may be distinguished, should the higher frequency waves be strong enough to clearly reflect off this unit. Furthermore some coal seams are described as coaliferous zones, rather than individual coal beds and reveal significantly lower impedance values than surrounding other rocks. Such zones might reach tens of feet in thickness.

Well 1 location is coincident with CBM point 9_57 (line 9) therefore it is convenient to tie reflectors seen on this line to known coal seams considering previously performed velocity analysis. In the interval between 0 and 300 milliseconds - a total of 6 reflectors were detected from CMP line 9 at depths corresponding to 26 ms 43 ms 90 ms 110 ms, 150 ms and 175 ms respectively (Figure 66).
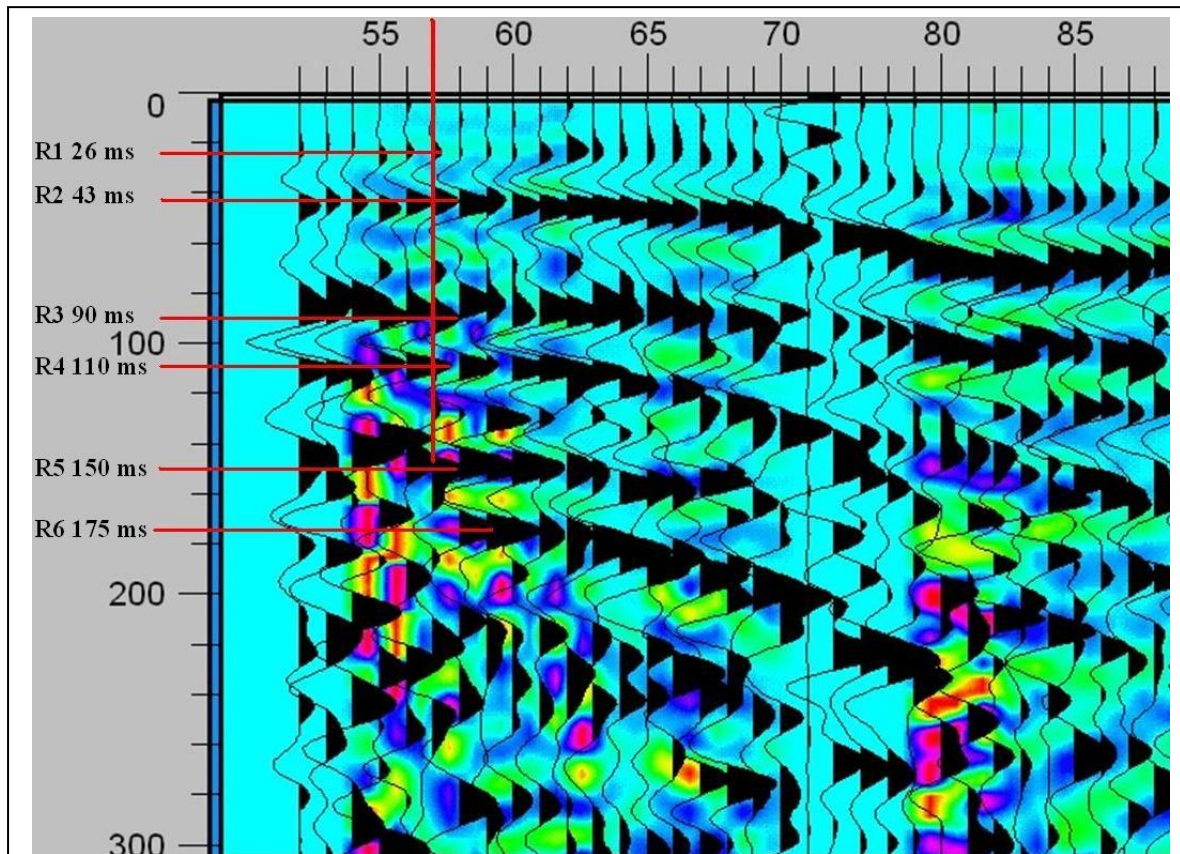
Figure 66. Delineation of six reflectors from the reflection seismic record derived from CMP line 9. Shaded peaks represent maximums of reflection coefficient, which according to our calculations should correspond to coal beds, exceeding 3.45 m in thickness.

Using the stratigraphic correlation between the two wells – velocity analysis was performed for well 1 analytically resulting in depth estimations for these anomalous reflectors recorded in Table 13. Please note that different velocities would change the estimated depth of these reflectors. More detailed explanation of reflector assignments can be found in "Appendix D" of this document.

The R6 reflector lies beyond the extent of both wells surveyed in the area under study, however according to various sources (Johnson, 1929; Milici et al, 2004) – its estimated depth corresponds to emplacement of Clarion #1 (Brooksville) coal bed, which is the

lowermost member of Allegheny group and according to the geologic data should be approximately 40 to 50 meters below the Lower Kittanning coal.

Name	Time (ms)	Calculated depth (m)	Reflector
R1	26	25	Brush Creek coal zone
R2	43	50	Upper Freeport coal
R3	90	103	Upper Kittanning coal
R4	110	125	Middle Kittanning coal
R5	150	181	Lower Kittanning coal
R6	175	219	Clarion #1 (Brooksville) coal

Table 13. Correlation of seismic data recorded at CMP location 9_57 with the stratigraphic column stratified from wire line log collected at coincident well 1.

The fact that reflectors on the seismic data align within reasonable error allowance with the known coal seams support the results of analytical velocity analysis performed for well 1. Furthermore, the correlated marker beds can be continued and traced at other CMP lines, allowing delineating coal seams. Analyzing the results of AVA-AVO analysis it becomes clear that many CMP lines show zones of anomalous Poisson's ratio or/and reflectivity (Figure 67, Table 13), however the factor of horizontal resolution has to be considered when grouping such traces inbetween the lines. For instance, taken a single CMP - the radius of unmigrated Fresnel zone for shallowest (20 m) detectable anomaly can be calculated as $\sqrt{(20 + \frac{V_{p\,avg}}{4f_d})^2 - 20^2} = 17.21\text{m}$ where "V_p avg" is the average P-wave velocity of the cross-section (2.81 km/s) and f_d – is the dominant frequency of the survey (110 Hz). Similarly for 60 meters of depth (which corresponds to approximate emplacement of Upper Freeport coal and 52 ms of 2-way travel time) – radius of Fresnel zone will be 28.41 meters.

The same principle is applicable for calculation of a given reflector footprint to the surface. It will be detectable on the surface within the distance from reference CMP equal to the radius of Fresnel zone (Sheriff, 1991). Therefore if an anomaly is present on a single trace

and does not show signatures on adjacent CMP lines – it must not be considered for further interpretation.

Figure 67. Anomalous zones detecting reflections from areas in the subsurface characterized by negative Poisson's ratio and S-wave reflectivity as identified by using Aki and Richards' approximation of Zoeppritz' equations. Zones are grouped according to their calculated depth, as derived from time-depth relationships.
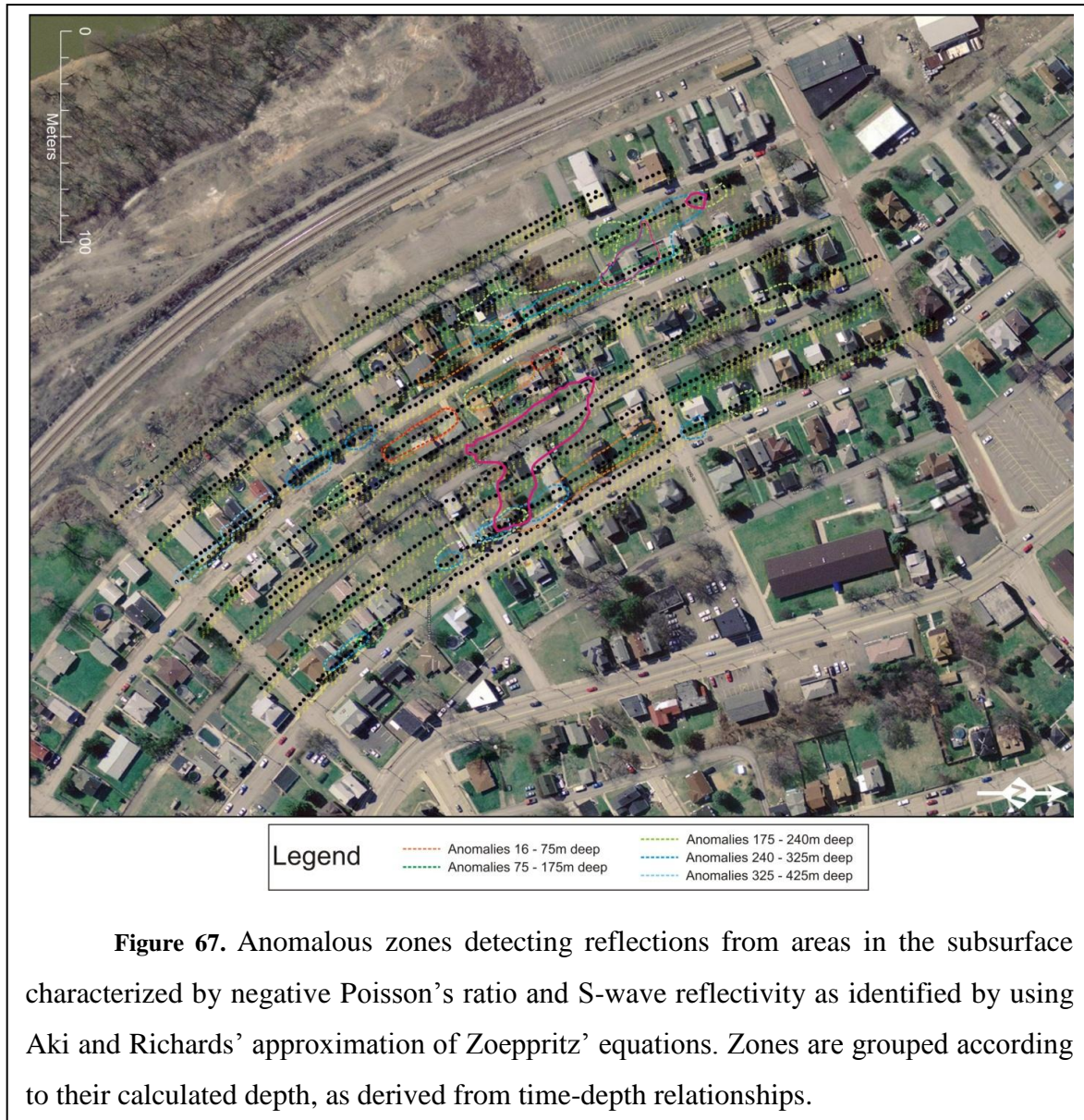
Considering the CMP line spacing of approximately 25 meters and the minimum required Fresnel zone diameter of 57 meters – the anomaly has to be traced on at least three adjacent lines to be considered exceeding the survey resolution. On Figure 67 only one area shows traceable signature wide enough to be interpreted as potential target. The anomaly can be traced from line 12 to line 15 (Table 14).

CMP Line Number	CMP Location	Two-way travel time (ms)
Line 7	85 to 98	0 to 60
Line 9	102 to 116	50
Line 10	127 to 132	50
Line 11	95 to 128	0 to 100
Line 13	**98 to 122**	40, 50, 60 and 80
Line 14	**98 to 121**	20, 40, 60 and 80
Line 15	**103 to 109**	40 and 70
Line 16	84 to 132	20 to 60
Line 17	69 to 76	50

Table 14. Intervals, characterized by anomalous Poisson's ratio and S-wave reflectivity distributions. Lines 13 to 15 feature interconnected continuous anomalous zone (bold script), which combined, exceeds diameter of calculated Fresnel zone for corresponding 2 way travel time and therefore comply with the resolution requirements for this survey.

Figure 68 and Figure 69 show what is interpreted to be representative of shallow natural gas reservoir. Here, 2-way travel time to the reservoir can be averaged at 60 milliseconds which for this particular location would correspond to 65 - 70 meters in depth and may be localized within the Mahoning sandstone unit adjacent to Upper Freeport coal and sealed by potentially impermeable shale number 3 from the above.
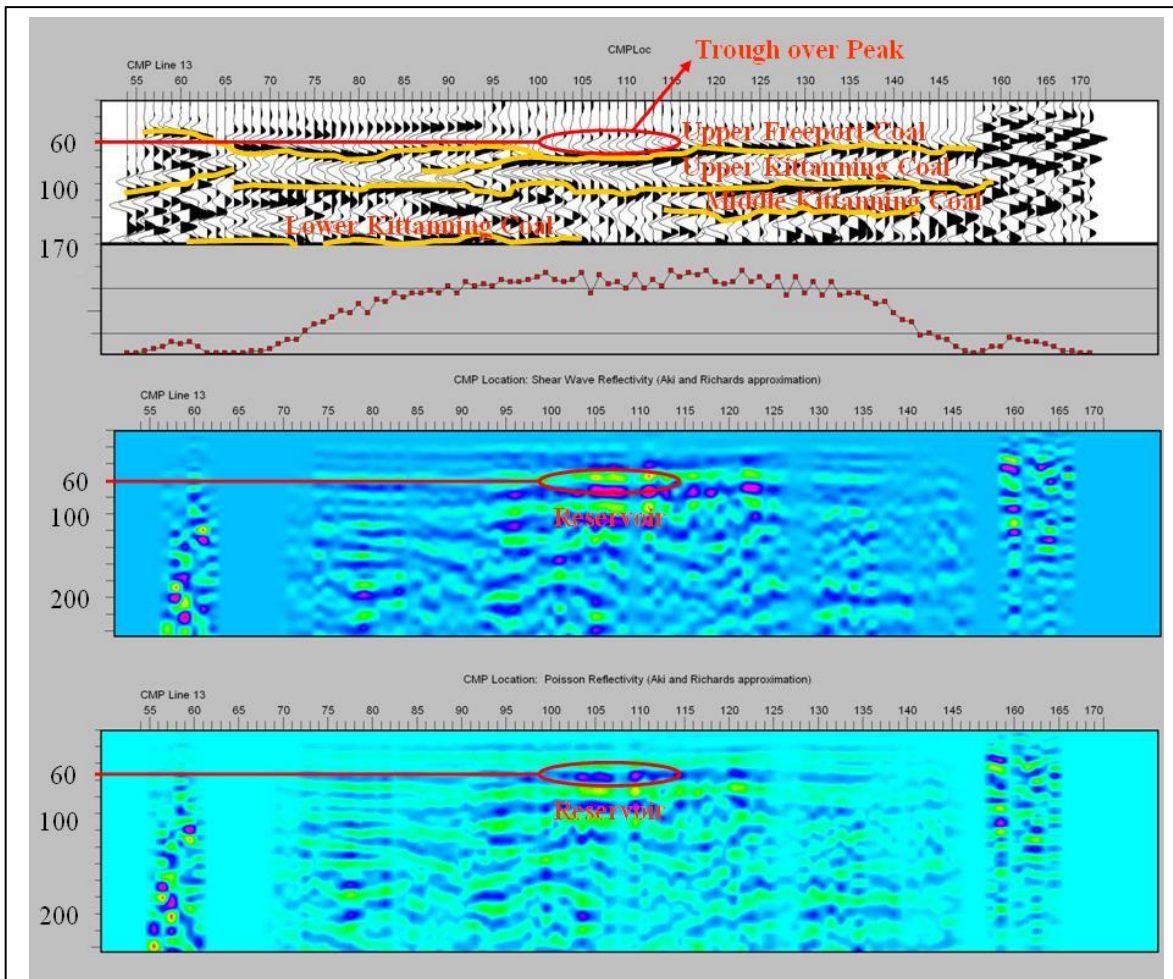
Figure 68. Shear wave reflectivity and Poisson reflectivity from CMP line 13 of the 3D reflection seismic survey. Enhanced parameter variation is observed between CMP locations 100 to 115.

139
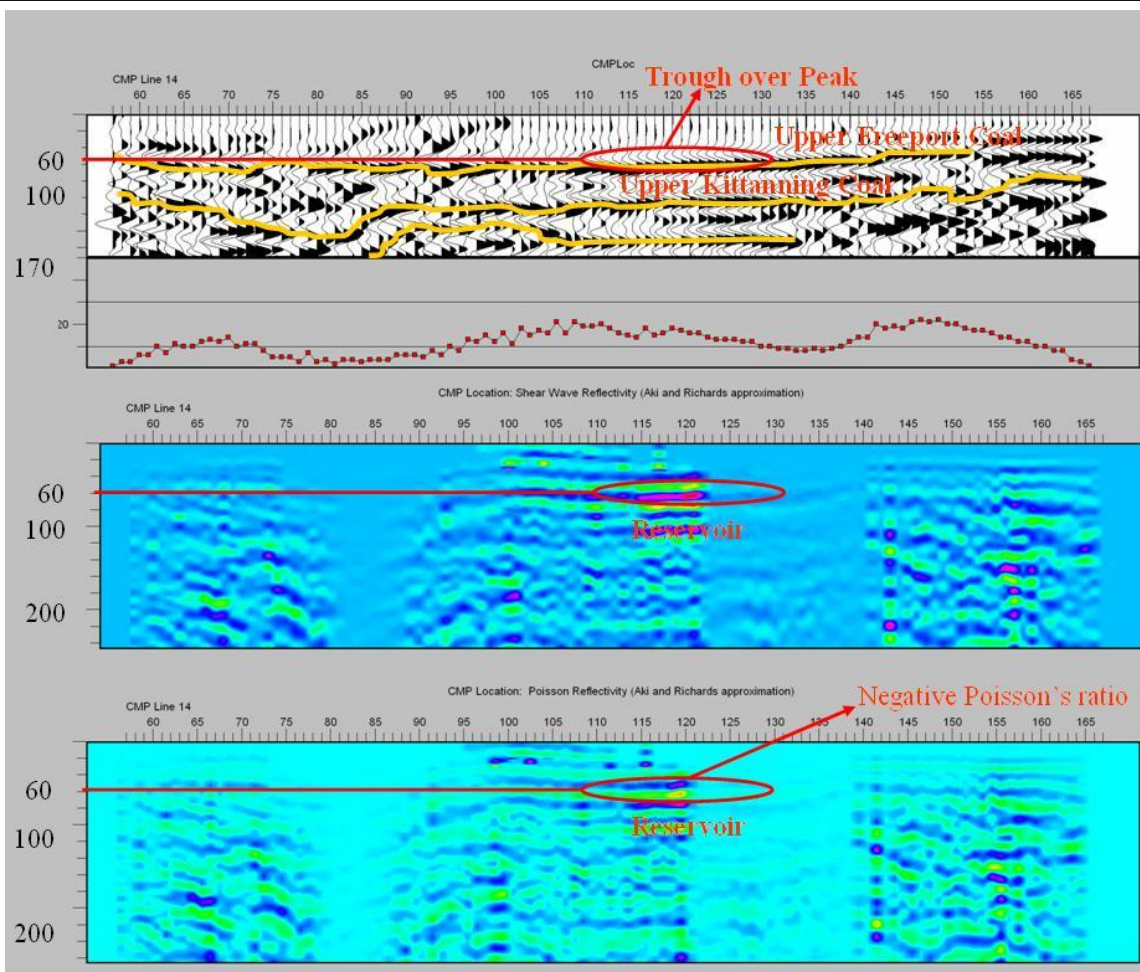
Figure 69. Seismic interpretation of line 14 (shallow reservoir). Enhanced parameter variation is observed between CMP locations 110 to 130.

2.5. DISCUSSION

2.5.1. Hydrologic setting and groundwater table variation effect on CH₄ release

The groundwater table geometry and depth in the study area can be estimated based on the interpretation of the two known apparent resistivity logs as well as on supplementary information acquired by members of EG&G during measurements of gas flow rates from some of the known vents. In Figure 70 resistivity log of well 1 is shown. Our interpretation is that the zone of rapid decrease in apparent resistivity is caused by transition into

Figure 70. Apparent resistivity well log from well 1. Depth is recorded in feet above mean sea level at point of observation.
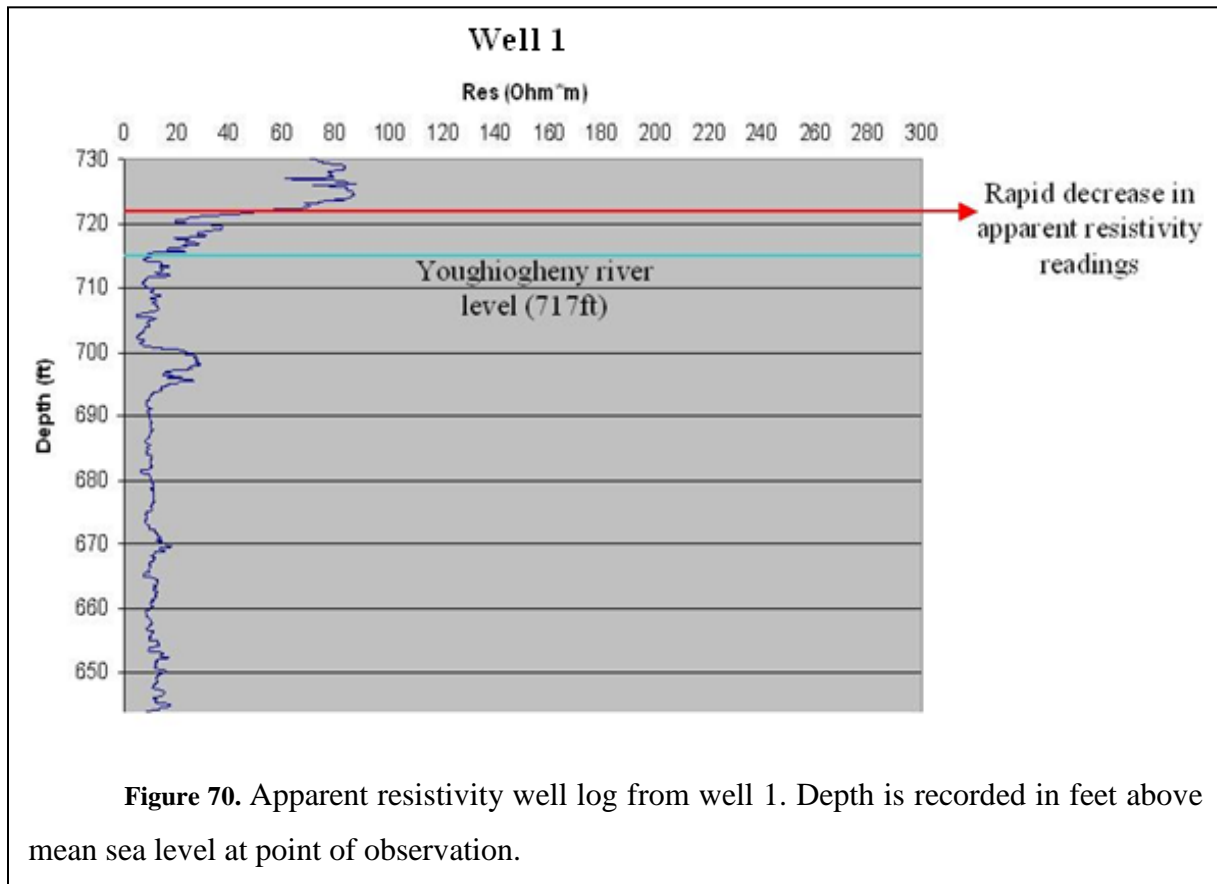
groundwater saturated vadoze zone. In general the total drop of resistivity readings is shown from 100 to 20 Ohm*m, which could be related to elevated or higher dissolved content of salts and minerals in the groundwater (a parameter known to significantly decrease fluid electrical resistivity). Therefore the elevation of groundwater above Youghiogheny river level at this location can be estimated equal to 6 ft (1.83 m).

Figure 71. Apparent resistivity well log at well 2. Depth is recorded in feet above mean sea level at point of observation.
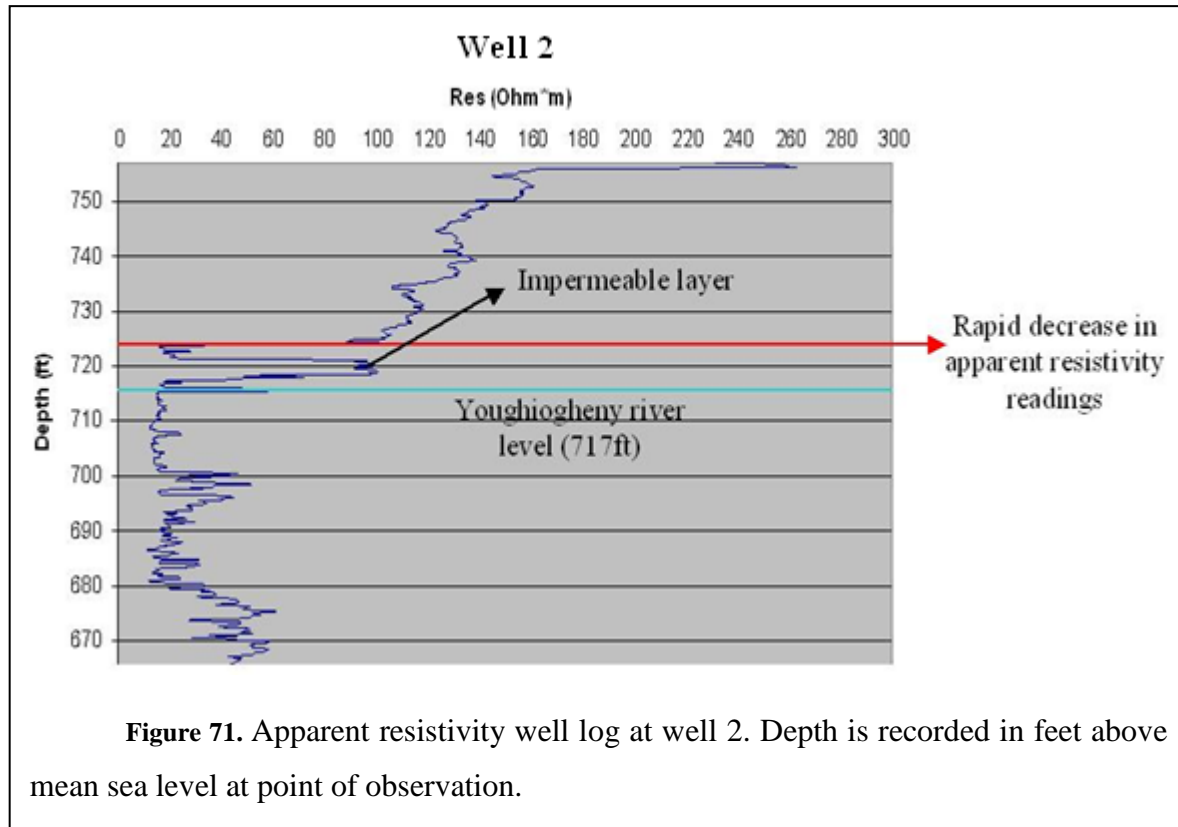
In Figure 71 the same principles have been applied to well 2 in order to estimate the water table location. In some localities local water tables include water that is perched above beds of lower permeability (Stephenson et al, 1981), so in our interpretation the spike in the resistivity data recorded between 718 and 721 ft (218.9 and 219.8 m) above MSL might be caused by presence of impermeable layer (clay or mudstone).

Several pumping tests were performed by EG&G members while examining some vents which were reported to leak CH_4. The idea of the tests was to measure CH_4 flow rate under normal hydrostatic pressure (no drawdown) and then to create an artificial hydrologic drawdown by pumping in order to examine the relationship between groundwater table and

142

CH_4 flow rate. Further a vacuum device operated on methane flowing from well (methane buster) was tested on three producing wells (well 1, well 2 and the closest to well 2 producing well at 4805 2-nd Street). Methane buster is a six-cylinder gasoline engine converted to be operated on CH_4. It is designed to degasify coal seams prior to mining operations. This device requires a minimum of 180 cf/h (cubic feet per hour) of steady CH_4 flow for autonomous functioning and once operational creates a vacuum of 0.8 psi. As no well in the area under study was producing the required amount of methane – the methane buster had to be operated from independent energy source.

The test performed at well 1 showed that a hydrologic drawdown of 150 ft (45.7 m) increased CH_4 production from 6.5 cf/h to 110 cf/h. After that, methane buster was started, which allowed to increase the flow by another 200% according to members of EG&G (Thomas et al, 2007). Although it was impossible to accurately measure the flow rate with methane buster running – it was possible to switch the device from external fuel source to the methane flowing directly from well and keep it running for almost 50 minutes.

During the test performed at well 2, hydrologic drawdown was measured every 30 minutes while groundwater was pumped out of the well at approximate rate of 12 gal/min (0.775 L/sec) (approximate rate provided by Mark Thomas in a telephone conversation). The groundwater table was encountered at the depth of 94 ft (28.66 m). The cumulative methane output prior to pumping test was recorded at 10 cf/h. With the groundwater level retreating 20 ft (6.1 m) downward – CH_4 output was recorded at 50 cf/h. Maximum groundwater drawdown was 80 ft (24.4 m) which resulted in the maximum methane production of 134 cf/h.

The fact that a notable drawdown (23.65 meters) was recorded during the first 150 minutes (2.5 hours) of test indicates that the aquifer subjected to pumping had been unconfined. Furthermore, according to Mark Thomas (Thomas et al, 2007) upon the shut down of water pump while the groundwater level was at its lowest – it was recorded to gain approximately 40 ft (12.2 m) in roughly 2 minutes (Thomas et al, 2007), which suggests that the aquifer although unconfined, vertically heterogeneous in terms of hydraulic conductivity.

The indicated depth of maximum groundwater drawdown approximately corresponds to the top of Mahoning sandstone, while strata 40 ft above this level corresponds to Brush creek marine zone (including: number 2 limestone or shale, number 2 shale, number 1 limestone or shale and number 1 shale, see Table 2 for details) and the basal part of Buffalo member (Buffalo sandstone 2 and Buffalo limestone or shale, see Table 2 for details). Therefore it is fair to conclude that all these units depict high potential for fluid migration, at least in the vicinity of well 2, and therefore could act as a reservoir for natural gas, if capped by an appropriate sealing unit or a lithologic trap.

Along profile 1 shown in Figure 72 the groundwater table is drawn calculated from the interpolation of geophysically derived data without accounting for perched watertable conditions (assuming vertically homogeneous watershed). These calculations allow estimating hydrostatic pressure over the mined coal seam.
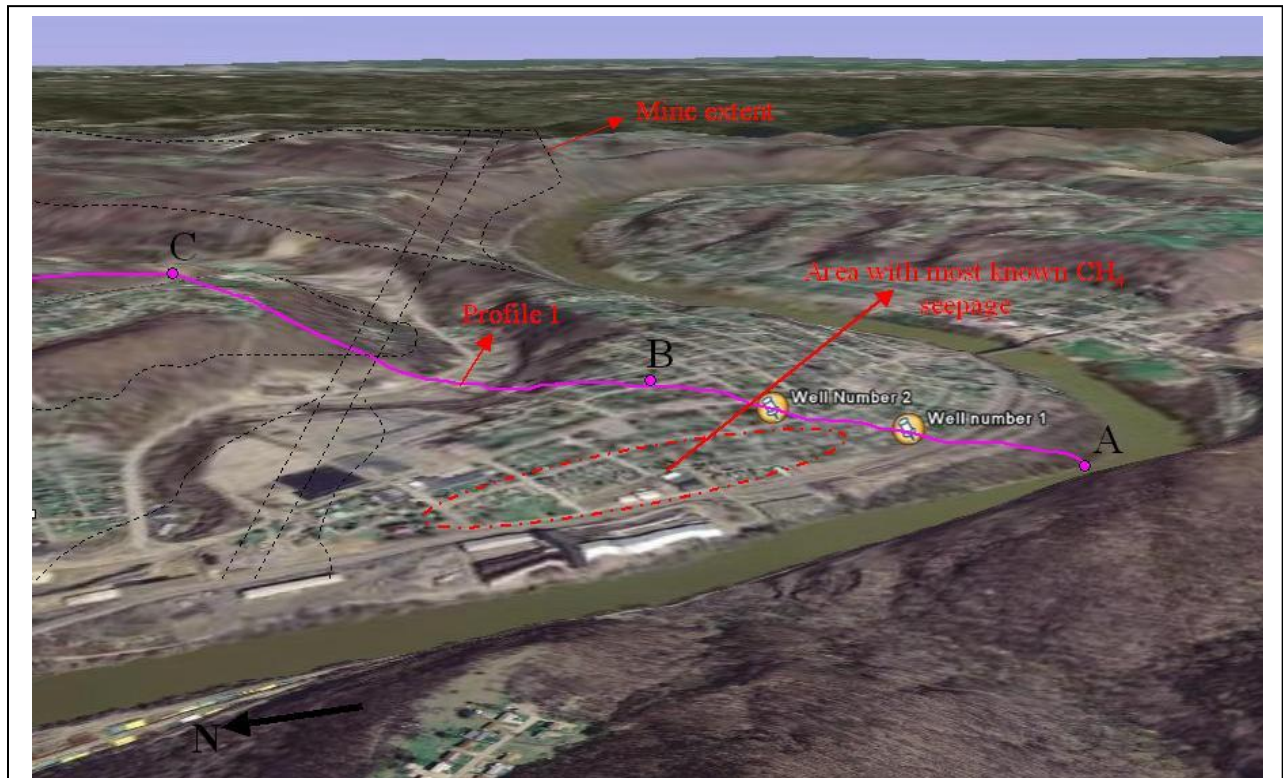
Figure 72. Profile across Versailles, PA: (A): Youghiogheny River level; (B): Top of the first hill; (C): Top of the second hill. Dashed line schematically pictures the extent of existing mine.

To simplify this model we assume a sub-horizontal dip of the Upper Freeport coal throughout the extent of profile 1, Figure 73. In our calculations the minimum thickness of the aquifer above the top of Upper Freeport coal in the area of our study is 107 ft (32.6 m) (underneath the Youghiogheny River) while the maximum is 36.05 meters (underneath point C on profile 1). This means that the hydrostatic pressure confining methane inside the coal seam (without accounting for time-varying atmospheric pressure) ranges from 319.68 Kpa (3.2 Bars) to 353.29 Kpa (3.53 Bars) (or 4.2 and 4.53 bars accounting for the atmospheric pressure respectively).

Figure 73. Cross-section (profile 1). Migration of Coal Bed Methane (CBM) due to lowered hydrostatic pressure caused by groundwater pumping during mining operations.
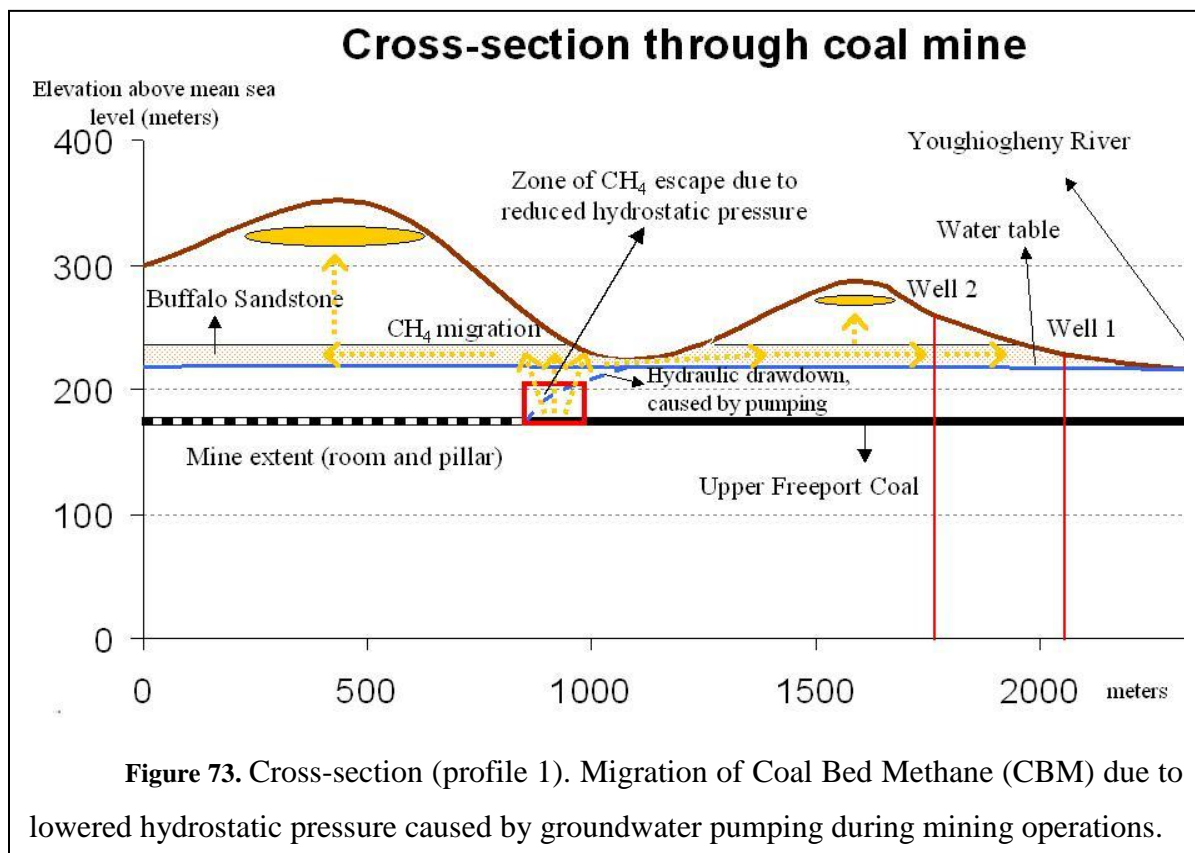
2.5.2. Existence and extent of depressurized zone adjacent to active coal mine

Newman (1972) published a solution for groundwater flow equation assuming that:

- The aquifer is unconfined
- The vadose zone has no influence on the drawdown
- Water initially pumped comes from the instantaneous release of water from elastic storage
- The effects of gravity drainage will be seen if the well is pumped long enough
- The drawdown is negligible compared to the saturated thickness of the aquifer
- The specific yield is at least 10 times the elastic storativity
- The aquifer can be anisotropic having a distinct vertical and horizontal hydraulic conductivity.

In an underground mine encountered groundwater is removed by pumping stations. Groundwater potentiometric surfaces are therefore affected and a cone of hydrologic depression of the water table develops around the mine (Figure 74). The geometry of the cone is a complex function of hydraulic conductivity (k), thickness of the aquifer (b) and pumping ratio (Q). In the case of the Hubbert coalmine the aquifer is considered unconfined and therefore total drawdown can be expressed in form of equation 2.23 (Fetter, 1994).

$$\mathbf{h_0}^2 - \mathbf{h}^2 = \frac{Q}{\pi k} \ln(\frac{r_2}{r_1}) \quad \textbf{(2.23)}$$

Where h_0-h is the drawdown

Q –groundwater discharge rate of the pumping station

k –hydraulic conductivity

r_1 and r_2 are two arbitrary distances from the pumping well (in our case – horizontal distances from a pumping station)
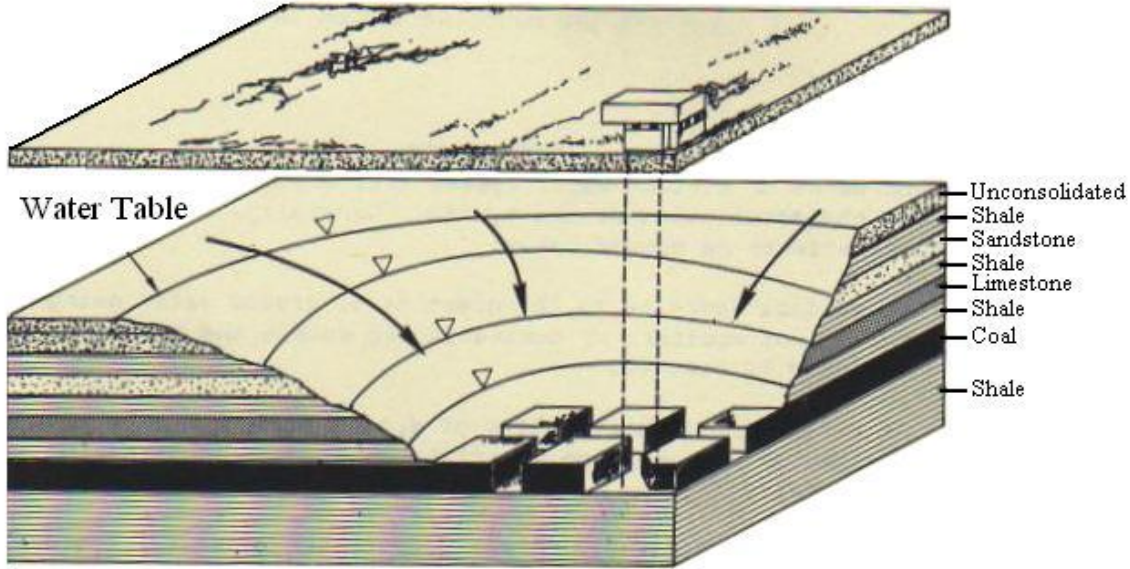
Figure 74. Drawdown of groundwater table due to underground mining operations (Stephenson et al, 1981).

From experiments performed with rocks encountered in the area we estimate that the hydraulic conductivity ranges from $6.42*10^{-5}$ cm/s to $4.95*10^{-7}$ cm/s. The total maximum drawdown can be calculated as maximum depth to Upper Freeport coal from the top of watertable (36.05 m) plus the thickness of Upper Freeport bed (4.88 m), since the groundwater level in the mine had to be at, or more likely below, the base of mined coal bed; therefore $(h_0-h)_{max}$, where h_0 is the base of the coal seam and h is the normal water table prior to pumping, varies from 37.5 m to 40.93 m.

Pumping rates in Hubbert mine are not known to us, however a reasonable range can be estimated to be of the order of 100 gallons per minute (0.00646 m^3/sec). Hydraulic conductivity over the order of 10^{-5} cm/s is considered impermeable (Dwyer, 2000) therefore our calculations are based on maximum measured hydraulic conductivity. Considering these parameters cone of depression created by pumping stations has to be calculated in accordance to equation 2.24, which is derived directly from equation 2.23:

$$r_2 = \frac{r_1}{e^{\frac{\pi k (h_2^2 - h_1^2)}{Q}}} \quad \textbf{(2.24)}$$

Using the values estimated above (r_1 = 1m, Q = 0.00646 m^3/sec, k = 6.42*10^{-7} m/sec, h_1 = 177 m, h_2 = 218 m) and equation 2.24 - the cone of depression of the water table ranges in the order of tens of meters for the abandoned Hubbert mine workings and is equal to exactly 78.5 meters for these specific parameters.

In Figure 72, profile 1 is depicted with the estimated drawdown of the groundwater level caused by a water pump installed to keep the mine working dry. The drawdown in the groundwater surface would have caused a drop in hydrostatic pressure known to seal the cleat system in a coal seam and to trap CH_4 inside. Misbalance in internal pressure of CH_4 inside the cleat systems of Upper Freeport coal versus the confining groundwater pressure could have caused further escape of the gas. Therefore necessary conditions were created for CH_4 to migrate upward in order and restore pressure balance.

The relationship between hydrostatic pressure, the fracture pressure and the lithostatic pressure is fundamental in understanding pore pressures and are shown simply in Figure 75.
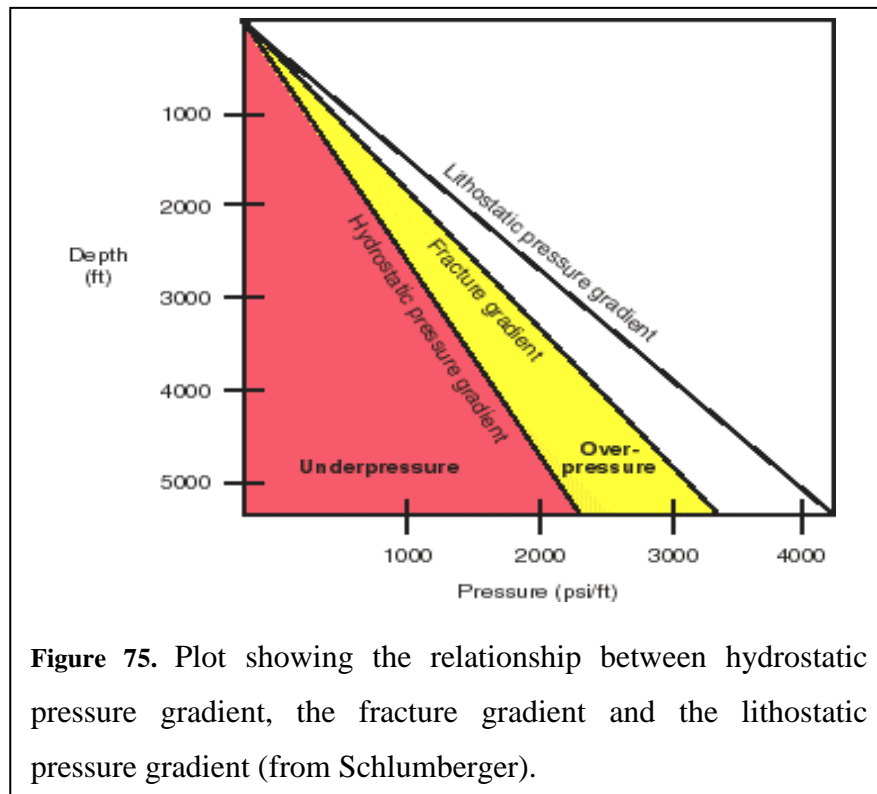
Figure 75. Plot showing the relationship between hydrostatic pressure gradient, the fracture gradient and the lithostatic pressure gradient (from Schlumberger).

Figure 76. Depressurized zone (mine workings limits from the GIS database prepared by Mr. Mark Thomas of EG&G). Note that no known vents are situated directly above the mine workings, however numerous are adjacent to it and located directly in depressurized zone. Those vents localized further south, in the vicinity of the logged wells are in the area of lower GW table, which in accordance with our interpretation, would leave more accommodation space for hydrocarbon accumulation.

149

In coal mine workings it is customary to install ventilation system in order to vent CH_4 out of the mine and prevent it from accumulating anywhere inside the workings, therefore because of venting it is unlikely that CH_4 would have accumulated directly above the mine workings, unless it later has migrated there through permeable bedrock overlaying the mine. This fits the observation that during the active use of the Hubbert mine there were no incidents reported of CH_4 leakage to the surface within the study region.

In Figure 76 a map of estimated depressurized zones around the coalmine is depicted overlain by digital elevation model represented by the transparent color grid. The buffer zone around the mine workings was set to 100 meters, which reasonably corresponds to our interpretation of depressurization extent that was expected from our calculations.

2.5.3. Methane escape mechanism

In our interpretation when the mining operations stopped the pumping stations in the mine were no longer active and the drawdown in local groundwater table eventually disappeared. When groundwater level was restored to its original elevation it trapped some of the earlier released CH_4 inside the adjacent rock units. The unit allowing such CH_4 migration may be Mahoning sands, as well as Brush Creek marine zone. From the field observations we learned about rapid facies variations within Buffalo member and that some of its facies due to their porosity and permeability may allow potential travel of natural gas, while some can restrict this migration. Therefore presence of such lithologic variability may create necessary conditions for lithologic traps in addition to stratigraphic traps. Apparently upward migration is widely available by extensive and dense well system present in the area, therefore in order to restrict the escape – an impermeable layer must cover the surface. In regards to this matter, variation in overlying soil characteristics (Ackenheil, 1968; USDA, 2006), such as clay content, slope angle, consolidation and sorting may be highly significant in focusing the leakage of methane to a particular zone on the surface.

Another scenario of CH_4 escape mechanism can be related to potential surface subsidence due to mining activity extent or due to hydrocarbon extraction from the area in the past.

Among the environmental impacts of coal mining are changes in groundwater table due to subsidence, especially in those areas, where groundwater table is of perched nature (Dittman and Vosen, 1999). Furthermore there is a possibility that subsidence may lead to subsurface shear failure, which will enhance vertical permeability (Lawless et al, 2003). Potentially subsidence within the extent of a coal mine can alter natural routing of groundwater, thus creating zones of excessive hydrostatic pressure as well as depressurized zones. Furthermore, subsidence around coal mine in the area under study if proven would have resulted in establishment of extensive fracture systems adjacent to mine's boundaries. Such fracture system could have become a natural pathway for CH_4 migration and escape. Dittman and Vosen also refer to the fact that formation of subsidence takes 3 to 5 years to complete, which corresponds to the timing of first reported incident of methane leakage in area of interest. However in order to support this theory further detailed retro-dated analysis of surface geometry changes in the area as well as consistent groundwater table monitoring records at dense net of groundwater observation wells are required (Dittman and Vosen, 1999).

However in both cases it is likely that structures controlling CH_4 release to the surface are the soil types (Figure 77). Table 15 provides comprehensive description of soil types where limits of depressurized zone calculated earlier contain either known vents installed for CH_4 ventilation or are penetrated by older wells of initial gas field.

2.5.4. Soils in area under study

Soil types in area under study can be represented by a single soil type, as well as by a combination of up to 3 different soil types. The most important factor contributing to classification of these soils as permeable or impermeable is the hydraulic conductivity. The latter is being classified into 4 groups (Table 15), however according to Code of Federal Regulations for the final cover system, designed to prevent methane leakage from solid landfills (40 CFR 258.60 (a)(1), where methane is constantly being produced by process of biodegradation, a maximum hydraulic conductivity of $1*10^{-5}$ cm/s (0.1 μm/s) is required

for a suitable soil cover (Dwyer, 2000). Therefore any soil type with hydraulic conductivity smaller than indicated is considered impermeable for methane.

Urban land (UB, Figure 77, Table 15) is mainly paved, 6 inch (15 cm) deep layer, very impermeable, except for discontinuities, such as potholes, cracks and engineered openings. USDA is not providing any quantitive interpretation of this coverage type in terms of hydraulic conductivity

In case of URB coverage (Figure 77, Table 15) – the soil is composed of 3 soil types: Urban land, Rainsboro and Wet Spots (USDA, 2006). Urban land comprises up to 85% of total URB coverage. Rainsboro soil is of hydrologic type C (moderately permeable), however at depths from 26 to 60 inches (0.66 m to 1.5 m) becomes virtually impermeable for methane ($5*10^{-5}$ cm/s to $42.3*10^{-5}$ cm/s). This soil type underlays the Urban land and is rarely interrupted by "wet spots", which account for 5% of coverage and show very similar hydrologic coefficients as Rainsboro type, except for they belong to hydrologic type D (Table 15). Overall URB can be considered impermeable and in our view can create potential seal for old wells if sufficient thickness is present. Rainsboro soil type is interpreted as fair final cover for a landfill in terms of permeability (USDA, 2006). URC coverage is very similar to URB coverage, except for Wet Spots are missing out, and substituted by Urban land.

Cover types UCD and UCE both consist of 55% urban land and 45% - of Culleoka soil type and vary only in steepness of the slope (UCD – moderately steep, UCE – steep). Culleoka soil type belongs to hydrologic group B (Table 15) and is recorded to the depth of 31 in (80 cm). Its hydrologic conductivity varies with depth, but reveals a thin impermeable layer approximately 5 cm thick at the very bottom of the layer. According to the USDA classification – Culleoka soil appears to be poor final cover for landfill in terms of methane permeability and layer thickness. Therefore it is most likely that in areas with UCD and UCE coverage methane will be escaping.

GQF coverage is a very steeply dipping 50%/50% complex of Upshur and Gilpin soil type. Gilpin soil forms a 31 in (90 cm) layer of hydrologic type C. The lowest hydraulic permeability is recorded in the lowest part of the layer, which appears to be most consolidated with up to 35% of clay particles. Upshur soil is thicker (1.73 m) and less permeable than Gilpin, but also much consolidated. Upshur belongs to hydrologic class D soil type (Table 15), with the lowest permeability recorded also at the base (lowest 30 cm of the layer). Due to steepness of the slope where GQF coverage occurs – it is very unlikely that any direct infiltration of methane is occurring within the extent of this coverage.

GIC and GID are represented by a single soil type (Gilpin) described above. The difference between coverage types is in the slope angle (8-15% in GIC case and 15 – 25% in GID case). As mentioned earlier, Gilpin soil type belongs to hydrologic category C, which in combination with the slope angle makes it unlikely for methane to seep within the extent of GIC and GID coverage.

Land covers EVC and EVD are comprised by same soil types, including Ernest (hydrologic group C), Vandergrift (group C) and Brinkertorn (Group D) soils. Although percentage of these soil components varies as well as the slope angle – in terms of weighted average hydraulic conductivity both covers show equal values (Table 15). They extend to the depth of 72 in (1.83 m) and each soil type has a fairly thick impermeable layer within its structure: Ernest – 28 – 72 in (0.71 m – 1.83 m); Vandergrift – 8 – 60 in (0.2 m – 1.52 m); Brinkerton – 24 – 60 in (0.6 m – 1.52 m) (USDA, 2006). In our vision, both of these land covers would restrict vertical methane migration if sufficient cover over a leaking well is provided.

To summarize the soil type investigation – it is most likely that CH^4 leakage would be seen within the extent of coverage dominated by Urban land with significant amount of surface disruptions, as well as within the extent of poorly consolidated soil types with low clay content. Slope angle is also seen as a significant factor, therefore Coverages UB, URB and URC are most likely to host leakage, UCD and UCE are also likely, but with slightly

smaller chance of occurrence, while the rest of the land cover types are not seen as suitable for gas infiltration.

Figure 77. Soil map of region under study derived from Ackenheil (1968). For detailed soil type classification refer to Table 15.

In addition it was reported that intensity of CH^4 production from engineered vents depends on precipitation (more CH^4 production is recorded during heavy rain and storm events). This might be due to the fact that wet soils restrict upward migration of fluids and therefore force excessive gas accumulations to exit via ventilation systems.

Therefore up to date there might be very shallow accumulations of CH_4 present in the near surface reservoirs unable to escape because of an impermeable confining soil layer. Such reservoirs would be undetectable using conventional 3D seismic surveying because of their

154

emplacement close to the low velocity zone and significant amount of noise in this range; however very high frequency seismic reflection survey might be capable of their detection.

Some indication of such reservoir presence was acquired from interpretation of shallow marine seismic data, where zones of potential natural gas escape were outlined. This observation was visually confirmed during one of the field trips by noting bubbles of gas uprising from the bottom of Youghiogheny river. The fact that bottom of the river is covered by loose, permeable quaternary alluvium is another argument in support of land cover as a major controlling factor for CH4 release.

Soil name	Soil composition by types	% of volume	Hydraulic group *	Saturated hydraulic conductivity (μm/s)	Weighted hydraulic conductivity (μm/s)	Sand/silt/clay (%)	Moist bulk density (g/cm³)	Weighted average density (g/cm³)	Known old wells	Known vents	Remarks
URB	Urban land	80	N/A	N/A	N/A	N/A	N/A	N/A	Multiple	Multiple	Diverse material, high hydraulic conductivity
	Rainsboro	15	C	0.42 - 42.34		11.4/68.6/20	1.65				Parent material - old alluvium
	Wet spots	5	D	0.42 - 14.11		11.3/67.7/21	1.5				Minor component
URC	Urban land	85	N/A	N/A (Very low)	N/A	N/A	N/A	N/A	Multiple	1	
	Rainsboro	15	C	0.42 - 42.34		11.4/68.6/20	1.65				
UCD/UCE	Urban land	55	N/A	N/A (Very low)	N/A	N/A	N/A	N/A	Multiple	Few	
	Culleoka	45	B	4.23 - 42.34		26.3/52.7/21	1.35				Indurated
UB	Urban land	N/A	N/A	N/A	N/A	N/A	N/A	N/A	Multiple	Multiple	Diverse material, high hydraulic conductivity
GQF	Gilpin	50	C	1.41 - 14.11	4.965	26.3/52.7/21	1.35	1.355	Multiple	None	Very strongly cemented
	Upshur	50	D	0 - 4.34		9/59/32	1.4				Very strongly cemented
GIC/GID	Gilpin	100	C	1.41 - 14.11	7.76	26.3/52.7/21	1.35	1.35	Yes	None	Very strongly cemented
EVC	Ernest	55	C	0.42 - 14.11	7.265	29.1/53.4/17.5	1.45	1.4725	Yes	None	Colluvium derived from acid shale and siltstone
	Vandergrift	35	C	0.42 - 14.11		22.4/55.1/22.5	1.5				Red residuum from calcareous shale, indurated
	Brinkertorn	10	D	0.42 - 14.11		7.2/70.3/22.5	1.5				
EVD	Ernest	65	C	0.42 - 14.11	7.265	29.1/53.4/17.5	1.45	1.4675	Yes	None	
	Vandergrift	25	C	0.42 - 14.11		22.4/55.1/22.5	1.5				
	Brinkertorn	10	D	0.42 - 14.11		7.2/70.3/22.5	1.5				

Table 15. Physical properties of soil types that seal calculated depressurized zone adjacent to mine workings and contain known old wells.

* B. The soils have a moderate infiltration rate when thoroughly wetted. They chiefly are moderately well drained to well drained soils that have moderately fine to moderately coarse textures. They have a moderate rate of water transmission.

C. The soils have a slow infiltration rate when thoroughly wetted. They chiefly have a layer that impedes downward movement of water or have moderately fine to fine texture. They have a slow rate of water transmission.

D. The soils have a very slow infiltration rate when thoroughly wetted. They chiefly consist of clay soils that have a high swelling potential, soils that have a permanent high water table, soils that have a clay pan or clay layer at or near the surface, and shallow soils over nearly impervious material. They have a very slow rate of water transmission.

2.5.4. Conclusions

Combination of geologic and geophysical data sets collected as a part of Versailles project reveal the source of gas as well as its migration routes and extent. 3D seismic survey allowed delineation of potential gas reservoirs in the subsurface. The presence of shallower reservoirs although unproven by 3D seismic data, was predicted by analyzing the hydrology and lithology of the area and found support after interpretation of shallow marine seismic data. Integration of the stratigraphic record with interpretation of downhole geophysics gave an objective understanding of play elements relative to local hydrocarbon distribution and rock tests conducted upon completion of field studies allowed to evaluate hydrologic characteristics of Buffalo member (Conemaugh group) as well as to predict possible gas migration routes.

Several alternative models of CH_4 migration and escape are proposed as a result of collaborative efforts of diverse specialists, however mostly it was agreed that a major factors controlling the escape of gas to the surface are the types of soil cover, presence of known wells facilitating vertical migration of gas and hydrologic properties of rock units adjacent to hydrologically depressurized zone of CH_4 escape. Therefore a composite prognosis map of Versailles was compiled, which includes urbanized zones, where conditions are favorable for CH_4 to be seeping through the surface, creating potentially hazardous situations (**Figure 78**). This prognosis map includes intersection of a 675 meter buffer zone around the Hubbert mine, which was as it is believed responsible for providing necessary conditions with permeable soil types, underlying urban lands with known buildings present within their extent and 50 m buffers around each known well.
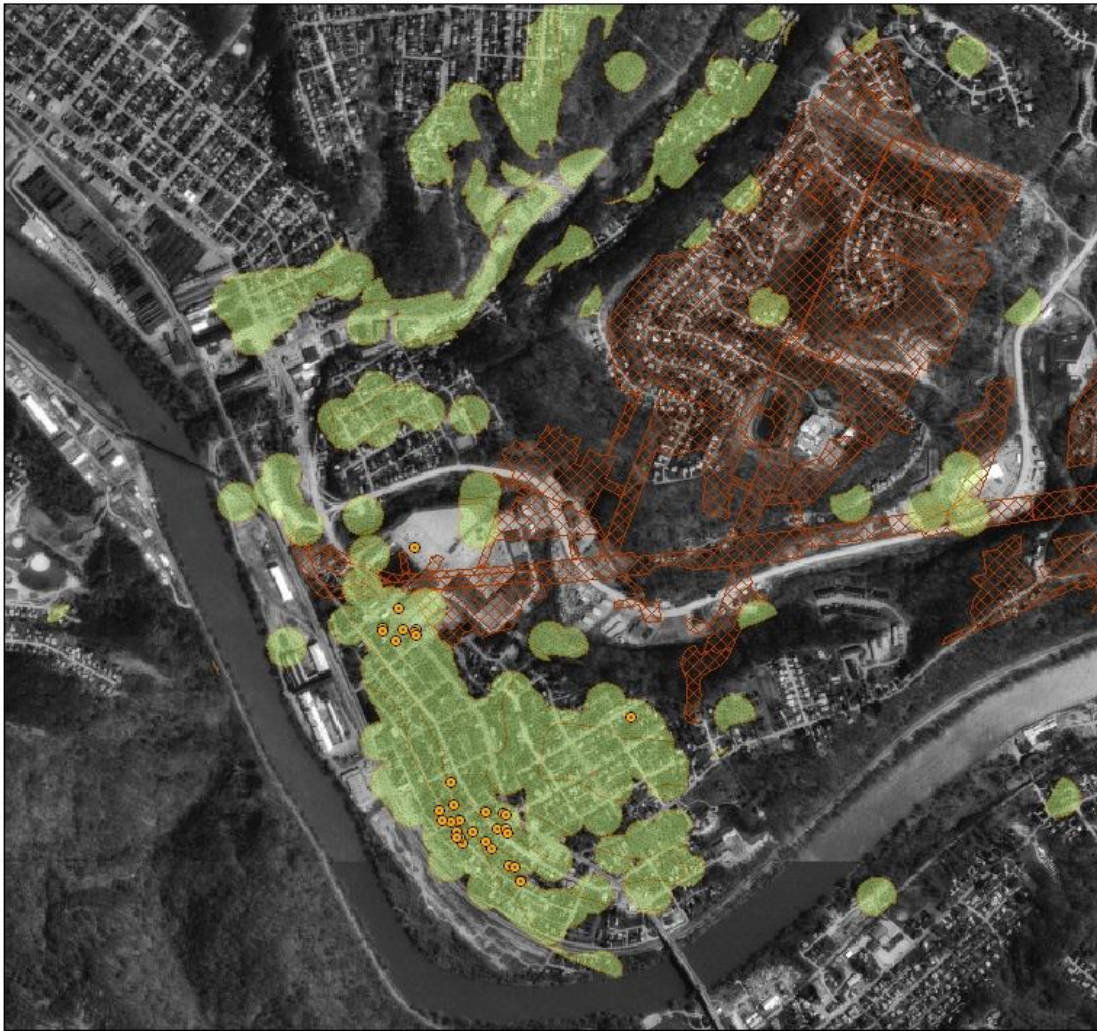
Figure 78. Map of potential hazard extent beyond known incidents (prognosis map). Map is derived from intersecting a 675 m buffer zone around the abandoned mine (equal to the greatest distance from a functioning vent to the nearest mapped mine boundary) with urban zoning, underlain by permeable soil types and with zones which contain known abandoned gas wells of abandoned McKeesport gas field.

158

APPENDIX A "LIST OF 14 COAL SLURRY IMPOUNDMENTS SELECTED BY MSHA FOR GEOPHYSICAL SURVEYING BASED ON THEIR POTENTIAL FOR MALFUNCTION AND HAZARD EXTEND"

County	Impoundment Name	City	Company	MSHA Hazard	WVDEP status
Boone	Pond Fork Slurry Impoundment	Bob White	Jupiter Coal Company	High	Abandoned, modified to slurry cell disposal
Boone	Chess Processing Refuse Disposal Area #1	Sylvester	Elk Run Coal Company	High	On-ground remedial measures completed
Boone	**Jarrels Branch Slurry mpoundment***	Wharton	Eastern Associated Coal Company	Moderate	
Boone	Road Fork Coal Refuse Disposal Facility	Uneeda	Omar mining Company	High	On-ground remedial measures active
Kanawha	Dunn Hollow Coal Refuse Dam	Cannelton	Cannelton Industries	High	
Logan	**Monclo Refuse Dam Impoundment***	Sharples	Hobert Mining	High	
McDowell	Pond #2	Gary	Antaeus Gary Project	Moderate	Abandoned, not impounding
McDowell	Pond #1	Gary	Antaeus Gary Project	Moderate	Abandoned, not impounding
Mercer	Tolliver ranch Coal Refuse Dam	McComas	Consolidation Coal Company	High	Abandonment proceeding
Mercer	Turkey Gap Coal Refuse dam	Dott	Consolidation Coal Company	High	
Mingo	Ben Creek Slurry Impoundment	Wharncliffe	MingoLogan Coal Company	High	
Nicholas	Crooked Run Coal Refuse Dam	Tioga	Gauley Eagle Holdings	High	
Raleigh	**Brushy Fork Slurry Impoundment***	Paxville	Marfork Coal Company	Moderate	
Raleigh	East Gulf Complex Killarney Refuse Area	East Gulf	Left Fork Processing, LLC	High	
Wyoming	Joe Branch Coal Refuse Dam	Itmann	Consolidation Coal Company	High	

* Impoundments selected for additionalfieldstudy.

APPENDIX B "LIST OF COAL SLURRY IMPOUNDMENT FAILURES"

Year	Spill Volume (Gallons)	Company	Town	County	State	River System
1972	132,000,000	Pittston Coal Company	Lorado	Logan	WV	Guyandotte River
1977	2,200,000	Island Creek Coal Company	Bob White	Boone	WV	Lttle Coal River
1980	168,000	Philpot Coal Corp.		Raleigh	WV	
1980	No data	Unknown		Mercer	WV	
1981	No data	Belva Coal Co.	Earling	Logan	WV	Guyandotte
1981	25,000,000	Eastover Mining Company	Ages	Harlan	KY	Cumberland River
1987	7,500,000	Unknown		Floyd	KY	
1987	23,000,000	Peabody Coal Company	Montcoal	Raleigh	WV	Coal River
1988	6,500,000	Tennessee Consolidated Coal Co.	Whitwell	Marion	TN	Tennessee River
1991	10,000,000	Great Western Coal, Inc.	Coalgood	Harlan	KY	Cumberland River
1994	375,000	Consolidation Coal Company	Granville	Monongalia	WV	Monongahela River
1994	112,000,000	Massey Energy Company	Inez	Martin	KY	Big Sandy River
1994	14,000,000	Cumberland Coal Company		Harlan	KY	
1995	No data	Lady H Coal Co.	Green Valley	Nicholas	WV	Gauley River
1995	1,200,000	Consolidation Coal Company	Oakwood	Buchanan	VA	Big Sandy River
1996	1,000,000	Arch Coal, Inc.	St. Charles	Lee	VA	Powell River
1996	6,000,000	Arch Coal, Inc.	St. Charles	Lee	VA	Powell River
1996	4,000,000	Consolidation Coal Company	Oakwood	Buchanan	VA	Big Sandy River
1997	1,000	Ashland Coal	Julian	Boone	WV	Little Coal River
1997	1,000,000	Ashland Coal	Julian	Boone	WV	Little Coal River
1999	No data	Massey Energy Company	Sundial	Raleigh	WV	Coal River

Year	Amount	Company	Town	County	State	River
1999	1,500	Massey Energy Company	Sylvester	Boone	WV	Coal River
1999	2,200	Massey Energy Company	Sylvester	Boone	WV	Coal River
2000	309,000,000	Massey Energy Company	Inez	Martin	KY	Big Sandy River
2001	1,000,000	Premier Elkhorn Coal Co.	Jenkins	Letcher	KY	
2001	30,000	Massey Energy Company	Uneeda	Boone	WV	Little Coal River
2001	No data	Massey Energy Company	Quinland	Boone	WV	Little Coal River
2001	50,000	Massey Energy Company	Dehue	Logan	WV	Guyandotte River
2001	15,000	Massey Energy Company	Madison	Boone	WV	Little Coal River
2001	No data	Massey Energy Company	Quinland	Boone	WV	Little Coal River
2001	No data	Massey Energy Company	South Williamson	Pike	KY	Big Sandy River
2001	4,000	Massey Energy Company	Sidney	Pike	KY	Big Sandy River
2002	No data	Massey Energy Company	Quinland	Boone	WV	Little Coal River
2002	135,000	Massey Energy Company	Sidney	Pike	KY	Big Sandy River
2002	10,000,000	Abandoned Mine Land	Wilcoe	McDowell	WV	Big Sandy River
2002	25,000	Arch Coal	Julian	Boone	WV	Little Coal River
2002	20,000	Massey Energy Company	Delbarton	Mingo	WV	Big Sandy River
2002	100,000	Massey Energy Company	Dehue	Logan	WV	Guyandotte River
2002	No data	James River Coal Company	Slemp	Perry	KY	Kentucky River
2003	1,000	Massey Energy Company	Summersville	Nicholas	WV	Gauley River
2003	No data	Massey Energy Company	Uneeda	Boone	WV	Little Coal River
2003	No data	Abandoned Mine Land	Sprattsville	Mingo	WV	Guyandotte River
2003	20,000	Massey Energy Company	Sidney	Pike	KY	Big Sandy River
2003	27,000	Massey Energy Company	Dehue	Logan	WV	Guyandotte River
2003	No data	Falcon Land Co.	Omar	Logan	WV	Guyandotte River

161

2003	No data	Falcon Land Co.	Omar	Logan	WV	Guyandotte River
2003	No data	James River Coal Company	Slemp	Perry	KY	Kentucky River
2003	250,000	Massey Energy Company	Prenter	Boone	WV	Big Coal River
2003	250,000	Massey Energy Company	Uneeda	Boone	WV	Little Coal River
2003	No data	White Mountain Mining Co.	Rhodell	Raleigh	WV	Guyandotte River
2003	No data	Rapoca Group	Big Rock	Buchanan	VA	Big Sandy River
2003	1,000	Island Creek Coal Co.	Oakwood	Buchanan	VA	Big Sandy River
2004	No data	Massey Energy Company	Dehue	Logan	WV	Guyandotte

APPENDIX C "SHOTPOINT LOCATIONS"

1	1	1965238.6	14643575.7
1	2	1965204.6	14643610.4
1	4	1965186.1	14643637.1
1	5	1965156.0	14643667.8
1	6	1965126.4	14643699.1
1	7	1965099.7	14643728.5
1	8	1965071.3	14643759.0
1	9	1965050.0	14643786.5
1	10	1965020.4	14643819.6
1	11	1964995.0	14643850.7
1	12	1964966.7	14643884.0
1	13	1964945.2	14643912.8
1	14	1964923.8	14643946.4
1	15	1964904.3	14643985.5
1	16	1964888.1	14644019.7
1	17	1964867.5	14644052.5
1	18	1964845.7	14644084.2
1	19	1964824.5	14644118.7
1	20	1964804.0	14644154.3
1	21	1964785.1	14644192.4
1	22	1964766.5	14644228.0
1	23	1964745.0	14644266.5
1	24	1964731.1	14644298.9
1	25	1964713.1	14644335.9
1	26	1964695.7	14644377.2
1	27	1964679.7	14644408.6
1	28	1964667.3	14644444.3

163

1	29	1964652.7	14644479.4
1	30	1964639.0	14644515.5
1	31	1964621.9	14644554.7
2	32	1965346.6	14643682.6
2	33	1965314.8	14643708.2
2	34	1965286.0	14643734.4
2	35	1965255.9	14643759.0
2	36	1965227.1	14643790.2
2	37	1965200.5	14643817.7
2	38	1965176.0	14643848.3
2	39	1965149.2	14643877.0
2	40	1965125.0	14643908.2
2	41	1965097.4	14643937.6
2	42	1965074.2	14643968.0
2	43	1965048.3	14644000.9
2	44	1965025.9	14644032.1
2	45	1965004.0	14644064.7
2	46	1964981.3	14644099.3
2	47	1964960.2	14644132.3
2	48	1964936.6	14644167.2
2	49	1964912.8	14644203.1
2	50	1964892.1	14644239.7
2	51	1964877.3	14644275.5
2	52	1964858.9	14644304.0
2	53	1964842.5	14644339.8
2	54	1964824.5	14644375.0
2	55	1964809.7	14644404.2
2	56	1964789.0	14644450.6
2	57	1964771.0	14644486.4
2	58	1964739.7	14644564.4
2	59	1964723.0	14644602.9
3	60	1965455.7	14643755.4
3	61	1965424.8	14643776.8
3	62	1965395.6	14643808.4
3	63	1965364.4	14643837.3
3	64	1965340.0	14643860.9

3	65	1965308.8	14643893.2
3	66	1965285.8	14643924.9
3	67	1965256.4	14643952.8
3	68	1965229.3	14643981.6
3	69	1965202.9	14644011.9
3	70	1965174.9	14644045.9
3	71	1965153.0	14644073.6
3	72	1965130.3	14644106.7
3	73	1965107.3	14644140.3
3	74	1965082.7	14644171.8
3	75	1965059.4	14644211.9
3	76	1965042.3	14644243.8
3	77	1965021.2	14644280.6
3	78	1965004.0	14644313.0
3	79	1964984.2	14644350.3
3	80	1964968.2	14644388.7
3	81	1964951.0	14644420.4
3	82	1964929.1	14644463.3
3	83	1964915.7	14644501.2
3	84	1964900.6	14644536.4
3	85	1964882.4	14644574.3
3	86	1964864.6	14644607.4
3	87	1964848.4	14644644.8
3	88	1964833.1	14644679.5
3	89	1964812.7	14644714.0
3	90	1964795.2	14644755.1
3	91	1964785.1	14644794.4
3	92	1964771.5	14644826.4
4	93	1965640.1	14643945.8
4	94	1965610.9	14643972.6
4	95	1965578.8	14643997.5
4	96	1965549.9	14644016.9
4	97	1965524.5	14644049.4
4	98	1965489.5	14644070.2
4	99	1965462.4	14644100.3
4	100	1965434.7	14644129.4

4	101	1965409.1	14644160.2
4	102	1965384.5	14644189.2
4	103	1965358.8	14644221.5
4	104	1965335.6	14644253.9
4	105	1965316.5	14644291.3
4	106	1965296.5	14644320.9
4	107	1965274.4	14644360.0
4	108	1965258.0	14644394.3
4	109	1965234.8	14644426.0
4	110	1965208.8	14644455.8
4	111	1965190.8	14644490.2
4	112	1965174.6	14644528.2
4	113	1965158.0	14644563.7
4	114	1965146.3	14644594.7
4	115	1965127.4	14644636.2
4	116	1965114.1	14644672.9
4	117	1965096.0	14644709.5
4	118	1965078.7	14644745.0
4	119	1965064.2	14644781.8
4	120	1965054.9	14644820.5
4	121	1965041.0	14644855.7
4	122	1965023.1	14644893.1
4	123	1965005.5	14644932.0
4	124	1964983.6	14644969.5
4	125	1964964.1	14645005.0

APPENDIX D "VELOCITY ANALYSIS DATA"

Abbreviations
UFSS - Upper Freeport Sandstone
LFC - Lower Freeport Coal
UKC - Lower Kittanning Coal
MKC - Middle Kittanning Coal
LKC - Lower Kittanning Coal
SS - sandstone
LS - Limestone
Sh - shale
R1 - Reflector 1 (see CMP line 9)
R2 - Reflector 2 (see CMP line 9)
R3 - Reflector 3 (See CMP line 9)
R4 - Reflector 4 (see CMP line 9)
R5 - Reflector 5 (see CMP line 9)
R6 - Reflector 6 (see CMP line 9)

2 way travel time, ms	Depth, meters	Depth, feet	Name	Reflector
1	0.455	1.4924	LVZ	
2	0.91	2.9848		
3	1.365	4.4772		
4	1.82	5.9696		
5	2.275	7.462		
6	2.73	8.9544		
7	3.185	10.4468		
8	3.64	11.9392		
9	4.095	13.4316		
10	4.55	14.924		
11	5.005	16.4164		
12	6.045	19.8276	BSS	
13	7.59	24.8952		
14	9.135	29.9628		
15	10.68	35.0304		
16	12.225	40.098		
17	13.77	45.1656		
18	15.315	50.2332		
19	16.07	52.7096	Coal	
20	16.825	55.186		
21	17.58	57.6624		
22	19.065	62.5332	LS	
23	20.55	67.404		
24	22.095	72.4716	SS	
25	23.64	77.5392		
26	25.4125	83.353	Shale	
27	26.1675	85.8294	BCC	R1
28	27.6525	90.7002	LS	
29	29.1375	95.571		
30	30.6225	100.4418		
31	32.1075	105.3126		
32	33.5925	110.1834		
33	35.0775	115.0542		
34	36.5625	119.925		
35	38.0475	124.7958		

36	39.5325	129.6666		
37	41.0775	134.7342	MSS	
38	42.6225	139.8018		
39	44.1675	144.8694		
40	45.7125	149.937		
41	47.2575	155.0046		
42	49.03	160.8184	Sh	
43	50.8025	166.6322		
44	51.653	169.4218	UFC	R2
45	52.423	171.9474		
46	53.193	174.473		
47	53.963	176.9986		
48	54.733	179.5242		
49	55.503	182.0498		
50	56.273	184.5754		
51	57.043	187.101		
52	58.243	191.037	UFLS	
53	59.443	194.973		
54	60.643	198.909		
55	61.843	202.845		
56	63.043	206.781		
57	64.243	210.717		
58	65.443	214.653		
59	66.643	218.589		
60	67.843	222.525		
61	68.613	225.0506	UFSS	
62	69.383	227.5762		
63	70.153	230.1018		
64	70.923	232.6274		
65	71.633	234.9562	LFC	
66	72.343	237.285		
67	73.053	239.6138		
68	75.003	246.0098	LS (shaly)	
69	76.953	252.4058		
70	79.053	259.2938	SS	
71	80.678	264.6238	LS (shaly)	

72	82.303	269.9538		
73	83.928	275.2838		
74	85.553	280.6138		
75	87.178	285.9438		
76	88.803	291.2738		
77	89.893	294.849	SS	
78	91.833	301.2122	LS (shaly)	
79	93.773	307.5754		
80	95.713	313.9386		
81	96.718	317.235	Sh	
82	97.723	320.5314		
83	98.423	322.8274	LS (shaly)	
84	99.123	325.1234		
85	99.823	327.4194		
86	100.523	329.7154		
87	101.223	332.0114		
88	101.923	334.3074		
89	102.623	336.6034		
90	103.323	338.8994		
91	104.068	341.343	UKC	R3
92	104.813	343.7866		
93	105.558	346.2302		
94	106.303	348.6738		
95	107.798	353.5774	LS	
96	109.293	358.481		
97	110.788	363.3846		
98	112.283	368.2882		
99	113.778	373.1918		
100	114.813	376.5866	SS	
101	115.848	379.9814		
102	116.883	383.3762		
103	117.918	386.771		
104	118.953	390.1658		
105	119.988	393.5606		
106	121.023	396.9554		
107	122.058	400.3502		

108	123.093	403.745		
109	124.128	407.1398		
110	125.163	410.5346		R4
111	126.198	413.9294		
112	127.233	417.3242		
113	127.983	419.7842	MKC	
114	128.733	422.2442		
115	129.483	424.7042		
116	131.478	431.2478	Sh	
117	133.473	437.7914		
118	135.853	445.5978	SS	
119	138.663	454.8146		
120	140.068	459.423		
121	141.473	464.0314	Sh	
122	142.878	468.6398		
123	144.283	473.2482	SS	
124	145.688	477.8566		
125	147.093	482.465		
126	148.498	487.0734		
127	149.903	491.6818		
128	151.308	496.2902		
129	152.713	500.8986		
130	154.118	505.507		
131	155.523	510.1154		
132	156.928	514.7238		
133	158.333	519.3322		
134	159.738	523.9406		
135	161.143	528.549		
136	162.548	533.1574		
137	163.953	537.7658		
138	165.358	542.3742		
139	166.763	546.9826		
140	168.168	551.591		
141	169.573	556.1994		
142	170.978	560.8078		
143	172.383	565.4162		

144	173.788	570.0246		
145	175.193	574.633		
146	176.598	579.2414		
147	178.003	583.8498		
148	179.408	588.4582		
149	180.813	593.0666		R5
150	182.218	597.675		
151	183.623	602.2834		
152	185.028	606.8918		
153	186.433	611.5002		
154	187.838	616.1086		
155	189.243	620.717		
156	190.648	625.3254		
157	192.053	629.9338		
158	193.458	634.5422		
159	194.863	639.1506		
160	196.268	643.759		
161	197.673	648.3674		
162	199.078	652.9758		
163	200.483	657.5842		
164	201.888	662.1926		
165	203.293	666.801		
166	204.698	671.4094		
167	206.103	676.0178		
168	207.508	680.6262		
169	208.913	685.2346		
170	210.318	689.843		
171	211.723	694.4514		
172	213.128	699.0598		
173	214.533	703.6682		
174	215.938	708.2766		
175	217.343	712.885		
176	218.748	717.4934		R6
177	220.153	722.1018		
178	221.558	726.7102		
179	222.963	731.3186		

180	224.368	735.927		
181	225.773	740.5354		
182	227.178	745.1438		
183	228.583	749.7522		
184	229.988	754.3606		
185	231.393	758.969		
186	232.798	763.5774		
187	234.203	768.1858		
188	235.608	772.7942		
189	237.013	777.4026		
190	238.418	782.011		
191	239.823	786.6194		
192	241.228	791.2278		
193	242.633	795.8362		
194	244.038	800.4446		
195	245.443	805.053		
196	246.848	809.6614		
197	248.253	814.2698		
198	249.658	818.8782		
199	251.063	823.4866		
200	252.468	828.095		
201	253.873	832.7034		
202	255.278	837.3118		
203	256.683	841.9202		
204	258.088	846.5286		
205	259.493	851.137		
206	260.898	855.7454		
207	262.303	860.3538		
208	263.708	864.9622		
209	265.113	869.5706		
210	266.518	874.179		
211	267.923	878.7874		
212	269.328	883.3958		
213	270.733	888.0042		
214	272.138	892.6126		
215	273.543	897.221		

216	274.948	901.8294		
217	276.353	906.4378		
218	277.758	911.0462		
219	279.163	915.6546		
220	280.568	920.263		
221	281.973	924.8714		
222	283.378	929.4798		
223	284.783	934.0882		
224	286.188	938.6966		
225	287.593	943.305		
226	288.998	947.9134		
227	290.403	952.5218		
228	291.808	957.1302		
229	293.213	961.7386		
230	294.618	966.347		
231	296.023	970.9554		
232	297.428	975.5638		
233	298.833	980.1722		
234	300.238	984.7806		
235	301.643	989.389		
236	303.048	993.9974		
237	304.453	998.6058		
238	305.858	1003.214		
239	307.263	1007.823		
240	308.668	1012.431		
241	310.073	1017.039		
242	311.478	1021.648		
243	312.883	1026.256		
244	314.288	1030.865		
245	315.693	1035.473		
246	317.098	1040.081		
247	318.503	1044.69		
248	319.908	1049.298		
249	321.313	1053.907		
250	322.718	1058.515		
251	324.123	1063.123		

252	325.528	1067.732		
253	326.933	1072.34		
254	328.338	1076.949		
255	329.743	1081.557		
256	331.148	1086.165		
257	332.553	1090.774		
258	333.958	1095.382		
259	335.363	1099.991		
260	336.768	1104.599		
261	338.173	1109.207		
262	339.578	1113.816		
263	340.983	1118.424		
264	342.388	1123.033		
265	343.793	1127.641		
266	345.198	1132.249		
267	346.603	1136.858		
268	348.008	1141.466		
269	349.413	1146.075		
270	350.818	1150.683		
271	352.223	1155.291		
272	353.628	1159.9		
273	355.033	1164.508		
274	356.438	1169.117		
275	357.843	1173.725		
276	359.248	1178.333		
277	360.653	1182.942		
278	362.058	1187.55		
279	363.463	1192.159		
280	364.868	1196.767		
281	366.273	1201.375		
282	367.678	1205.984		
283	369.083	1210.592		
284	370.488	1215.201		
285	371.893	1219.809		
286	373.298	1224.417		
287	374.703	1229.026		

288	376.108	1233.634		
289	377.513	1238.243		
290	378.918	1242.851		
291	380.323	1247.459		
292	381.728	1252.068		
293	383.133	1256.676		
294	384.538	1261.285		
295	385.943	1265.893		
296	387.348	1270.501		
297	388.753	1275.11		
298	390.158	1279.718		
299	391.563	1284.327		
300	392.968	1288.935		

BIBLIOGRAPHY

2001, EM Flow electromagnetic data display, analysis and interpretation, Encom Technology Pty Ltd.

Ackenheil, A.C., 1968, Mining and Physiographic study of Allegheny County, PA: Pittsburgh, prepared for the board of County commissioners.

AGI, 2005, EarthImager 2D: Austin, TX, AGI.

Aki, K., Richards, P.G., 1979, Quantities Seismology Theory and Methods: San Francisco, 932 p.

Al-Fouzan, F., Harbert, W., Dilmore, R., Hammack, R., Veloski, G., and Ackman, T., 2004, Methods for Removing Signal Noise from Helicopter Electromagnetic Survey Data, Mine Water and the Environment, v. 23, p. 28-33.

Allison, M.L., 2001, Geology of Natural Gas Pathways and Accumulations under Hutchinson, Kansas: Topeka, Kansas House Utilities Committee.

Avdeev, D.V., 2005, Three-dimensional electromagnetic modeling and inversion from theory to application: Surveys in Geophysics, v. 26, p. 767-799.

Bond, L.O., ALger, R.P., Schmidt, A.W., 1969, Well Log Applications in Coal Mining and Rock Mechanics, Annual AIME meeting: Washington, DC, Society of Mining Engineers.

Bruner, K.R., Oldham, A. V., Repine, T. E., Markowski, A. K., Harper, J. A., 1998, Geological aspects of coal bed methane in the northern Appalachian coal basin, southwestern Pennsylvania and north-central West Virginia, Gas Research Institute, p. 72.

Buttkus, B., 2000, Spectral Analysis and Filter Theory in Applied Geophysics Springer, 667 p.

Cernica, J.N., 1995, Soil Mechanics: New York, Department of Civil Engineering, Youngstown State University.

Christensen, N.B., 2002, A generic 1-D imaging method for transient electromagnetic data: Geophysics, v. 67, p. 438 - 447.

Campbell, T., Nicolaides, R.A., Salas, M. D. , 1997, Computational Electromagnetics and Its Applications: University of Michigan, Kluwer Academic Publisher, p. 315.

Carter, K.M., 2007, Subsurface rock correlation diagram, oil and gas producing regions of Pennsylvania, 4-th series, Pennsylvania Geological Survey.

Claerbout, J.F., Dohrety, S.M., 1985, Downward continuation of moveout-corrected seismograms, in Gardner, G. H. F., Ed., Migration of seismic data: Geophysics, v. 37, p. 741 - 768.

Constable, S.C., Parker, R.L., Constable C.G., 1987, Occam's inversion: A practical algorithm for generating smooth models from electromagnetic sounding data: : Geophysics, v. 52, p. 289 - 300.

Cooper, B.N., 1944, Geology and Mineral resources of the Burkes Garden quadrangle, Virginia: Virginia Geological Survey Bulletin v. 60.

Cordsen, A., Galbraith, M., Pierce, J., 2000, Planning Land 3-D Seismic Surveys, Geophysical Developments, Society of Exploration Geophysicists: p. 214.

Cox, L.H., Zhdanov, M.S., 2007, Advanced Computational Methods of Rapid and Rigorous 3-D Inversion of Airborne Electromagnetic Data: Communications in computational physics, v. 3, p. 160 - 179.

Davies, W.E., Bailey, J.F., and Kelly, D.B., 1972, West Virginia's Buffalo Creek flood - a study of the hydrology and engineering geology: U.S. Geological Survey Circular, v. 667.

Dittman, C., Vosen, P., 1999, Test Site Report for the "Kirchheller Heide" Area at Bottrop, Germany for the EU-Project MINEO, EU-Project MINEO.

Dmitriev, V.I., 1969, Electromagnetic Fields in Inhomogeneous Media: Moscow, Moscow State University.

Dobrin, M.B., 1976, Introduction to Geophysical Prospecting: New York, McGraw-Hill.

Donaldson, A.C., Eble, C., 1991, Pennsylvanian coals of central and eastern United states, *in* Gluskoter, H.J., Rice, D.D and Taylor, R.B.,ed., The Geology of North America: Boulder, CO, USGS, p. 523 - 545.

Dwyer, S.F., 2000, Landfill Covers: Is it Time to Change Current Regulations, Sandia Report: Albouquerque, NM, Sandia National Laboratories, p. 19.

Edmunds, W.E., Skema, V. W. Flint, N. K., 1999, The geology of Pennsylvania Special Publication - Geological Survey of Pennsylvania.

Englund, K.J., Arndt, H.H., Henry T.W., 1979, Proposed Pennsylvanian System Stratotype, Virginia and West Virginia, Ninth International Congress of Carboniferous Stratigraphy and Geology meeting: Washington, D.C., American Geological Institute, p. 136.

Farquharson, C.G., Oldenburg D.W., 1998, Nonlinear inversion using general measures of data

misfit and model structure: Geophysical Journal, v. 134, p. 213-227.

Farquharson, C.G., Oldenburg, D. W., 2004, A Comparison of Automatic Techniques for Estimating the Regularization Parameter in Non-Linear Inverse Problems: Geophysics, v 69, p. 411-425.

Fedorko, N., Blake, M., 1998, A Geologic Overview of Mountaintop Removal Mining in West Virginia, West Virginia Geological and Economic Survey.

Fitterman, D.V., Deszcz-Pan, M., 1998, 1998, Helicopter EM mapping of saltwater intrusion in Everglades National Park, Florida: Exploration Geophysics, v. 29, p. 240 - 243.

Fraser, D.C., 1976, Resistivity Mapping with Airborne Multicoil Electromagnetic System: Geophysics, v. 41, p. 62 - 78.

Fraser, D.C., 1978, Resistivity mapping with an airborne multicoil electromagnetic system: Geophysics, v. 43, p. 114-172.

Fraser, D.C., 1979, The Multicoil II Airborne Electromagnetic System: Geophysics, v. 44, #8, p. 1367-1394.

Fugro Airborne Surveys, 2002, Logistics report helicopter-borne resolve electromagnetic and magnetic geophysical survey Kettle Creek, Pennsylvania, Mississauga, ON.

Gassmann, F., 1951, Elastic waves through a packing of spheres: Geophysics, v. 16, p. 673-685.

GeoQuest, I., 1981, Applied Seismic Stratigraphic Interpretation manual: Houston, TX, p. 416-417.

Gordon-Mackenzie, J., and Henry, T.W, 1990, Marginovatia, a mid-Carboniferous genus of linoproductid brachiopods: Journal of Palaeontology, v. 64, p. 532-551.

180

Griffith, D., 1999, Introduction to Electrodynamics, Prentice-Hall, p. 576.

Gupta, R.P., Singhal, B.S., 1999, Applied Hydrology of Fractured Rocks, Springer.

Haber, E., Ascher, U., Oldenburg, D.W., 2004, Inversion of 3D electromagnetic data in frequency and time using an inexact all-at-once approach: Geophysics, v. 69, p. 1216 - 1228.

Haber, E., 2005, Quasi–Newton Methods for Large-Scale Electromagnetic Inverse Problems: Inverse Problem, v. 21, p. 305-323.

Halliday, D., 1960, Physics Part II: New York, John Wiley and Sons, p. 925.

Hammack, R.W., and Mabie, J.S., 2002, Airborne EM and magnetic surveys find fault(s) with Sulphur Bank mercury mine Superfund site: The Leading Edge, v. 21.

Hammack, R., Kaminskiy V., Harbert, W., Lipinski, B., Sams, J., Veloski, G., Ackman, T., 2007, Using Airborne Electromagnetic Surveys to identify potential hazards at coal waste impoundments. Examples from West Virginia (currently in review).

Harper, J.A., Laughrey, 1987, Geology of the oil and gas fields of southwestern Pennsylvania, Pennsylvania Bureau of Topographic and Geologic Survey, Mineral Resources, p. 166.

Harper, J.A., 1989, J.A. Upper Devonian and Lower Mississippian stratigraphy and depositional systems, in Geology in the Laurel Highlands of Southwestern Pennsylvania, 54th Annual Field Conference of Pennsylvania Geologists, p. 191 - 202.

Hatcher, R.D., Jr.,, 1989, Tectonic synthesis of the U.S. Appalachians: Geological Society of America, v. F-2, p. 511 - 535.

Hennen, R.V., Gawthrop, R.M., 1915, Geology of Wyoming and McDowell Counties, West Virginia Geological Survey County Report, p. 783.

Henry, T.W.G., M., Jr, 1979, Late Devonian through Early Permian invertebrate faunas in proposed Pennsylvanian system stratotype area, Guidebook series, Volume 1, p. 97 - 104.

Hohmann, G.W., 1975, Three-Dimensional Induced-Polarization and Electromagnetic Modeling: Geophysics, v. 40, p. 309 - 324.

Huang, Y.H., 1983, Stability Analysis of Earth Slopes: New York, Van Nostrand Reinhold, 305 p.

Huang, H., Palacky, G.H., 1991, Damped least-squares inversion of time domain airborne EM data based on singular value decomposition: Geophysical prospecting, v. 39, p. 827 - 844.

ICOLD, 2001, Tailings Dams - Risk of Dangerous Occurrences - Lessons Learnt from Practical Experiences: Paris, International Commission of Large Dams; Committee on Tailings Dams and Waste Lagoons, p. 144.

Johnson, M.E., 1929, Topographic and geologic atlas of Pennsylvania: Pittsburgh, Pennsylvania Geological survey.

Jones, C.E., 2005, History of the Earth Lecture Notes, *in* Kaminski, V., ed.: Pittsburgh, PA, University of Pittsburgh.

Kaminski, V., Hammack, R., Harbert, W., Ackman, T., 2006, Using Geophysical Methods to Identify Potential Hazards in Coal Waste Impoundments, Society of Mining Engineers (SME), v. 3: St. Louis, MO.

Kant, S., 2004, Seismic Signal Processing with special reference to anisotropy. , Springer, 636 p.

182

Laughrey, C.D., Baldassare, F.J., 1998, Geochemistry and origin of some natural gases in the Plateau Province, central Appalachian basin, Pennsylvania and Ohio: American Association of Petroleum Geologists Bulletin, v. 82, p. 317-335.

Lawless, J., Okada, W., Terzaghi, S. White, P., Gilbert, C., 2003, Two dimensional subsidence modelling at Wairakei - Tauhara, New Zealand, International Geothermal conference, session 12: Reykjavik.

Lide, 1991, CRC Handbook of Chemistry and Physics: Boca Raton, FL, CRC Press.

Liner, C.L., 2004, Elements of 3D seismology, PennWell Books, p. 608.

Liu, G., Becker, A., 1990, Two-dimentional mapping of sea ice keels with airborne electromagnetics: Geophysics, v. 55, p. 239 - 248.

Lyahov, J.C., Ettensohn F.R. , 1995, Reevaluation of the Bedford-Berea sequence in Ohio and adjacent states: forced regression in a foreland basin, Special paper, GSA, p. 68.

Macnae, J.C., Smith, R., Polzer, B.D., Lamontagne, Y., Klinkert, P.S., 1991, Conductivity-depth imaging of airborne electromagnetic step-response data: Geophysics, v. 56, p. 102 - 114.

Martino, R.L., 1996, Stratigraphy and depositional environments of the Kanawha formation (Middle Pennsylvanian) southern West Virginia: Huntington, W.V., Department of Geology, Marshal University.

Mavko, G., Mukerji, T., Dvorkin, J., 1998, The Rock Physics Handbook: Cambrige, UK, Cambrige University Press, p. 339.

Maxwell, J.C., 1861, On Physical Lines of Force: Philosophical Magazine and Journal of Science, v. 4.

Mayne, W.H., 1962, Common reflection point horizontal data stacking techniques: Journal of Geophysics, v. 27, p. 927-938.

McDaniel, B.A., 2006, Subsurface stratigraphy and depositional controls on late Devonian - early Mississipean sediments in Southwestern Pennsylvania: Morgantown, WV, West Virginia University.

McNeill, J.D., 1980, Electromagnetic Terrain Conductivity Measurement at Low Induction Numbers, technical note TN-6: Mississauga, ON, Geonics, Ltd.

MSHA, M.S.a.H.A., 1974, Design guidelines for Coal Refuse Piles and Water, Sediment or Slurry Impoundments and Impounding Structures, Informational report, U.S. Department of Labour.

Mundry, E., 1984, On the interpretation of airborne electromagnetic data for the two-layer case: Geophysical prospecting, v. 32, p. 336-346.

Newman, S.P., 1972, Theory of flow in unconfined aquifers considering delayed response of the water table: Water Resources Research v. 8, p. 1031-1045.

Nissen, S.E., Watney, W., Xia, J., 2003, Natural Gas Explosions in Hutchinson, Kansas: Detecting Gas with High-Resolution Seismic Data (abs): GSA Abstracts with Programs, v. 35.

NRC, National Research Counsil, 2002, Coal Waste Impoundments Risks, Responses, and Alternatives: Washington, DC, National Academy Press, p. 248.

Ostrander, W.J., 1984, Plane-wave reflection coefficients for gas sands at non-normal angles of incidence: Geophysics, v. 49, p. 1637-1648.

Pabitra, N.S., Goode, P.A., 1992, Influence of temperature on electrical conductivity on shaly

sands: Geophysics, v. 57, p. 89-96.

Paine, J., 2003, Determining salinization extent, identifying salinity sources, and estimating chloride mass using surface, borehole, and airborne electromagnetic induction methods: Water Resource Research, v. 39.

Peng S., C.H., Yang R., Gao Y., Chen X., 2006, Factors facilitating or limiting the use of AVO for coal-bed methane. Geophysics, v. 71, # 4, p. C49 - C56.

Pennsylvania Bureau of Topographic and Geologic Survey, D.o.C.a.N.R., 2001, Bedrock Geology of Pennsylvania Harrisburgh, PA, Pennsylvania Bureau of Topographic and Geologic Survey.

Polzer, B.D., 1985, The interpretation of inductive transient magnetic sounding data: Research in Applied Geophysics, University of Toronto, v. 36.

Prothero, D.R., Dott R. H., 2002, Evolution of the Earth: Boston, McGraw Hill, p. 672.

Puglio, D.G., Innacchione, A. T., 1979, Geology, mining, and methane content of the Freeport and Kittanning coalbeds in Indiana and surrounding counties, Pennsylvania, Report of Investigations U.S. Bureau of Mines p. 35.

Raiche, A., 1974, An Integral Equation Approach to Three-Dimensional Modeling: Geophysics, v. 36, p. 363–376.

Reeves, T.K.S., B., Banerjee, S., Guo, G., Volk, L., Djikine, D., George, S., 1999, An exploration3D seismic field test program in Osage county, Oklahoma: Bartlesville, OK.

Reid, J.E., Pfaffling, A., Vrbancich, J., 2006, Airborne electromagnetic footprints in 1D earths: Geophysics, v. 71, p. G63 - G72.

Reger, D.B., 1926, Mercer, Monroe and Summers Counties, County report, West Virginia Geological Survey p. 963.

Reynolds, J.M., 1997, Introduction to Applied and Environmental Geophysics: New York, John Wiley and Sons, p. 796.

Riley, W.F., Sturges, L.D., Morris, D.H., 2007, Mechanics of Materials: New York, John Wiley and Sons, 711 p.

Ruppert, L.F., Tewalt, S.L., Wallack, R.N., Bragg, L.J., Brezinski, D.K., Carlton, R.W., Butler, D.T., Calef, F.J. III, 2001, A Digital Resource Model of the Middle Pennsylvanian Upper Freeport Coal Bed, Allegheny Group, Northern Appalachian Basin Coal Region, U.S.A.: 2000 Resource Assessment of Selected Coal Beds and Zones in the Northern and Central Appalachian Basin Coal Regions, by Northern and Central Appalachian Basin Coal Regions Assessment Team, p. D1-D97 [CD-ROM].

Rutherford, S.R., Williams, R.H., 1989, Amplitude-versus-offset variations in gas sands: Geophysics, v. 54, p. 680-688.

Sattel, D., 2005, 2005, Inverting airborne electromagnetic (AEM) data with Zohdy's method: : Geophysics, v. 70, p. 77-85.

Saxena, K.R., 1994, Geotechnical Engineering Emerging Trend, Taylor and Frencis, 410 p.

Schneider, W.A., 1984, The Common Depth Point Stack, IEEE, Volume 72, issue 10, p. 1238-1254.

Sengpiel, K.P., 1988, Approximate inversion of airborne EM data from a multilayered ground: Geophysics Porspecting, v. 36, p. 446-459.

Sengpiel, K.P., Siemon, 2000, Advanced inversion methods for AEM exploration: 36, p. 446 -

459.

Sharma, P.V., 1986, Geophysical Methods in Geology: New York, Elsevier Science, p. 428.

Sheriff, R.E., 1991, Encyclopedic Dictionary of Exploration Geophysicists, 384 p.

Sheriff, R.E., Geldart, L.P., 1995, Exploration seismology: Cambrige, UK, Cambrige University press, p. 624.

Sheriff, R.E., 1996, Understanding the Fresnel zone: Search and Discovery article #40014, Geophysical corner, SEG.

Shevnin, V., Rodriguez, O.D., Mousatov, A., Hernandez, D.F., Martinez, H.Z., Ryjov, A., 2006, Estimation of soil petrophysical parameters from resistivity data: application to oil-contaminated site characterization: Geophysics International, v.45, #.2; p. 99 -113.

Solymar, L., Walsh, Donald., 2004, Electrical Properties of Materials: Oxford, UK, Oxford University Press, p. 416.

Sqarek, J., Dawson, M., 2006, Colbed methane expands in Canada: Oil and Gas Journal, p. 37 - 40.

Stephenson, D.E., Agnew, A. P., Anderson M.P., Baker W.H., Brimhall R.M., Caruccio F.T. Cherry J.A., Dreezen V.H., Groat C. G., Leavitt B.R., Lord W. B., McDonald J.B., Pettyjohn W.A., Sendelin L.V.A., Sommers D.A., Thompson D. R., Van Voast V., Woessner, W. W., Yare, B.S., 1981, Coal Mining and groundwater resources in the United States: Washington, DC, National Academy Press.

Stout, W., Morgan, J. J. , 1943, Sandstones and conglomerates in Ohio: Columbus, OH, Geological survey of Ohio, v. XLIV, p. 75 - 88.

Tabarovsky, L.A., 1975, Application of Integral Equation Method to Geoelectrical Problems: Novosibirsk, Russia, Nauka, p. 142.

Tatham, R.H., 1982, Vp/Vs and lithology: Geophysics, v. 47, p. 336-344.

Telford, W.M., Geldart, L.P., Sheriff, R.E., 1990, Applied Geophysics: Cambroge, UK, Cambrige University Press.

Thomas, M., 2006, *personal communication w.* V. Kaminski

Tikhonov, V.I., 1963, Regularization of incorrectly posed problems: Soviet Math. Dokl., v. 4, p. 1624 - 1627.

Tikhonov, A.N., Arsenin, V. Y., 1977, Solutions of Ill-posed Problems: New York, John Wiley and Sons, p. 258.

UBC-GIF, 2000, EM1DFM, A program library for forward modeling and inversion of frequency domain electromagnetic data over 1D structures (http://www.eos.ubc.ca/ubcgif/iag/sftwrdocs/em1dfm/intro.html).

U.S.D.A., 2006, Soil Survey Geographic (SSURGO) database for Allegheny County, Pennsylvania: Fort Worth, TX, Department of agriculture, Natural Resources Conservation Service.

U.S.D.A., 2006, Soil Survey Geographic database for Allegheny County, Pennsylvania, *in* Service, N.R.C., ed.: Fort Worth, TX, United States Department of Agriculture.

Valentino, D.W., Gates, A. E. and Glover, L., 1994, Late Paleozoic transcurrent tectonic assembly of the central Appalachian Piedmont: Tectonics, v. 13, p. 110 - 126.

Veloski, G., Lynn, 2005, EM data viewer: Pittsburgh, PA, National Energy Technology

Laboratory, US Department of Energy (computer software).

Wagner, W.R., Craft, J.L., Heyman, L. Harper, J.A., 1975, Greater Pittsburgh region geologic map and cross sections, 4-th Series, Map 42: Pittsburgh, Pennsylvania Geological Survey.

Ward, P.E., Wilmoth, B.M., 1968, Ground-Water Hydrology of the Monongahela River Basin in West Virginia: WV Geological and Economic Survey, v. 54.

Waters, K.H., 1978, Reflection Seismology - a tool for energy resource exploration: New York.

Weidelt, P., 1975, Electromagnetic Induction in 3D Structures: Geophysics, v. 41, p. 85-109.

Wendroth, O., Koszinski, S., Pena - Yevtukhiv, E., 2006, Spatial Association among Soil Hydraulic Properties, Soil Texture and Geoelectric Resistivity: Vadoze Zone Journal, v. 5, p. 341 - 355.

White, I.C., 1891, Stratigraphy of the bituminous coal field of Pennsylvania, Ohio, and West Virginia: U.S. Geological Survey Bullletin, v. 65, p. 212.

WVGES, 1968, Geologic Map of West Virginia, West Virginia Geologic and Economic Survey.

Xia, J., 2002, Using electromagnetic methods to locate abandoned brine wells in Hutchinson, Kansas, SAGEEP: Las Vegas, NV, Proceedings published on CD, p. 11.

Yakubovsky, Y.V., Lyahov, L.L., 1988, Electrorazvedka (published in Russian): Moscow, Russia, Nedra, 394 p.